

2015

Nature of magnetic excitations in the iron pnictides and its pertinence to superconductivity as studied by inelastic neutron scattering

Gregory Scott Tucker
Iowa State University

Follow this and additional works at: <http://lib.dr.iastate.edu/etd>



Part of the [Condensed Matter Physics Commons](#)

Recommended Citation

Tucker, Gregory Scott, "Nature of magnetic excitations in the iron pnictides and its pertinence to superconductivity as studied by inelastic neutron scattering" (2015). *Graduate Theses and Dissertations*. 14455.
<http://lib.dr.iastate.edu/etd/14455>

This Dissertation is brought to you for free and open access by the Graduate College at Iowa State University Digital Repository. It has been accepted for inclusion in Graduate Theses and Dissertations by an authorized administrator of Iowa State University Digital Repository. For more information, please contact digirep@iastate.edu.

Nature of magnetic excitations in the iron pnictides and its pertinence to
superconductivity as studied by inelastic neutron scattering

by

Gregory Scott Tucker

A dissertation submitted to the graduate faculty
in partial fulfillment of the requirements for the degree of
DOCTOR OF PHILOSOPHY

Major: Condensed Matter Physics

Program of Study Committee:
Robert J. McQueeney, Co-major Professor
Alan I. Goldman, Co-major Professor
Andreas Kreyssig
Bruce N. Harmon
James Cochran
Scott Beckman

Iowa State University

Ames, Iowa

2015

Copyright © Gregory Scott Tucker, 2015. All rights reserved.

For my wife, Gwendolyn.

TABLE OF CONTENTS

LIST OF TABLES	vi
LIST OF FIGURES	vii
ACKNOWLEDGEMENTS	xiii
ABSTRACT	xiv
CHAPTER 1 OVERVIEW	1
CHAPTER 2 INTRODUCTION	4
2.1 Superconductivity	4
2.1.1 Conventional superconductors	6
2.1.2 Unconventional superconductors	8
2.2 Iron-Based Superconductors	9
2.2.1 Iron pnictides	12
2.2.2 BaFe_2As_2	14
2.3 $\text{Ba}(\text{Fe}_{1-x}\text{Co}_x)_2\text{As}_2$	17
2.3.1 Superconductivity	17
2.3.2 Structure	20
2.3.3 Magnetic order	20
2.3.4 Band structure and Fermi surface	29
2.3.5 Phase diagram	35
2.3.6 Spin excitations	37
2.4 Motivation	42
CHAPTER 3 TECHNIQUES	44
3.1 Scattering	44
3.1.1 Diffraction	50
3.1.2 Inelastic scattering	56
3.2 Neutron Spectroscopy Techniques	60
3.2.1 Triple-axis	61
3.2.2 Time-of-flight	65
CHAPTER 4 METHODS AND PROCEDURES	69
4.1 Modeling Normal State Spin Excitations	71

4.1.1	Heisenberg model	71
4.1.2	BaFe ₂ As ₂	75
4.1.3	Spinwave model	76
4.1.4	Diffusive model	79
4.1.5	Ballistic model	83
4.2	Modeling Superconducting State Spin Excitations	85
4.2.1	Rescaled resonance model	85
4.2.2	Empirical resonance model	87
4.3	Neutron Scattering Data Analysis	90
4.3.1	Analysis of time-of-flight neutron scattering data	90
4.3.2	Analysis of triple-axis neutron scattering data	92
CHAPTER 5 RESULTS		94
5.1	Experiment Details and Data	94
5.1.1	ARCS time-of-flight spectrometer	94
5.1.2	HB3 triple-axis spectrometer	102
5.2	Ba(Fe _{1-x} Co _x) ₂ As ₂ and the Spinwave Model	105
5.2.1	High-energy time-of-flight analysis	105
5.2.2	High-energy time-of-flight composition dependence	109
5.2.3	Low-energy triple-axis composition dependence	112
5.3	Ba(Fe _{1-x} Co _x) ₂ As ₂ and the Diffusive Model	117
5.3.1	High-energy time-of-flight analysis	117
5.3.2	Low-energy triple-axis composition dependence	121
5.4	A Comparison of the Spinwave and Diffusive Models	121
5.4.1	High-energy time-of-flight	121
5.4.2	Low-energy triple-axis	128
5.5	Ba(Fe _{1-x} Co _x) ₂ As ₂ in the Superconducting State	132
5.6	Ba(Fe _{1-x} TM _x) ₂ As ₂	142
CHAPTER 6 SUMMARY		148
6.1	Discussion	148
6.2	Outlook	150
APPENDIX A EXPERIMENTAL DATA AND DETAILS		152
APPENDIX B SCANDATA.M		168
APPENDIX C INSTRUMENT RESOLUTION		211
APPENDIX D NORMALIZATION		217
APPENDIX E NEUTRON SCATTERING BACKGROUND		225

BIBLIOGRAPHY 230

LIST OF TABLES

Table 3.1	Properties of the neutron	46
Table 3.2	Neutron moderator energy ranges	48
Table 5.1	Time-of-flight derived $\text{Ba}(\text{Fe}_{0.953}\text{Co}_{0.047})_2\text{As}_2$ fit parameter values for the ballistic model.	107
Table 5.2	Composition dependence of $A(\text{Fe}_{1-x}\text{Co}_x)_2\text{As}_2$ ($A = \text{Ca}, \text{Sr}, \text{Ba}$) transverse propagation velocity and anisotropy of spin fluctuations.	112
Table 5.3	Fit parameter values for the spin wave model fit to low-energy triple-axis data	117
Table 5.4	Time-of-flight derived $\text{Ba}(\text{Fe}_{0.953}\text{Co}_{0.047})_2\text{As}_2$ fit parameter values for the diffusive model	120
Table 5.5	Fit parameter values for the diffusive model fit to low-energy triple-axis data	125
Table A.1	Details of the coaligned single-crystal samples used in this study.	167
Table C.1	Details of the HB3 triple-axis spectrometer relevant for the Popovici instrumental resolution approximation.	215

LIST OF FIGURES

Figure 2.1	Low temperature resistance of mercury	5
Figure 2.2	Phase diagram for the heavy fermion compound CeRhIn ₅	10
Figure 2.3	Phase diagram for electron and hole doping in cuprates	11
Figure 2.4	The room temperature crystallographic structure of BaFe ₂ As ₂	15
Figure 2.5	The low temperature crystallographic structure of BaFe ₂ As ₂	16
Figure 2.6	Room-temperature-normalized resistivity for Ba(Fe _{1-x} Co _x) ₂ As ₂	18
Figure 2.7	Low-field-normalized magnetization for Ba(Fe _{1-x} Co _x) ₂ As ₂	19
Figure 2.8	Orthorhombic distortion parameter, δ , as a function of temperature for Ba(Fe _{1-x} Co _x) ₂ As ₂ at various x	21
Figure 2.9	Applied-field-normalized magnetization for Ba(Fe _{1-x} Co _x) ₂ As ₂	23
Figure 2.10	Four tetragonal unit cells of BaFe ₂ As ₂ in the low-temperature stripe antiferromagnetic state	24
Figure 2.11	Stripe antiferromagnetic order parameter, M^2 , as a function of re- duced temperature for Ba(Fe _{1-x} Co _x) ₂ As ₂ at various x	26
Figure 2.12	Neutron diffraction scans across \mathbf{Q}_{AFM} for various cobalt concentra- tions in Ba(Fe _{1-x} Co _x) ₂ As ₂	27
Figure 2.13	Temperature dependence of integrated intensity and incommensura- bility of the antiferromagnetic order for Ba(Fe _{0.944} Co _{0.056}) ₂ As ₂	28
Figure 2.14	BaFe ₂ As ₂ calculated band structure	30
Figure 2.15	Angle-resolved photoemission spectroscopy Ba(Fe _{1-x} Co _x) ₂ As ₂ data	31

Figure 2.16	Angle-resolved photoemission spectroscopy determined Fermi surfaces for $\text{Ba}(\text{Fe}_{1-x}\text{Co}_x)_2\text{As}_2$	32
Figure 2.17	Angle-resolved photoemission spectroscopy determined Fermi surfaces for $\text{Ba}(\text{Fe}_{0.975}\text{Co}_{0.025})_2\text{As}_2$	32
Figure 2.18	An illustration of the simplified band structure model for the iron pnictides	33
Figure 2.19	Calculated stripe antiferromagnetic order parameter, M^2 , as a function of reduced temperature for $\text{Ba}(\text{Fe}_{1-x}\text{Co}_x)_2\text{As}_2$ at various x . . .	34
Figure 2.20	A comparison of the calculated and measured stripe antiferromagnetic ordered moment size for $\text{Ba}(\text{Fe}_{1-x}\text{Co}_x)_2\text{As}_2$	34
Figure 2.21	Temperature-composition phase diagram for $\text{Ba}(\text{Fe}_{1-x}\text{Co}_x)_2\text{As}_2$	35
Figure 2.22	Under- and optimally-doped $\text{Ba}(\text{Fe}_{1-x}\text{Co}_x)_2\text{As}_2$ refined temperature-composition phase diagram.	36
Figure 2.23	Temperature dependence of the spin excitations in BaFe_2As_2	39
Figure 2.24	$\text{Ba}(\text{Fe}_{0.925}\text{Co}_{0.075})_2\text{As}_2$ spin excitations as a function of temperature	40
Figure 2.25	Temperature dependence of the calculated superconducting gap magnitudes in $\text{Ba}(\text{Fe}_{0.946}\text{Co}_{0.054})_2\text{As}_2$	41
Figure 3.1	Particle wavelength versus energy	45
Figure 3.2	An illustration of coherent elastic scattering	53
Figure 3.3	An illustration of higher-order harmonic diffraction	54
Figure 3.4	An illustration of a triple-axis spectrometer	63
Figure 3.5	An illustration of a Fermi chopper	67
Figure 3.6	An illustration of a time-of-flight spectrometer	67
Figure 4.1	An illustration of the spinwave model as a function of E and q	78
Figure 4.2	An illustration of the diffusive model as a function of E and q	81

Figure 4.3	An illustration of the diffusive model with anisotropic correlation length and Landau damping as a function of E and \mathbf{q}	84
Figure 4.4	An illustration of the resonance model as a function of E and q . . .	88
Figure 4.5	An illustration of the empirical superconducting model double step function	90
Figure 5.1	Inelastic neutron scattering data measured on $\text{Ba}(\text{Fe}_{0.953}\text{Co}_{0.047})_2\text{As}_2$ at $T = 5$ K using ARCS with $E_i = 250$ meV	96
Figure 5.2	Comparison of $T = 5$ K and $T = 70$ K inelastic neutron scattering data measured on $\text{Ba}(\text{Fe}_{0.953}\text{Co}_{0.047})_2\text{As}_2$	97
Figure 5.3	Summed $T = 5$ K and 70 K inelastic neutron scattering data measured on $\text{Ba}(\text{Fe}_{0.953}\text{Co}_{0.047})_2\text{As}_2$ using ARCS with $E_i = 250$ meV	99
Figure 5.4	Slices through background subtracted $\text{Ba}(\text{Fe}_{0.953}\text{Co}_{0.047})_2\text{As}_2$ time-of-flight data with $E_i = 50$ meV	100
Figure 5.5	Superconducting minus normal state $\text{Ba}(\text{Fe}_{0.953}\text{Co}_{0.047})_2\text{As}_2$ time-of-flight data with $E_i = 50$ meV	101
Figure 5.6	Cuts through background subtracted $\text{Ba}(\text{Fe}_{0.953}\text{Co}_{0.047})_2\text{As}_2$ time-of-flight data with $E_i = 50$ meV	103
Figure 5.7	Temperature dependence of \mathbf{Q}_{AFM} spectra for $\text{Ba}(\text{Fe}_{0.985}\text{Co}_{0.015})_2\text{As}_2$ and $\text{Ba}(\text{Fe}_{0.967}\text{Co}_{0.033})_2\text{As}_2$	104
Figure 5.8	$\text{Ba}(\text{Fe}_{1-x}\text{Co}_x)_2\text{As}_2$ inelastic intensity near \mathbf{Q}_{AFM}	106
Figure 5.9	Calculations of the inelastic neutron scattering spectrum as obtained from a ballistic model of over-damped spin waves.	108
Figure 5.10	Transverse spin wave velocity in $\text{Ba}(\text{Fe}_{1-x}\text{Co}_x)_2\text{As}_2$ as a function of cobalt concentration	113
Figure 5.11	Temperature dependence of inelastic neutron scattering intensity from $\text{Ba}(\text{Fe}_{0.985}\text{Co}_{0.015})_2\text{As}_2$ and $\text{Ba}(\text{Fe}_{0.967}\text{Co}_{0.033})_2\text{As}_2$	114
Figure 5.12	Inelastic neutron scattering intensity for the series of $\text{Ba}(\text{Fe}_{1-x}\text{Co}_x)_2\text{As}_2$ compounds, fit to the spinwave model	116

Figure 5.13	Calculations of the inelastic neutron scattering spectrum as obtained from a model of itinerant diffusive spin fluctuations	119
Figure 5.14	Inelastic neutron scattering intensity for the series of $\text{Ba}(\text{Fe}_{1-x}\text{Co}_x)_2\text{As}_2$ compounds, fit to the diffusive mode	122
Figure 5.15	Time-of-flight constant energy cuts for $\text{Ba}(\text{Fe}_{0.953}\text{Co}_{0.047})_2\text{As}_2$ showing best-fit lines for the diffusive and ballistic models	123
Figure 5.16	Time-of-flight constant- Q cuts for $\text{Ba}(\text{Fe}_{0.953}\text{Co}_{0.047})_2\text{As}_2$ showing best-fit lines for the diffusive and ballistic models	124
Figure 5.17	Inelastic neutron scattering intensity for a series of $\text{Ba}(\text{Fe}_{1-x}\text{Co}_x)_2\text{As}_2$ compound	129
Figure 5.18	Model parameters for a series of $\text{Ba}(\text{Fe}_{1-x}\text{Co}_x)_2\text{As}_2$ compounds . . .	130
Figure 5.19	$\text{Ba}(\text{Fe}_{0.960}\text{Co}_{0.040})_2\text{As}_2$ triple-axis energy spectra and best-fit lines . .	133
Figure 5.20	$\text{Ba}(\text{Fe}_{0.960}\text{Co}_{0.040})_2\text{As}_2$ triple-axis momentum scans and best-fit lines	134
Figure 5.21	$\text{Ba}(\text{Fe}_{0.953}\text{Co}_{0.047})_2\text{As}_2$ triple-axis energy spectra and best-fit lines . .	135
Figure 5.22	$\text{Ba}(\text{Fe}_{0.953}\text{Co}_{0.047})_2\text{As}_2$ triple-axis momentum scans and best-fit lines	136
Figure 5.23	$\text{Ba}(\text{Fe}_{0.945}\text{Co}_{0.055})_2\text{As}_2$ triple-axis energy spectra and best-fit lines . .	137
Figure 5.24	$\text{Ba}(\text{Fe}_{0.945}\text{Co}_{0.055})_2\text{As}_2$ triple-axis momentum scans and best-fit lines	138
Figure 5.25	Integrated spectral weight as a function of x in $\text{Ba}(\text{Fe}_{1-x}\text{Co}_x)_2\text{As}_2$.	139
Figure 5.26	Superconducting minus normal state $\text{Ba}(\text{Fe}_{1-x}\text{Co}_x)_2\text{As}_2$ binned data	141
Figure 5.27	Integrated moving spectral weight as a function of $(\Delta\mu)^2$	142
Figure 5.28	Slices through background subtracted $\text{Ba}(\text{Fe}_{1-x}\text{TM}_x)_2\text{As}_2$ time-of-flight data with $E_i = 50$ meV	144
Figure 5.29	Cuts through background subtracted $\text{Ba}(\text{Fe}_{1-x}\text{TM}_x)_2\text{As}_2$ time-of-flight data with $E_i = 50$ meV	146
Figure A.1	All measured normal state $\text{Ba}(\text{Fe}_{0.985}\text{Co}_{0.015})_2\text{As}_2$ triple-axis data . .	153

Figure A.2	All measured normal state $\text{Ba}(\text{Fe}_{0.967}\text{Co}_{0.033})_2\text{As}_2$ triple-axis data . . .	154
Figure A.3	All measured constant- Q normal state $\text{Ba}(\text{Fe}_{0.960}\text{Co}_{0.040})_2\text{As}_2$ triple-axis data	155
Figure A.4	All measured constant- E normal state $\text{Ba}(\text{Fe}_{0.960}\text{Co}_{0.040})_2\text{As}_2$ triple-axis data	156
Figure A.5	All measured constant- Q normal state $\text{Ba}(\text{Fe}_{0.953}\text{Co}_{0.047})_2\text{As}_2$ triple-axis data	157
Figure A.6	All measured constant- E normal state $\text{Ba}(\text{Fe}_{0.953}\text{Co}_{0.047})_2\text{As}_2$ triple-axis data	158
Figure A.7	All measured constant- Q normal state $\text{Ba}(\text{Fe}_{0.945}\text{Co}_{0.055})_2\text{As}_2$ triple-axis data	159
Figure A.8	All measured constant- E normal state $\text{Ba}(\text{Fe}_{0.945}\text{Co}_{0.055})_2\text{As}_2$ triple-axis data	160
Figure A.9	All measured constant- Q superconducting state $\text{Ba}(\text{Fe}_{0.960}\text{Co}_{0.040})_2\text{As}_2$ triple-axis data	161
Figure A.10	All measured constant- E superconducting state $\text{Ba}(\text{Fe}_{0.960}\text{Co}_{0.040})_2\text{As}_2$ triple-axis data	162
Figure A.11	All measured constant- Q superconducting state $\text{Ba}(\text{Fe}_{0.953}\text{Co}_{0.047})_2\text{As}_2$ triple-axis data	163
Figure A.12	All measured constant- E superconducting state $\text{Ba}(\text{Fe}_{0.953}\text{Co}_{0.047})_2\text{As}_2$ triple-axis data	164
Figure A.13	All measured constant- Q superconducting state $\text{Ba}(\text{Fe}_{0.945}\text{Co}_{0.055})_2\text{As}_2$ triple-axis data	165
Figure A.14	All measured constant- E superconducting state $\text{Ba}(\text{Fe}_{0.945}\text{Co}_{0.055})_2\text{As}_2$ triple-axis data	166
Figure C.1	An illustration of triple-axis instrumental resolution effects	212
Figure C.2	Triple-axis instrumental resolution approximation for a transverse acoustic phonon in $\text{Ba}(\text{Fe}_{0.985}\text{Co}_{0.015})_2\text{As}_2$	214

Figure E.1	Constant-energy illustration of the time-of-flight background estimate technique	227
Figure E.2	Constant- K illustration of the time-of-flight background estimate technique	228

ACKNOWLEDGEMENTS

This work was supported by the U.S. Department of Energy, Office of Basic Energy Sciences, Division of Materials Sciences and Engineering at the Ames Laboratory under contract number DE-AC02-07CH11358. The Ames Laboratory is operated for the U.S. Department of Energy by Iowa State University. IS-T3130 is the document number assigned to this dissertation.

I would like to thank my committee co-chairs, Robert J. McQueeney and Alan I. Goldman, and my committee members, Andreas Kreyssig, Bruce N. Harmon, James Cochran, and Scott Beckman, for their guidance and support throughout the course of this research.

In addition, I would like to thank my friends, colleagues, the department faculty and staff for making my time at Iowa State University a wonderful experience. I want to also offer my appreciation to the instrument scientists and technicians who supported my research efforts and, without whom, this dissertation would not have been possible.

Finally, thanks to my family for their encouragement and to my wife for her years of patience, respect, support, and love.

ABSTRACT

Unconventional superconductivity and antiferromagnetism are often found in close proximity to one another. For the series of compounds $\text{Ba}(\text{Fe}_{1-x}\text{Co}_x)_2\text{As}_2$, which possesses both antiferromagnetism and superconductivity for the under-doped range of composition, this observation is certainly true. The close proximity, and in fact coexistence for under-doped $\text{Ba}(\text{Fe}_{1-x}\text{Co}_x)_2\text{As}_2$, of antiferromagnetism and superconductivity has encouraged speculation that antiferromagnetic spin fluctuations may mediate the electron pairing interaction in unconventional superconductors. Previous studies indicated that the spin fluctuations at optimally-doped $\text{Ba}(\text{Fe}_{1-x}\text{Co}_x)_2\text{As}_2$ are diffusive, while those at BaFe_2As_2 are well defined spin wave excitations. Therefore, the nature of magnetic excitations in $\text{Ba}(\text{Fe}_{1-x}\text{Co}_x)_2\text{As}_2$ must change with the introduction of cobalt; but it is unclear if that change is merely a consequence of the loss of antiferromagnetic order, or a necessary ingredient for the appearance of superconductivity. To resolve this uncertainty, this work has been undertaken to study the spin fluctuations of five $\text{Ba}(\text{Fe}_{1-x}\text{Co}_x)_2\text{As}_2$ compositions varying in cobalt concentration from lightly-doped to nearly optimally-doped as well as representative samples of other, non-superconducting, transition metal substituted BaFe_2As_2 compounds. The spin fluctuations of these samples, in their antiferromagnetically ordered and (where possible) superconducting states have been studied via triple-axis and time-of-flight inelastic neutron scattering, and definitively determine the importance of spin fluctuations for superconductivity in $\text{Ba}(\text{Fe}_{1-x}\text{Co}_x)_2\text{As}_2$.

CHAPTER 1 OVERVIEW

Superconductors can conduct electricity without resistive loss and, consequently, have potential technological applications. Superconductivity was first discovered in 1911 in mercury, which is a type-I superconductor. All type-I superconductors have limited technological utility because their superconducting state is not robust against magnetic fields or large electrical current flows. In contrast, there are materials which remain superconducting in the presence of moderate-to-strong magnetic fields and moderate-to-large electrical currents, called type-II superconductors.

The first widely-accepted theory describing superconductivity was published in 1957, forty-six years after the discovery of superconductivity. This so-called BCS theory showed how an arbitrarily weak attractive potential can provide a pairing mechanism between otherwise-repulsive electrons, at sufficiently low temperature. The paired electrons can participate in Bose-Einstein condensation after which they become insensitive to small perturbations and, as a result, flow without resistance. The BCS theory was conceived with the electron-phonon interaction in mind and materials which have properties predicted by the electron-phonon BCS theory are called conventional superconductors.

There exist materials which have superconducting properties that are not described by the electron-phonon BCS theory, these are the unconventional superconductors. Unconventional superconductivity is often found in close proximity to a different ground state, e.g., magnetic order. The close proximity to such an ordered ground state has led to speculation about the role of fluctuations in that order for unconventional superconductivity.

The discovery of the cuprate unconventional superconductors was first reported in 1986, and in less than one year it was reported that some cuprates remain superconducting at

temperatures at (and above) the boiling point of nitrogen. The cuprates superconductors are ceramics and in close proximity to a Mott insulating ground state. Due to the ready availability of nitrogen in our atmosphere and its relatively-easy liquefaction, the cuprate superconductors are technologically relevant despite difficulties related to manufacturing wires from ceramics. This utility, however, has not precipitated a widely-accepted theory of the superconductivity in the cuprates or other unconventional superconductors.

In 2008, high-temperature superconductivity was reported in an iron pnictide compound, sparking world wide interest in this new class of unconventional superconductors. The iron pnictide superconductors are in close proximity to an antiferromagnetically ordered ground state, and it is widely hoped that careful studies of fluctuations of the antiferromagnetic state will yield useful information about superconductivity in the iron pnictides. And, perhaps, give rise to a predictive theory for unconventional superconductivity.

This work aims to determine the importance of spin fluctuations for superconductivity in the iron pnictide superconductors. Because of its magnetic moment and typical energy, the thermal neutron is uniquely suitable for the study of antiferromagnetic spin fluctuations. Inelastic neutron scattering experiments have been performed on a series of unconventional superconductor samples and closely-related non-superconductor samples, collectively $\text{Ba}(\text{Fe}_{1-x}\text{TM}_x)_2\text{As}_2$ [TM = transition metal; $x = (0,1)$, the substitution fraction of the transition metal for iron], in order to study the relationship between spin fluctuations and superconductivity.

In this dissertation, chapter 2 provides a more-extensive introduction to superconductivity, the iron-pnictide superconductors, and the main focus of this work, $\text{Ba}(\text{Fe}_{1-x}\text{Co}_x)_2\text{As}_2$. A general introduction to scattering techniques and an in-depth discussion of inelastic neutron scattering is given in chapter 3. The tools developed-for and used-in this study are detailed in chapter 4. Chapter 5 presents inelastic neutron scattering data and results from applying my analysis techniques and models to the $\text{Ba}(\text{Fe}_{1-x}\text{Co}_x)_2\text{As}_2$ series and individual

Ba(Fe_{1-x}TM_x)₂As₂ compounds, namely that strong damping of spin fluctuations and large low-energy spectral weight are requisite for iron pnictide superconductivity. Finally, chapter 6 summarizes what spin fluctuations tell us about superconductivity in the iron pnictide unconventional superconductors.

CHAPTER 2 INTRODUCTION

2.1 Superconductivity

Superconductivity is a state of zero electrical resistivity and, consequently, infinite conductivity. This allows for the presence of persistent currents in superconducting materials. If a magnetic field is applied to a superconductor, an opposing persistent current will be induced which may perfectly cancel the applied field such that no field penetrates the superconducting material; this is the Meissner effect and as a result some superconductors are perfectly diamagnetic. Since superconducting materials conduct electricity without loss they have potential applications anywhere resistive losses are detrimental, such as energy transmission or the production of static magnetic fields.

An immeasurably small resistance at near-zero temperature was first reported for mercury by Kamerlingh Onnes in 1911 [1] who first postulated that this small resistance was consistent with his theory of resistance in pure metals; namely that the immeasurable small value was part of a linear temperature dependence of the resistance and was therefore finite at finite temperature but too small to be measured with the initial setup [2]. Shortly thereafter, higher sensitivity measurements continued to indicate zero resistance and Kamerlingh Onnes made the observation of a sharp increase in resistance at (slightly higher) finite temperature, as shown in figure 2.1, thus providing the first clear measure of the superconducting transition [3].

Following the discovery of superconductivity in mercury, a large number of other elements and alloys were discovered to be superconductors at low temperature [4]. The vast majority of the elemental superconductors exhibit perfect diamagnetism; this perfect Meissner effect

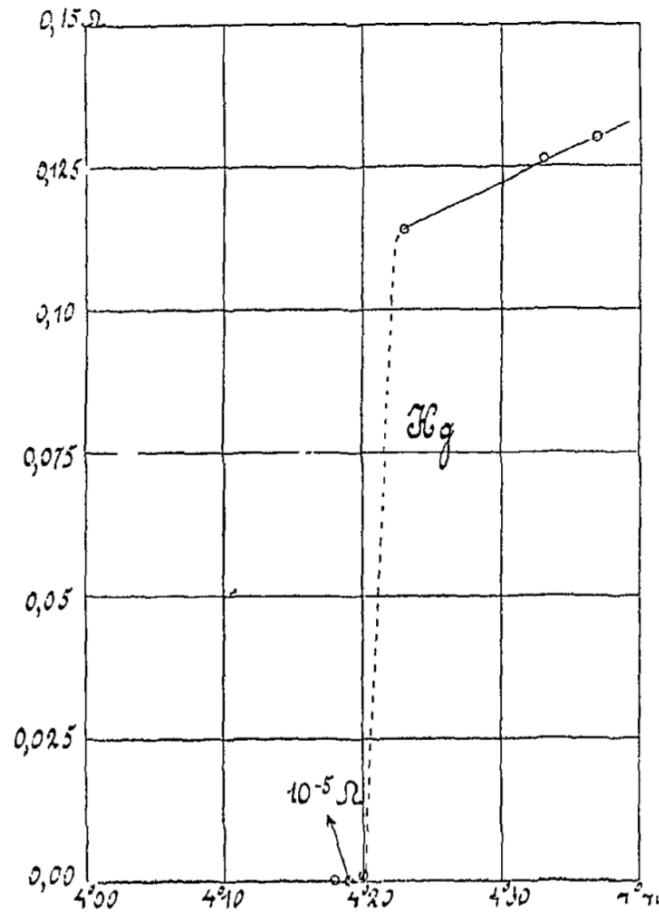


FIGURE 2.1. The low temperature resistance of mercury measured on warming and reproduced from Reference [3]. At low temperatures the immeasurably small resistance is due to mercury being a superconductor with zero resistivity. The sharp increase in resistance at finite temperature, in this case near 4.2 K, is a hallmark of superconductivity and is the critical superconducting temperature T_c . The unlabeled axes are temperature in Kelvin (abscissa) and resistance in Ohms (ordinate).

can only be maintained if the applied magnetic field energy is smaller than the energy obtained during the transition to the superconducting phase (which is typically small) and therefore weak magnetic fields are sufficient to destroy superconductivity in most elemental superconductors [5]. In contrast, some superconductors are not perfectly diamagnetic and instead allow a coexistence of normal and superconducting states. As has been shown by Abrikosov, this coexistence occurs when a magnetic field penetrates in the form of flux lines (which are normal at their core) without destroying the continuous superconducting currents [6]. Superconductors which are perfectly diamagnetic throughout their bulk, below a critical magnetic field, are called Type-I superconductors. Those that are perfectly diamagnetic below a lower critical field and allow the penetration of magnetic fields between a lower and upper critical field are denoted as Type-II. It is possible for a Type-I superconducting material to have macroscopically phase-separated superconductivity and normal behavior at the same time, dependent upon the geometric demagnetization factor; this phase-separated state is called the intermediate state [7]. Type-II superconductors can typically tolerate much larger magnetic fields than Type-I superconductors and accordingly are more suitable for the production of higher magnetic fields [5].

Despite this breadth of experimentally accessible superconductors, no viable theory of superconductivity existed until forty-six years after the discovery of the phenomenon.

2.1.1 Conventional superconductors

In 1950 Fröhlich put forward a theory in which the interaction between the electron and crystal lattice, the electron-phonon interaction, was responsible for superconductivity [8] and subsequently showed that his theory was consistent with experimental evidence that the superconducting transition temperature of an element was inversely proportional to the square root of the isotopic mass [9]. Prompted by the same experimental observations Bardeen independently – and nearly simultaneously – proposed another theory which could

explain the so-called isotope effect [10]. Ultimately these theories were proven inadequate, but they led the way to further, more successful, theories of superconductivity [11, 12]. This line of inquiry culminated in the BCS theory of superconductivity, described by J. Bardeen, L. N. Cooper, and J. R. Schrieffer [13, 14].

The BCS theory describes how electrons, through a weak attractive interaction, can form into pairs – so called Cooper-pairs. Specifically, the weak attractive interaction in the BCS theory is provided by lattice vibrations (phonons). Scattering processes between electrons and the crystal lattice, comprised of positively charged nuclei, deform the lattice and its positive charge distribution. Because of the large mass difference between nuclei and electrons this induced positive charge takes significantly longer to dissipate than the time the electron stays in the vicinity. This allows for the attraction of a second electron by the induced positive charge which is ultimately a lattice-mediated attraction between electrons.

These Cooper-pairs are comprised of two spin one-half electrons, which each fermions, with their spins anti-parallel (or, perhaps, parallel) and, ergo, have integer spin. Consequently Cooper-pairs do not follow fermionic statistics but instead behave as bosons. This bosonic nature allows the Cooper-pairs to form a Bose-Einstein-condensate whereby all Cooper-pairs can occupy the same highly-degenerate ground state [15]; it is important to note that, since some fraction of the Cooper-pairs will be broken at any finite temperature below T_c and since there are no Cooper-pairs above T_c , the total number of bosons is not conserved and the Cooper-pair quasiparticles are not a pure Bose-Einstein-condensate. Furthermore, there is no excited state above the Bose-Einstein-condensate ground state within an energy gap of magnitude $\Delta \in \mathcal{O}(k_B T_c)$. As a result of this energy gap, the Cooper-pairs are insensitive to small perturbations and can not be scattered by small lattice defects or impurities. Without a means by which to dissipate energy the Cooper-pairs flow without resistance and the material containing them is, by definition, a superconductor.

The BCS theory, although conceived with the electron-phonon interaction in mind, is not limited to a specific attractive potential. For the electron-phonon interaction, the BCS theory is able to correctly predict, among many other properties, the superconducting transition temperature (T_c) from the strength of the electron-phonon interaction, the electronic density of states at the Fermi surface, and the characteristic phonon energy. In simple cases of mono-atomic materials BCS theory also correctly reproduces the dependence of T_c on the isotopic mass, namely that

$$T_c \propto \frac{1}{\sqrt{M}}. \quad (2.1)$$

There are large number of superconductors for which the BCS theory with an electron-phonon interaction is a correct description of their physical properties, which are collectively called conventional superconductors.

2.1.2 Unconventional superconductors

In recent decades, the search for better superconductors has led to a number of empirical rules, most famously those proposed by Bernd T. Matthias:

1. a high symmetry is good, with cubic being the best,
2. a high density of electronic states is good,
3. stay away from oxygen,
4. stay away from magnetism,
5. stay away from insulators,
6. stay away from theorists;

all of which have been disproved to some degree [16]. A more recent set of empirical rules for what is beneficial for superconductivity:

1. reduced dimensionality,
2. transition metal and other ions with effectively-large Coulomb repulsion,
3. light atoms,
4. charged and multivalent ions,
5. low dielectric constant;

are not entirely self-consistent by design in order to create materials with competing phases, from which superconductivity might emerge [17]. These rules point to normal state behavior

with which previous theories are inconsistent, and significant improvements are required for the previous theories to become consistent with this novel behavior [5]. Many new superconductors tend to have complex phase diagrams as a function of chemical composition, the application of external pressure, or the application of an external magnetic field [5, 18]. The physical properties of these superconductors can not be adequately described by the electron-phonon BCS theory and they have been deemed unconventional superconductors. A number of families of unconventional superconductors are known to exist including: the heavy fermion superconductors [19], the cuprate superconductors [20], and organic superconductors [21, 22].

Competing ground states appear to precipitate the presence of superconductivity. In many cases fluctuating degrees of freedom are involved in the vicinity of magnetic or structural phase transitions and are responsible for the destruction of the order across the phase boundary [5]. Therefore, many theories ascribe the emergence of superconductivity to such fluctuations – as has been theorized for the systems mentioned above [23–26]. Given the fact that the classic characteristics of superconductors (e.g., the Meissner effect) occur independently of the microscopic mechanism, the analysis of phase diagrams with competing ordered states (see, e.g., figures 2.2 and 2.3) and a detailed study of the normal (non-superconducting) state provide important clues concerning the quantum mechanical origin of the Cooper pairing [5].

2.2 Iron-Based Superconductors

Iron was, at one point, deemed deleterious to all superconductivity due to its strong magnetic moment [29]. In the case of conventional superconductivity, this remains true as the presence of magnetic impurities in superconductors decreases their superconducting transition temperatures through spin-flip scattering which breaks Cooper pairs [30]. In some cases, such as the Chevrel compounds RMo_6Se_8 or boron carbides RNi_2B_2C (R =rare earth metal) magnetism and superconductivity coexist, though they do so without impacting each other

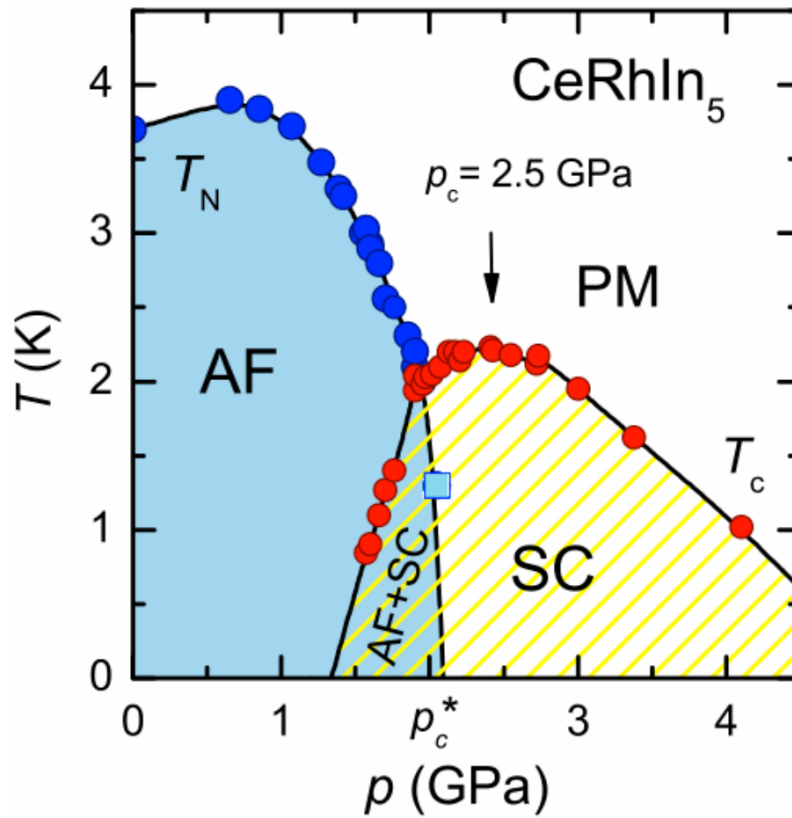


FIGURE 2.2. A phase diagram reproduced from Reference [27] showing the temperature-pressure dependence of the superconducting and antiferromagnetic phases in the heavy fermion compound CeRhIn₅. Here the application of pressure suppresses the antiferromagnetic order and eventually produces a superconducting state at low temperature.

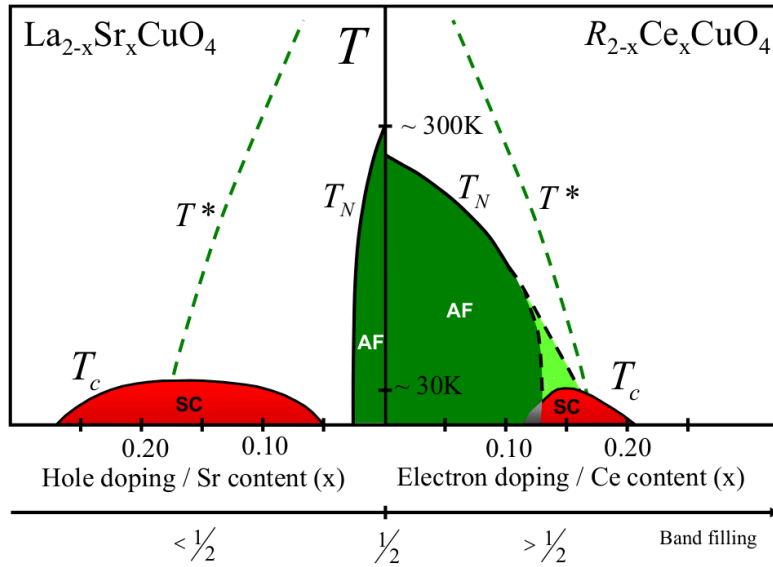


FIGURE 2.3. A phase diagram reproduced from Reference [28] showing the temperature-composition dependence of the superconducting and antiferromagnetic phases in two cuprate compounds. For $R_{2-x}Ce_xCuO_4$ ($R =$ rare earth), the horizontal axis represents the cerium concentration as x where replacing rare earth atoms by cerium atoms adds extra electrons to the compound, which is referred to as electron doping. For $La_{2-x}Sr_xCuO_4$ the horizontal axis is reversed and represents the strontium concentration as x where replacing lanthanum atoms by strontium atoms removes electrons from the compound, which is referred to as hole doping. In either case, electron or hole doping suppresses the antiferromagnetic order and eventually produces a superconducting state at low temperature.

significantly. For example, the localized $4f$ shell electrons of the rare earth are responsible for magnetic order while conduction electrons are responsible for the formation of Cooper pairs [5]. It is also possible that, so long as the coherence length of a superconducting state is large in comparison to the size of a magnetic unit cell, that the presence of antiferromagnetic order may not be as deleterious to the superconductivity as a ferromagnetic state built from the same magnetic moments; since the average magnetization of an antiferromagnet is zero over length scales greater than the magnetic unit cell.

A number of compounds containing nonmagnetic iron have been discovered; first U_6Fe by Chandrasekhar and Hulm in 1958 with $T_c = 3.86$ K [31], followed by Th_7Fe_3 by Matthias et al. in 1961 with $T_c = 1.86$ K [32], $Lu_2Fe_3Si_5$ by Braun in 1980 with $T_c = 6.1$ K [33], $LaFe_4P_{12}$ by Meisner in 1981 with $T_c = 4.08$ K [34], and $\beta''-(bedt-ttf)_4[(H_2O)Fe(C_2O_4)_3] \cdot PhCN$ by Graham et al. in 1995 with $T_c = 8.5$ K [35].

Meisner's discovery of $LaFe_4P_{12}$ marked the first superconducting compound containing both iron and a pnictogen (an element from the column of the periodic table containing nitrogen and phosphorous). Continuing on along the same vein, Shirovani et al. reported in 2003 that replacing the lanthanum with yttrium forms YFe_4P_{12} with $T_c = 7$ K [36]. In 2006 Kamihara et al. [37] reported the discovery of superconductivity in $LaFePO$ at $T_c = 3$ K and that, by substituting fluorine for oxygen in $LaFePO_{1-x}F_x$, the superconducting transition temperature could be increased to 5 K. After a subsequent report in 2008 by Kamihara et al. [38] that replacing phosphorous with arsenic further increases the superconducting transition temperature to $T_c = 26$ K in $LaFeAsO_{1-x}F_x$, interest in these and related iron-based superconductors skyrocketed worldwide.

2.2.1 Iron pnictides

While the skutterudite iron-based superconductors RFe_4P_{12} ($R =$ yttrium, lanthanum) have a three dimensional iron structure of Fe-P octahedra, the iron in $LaFePnO_{1-x}F_x$ ($Pn =$

phosphorus, arsenic) forms a layered structure comprised of Fe-*Pn* tetrahedra [37]. This same layered Fe-*Pn* tetrahedral structure is common to other subsequently discovered iron-based superconductors and is the source of the class name iron pnictide – used to identify all compounds containing these common Fe-*Pn* tetrahedra layers. This layered transition-metal structure is somewhat reminiscent of the extensively studied cuprate superconductors, which contain Cu-O layers, and the similarity between the cuprate and iron pnictide superconductors is at least partially responsible for the rapid increase in research of iron-based superconductors after 2008 [39].

In very quick order it was reported by Takahashi et al. [40] that by applying pressure to $\text{LaFeAsO}_{1-x}\text{F}_x$ the superconducting transition temperature could be increased to $T_c = 43$ K. Furthermore, by replacing the nonmagnetic rare earth lanthanum by one or more magnetic rare earths the superconducting transition temperature can be pushed as high as $T_c = 56.3$ K [41–44]. In contrast to the nonmagnetic rare earth varieties the application of pressure to these higher- T_c variants suppresses the superconducting transition to lower temperatures [45].

Early on, an intense search of the periodic table for other compounds containing layers of Fe-*Pn* tetrahedra was started; which led to the discovery of additional classes of iron pnictides. Among those are the 122 compounds, AEFe_2Pn_2 and RFe_2Pn_2 (E =alkaline earth metal, Pn =pnictogen, R =rare earth metal) [46–48]; and the 111 compounds, AFePn (A =alkali metal, Pn =pnictogen) [49–51]. The discovery of these other iron pnictide classes prompted the naming of RFeAsO compounds as the 1111 class. Further exploratory efforts through the periodic table led to the discovery of the iron chalcogenide superconductors, such as FeSe which exhibits superconductivity below $T_c = 8$ K [52]. The iron chalcogenides are similar to the iron pnictides in that they contain a layered Fe-*Ch* (Ch =chalcogenide) structure reminiscent of the Fe-*Pn* layered structure of the iron pnictides. FeSe is a member of the 11 family of iron chalcogenide superconductors.

2.2.2 BaFe₂As₂

Despite the fact that the 1111 compounds were discovered first, the majority of research effort has been invested in the 11 and 122 compounds due to the availability of large single crystal samples. Within the 122 compounds one particular parent compound, BaFe₂As₂, has held a great deal of interest. One explanation for this interest is that BaFe₂As₂ can exhibit superconductivity via a variety of methods: the application of pressure produces a superconducting state with characteristic temperature as high as $T_c = 30$ K [53]; substitution of potassium for barium produces maximal $T_c = 38$ K for Ba_{0.6}K_{0.4}Fe₂As₂ [54]; substitution of phosphorus for arsenic produces maximal $T_c = 30$ K for BaFe₂(As_{0.68}P_{0.32})₂ [55]; and, perhaps somewhat surprisingly given e.g., the sensitivity of unconventional superconductivity to disorder in the copper-oxygen planes of the cuprates, a long list of different transition metal elements can be substituted for iron to produce a superconductor, specifically any one of (cobalt, nickel, ruthenium, rhodium, palladium, iridium, platinum).

At ambient temperature BaFe₂As₂ is paramagnetic and has the body-centered-tetragonal $I4/mmm$ crystallographic structure characteristic of ThCr₂Si₂, shown in figure 2.4, with lattice constants $a = 3.9621(8)$ Å and $c = 13.018(2)$ Å [56]. Upon cooling BaFe₂As₂ undergoes an orthorhombic structural transition to $Fmmm$ at $T_S = 134.5$ K followed by the appearance of long range antiferromagnetic order at $T_N = 133.75$ K [57]. Figure 2.5 shows the low temperature $Fmmm$ unit cell and antiferromagnetic order of BaFe₂As₂. The antiferromagnetic (AFM) order is characterized by antiferromagnetic correlations between neighboring iron atoms along the orthorhombic \mathbf{a} direction, ferromagnetic correlations along the orthorhombic \mathbf{b} direction, and antiferromagnetic correlations along the \mathbf{c} direction. This antiferromagnetic order is often referred to as stripe antiferromagnetism and has the magnetic propagation vector $\boldsymbol{\tau} = (\frac{1}{2} \frac{1}{2} 1)_T = (101)_O$ where the subscript T indicates that the tetragonal unit cell indices are used or the subscript O indicates that the orthorhombic cell is used.

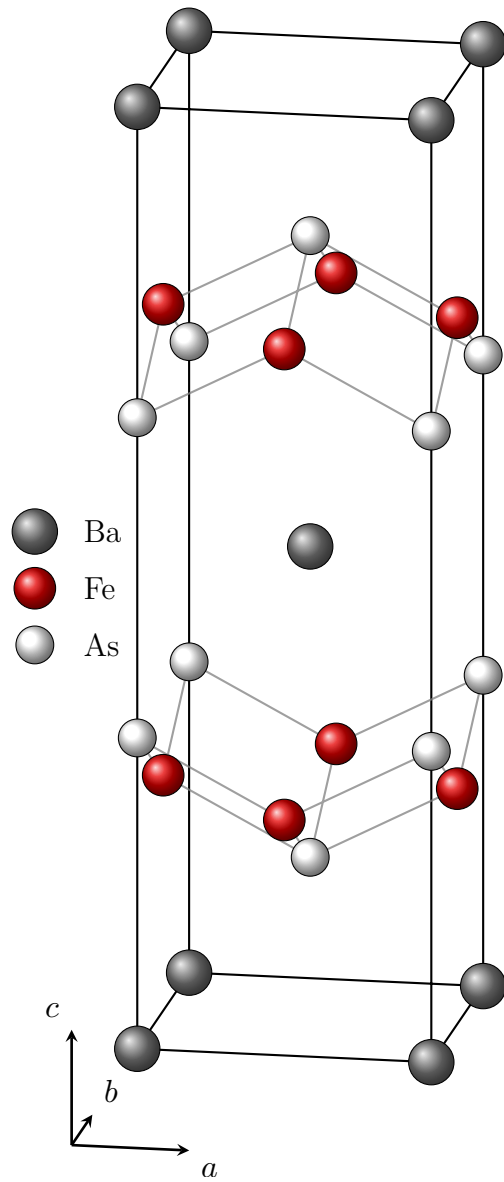


FIGURE 2.4. The room temperature crystallographic structure of BaFe₂As₂, with space group $I4/mmm$.

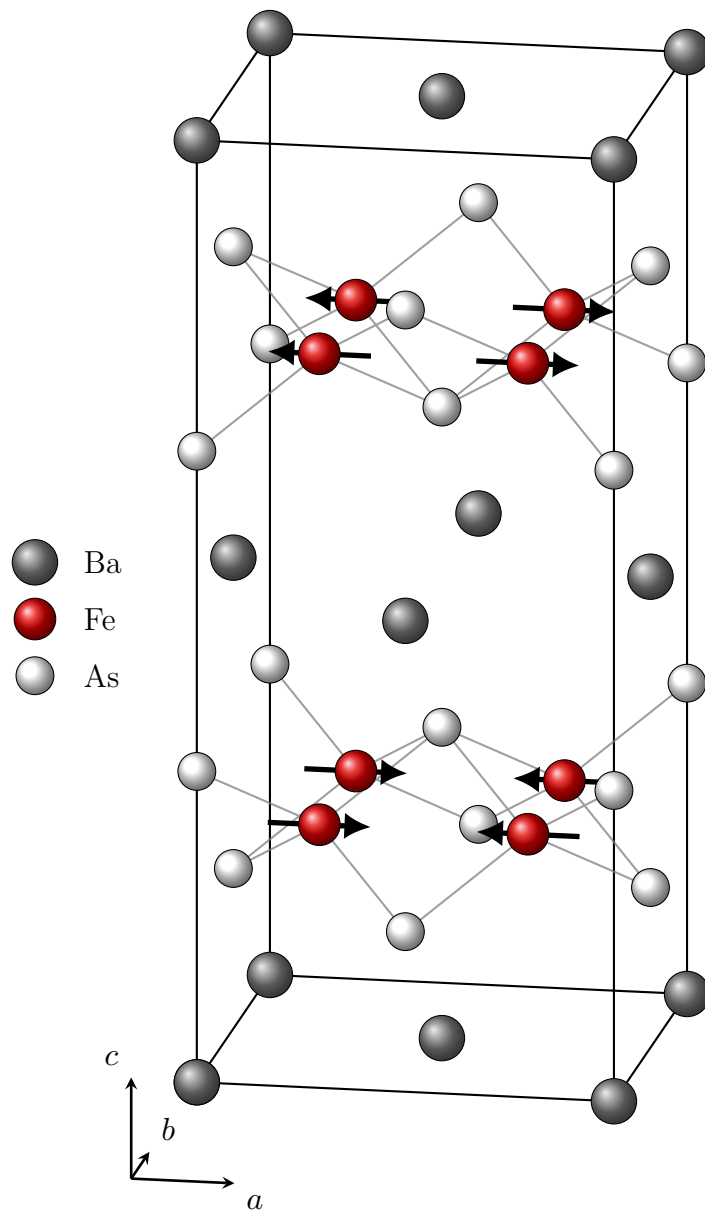


FIGURE 2.5. The low temperature crystallographic structure of BaFe₂As₂, with space group *Fmmm*. The directions of the stripe antiferromagnetically ordered iron moments are also shown as black arrows overlaid on the iron atoms.

Due to the availability of a wide range of routes to achieve superconductivity in the iron pnictides it would be impossible to produce a fully-comprehensive in-depth study of the properties of iron pnictide superconductors and, consequently, some focus is required. In this work, focus has been placed on cobalt substitution for iron in BaFe_2As_2 since: (i) cobalt is an easy analog for other transition metal dopants in BaFe_2As_2 ; (ii) transition metal substitution-induced superconductivity is, perhaps, similar to pressure-induced, alkaline earth metal substitution-induced, and pnictogen substitution-induced superconductivity in BaFe_2As_2 ; (iii) superconductivity in BaFe_2As_2 -based compounds is characteristic of all 122 compounds; and (iv) the 122 compounds are likely a good representative of the iron pnictides as a whole. As such, all further discussion will be limited to $\text{Ba}(\text{Fe}_{1-x}\text{Co}_x)_2\text{As}_2$.

2.3 $\text{Ba}(\text{Fe}_{1-x}\text{Co}_x)_2\text{As}_2$

Following initial interest in 1111 compounds, superconductivity was discovered in the 122 compounds in potassium-substituted BaFe_2As_2 [54]. Due to high reactivity and rapid oxidation at ambient conditions, the substitution of an alkali metal for an alkaline earth metal can be troublesome and, as a result, other means of inducing superconductivity in BaFe_2As_2 were explored, including substituting cobalt for iron to produce $\text{Ba}(\text{Fe}_{1-x}\text{Co}_x)_2\text{As}_2$ [58].

2.3.1 Superconductivity

As shown in figure 2.6, the resistivity of BaFe_2As_2 remains finite down to $T_{\text{min}} = 2$ K and due to the relatively large value of its residual resistivity ratio (the ratio of zero-temperature resistivity to room-temperature resistivity) BaFe_2As_2 is often referred to as a poor metal. By introducing small amounts of cobalt for iron the residual resistivity ratio, which can be approximated by extrapolating the data in the inset of figure 2.6 to $T = 0$, increases as one would expect for a random distribution of dopant atoms due to impurity scattering [59, p. 321].

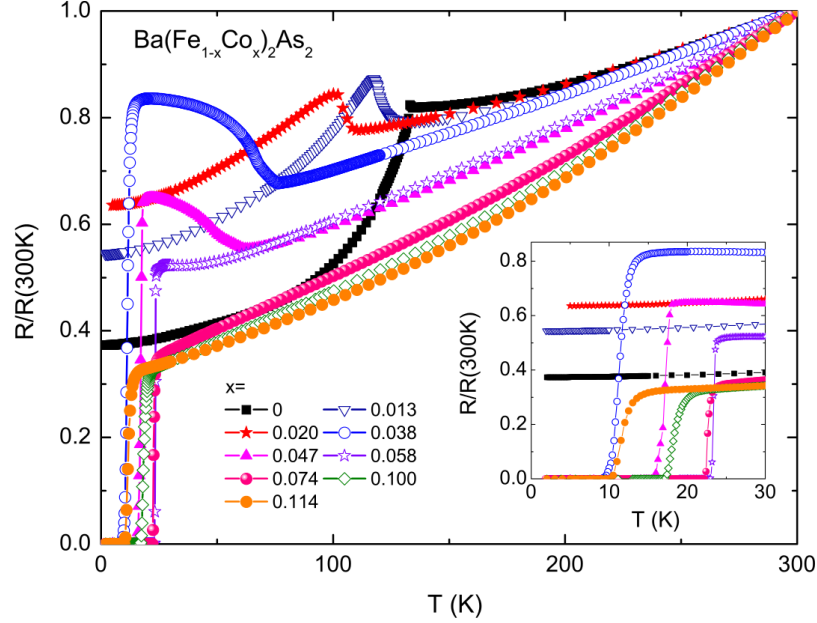


FIGURE 2.6. Room-temperature-normalized resistivity for various x in $\text{Ba}(\text{Fe}_{1-x}\text{Co}_x)_2\text{As}_2$, reproduced from Reference [60]. For low cobalt concentrations the resistivity decreases with decreasing temperature and shows one or two changes in slope, indicative of a phase transition, yet remains finite at the lowest measured temperature of $T \sim 2$ K. Above a critical concentration $x_c \sim 0.038$ the low-temperature resistivity drops to zero upon entering a superconducting state. Further increasing the cobalt concentration beyond $x \sim 0.058$ removes any evidence of the higher-temperature phase transition(s).

Further increasing the concentration of cobalt introduces a sudden drop to zero resistivity at a characteristic temperature, T_c , which is a hallmark of superconductivity. Evidence for superconductivity is also shown in figure 2.7 where the low-temperature magnetization approaches complete diamagnetism for the zero-field-cooled case below T_c , indicating bulk superconductivity.

If one defines the critical concentration for the appearance of superconductivity, x_c , as that concentration which would have a superconducting transition $T_c = 0$ K, then the data in figure 2.6 clearly indicate that $x_c < 0.038$ and that likely $x_c > 0.020$.

Examining the inset of figure 2.6, it is clear that the superconducting transition temperature, T_c , increases with cobalt concentration up to $x = 0.058$. For higher cobalt concentrations

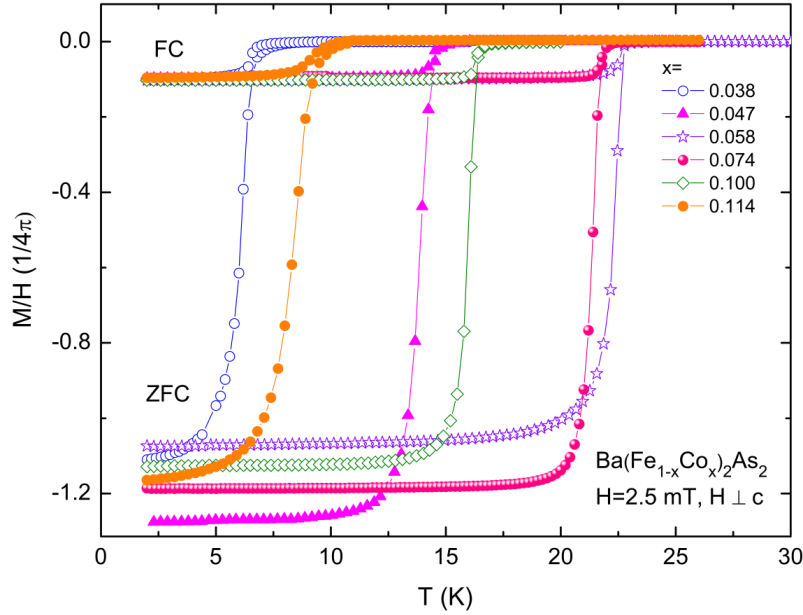


FIGURE 2.7. Magnetization divided by applied field, M/H , as a function of temperature for $\text{Ba}(\text{Fe}_{1-x}\text{Co}_x)_2\text{As}_2$, reproduced from Reference [60]. Here a field of 2.5 mT was applied perpendicular to the crystallographic c axis. Zero-field-cooled-warming data as well as field cooled data are shown.

T_c then decreases and, beyond the doping range shown in figure 2.6, superconductivity disappears entirely. This “bubble” of superconductivity seems to be a general characteristic of unconventional superconductors and is often referred to as the superconducting dome. For $\text{Ba}(\text{Fe}_{1-x}\text{Co}_x)_2\text{As}_2$, the optimal doping level (x_o), where T_c is a maximum, appears to occur somewhere between $0.058 < x_o < 0.074$; however, the change in T_c with x is small in this concentration range and cobalt concentrations over the range $0.06 < x_o < 0.08$ are typically referred to as optimally-doped. Superconducting $\text{Ba}(\text{Fe}_{1-x}\text{Co}_x)_2\text{As}_2$ compounds with $x < x_o$ are called under-doped, and those with $x > x_o$ are termed over-doped. $\text{Ba}(\text{Fe}_{1-x}\text{Co}_x)_2\text{As}_2$ with $0 < x < x_c$ remain poor metals in their ground state and are collectively referred to as the lightly-doped compounds.

2.3.2 Structure

Like BaFe_2As_2 , $\text{Ba}(\text{Fe}_{1-x}\text{Co}_x)_2\text{As}_2$ has a tetragonal $I4/mmm$ structure at room temperature, independent of cobalt concentration. For low levels of cobalt substitution, cooling $\text{Ba}(\text{Fe}_{1-x}\text{Co}_x)_2\text{As}_2$ below ambient temperature leads to the same orthorhombic structural transition as found for BaFe_2As_2 , except that T_S is suppressed with increasing cobalt concentration. Evidence for this structural transition is seen in the resistivity data presented in figure 2.6 as a discontinuity in the derivative of the resistivity versus temperature curve.

Figure 2.8, reproduced from Reference [61], shows a measure of the orthorhombic distortion, δ , for various x in $\text{Ba}(\text{Fe}_{1-x}\text{Co}_x)_2\text{As}_2$, characterized by

$$\delta = \frac{a - b}{a + b} \quad (2.2)$$

where a and b are lattice parameters of the orthorhombic unit cell. If $a = b$, the structure is tetragonal and $\delta = 0$. Below the structural transition temperature, T_S , $a \neq b$ and, consequently, the orthorhombic distortion becomes finite, with $\delta > 0$ (and $a > b$).

The magnitude of the orthorhombic distortion increases below the onset of orthorhombic order at T_S and, for cobalt concentrations which exhibit superconductivity like those shown in figure 2.8, δ decreases below T_c . This decrease in orthorhombicity is an indication that superconductivity and the orthorhombic distortion compete. In fact, the maximum magnitude of the orthorhombic distortion decreases as the cobalt concentration is increased and, as optimal doping is approached, the orthorhombic distortion is absent – first deep within the superconducting state and then entirely.

2.3.3 Magnetic order

Like BaFe_2As_2 , lightly- and under-doped $\text{Ba}(\text{Fe}_{1-x}\text{Co}_x)_2\text{As}_2$ exhibit long range antiferromagnetic order at low temperatures. Evidence for this magnetic transition is seen in

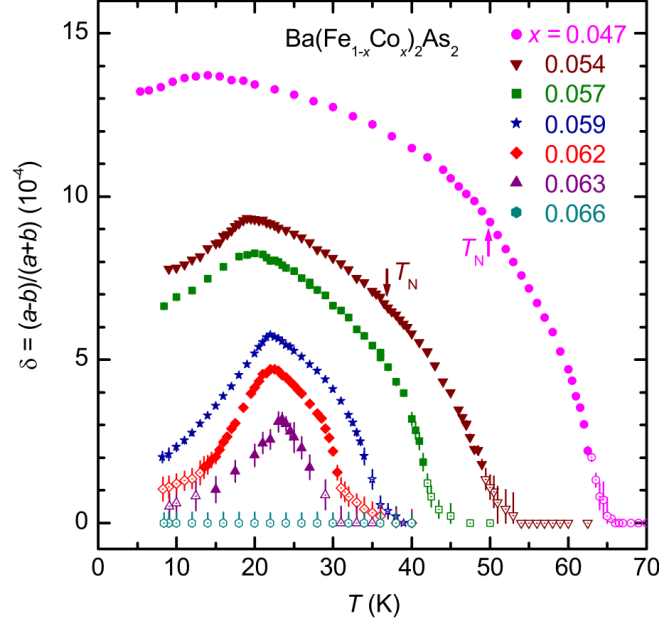


FIGURE 2.8. Orthorhombic distortion parameter, δ , as a function of temperature at $x = \{0.047, 0.054, 0.057, 0.059, 0.062, 0.063, 0.066\}$ in $\text{Ba}(\text{Fe}_{1-x}\text{Co}_x)_2\text{As}_2$, reproduced from Reference [61]. The orthorhombic distortion parameter is the normalized difference between the orthorhombic a and b lattice parameters, and is defined as $\delta = \frac{a-b}{a+b}$. For high temperatures $\text{Ba}(\text{Fe}_{1-x}\text{Co}_x)_2\text{As}_2$ is tetragonal and there is no orthorhombic distortion, i.e., $\delta = 0$. The temperature where δ deviates from 0 is T_S , which is clearly suppressed with increasing cobalt concentration. Until, for $x = 0.066$, the orthorhombic distortion is zero at all temperatures and $\text{Ba}(\text{Fe}_{0.934}\text{Co}_{0.066})_2\text{As}_2$ is tetragonal even at base temperature. The onset of superconductivity is clearly evident in this orthorhombic distortion data as a decrease in the orthorhombic distortion below T_c . As T_c increases the maximum value of δ decreases until, near optimal doping, the orthorhombic distortion is zero at all temperatures.

the magnetization data presented in figure 2.9 as a discontinuity in the derivative of the magnetization over applied field versus temperature curve. Similarly, a discontinuity in the resistivity data presented in figure 2.6 is also evident at the same temperatures and indicates the same magnetic transition.

Because the orthorhombic distortion at low temperatures in lightly- and under-doped $\text{Ba}(\text{Fe}_{1-x}\text{Co}_x)_2\text{As}_2$ is small and not easily resolved by neutron diffraction, descriptions of neutron scattering data often utilize the tetragonal reciprocal lattice notation when reporting details of the antiferromagnetic magnetic structure. Figure 2.10 shows four tetragonal unit cells of BaFe_2As_2 in the low-temperature stripe antiferromagnetic state – ignoring the small orthorhombic distortion. Included in figure 2.10 are the iron moments and their orientations, plus highlighted planes of iron moments that describe the antiferromagnetic wavevector, \mathbf{Q}_{AFM} . Note that, due to a 45° rotation about \mathbf{c} between the tetragonal and orthorhombic unit cells, the iron ordered moment direction appears to be different in the two representations with $\hat{\boldsymbol{\mu}} = \frac{\sqrt{2}}{2} [110]_{\text{T}} = [100]_{\text{O}}$, where the subscripts T and O indicate that tetragonal and orthorhombic notation are used, respectively. That is, the iron moments point along the basal-plane diagonal in the tetragonal representation and along the \mathbf{a} direction in the orthorhombic representation.

The order parameter for long-range magnetic order, represented by the magnitude of the sublattice magnetization, proportional to the square root of the integrated intensity of the associated magnetic Bragg reflection, and described by a propagation vector which can be added to any crystallographic reciprocal lattice vector to yield a magnetic reciprocal lattice vector. For antiferromagnetic order the magnetic propagation vector is typically non-zero and (if the magnetic propagation vector is not also a crystallographic reciprocal lattice vector) the magnetic reciprocal lattice points do not coincide with crystallographic reciprocal lattice points. In this case, the intensity measured for a magnetic Bragg reflection can be uniquely attributed to the magnetic order and is proportional to the square of the

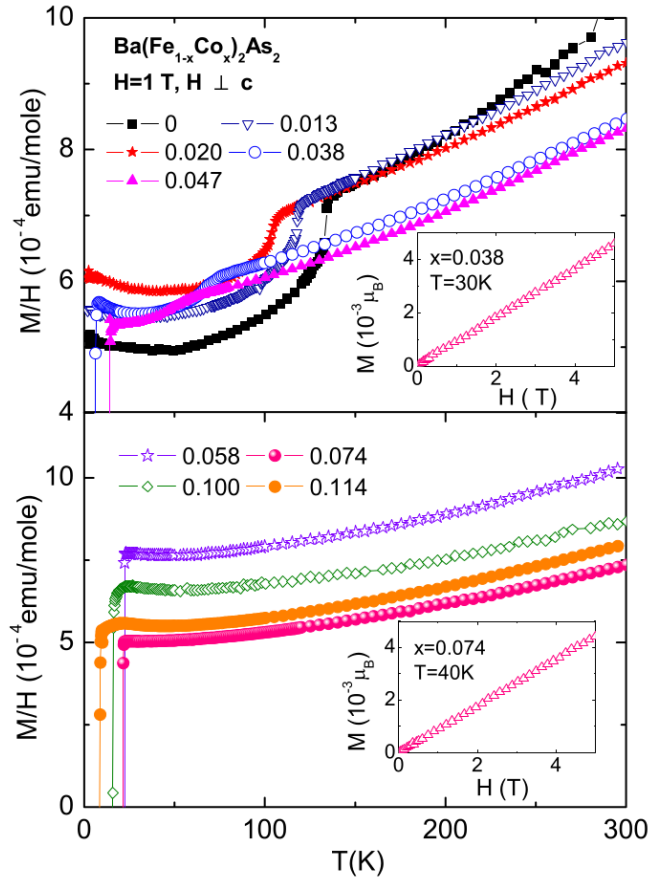


FIGURE 2.9. Magnetization divided by applied field, M/H , as a function of temperature for $\text{Ba}(\text{Fe}_{1-x}\text{Co}_x)_2\text{As}_2$, reproduced from Reference [60]. Here a field of 1 T was applied perpendicular to the crystallographic c axis. The top panel shows data for cobalt concentrations no greater than $\text{Ba}(\text{Fe}_{0.953}\text{Co}_{0.047})_2\text{As}_2$, while the bottom panel contains data for higher cobalt concentrations. In both panels an inset shows a linear dependence of the magnetization on applied field for select compositions.

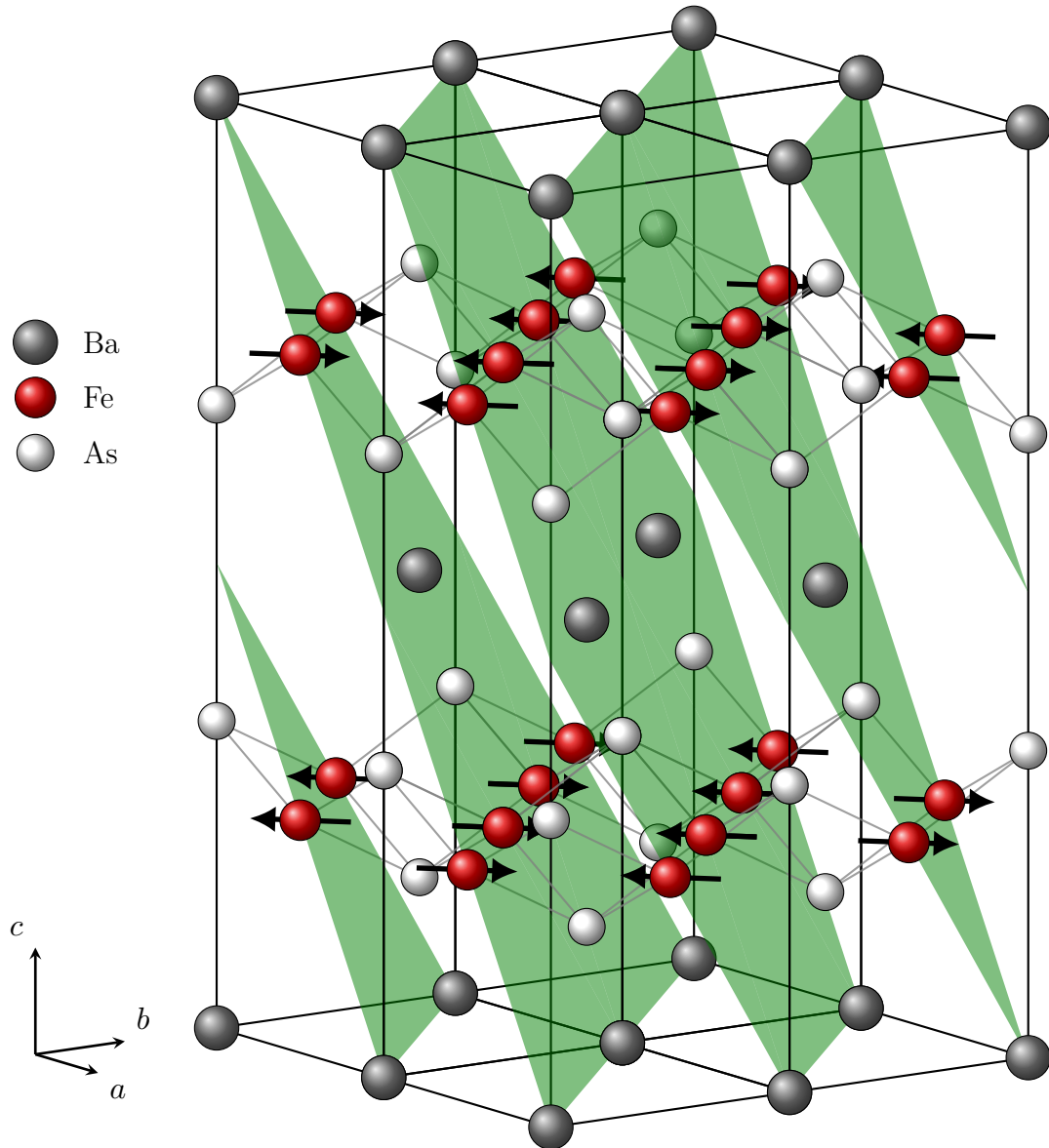


FIGURE 2.10. Four tetragonal unit cells of BaFe_2As_2 in the low-temperature stripe antiferromagnetic state, ignoring the small orthorhombic distortion. Iron moments and their directions are indicated as black arrows. The green shaded regions highlight planes of iron moments that contribute to the $Q_{\text{AFM}} = (\frac{1}{2} \frac{1}{2} 1)$ Bragg reflection.

magnitude of the ordered magnetic moment. Figure 2.11 shows the integrated intensity of the $\mathbf{Q}_{\text{AFM}} = (\frac{1}{2} \frac{1}{2} 3)_{\text{T}} = (103)_{\text{O}}$ Bragg reflection as a function of reduced temperature for a series of cobalt levels in $\text{Ba}(\text{Fe}_{1-x}\text{Co}_x)_2\text{As}_2$. Like the structural phase transition, the antiferromagnetic phase transition is suppressed to lower temperature with increasing cobalt concentration – this is not evident in figure 2.11 since the temperature has been rescaled by the antiferromagnetic ordering temperature, T_{N} , for each sample but is clearly seen also by resistivity and magnetization measurements as shown in figures 2.6 and 2.9. For non-superconducting samples, the antiferromagnetic order parameter increases below T_{N} and reaches a maximum at zero temperature; the data presented in figure 2.11 has been normalized by the zero-temperature extrapolated value of the squared ordered moment per iron of BaFe_2As_2 . For samples which manifest superconductivity at low temperatures the magnitude of the ordered moment per iron reaches a maximum at the superconducting transition temperature, T_{c} , and decreases as the temperature is further lowered. As the cobalt concentration approaches optimal doping the antiferromagnetic order in the superconducting state is completely suppressed. This is evidence that stripe antiferromagnetic order and superconductivity compete in under-doped $\text{Ba}(\text{Fe}_{1-x}\text{Co}_x)_2\text{As}_2$. Given also the observation of reentrant behavior of the orthorhombic distortion and the lack of any observed coexistence of orthorhombic and tetragonal order by x-ray diffraction, it seems likely that superconductivity and antiferromagnetism coexist within the same volume in under-doped $\text{Ba}(\text{Fe}_{1-x}\text{Co}_x)_2\text{As}_2$ and the competition is not a result of phase separation.

Further studies into the nature of the antiferromagnetic order in cobalt substituted BaFe_2As_2 found that when approaching optimal doping, and the complete suppression of long range antiferromagnetic order, the order becomes incommensurate with the crystallographic structure due to a doping-induced mismatch in the sizes of the hole- and electron-pockets leading to an imperfect Fermi surface nesting [63]. The incommensurate order propagation vector was found to be offset from the commensurate propagation vector $\boldsymbol{\tau}_{\text{c}} = [\frac{1}{2} \frac{1}{2} 1]_{\text{T}} =$

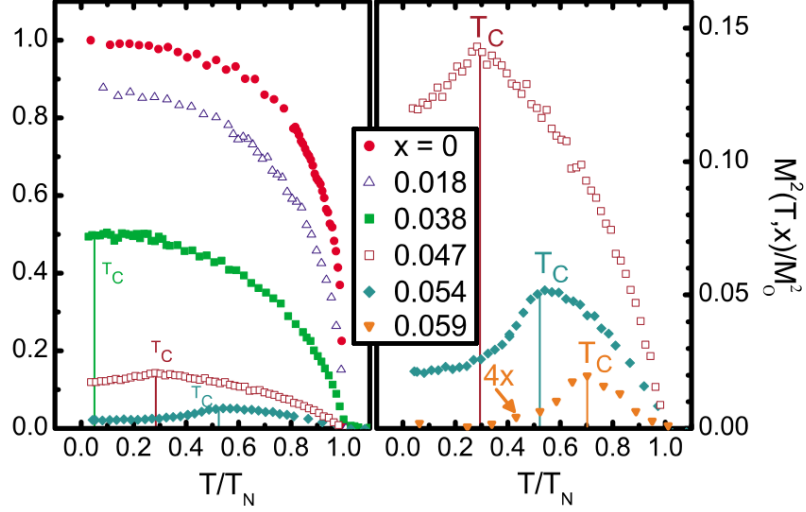


FIGURE 2.11. Stripe antiferromagnetic order parameter, integrated intensity at $\mathbf{Q}_{\text{AFM}} = (\frac{1}{2} \frac{1}{2} 3)_{\text{T}} = (103)_{\text{O}}$, for $x = \{0, 0.018, 0.038, 0.047, 0.054, 0.059\}$ in $\text{Ba}(\text{Fe}_{1-x}\text{Co}_x)_2\text{As}_2$, reproduced from reference [62]. The integrated intensity at \mathbf{Q}_{AFM} as a function of temperature and composition is proportional to the square of the ordered magnetic moment, $M^2(T, x)$. The data presented here has been normalized by the $T = 0$, $x = 0$ squared moment [$M_0 \equiv M(0, 0) = 0.87 \mu_{\text{B}}$], and is displayed as a function of reduced temperature T/T_{N} .

$[101]_{\text{O}}$ by $\epsilon = [\frac{1}{2}\epsilon \frac{1}{2}\bar{\epsilon} 0]_{\text{T}} = [0\epsilon 0]_{\text{O}}$,

$$\tau_{\text{ic}} = \tau_{\text{c}} \pm \epsilon \quad (2.3)$$

where the subscripts c and ic stand for commensurate and incommensurate, respectively. Figure 2.12 shows neutron diffraction measured intensity for a series of cobalt concentrations in $\text{Ba}(\text{Fe}_{1-x}\text{Co}_x)_2\text{As}_2$ nearing the complete suppression of long range antiferromagnetic order. At the lowest composition shown, $x = 0.054$, the scan in the $[010]_{\text{O}}$ direction across $\mathbf{Q}_{\text{AFM}} = (103)_{\text{O}}$ shows a single sharp peak indicative of long range commensurate stripe antiferromagnetic order. With increasing cobalt, the scans show two split peaks centered at \mathbf{Q}_{AFM} but offset by $\pm\epsilon$ first in addition to the single center peak and then in its stead. These side peaks are characteristic of an incommensurate antiferromagnetic order, and their appearance first as additional peaks is an indication that the transition in cobalt composition

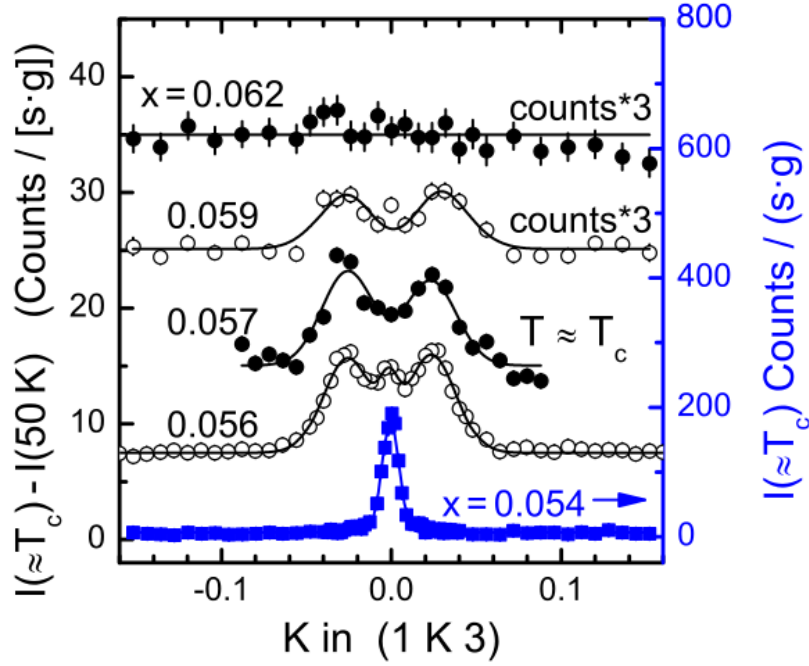


FIGURE 2.12. Neutron diffraction scans across $\mathbf{Q}_{\text{AFM}} = (103)_{\text{O}}$ in the $[010]_{\text{O}}$ direction for $x = \{0.054, 0.056, 0.057, 0.059, 0.062\}$ in $\text{Ba}(\text{Fe}_{1-x}\text{Co}_x)_2\text{As}_2$, reproduced from Reference [63]. These data have been normalized by counting time and sample mass, rescaled where indicated and offset vertically for clarity. The appearance of peaks to either side of \mathbf{Q}_{AFM} with cobalt composition is due to a first-order change in the long range antiferromagnetic order from commensurate to incommensurate near the total suppression of antiferromagnetism as optimal doping is approached.

is first-order in nature [63]. As noted by Pratt et al., “the sharpness of the superconducting transition, predictable evolution of T_{S} and T_{N} with relatively small changes in composition, and uniformity of the [wavelength dispersive x-ray spectroscopy] signal at multiple locations on the crystals confirm good chemical homogeneity with compositional spread $\delta x/x < 5\%$,” and, therefore, the coexistence of commensurate and incommensurate peaks is not likely due to sample inhomogeneity [63].

Figure 2.13 shows the temperature dependence of the integrated intensity of the incommensurate peaks for $\text{Ba}(\text{Fe}_{0.944}\text{Co}_{0.056})_2\text{As}_2$ (one of the compounds studied by Pratt et al.) as well as the temperature dependence of the magnitude of the incommensurability, ϵ . Like the commensurate order integrated intensity shown in figure 2.11, the integrated intensity

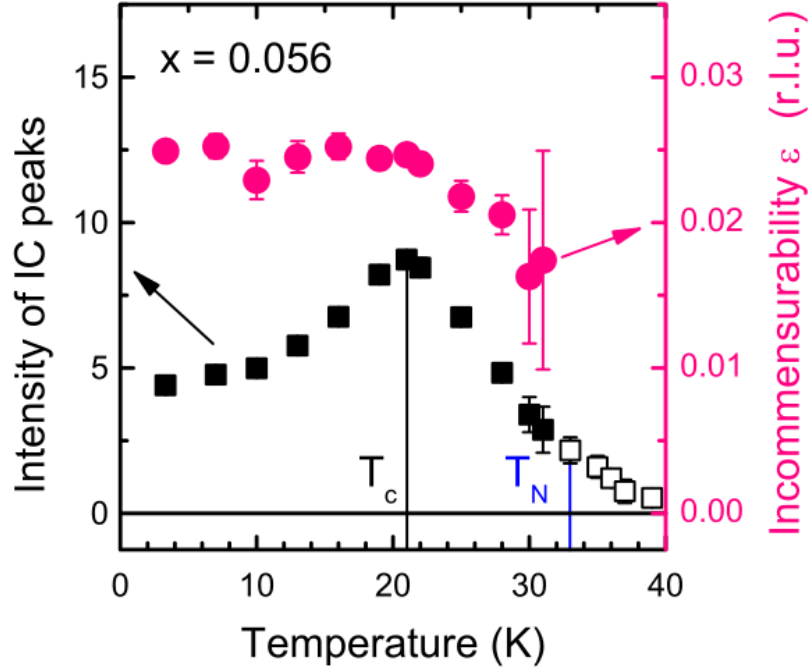


FIGURE 2.13. Integrated intensity and incommensurability of the antiferromagnetic order near $(103)_O$ for $\text{Ba}(\text{Fe}_{0.944}\text{Co}_{0.056})_2\text{As}_2$ as a function of temperature, reproduced from Reference [63]. The integrated intensity of all magnetic intensity near $(103)_O$ (open squares) and of the incommensurate side-peaks (solid squares) is presented in arbitrary units on the left ordinate; and like the commensurate order integrated intensity shown in figure 2.11, increases below T_N , reaches a maximum at T_c , and then decreases with decreasing temperature due to competition between antiferromagnetism and superconductivity. The incommensurability, ϵ , (closed circles) is shown in relative lattice units on the right ordinate. Above T_N the incommensurate peaks can not be separated from background or the central commensurate peak. Just below T_N , the incommensurability has a large uncertainty due to a continued difficulty in separating the commensurate and incommensurate signals. As the temperature is lowered further, the incommensurability reaches a steady value and remains approximately constant below T_c .

of the incommensurate peaks shown in figure 2.13 increases with increasing temperature while in the coexisting superconducting and antiferromagnetic phase, the integrated intensity reaches a maximum at the superconducting transition temperature, T_c , and then decreases as the antiferromagnetic transition temperature, T_N , is approached. At the same time, the incommensurability remains nearly constant with increasing temperature while in the coexisting phase, and then decreases slightly after the loss of superconductivity where the incommensurability has a large uncertainty due to a difficulty in separating the commensurate and incommensurate signals. Above T_N the incommensurate peaks can not be separated from background or the central commensurate peak, and figure 2.13 instead shows the integration of all intensity near $\mathbf{Q} = (1\ 0\ 3)_O$.

2.3.4 Band structure and Fermi surface

Since the parent compounds of the iron pnictide superconductors are antiferromagnetic metals at low temperatures, it seems appropriate to expect that their magnetic order comes from itinerant electrons. The small magnetic moment size measured by neutron scattering, as shown in figure 2.11, also points toward an itinerant description of the magnetism over a local-moment magnetism description. The resultant band dispersions from band structure calculations for BaFe_2As_2 are shown in figure 2.14. These calculated bands show hole-like bands at the Fermi level (zero Energy) around the Brillouin zone center [Γ , $\mathbf{Q} = (0\ 0\ 0)$] and electron-like bands around the Brillouin zone corner [X , $\mathbf{Q} = (\frac{1}{2}\ \frac{1}{2}\ 0)_T$]. Angle-resolved photoemission spectroscopy measurements, like those shown in figure 2.15, also show the presence of states around the Brillouin zone center and corner for $\text{Ba}(\text{Fe}_{1-x}\text{Co}_x)_2\text{As}_2$ and confirm that there are circular hole-like bands centered at Γ and elliptical electron-like bands at X . Independent of their observed origin, when the Γ hole bands are displaced by the vector $\mathbf{Q} = (\frac{1}{2}\ \frac{1}{2}\ 0)_T$ they overlap to an appreciable degree with the X electron bands. This so-called nesting, shown in figure 2.16, indicates that there is a significant density of

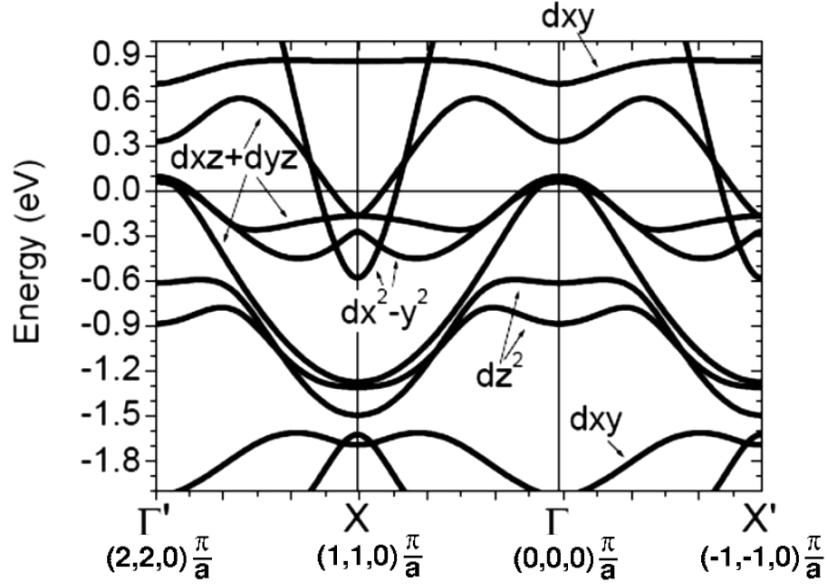


FIGURE 2.14. Resultant band structure calculations for BaFe_2As_2 showing the energy versus momentum dependence along the $[1\ 1\ 0]_{\text{T}}$ direction. This figure is reproduced from [64].

states connected by the nesting wavevector which will produce a peak in the magnetic susceptibility at the same wavevector that can lead to an instability toward spin density wave antiferromagnetic order. In the case of $\text{Ba}(\text{Fe}_{1-x}\text{Co}_x)_2\text{As}_2$, additional consideration of the three-dimensional nature of the Fermi surface indicates that the largest nesting (and largest peak in the susceptibility) occurs for the nesting wavevector $\mathbf{Q}_{\text{AFM}} = (\frac{1}{2}\ \frac{1}{2}\ 1)_{\text{T}}$. As shown in figure 2.17 upon entering the antiferromagnetic state, angle-resolved photoemission spectroscopy measurements indicate a hybridization between the hole and electron pockets; this hybridization is not unexpected for any order that introduces a larger unit cell (i.e., a superstructure) and could be an indication that the antiferromagnetic order is a result of itinerant processes [66].

Although full band structure calculations and angle-resolved photoemission spectroscopy measurements indicate that there are multiple hole pockets at Γ and multiple electron pockets at X , a simplified bandstructure model proposed by Fernandes et al. has been successful in describing the properties of $\text{Ba}(\text{Fe}_{1-x}\text{Co}_x)_2\text{As}_2$, including the coexistence of antiferromagnetism

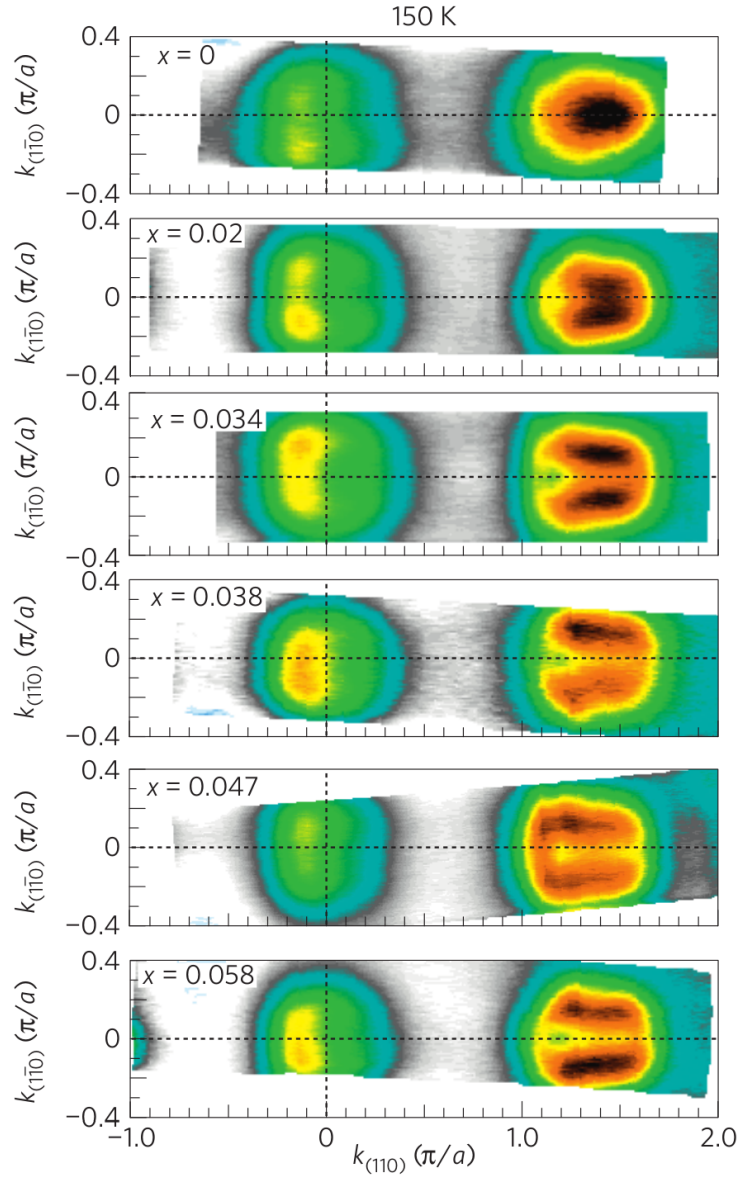


FIGURE 2.15. Angle-resolved photoemission spectroscopy data from lightly- to nearly optimally-doped $\text{Ba}(\text{Fe}_{1-x}\text{Co}_x)_2\text{As}_2$ at $T = 150$ K (within the tetragonal and paramagnetic state). This figure is reproduced from [65].

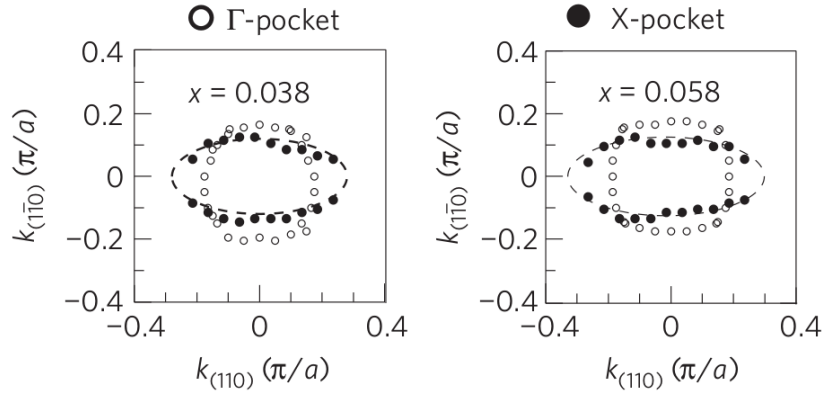


FIGURE 2.16. Offset angle-resolved photoemission spectroscopy determined Fermi surfaces for tetragonal and paramagnetic $\text{Ba}(\text{Fe}_{1-x}\text{Co}_x)_2\text{As}_2$, determined from data presented in figure 2.15. This figure is reproduced from [65].

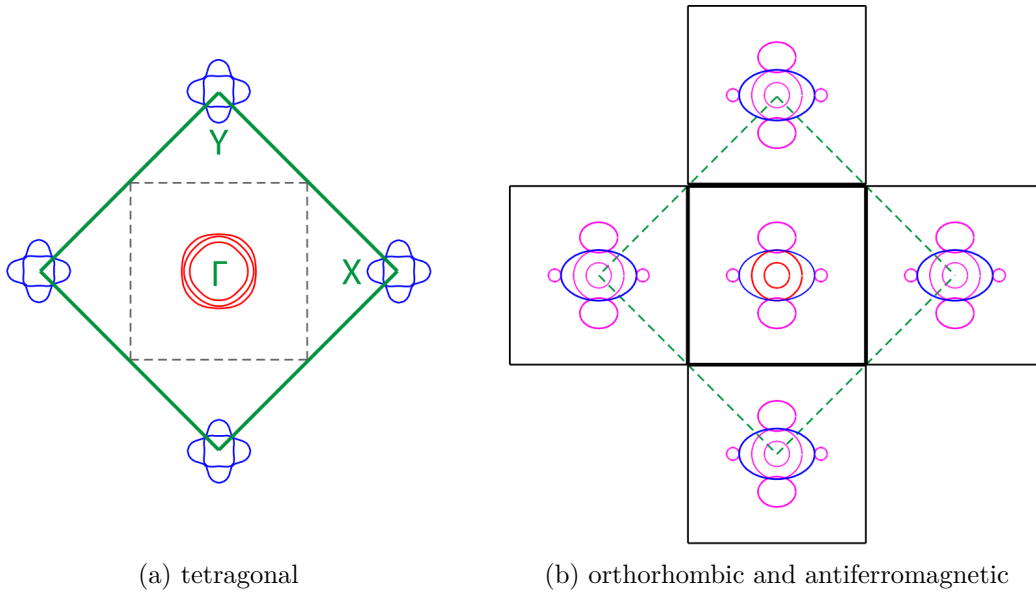


FIGURE 2.17. Fermi surfaces for the (a) tetragonal and (b) orthorhombic-antiferromagnetic states of under-doped $\text{Ba}(\text{Fe}_{0.975}\text{Co}_{0.025})_2\text{As}_2$ as determined from angle-resolved photoemission spectroscopy. This figure is reproduced from Reference [66]. As described by Yi et al., red bands are hole-like, blue bands are electron-like, and magenta bands are hybridizations of both hole- and electron-like bands.

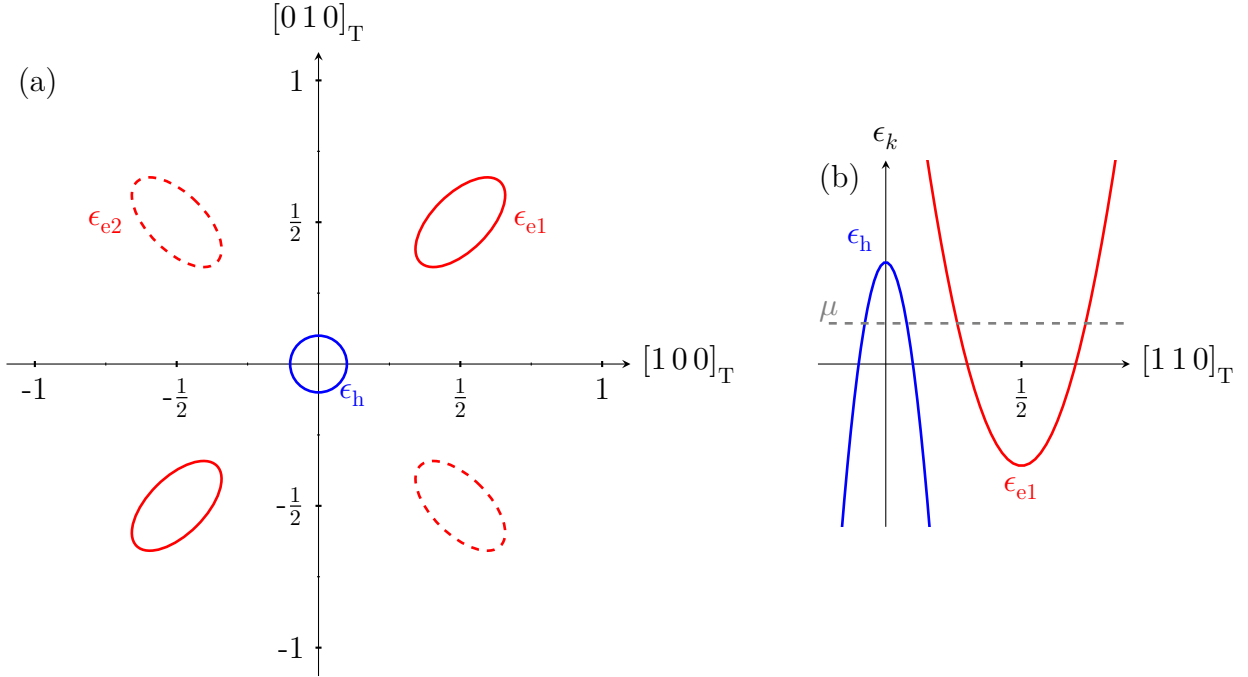


FIGURE 2.18. An illustration of the simplified model proposed by Fernandes et al. to describe the physical properties of the iron pnictides. Panel (a) shows the simplified band structure at the Fermi level as a function of the in-plane tetragonal wavevectors; the simplified model has one circular hole pocket at the zone-center and one or two elliptical electron pockets at the zone boundaries. Panel (b) shows the dispersion of the model bands along the $[110]_{\text{T}}$ direction, and the chemical potential, μ , which is included in the model to capture the effects of chemical doping (e.g., substituting cobalt for iron introduces additional electrons and raises the Fermi level). The solid hole and electron band are separated by the nesting vector and, often, the dashed electron pocket is not considered as the degeneracy between $[110]_{\text{T}}$ and $[\bar{1}10]_{\text{T}}$ is lifted by the appearance of orthorhombic order.

and superconductivity [62]. This simplified band structure model is illustrated in figure 2.18, which shows that the model considers one hole pocket at the zone center and one (or two) electron pocket(s) at the zone boundary. When describing the antiferromagnetic order in $\text{Ba}(\text{Fe}_{1-x}\text{Co}_x)_2\text{As}_2$ only two bands were considered by Fernandes et al. [62]. That two-band description was successful in reproducing the suppression of antiferromagnetic order with increasing cobalt in $\text{Ba}(\text{Fe}_{1-x}\text{Co}_x)_2\text{As}_2$ (compare figures 2.11 and 2.19), as shown in figure 2.20.

In this simplified model, the suppression of antiferromagnetic order comes as a result of the detuning of the Fermi surfaces of the electron and hole bands as the introduction of

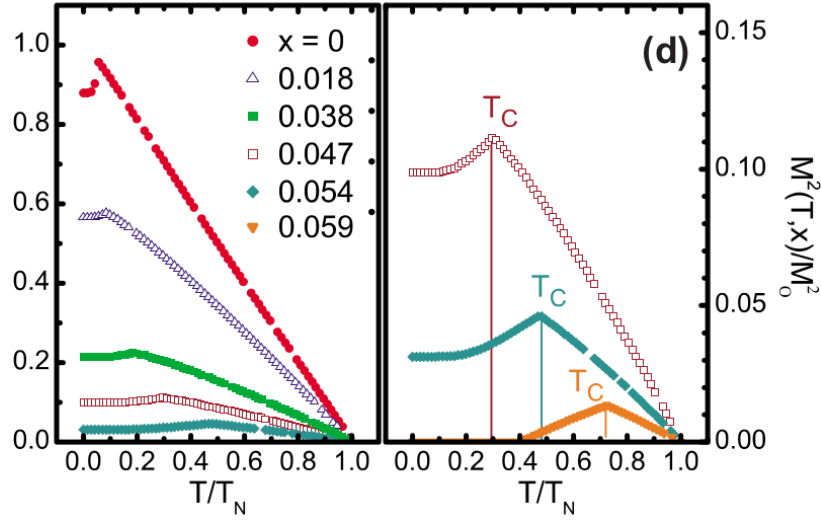


FIGURE 2.19. Calculated stripe antiferromagnetic order parameter utilizing a simplified band structure model, for $x = \{0, 0.018, 0.038, 0.047, 0.054, 0.059\}$ in $\text{Ba}(\text{Fe}_{1-x}\text{Co}_x)_2\text{As}_2$, reproduced from reference [62]. The data presented here has been normalized by the $T = 0$, $x = 0$ calculated squared moment, and is displayed as a function of reduced temperature T/T_N .

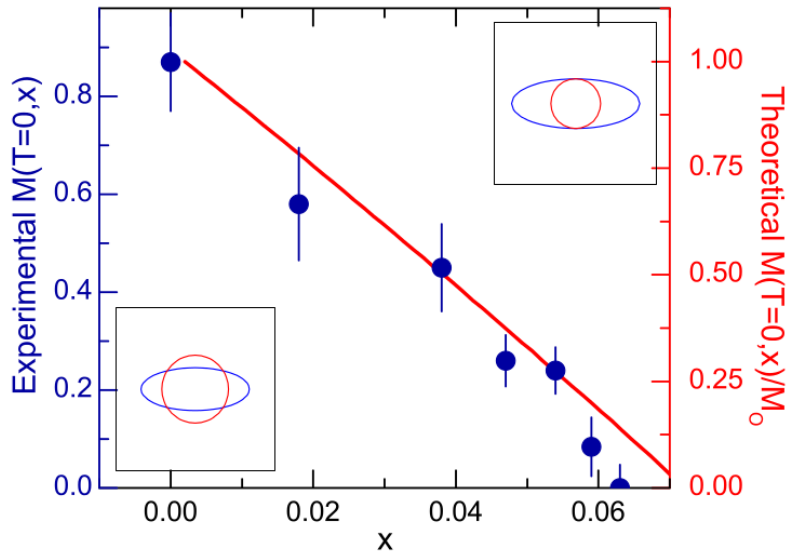


FIGURE 2.20. A comparison of the measured (from figure 2.11) and calculated (from the simplified band structure model) ordered moment size as a function of cobalt substituted into $\text{Ba}(\text{Fe}_{1-x}\text{Co}_x)_2\text{As}_2$, reproduced from reference [62]. The inset panels show how the electron and hole bands change with cobalt substitution.

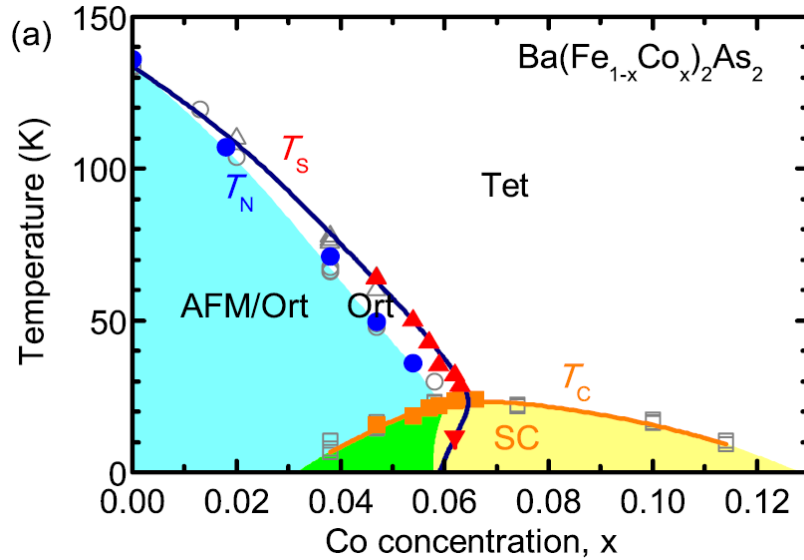


FIGURE 2.21. A phase diagram for $\text{Ba}(\text{Fe}_{1-x}\text{Co}_x)_2\text{As}_2$ spanning the range from BaFe_2As_2 to over-doped $\text{Ba}(\text{Fe}_{1-x}\text{Co}_x)_2\text{As}_2$. This data was originally presented by Nandi et al. in Reference [61] which was partially reproduced from Reference [60]. This figure is reproduced from Reference [67] in which Kim et al. explain that: gray open triangles represent resistance-derived data; gray open circles, magnetization-derived data; gray open squares, bulk measurements of T_c ; filled red triangles, T_S measured by x-ray diffraction; filled blue circles, T_N measured by neutron diffraction; and filled orange squares, values for T_c from x-ray and neutron data.

cobalt increases the model chemical potential, μ , thereby growing the electron band and shrinking the hole band at the Fermi surface. As the chemical potential is raised higher and the hole band becomes much smaller than the electron band, it is possible that the nesting wavevector can shift – in fact, this change in the nesting wavevector can explain the observed incommensurate antiferromagnetic order shown in figure 2.12.

2.3.5 Phase diagram

By pulling together resistivity data, like that presented in figure 2.6; bulk magnetization data, like that presented in figures 2.7 and 2.9; x-ray diffraction data, like that used to create figure 2.8; and neutron diffraction data, like that presented in figure 2.11; one can create a comprehensive temperature-composition phase diagram as in figure 2.21. Furthermore,

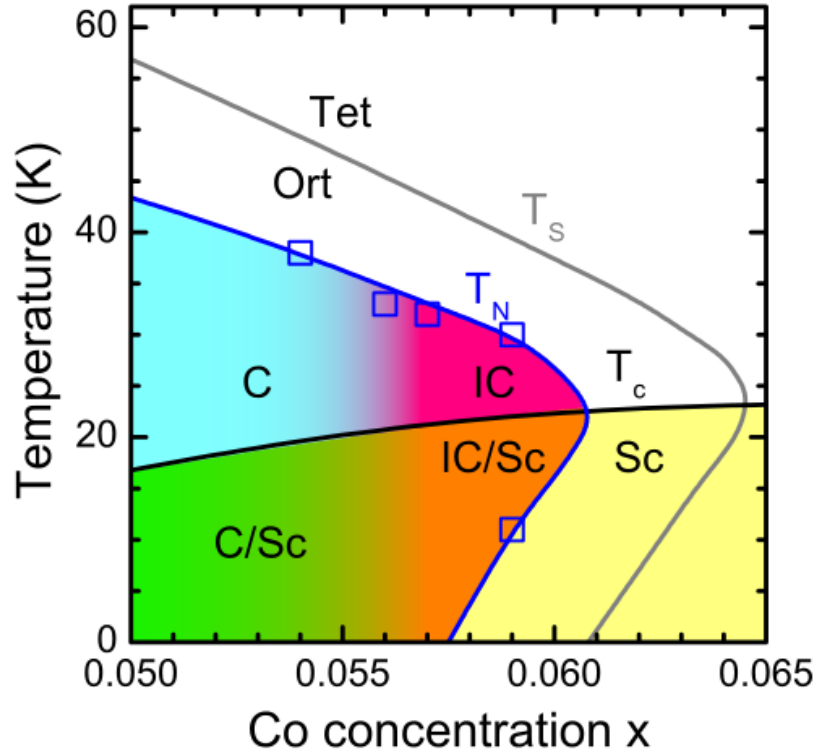


FIGURE 2.22. A section of the phase diagram presented in figure 2.21 updated to include information about the incommensurate antiferromagnetic order in $\text{Ba}(\text{Fe}_{1-x}\text{Co}_x)_2\text{As}_2$ near the complete suppression of long-range order; reproduced from Reference [63]. Open squares are data points extracted by Pratt et al. from their neutron diffraction data. Solid phase lines are representative of these new data points as well as those presented by Nandi et al. in Reference [61] and shown in figure 2.21.

including the incommensurate order information presented in figures 2.12 and 2.13 allows one to refine the phase diagram as has been done in figure 2.22.

These phase diagrams, no doubt, are reminiscent of those found for other unconventional superconductors – see, for example, figures 2.2 and 2.3 for representative phase diagrams for heavy fermion superconductors and cuprate superconductors, respectively. With them, they have in common: (i) a proximity to an antiferromagnetically ordered ground state; (ii) a suppression of that antiferromagnetically ordered state by some modification, be it applied pressure or the substitution of a constituent element by a dopant; and (iii) after sufficient suppression of the antiferromagnetic order by that modification, the onset of superconductivity.

Where $\text{Ba}(\text{Fe}_{1-x}\text{Co}_x)_2\text{As}_2$ differs from some unconventional superconductors is in that both long range antiferromagnetic order and superconductivity coexist and compete within the same volume in a small region of phase space, as indicated in figures 2.21 and 2.22 as green and orange shaded areas (which represent the coexistence of commensurate antiferromagnetism and superconductivity, and incommensurate antiferromagnetism and superconductivity, respectively).

2.3.6 Spin excitations

The phase diagrams in figures 2.21 and 2.22 give details of the static properties of $\text{Ba}(\text{Fe}_{1-x}\text{Co}_x)_2\text{As}_2$ but do not provide any information about dynamic properties.

As discussed previously, the conventional BCS theory can correctly predict the superconducting transition temperature of a compound from the value of the electron-phonon coupling constant (in addition to the characteristic phonon energy, and electronic density of states at the Fermi surface). The electron-phonon coupling constant can be determined from first-principles calculations and from inelastic neutron scattering measurements of the phonon spectra – a study by Christianson et al. combining both techniques to study $\text{LaFeAsO}_{1-x}\text{F}_x$ found their varied results to be in good agreement and determined the electron-phonon coupling constant [68]. The corresponding value of the superconducting transition temperature was determined to be less than 1 K, from which Christianson et al. concluded that the iron pnictide superconductors are not conventional electron-phonon mediated superconductors [68].

In as much as phonons can not be the sole superconducting pairing mechanism in unconventional superconductors, some other interaction must provide the attraction that supports the coupling of two otherwise-repulsive electrons into a Cooper-pair. Since unconventional superconductors are quite often derived from antiferromagnetic materials, it is plausible that fluctuations in the electron-spin system may provide a superconducting pairing mechanism.

One possibility is that magnons, which are the spin-system analog to phonons, are responsible for the pairing interaction. This has led to investigations of the magnetic excitations in BaFe_2As_2 and $\text{Ba}(\text{Fe}_{1-x}\text{Co}_x)_2\text{As}_2$.

The spin fluctuation spectra of BaFe_2As_2 deep within its antiferromagnetically ordered state, as well as at elevated temperatures below and above its antiferromagnetic ordering temperature, T_N , are shown in figure 2.23. The lowest-temperature BaFe_2As_2 magnetic excitations are well described by a spin wave model (with spin wave dispersion shown by the solid black lines) and, for elevated temperatures and energy transfers, the same model remains a correct qualitative description of the observed inelastic neutron scattering intensity [69].

For the case of optimally-doped $\text{Ba}(\text{Fe}_{1-x}\text{Co}_x)_2\text{As}_2$, there is no long range antiferromagnetic order at any temperature and the magnetic excitations no longer resemble spin waves. The inelastic neutron scattering energy spectra are shown for $\text{Ba}(\text{Fe}_{0.925}\text{Co}_{0.075})_2\text{As}_2$ in figure 2.24 above and below the superconducting transition temperature, T_c . Those data above T_c are diffusive in nature with very little momentum dependence and are characteristic of a nearly antiferromagnetic liquid [70]. A system which has no long-range magnetic order but that has antiferromagnetic interactions between neighboring spins will finite (in space and time) regions of correlated spins that can diffuse through the system – the excitations of such a magnetic system are characterized by the size and lifetime of the correlated regions. Below the superconducting transition temperature, as is common for unconventional superconductors, the superconducting resonance appears – which is visible in figure 2.24 as a peaked increase in intensity near an energy transfer of 10 meV.

The appearance of superconductivity introduces a gap in the density of states around the Fermi level. This superconducting gap, Δ_{SC} , prohibits excitations with $|E| < \mathcal{O}(\Delta_{\text{SC}})$. In the case of the simplified band structure model discussed previously, it was reported by Fernandes and Schmalian [71] that the magnitudes of the superconducting gaps at the hole and electron

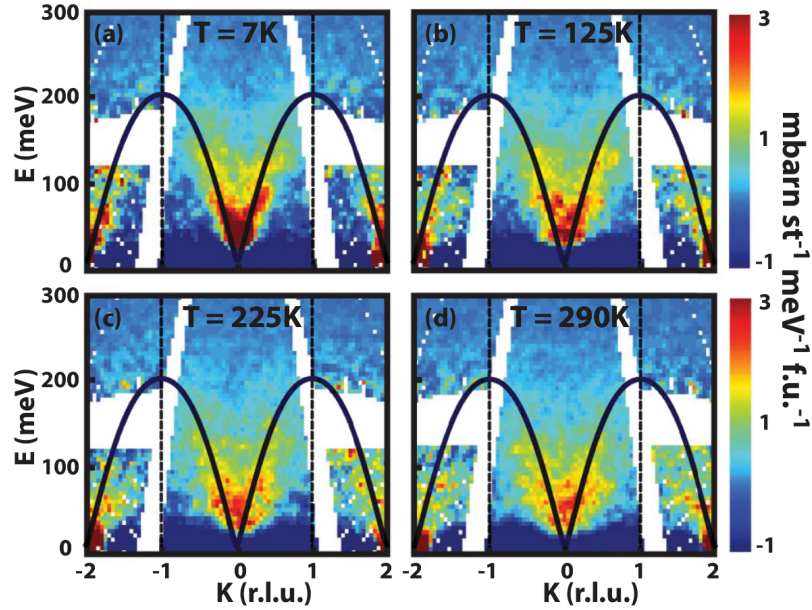


FIGURE 2.23. Inelastic neutron scattering intensity shows that the magnetic excitations in BaFe_2As_2 are well described by a model of spin wave excitations from a well-ordered antiferromagnetic system. This figure has been reproduced from Reference [69]. Data presented here is indexed in relative units of the low-temperature orthorhombic lattice and have had an estimated background, the average intensity in the region $1.8 < H < 2.2$, $-0.2 < K < 0.2$ r.l.u., subtracted. Furthermore, collected data with $H < 0$ were combined with symmetry equivalent data with $H > 0$ in order to improve the statistical quality of the displayed data. The solid line in each panel is the resulting dispersion of a spinwave model fit to the $T = 7$ K data; also shown is data obtained with $T = 125$, 225, and 290 K.

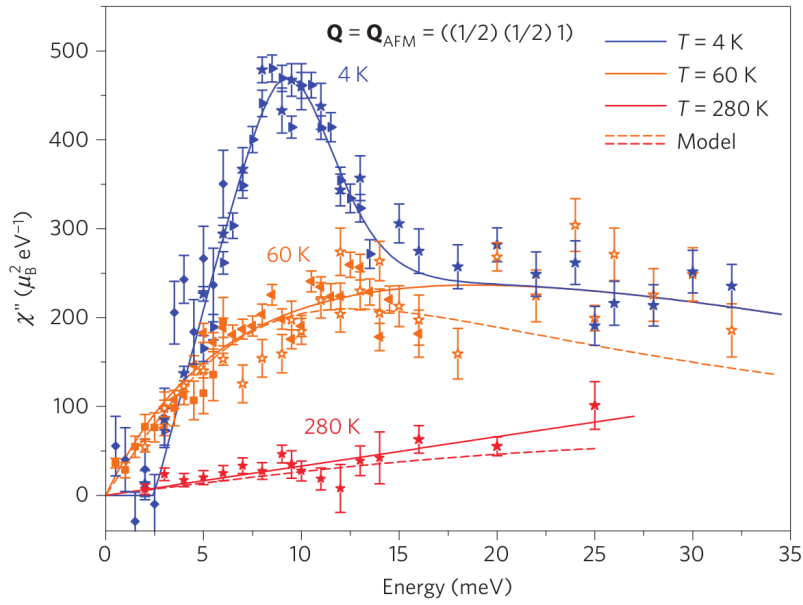


FIGURE 2.24. Corrected inelastic neutron scattering intensity measured from $\text{Ba}(\text{Fe}_{0.925}\text{Co}_{0.075})_2\text{As}_2$ for $T = 4, 60,$ and 280 K , reproduced from Reference [70]. Solid lines in this figure are guides to the eye, and dashed lines represent fits to a diffusive model functionally equivalent to that described by equation (4.34). The different symbol shapes indicate which of three different instruments was used to collect the data, and are discussed in detail by Inosov et al. in Reference [70].

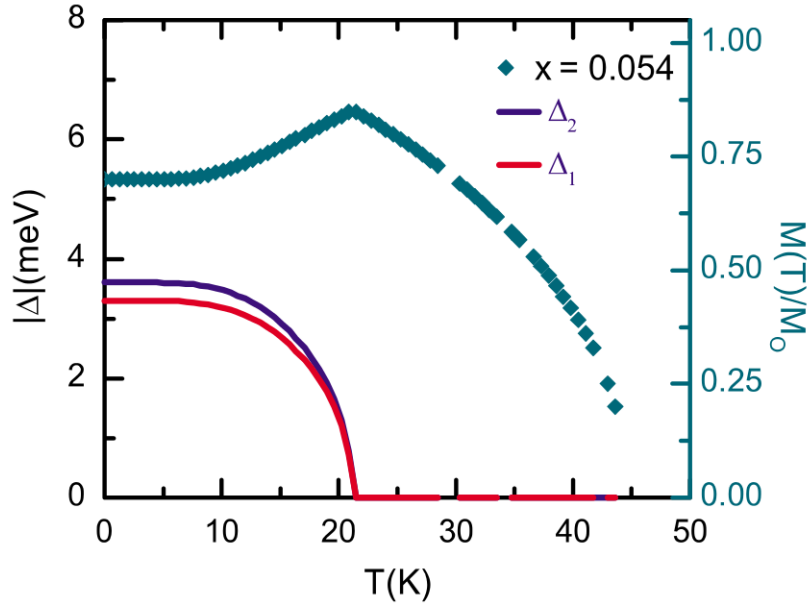


FIGURE 2.25. Calculated reduced moment size and superconducting gaps magnitude for the case of s^{+-} superconducting gap symmetry, reproduced from [71]. The superconducting gap on the electron band, Δ_1 , is of slightly higher magnitude than the gap on the hole band, Δ_2 , at temperatures below T_c .

bands should be similar, with the gap at the electron band being slightly larger, as shown in figure 2.25, and that the magnitude of each gap should be approximately constant for all parts of each band. Fernandes and Schmalian also reported that antiferromagnetism and superconductivity could not coexist if the gaps on both bands have the same sign (the so called s^{++} state), and that under special circumstances a change in the sign of the gap between the bands (the so called s^{+-} state) can give rise to a coexistence of antiferromagnetism and superconductivity, as has been observed for $\text{Ba}(\text{Fe}_{1-x}\text{Co}_x)_2\text{As}_2$. Since the antiferromagnetic order in $\text{Ba}(\text{Fe}_{1-x}\text{Co}_x)_2\text{As}_2$ appears to be dependent upon details of the band structure and Fermi surface, the opening of the superconducting gap could be responsible for the appearance of the superconducting resonance in these, and perhaps other, unconventional superconductors. While there seems to be consensus that a s^{+-} state can give rise to a superconducting resonance, no consensus is apparent for the case of an s^{++} state with some authors claiming a resonance is impossible [72] and others claiming the opposite [73].

2.4 Motivation

Unconventional superconductivity is found in close proximity to an antiferromagnetically ordered ground state. For $\text{Ba}(\text{Fe}_{1-x}\text{Co}_x)_2\text{As}_2$, which is itself antiferromagnetic and superconducting in the under-doped regime, this is no different. This proximity has spawned a great deal of speculation that spin fluctuations related to the antiferromagnetism in unconventional superconductors may take the place of phonons in conventional superconductors and provide the necessary interaction to form Cooper-pairs thereby enabling the superconducting state. Unfortunately no widely-accepted theory yet exists to explain precisely how antiferromagnetic spin fluctuations mediate superconductivity.

The spin fluctuations at optimally-doped $\text{Ba}(\text{Fe}_{1-x}\text{Co}_x)_2\text{As}_2$ are diffusive in nature, while in the parent compound BaFe_2As_2 they are well defined spin wave excitations. This change in the nature of spin fluctuations could be a consequence of the loss of antiferromagnetic order, in which case the character would change only when passing through the antiferromagnetic-paramagnetic phase boundary indicated in figure 2.21. Alternatively, the change in character could signal a shift towards more-itinerant electrons in $\text{Ba}(\text{Fe}_{1-x}\text{Co}_x)_2\text{As}_2$ independent of the antiferromagnetic order. If the first possibility holds true, then spin fluctuations likely can not provide the pairing mechanism for superconductivity in $\text{Ba}(\text{Fe}_{1-x}\text{Co}_x)_2\text{As}_2$ since antiferromagnetic order coexists with superconductivity in the under-doped compounds. The second possibility would be an indication that, at the very least, the itinerant electrons which participate in spin fluctuations are an important component for superconductivity in $\text{Ba}(\text{Fe}_{1-x}\text{Co}_x)_2\text{As}_2$.

Inelastic neutron scattering is the ideal probe to study spin fluctuations in condensed matter due to the magnetic moment and typical energy of a thermal neutron. I have used time-of-flight inelastic neutron scattering, with large energy transfers and large position-sensitive area detectors, and triple-axis inelastic neutron scattering, with low energy transfers and focused beams, to gain both a broad overview of the spin fluctuations in $\text{Ba}(\text{Fe}_{1-x}\text{TM}_x)_2\text{As}_2$

[(TM, x)=(Cr,0.06),(Co,0.047),(Cu,0.028)] and a parametric study of the spin fluctuations in a $\text{Ba}(\text{Fe}_{1-x}\text{Co}_x)_2\text{As}_2$ series ($x=0.015, 0.033, 0.04, 0.047, 0.055$). By studying spin fluctuations at multiple points throughout the $\text{Ba}(\text{Fe}_{1-x}\text{Co}_x)_2\text{As}_2$ T - x phase diagram, figure 2.21, and for related non-superconducting compositions, I am able to unambiguously differentiate between the two possibilities and find evidence that increased damping of the spin fluctuations with increasing cobalt is a requirement for the appearance of superconductivity in $\text{Ba}(\text{Fe}_{1-x}\text{Co}_x)_2\text{As}_2$.

CHAPTER 3 TECHNIQUES

3.1 Scattering

Interatomic distances in solids are typically on the order of an ångström ($1\text{\AA} \equiv 10^{-10}\text{m}$). Therefore, any probe used to study the microscopic structure of a solid must have a wavelength of a similar size. The de Broglie wavelength of any particle is given by

$$\lambda = \frac{h}{p} \quad (3.1)$$

where h is Planck's constant and p is the momentum of the particle. Non-relativistic massive particles, with $p = mv$, have their momenta and energies related by

$$E = \frac{p^2}{2m}. \quad (3.2)$$

By combining equations (3.1) and (3.2) it is clear that their de Broglie wavelength is inversely proportional to the square root of their energy,

$$\lambda = \frac{h}{\sqrt{2mE}}. \quad (3.3)$$

Massless particles, which have energy $E = pc$, have wavelengths inversely proportional to their energy

$$\lambda = \frac{hc}{E}. \quad (3.4)$$

Three typical probes for the study of condensed matter are the photon, the electron, and the neutron — their wavelengths as a function of energy are displayed in figure 3.1.

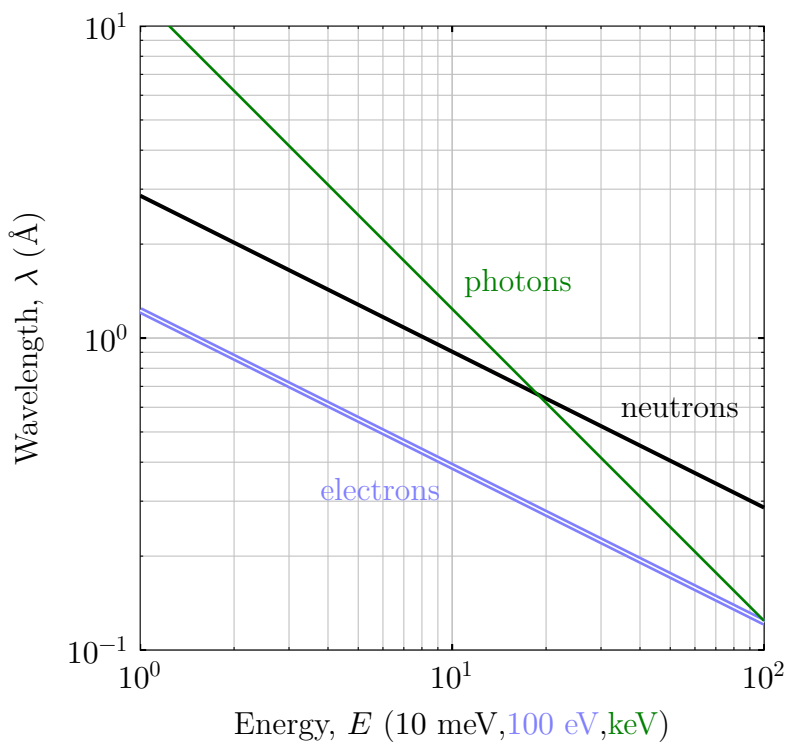


FIGURE 3.1. Wavelength versus energy for neutrons, electrons, and photons. The energy axis is in units of 10 meV for neutrons (—), 100 eV for electrons (—), and 1 keV for photons (—). Adapted from a figure by Kittel [74, p. 24].

TABLE 3.1. Properties of the neutron

property	value
mass, m_n /kg	1.675×10^{-27}
charge	0
spin	$\frac{1}{2}$
magnetic moment, μ_n/μ_N	-1.913

From figure 3.1 it is clear that photons, electrons, and neutrons all have wavelengths comparable to the interatomic length scales in condensed matter, but only the neutron has such a wavelength as well as an energy comparable to excitations in condensed matter, on the order of meV. Although it is possible to achieve meV resolution in the energy of keV energy photons (x-rays), part-per-million uncertainties are not easy to obtain and doing so requires a large sacrifice in intensity, practical only at a synchrotron x-ray source. In contrast, an energy resolution of ~ 1 meV for ~ 10 meV neutrons is only one-part-in-ten, and is much simpler to attain.

Neutrons feature other advantages as a scattering probe, as summarized in table 3.1. The neutron is chargeless and therefore has a large penetration depth through most materials. This allows for bulk scattering measurements and relatively easy implementation of various sample conditions — e.g., pressure, temperature, magnetic field, etc. — due to the neutron’s ability to penetrate through centimeter-sized samples and sample environment walls. Neutrons are spin- $\frac{1}{2}$ particles and therefore interact with magnetic moments through the dipole interaction, most importantly they can interact with unpaired electrons and are, therefore, sensitive to, e.g., antiferromagnetic order, to which other probes are ‘blind.’

Neutrons do have one significant drawback when compared to other scattering probes: their production in beams is difficult. Electron beams can be created by heating a filament until its temperature is high enough that electrons in the metal have enough energy to escape their potential well, at which point they ‘boil’ out of the filament and can be accelerated and focused by the application of electric and magnetic fields, due to their charge. Beams

of x-rays can be created in a lab by taking an electron beam and directing it onto a metal target, causing transitions between electron orbitals which emit characteristic x-ray radiation and bremsstrahlung. X-ray beams can also be produced by accelerating the same electron beam to near the speed of light in a storage ring, since the relativistic electrons must radiate light when accelerated at each turn and will emit x-rays if tuned properly, such a storage ring is called a synchrotron for historical reasons.

Free neutrons have a mean lifetime of $\tau = 885.7(8)$ s and decay via the pathway



thereby conserving charge and lepton number [75]. As a result, it is not possible to store free neutrons for any appreciable time and they must instead be freed from heavy nuclei shortly before their use in scattering experiments. While early experiments with neutrons used naturally radioactive Po α -particle bombardment of Be as a neutron source [76], modern facilities often utilize one of two methods to produce free neutrons on-demand: fission and spallation.

Fission is the act of a nucleus of an atom breaking apart into two or more smaller nuclei. Fission can take place spontaneously via radioactive decay or as the result of a nuclear reaction, e.g., the absorption of a thermal neutron by ^{235}U causes its nucleus to undergo fission. Isotopes of elements which can be forced to undergo fission through the absorption of a neutron are referred to as fissionable, and those that undergo fission after the absorption of a thermal neutron are further classified as fissile. Since heavy element nuclei tend to have a larger neutron to proton ratio than light elements (such that the inter-nucleon attractive strong force potential overcomes the inter-proton repulsive Coulomb potential) when a heavy element undergoes fission there are typically excess neutrons. Nuclear reactors use the excess neutrons from fission events to induce fission in fissile fuel and, by controlling the moderation and absorption of fission-emitted neutrons, thereby create a sustainable fission

TABLE 3.2. Neutron energy ranges for the named moderators, adapted from reference [77, p. 5]. The neutrons moderated by a named-moderator are often referred to by the moderator name; i.e., neutrons which pass through a thermal moderator are typically called thermal neutrons. Neutrons with energies below cold neutrons are called ultra-cold. Neutrons with energies above hot neutrons are called epithermal.

moderator	energy/meV	temperature/K	wavelength/Å
cold	0.1 – 10	1 – 120	30 – 3
thermal	5 – 100	60 – 1000	4 – 1
hot	100 – 500	1000 – 6000	1 – 0.4

chain reaction. Beam pipes in the side of an operating nuclear reactor make it possible to use excess neutrons, not needed to sustain the chain reaction, to perform scattering studies. In contrast to fission, which can take place spontaneously, spallation can only occur when a high-energy particle collides with, and breaks apart, a nucleus. The spallation event like fission produces free neutrons if a heavy target nucleus is chosen, such as lead, tungsten, or mercury. If a pulsed particle accelerator is utilized, it is possible to in turn produce pulses of neutrons via spallation.

Both fission and spallation produce a distribution of high-energy neutrons which are of limited utility for neutron scattering. In order to be used effectively in neutron scattering experiments, the neutrons must first be moderated to a more useful energy range. Moderation of takes place by allowing the neutrons to interact with a reservoir held at a fixed temperature, ideally comprised of atoms of similar mass to the neutron for efficient energy transfer in as few interactions as possible. After moderation, the neutron flux distribution takes on the form of a Maxwell-Boltzman distribution [77, p. 2] with

$$\phi(v) \propto v^3 \exp\left(-\frac{1}{2} \frac{mv^2}{k_B T}\right) \quad (3.6)$$

which peaks at

$$v = \sqrt{\frac{3k_B T}{m}}. \quad (3.7)$$

Since the energy of a non-relativistic neutron is given by its kinetic energy

$$E = \frac{1}{2}mv^2, \quad (3.8)$$

and recalling equation (3.3), it's clear that by changing the temperature of the neutron moderator one can change the peak energy and wavelength in the neutron flux distribution. Different ranges of neutron energies have been given names based on the relative temperature of the moderator which they have interacted with, as detailed in table 3.2. Because they are needed to sustain a fission chain reaction, all nuclear reactor neutron sources provide thermal neutrons after moderating high-energy neutrons with light- or heavy-water; spallation neutron sources also have thermal moderators for some of their beam lines due to the high utility of thermal neutrons. It is also common for both reactor and spallation sources to have one or more cold-temperature moderators for the production of cold neutrons, common cold moderator choices are liquid hydrogen, H, or liquid deuterium, ^2H .

Interactions between a scattering probe and a sample can be described by a scattering cross-section, which is a measure of the probability of that interaction taking place. For a known flux, Φ , of monochromatic unpolarized neutrons in a beam traveling along the polar axis of a coordinate system, the partial differential cross-section can be determined by placing an energy-discriminating detector, subtending a small solid angle $d\Omega$ at a position (θ, ϕ) , and measuring the rate of neutrons arriving with an energy between E and $E + dE$, $R(\theta, \phi, E)$, for all (θ, ϕ, E) .

$$\frac{d^2\sigma}{d\Omega dE}(\theta, \phi, E) = \frac{R(\theta, \phi, E)}{\Phi d\Omega dE} \quad (3.9)$$

as R^{-1} has units of time and Φ^{-1} has units of area and time, the cross-section, σ , must have units of area. By replacing the energy-discriminating detector with a detector which counts all neutrons, one would measure the differential cross-section, which is the energy-integrated

partial differential cross-section:

$$\frac{d\sigma}{d\Omega}(\theta, \phi) = \int dE \frac{d^2\sigma}{d\Omega dE}(\theta, \phi, E) \quad (3.10)$$

and, by integrating the differential cross-section over all directions (θ, ϕ) one can obtain the total cross-section

$$\sigma = \oint_{\Omega} d\Omega \frac{d\sigma}{d\Omega}(\theta, \phi). \quad (3.11)$$

3.1.1 Diffraction

As shown in figure 3.1 and highlighted in table 3.2, the wavelengths of thermal neutrons are on the order of a few ångström. When a thermal neutron interacts with a nucleus, it does so through the strong force which has a range on the order of fm ($10^{-15}\text{m}=10^{-5}\text{Å}$), which is significantly smaller than the neutron wavelength. When waves of any kind are scattered from an object which is small in comparison to their wavelength, the scattered waves are spherically symmetric [77, p. 7]. Utilizing the Born approximation, a neutron traveling along the \hat{z} direction with wavelength λ can be described as a plane wave

$$\psi_i = e^{ikz} \quad (3.12)$$

where $k = \frac{2\pi}{\lambda}$ is the wavenumber of the neutron and is the magnitude of the neutron wavevector

$$\mathbf{k} = \frac{\mathbf{p}}{\hbar} \quad (3.13)$$

where $\hbar = \frac{h}{2\pi}$ is Planck's reduced constant. If the neutron is scattered elastically from a (repulsive) nucleus at the origin of the coordinate system, then the scattered wavefunction is given by

$$\psi_s = -\frac{b}{r} e^{ikr} \quad (3.14)$$

since $r^2 = x^2 + y^2 + z^2$, ψ_s is spherically symmetric, and the parameterization of the strength of the interaction, b , is called the scattering length. From these wavefunctions one can calculate the cross section of this scattering process. The rate of scattered neutrons traveling with velocity v and passing through an area dA is given by

$$R = v dA |\psi_s|^2 = v dA \frac{b^2}{r^2} = vb^2 d\Omega \quad (3.15)$$

and the flux of incident neutrons is

$$\Phi = v |\psi_i|^2 = v. \quad (3.16)$$

Recalling equation (3.9), the definition of the partial differential cross-section and its relation to the differential cross-section and total cross-section equations (3.10) and (3.11) gives

$$\sigma = \oint_{\Omega} d\Omega b^2 = 4\pi b^2. \quad (3.17)$$

A more mathematically-rigorous derivation, like that presented by Squires, derives the same cross-section for a potential

$$V(\mathbf{r}) = \frac{2\pi\hbar^2}{m} b \delta(\mathbf{r}) \quad (3.18)$$

called the Fermi pseudopotential [77], where $\delta(\mathbf{r})$ is the Dirac delta-function which is one at $\mathbf{r} = 0$ and zero otherwise.

3.1.1.1 Nuclear diffraction

A general crystal lattice is comprised of unit cells described by the vectors \mathbf{a} , \mathbf{b} , and \mathbf{c} which span the unit-cell. For such a crystal, a general lattice vector is given by

$$\mathbf{l} = l_a \mathbf{a} + l_b \mathbf{b} + l_c \mathbf{c} \quad (3.19)$$

where the l_i are integers. This general unit cell has volume

$$v_0 = \mathbf{a} \cdot (\mathbf{b} \times \mathbf{c}). \quad (3.20)$$

The unit-cell vectors can be used to define a reciprocal lattice, described by the vectors

$$\mathbf{a}^* = \frac{2\pi}{v_0} \mathbf{b} \times \mathbf{c}, \quad \mathbf{b}^* = \frac{2\pi}{v_0} \mathbf{c} \times \mathbf{a}, \quad \text{and} \quad \mathbf{c}^* = \frac{2\pi}{v_0} \mathbf{a} \times \mathbf{b} \quad (3.21)$$

with reciprocal lattice vectors

$$\boldsymbol{\tau} = h\mathbf{a}^* + k\mathbf{b}^* + l\mathbf{c}^* \quad (3.22)$$

and which has volume

$$v_0^* = \mathbf{a}^* \cdot (\mathbf{b}^* \times \mathbf{c}^*) = \frac{(2\pi)^3}{v_0}. \quad (3.23)$$

It can be shown that the cross-section for coherent elastic scattering from a crystal lattice of nuclei is [77, p. 37]

$$\frac{d\sigma}{d\Omega} = N \sum_l e^{i\mathbf{Q} \cdot \mathbf{l}} \left| \sum_d \bar{b}_d e^{i\mathbf{Q} \cdot \mathbf{d}} e^{-W_d} \right|^2 \quad (3.24)$$

where where the first sum is over the N unit cells in the crystal, each located at \mathbf{l} , and the second sum is over the nuclei in each unit-cell, each located at $\mathbf{l} + \mathbf{d}$, and the term W_d is the Debye-Waller factor which accounts for the thermal motion of each nucleus. By evaluating the sum over l in equation (3.24), the coherent elastic cross-section is

$$\frac{d\sigma}{d\Omega} = N \frac{(2\pi)^3}{v_0} \sum_{\boldsymbol{\tau}} \delta(\mathbf{Q} - \boldsymbol{\tau}) |S_N(\mathbf{Q})|^2 \quad (3.25)$$

where $\mathbf{Q} \equiv \mathbf{k}_f - \mathbf{k}_i$ and

$$S_N(\mathbf{Q}) = \sum_d \bar{b}_d e^{i\mathbf{Q} \cdot \mathbf{d}} e^{-W_d} \quad (3.26)$$

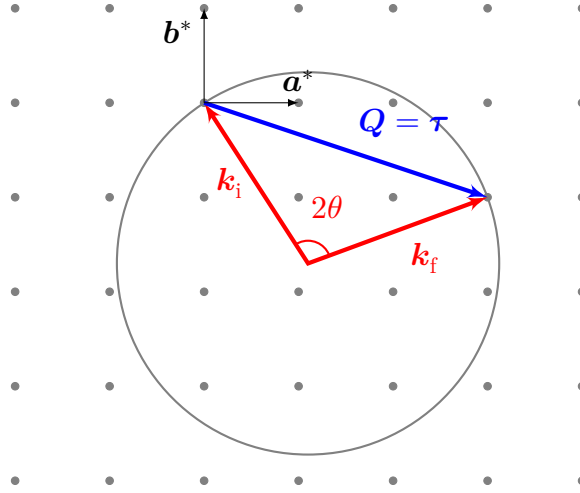


FIGURE 3.2. Coherent elastic scattering from a periodic crystal is possible only when $\mathbf{Q} \equiv \mathbf{k}_f - \mathbf{k}_i = \boldsymbol{\tau}$.

is the nuclear unit-cell structure factor. From equation (3.25), it is clear that scattering is only possible when

$$\mathbf{Q} = \mathbf{k}_f - \mathbf{k}_i = \boldsymbol{\tau}. \quad (3.27)$$

Figure 3.2 shows the condition for coherent elastic scattering; the scattering triangle defined by \mathbf{k}_i , \mathbf{k}_f and $\mathbf{Q} = \boldsymbol{\tau}$, with scattering angle 2θ , forms an isosceles triangle, and therefore

$$\frac{\tau}{2} = k \sin \theta \quad (3.28)$$

where $\tau = |\boldsymbol{\tau}| = n2\pi/d$, $k = |\mathbf{k}_i| = |\mathbf{k}_f|$ and θ is half the scattering angle. Recalling that $k = 2\pi/\lambda$, one can rearrange equation (3.28) into

$$n\lambda = 2d \sin \theta \quad (3.29)$$

which is the familiar Bragg's law, first formulated for the diffraction of x-rays.

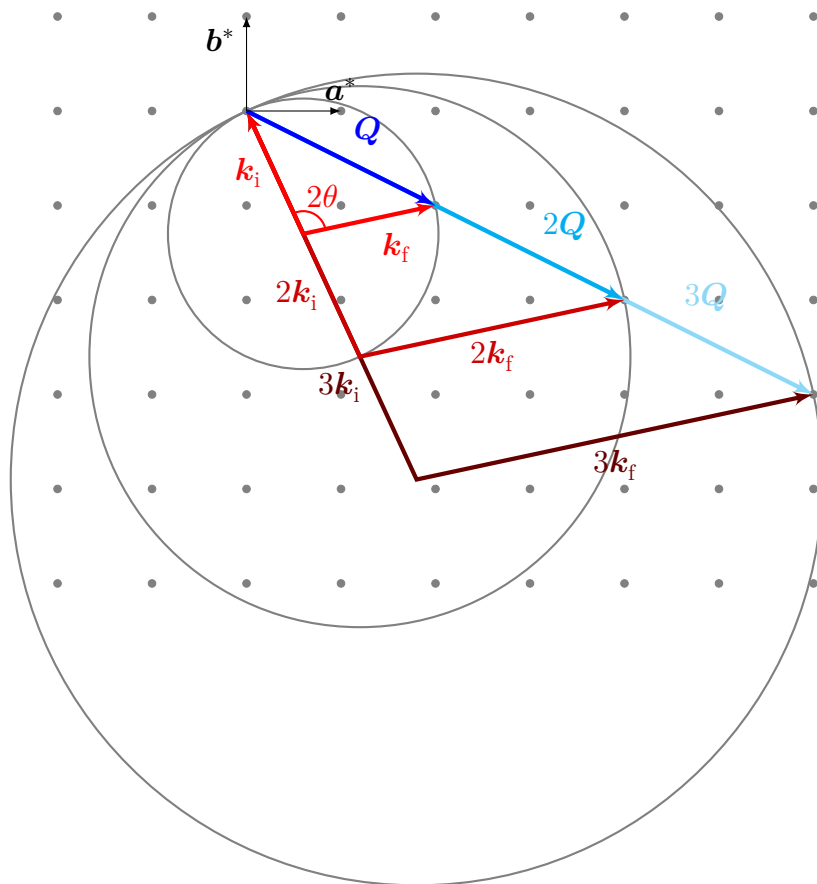


FIGURE 3.3. By definition, integer multiples of any reciprocal lattice vector τ are also lattice vectors of the same reciprocal lattice. Therefore, if the diffraction condition is satisfied for wavevector k_i , then it is satisfied for nk_i where $n = 1, 2, 3, \dots$ as well.

3.1.1.2 Magnetic diffraction

Since the neutron is a spin- $\frac{1}{2}$ particle, it is able to scatter from unpaired electrons via the dipole interaction. Unlike then nuclear interaction, the dipole interaction is spin-direction dependent and, consequently, the cross-sections for magnetic diffraction are somewhat more complex. The elastic cross-section for scattering unpolarized neutrons from a paramagnetic system of spins, where the relative orientation of any two spins is random, is given by Squires as

$$\frac{d\sigma}{d\Omega} = \frac{2}{3}(\gamma r_0)^2 N \left[\frac{1}{2} g F(\mathbf{Q}) \right]^2 e^{-2W} S(S+1) \quad (3.30)$$

where $F(\mathbf{Q})$ is the single-ion magnetic form factor and S is the magnitude of the paramagnetic spins [77, p. 144]. The spins in a ferromagnet align with their neighbors by definition, defining a spin-direction, however most ferromagnets form domains and the coherent elastic cross-section for unpolarized neutron scattering from a ferromagnet must incorporate this fact

$$\frac{d\sigma}{d\Omega} = (\gamma r_0)^2 N \frac{(2\pi)^3}{v_0} \langle S^\eta \rangle^2 \sum_{\tau} \left[\frac{1}{2} g F(\tau) \right]^2 e^{-2W} [1 - (\hat{\tau} \cdot \hat{\eta})_{\text{av}}^2] \delta(\mathbf{Q} - \tau) \quad (3.31)$$

where $\hat{\eta}$ is the mean direction of the spins, $\langle S^\eta \rangle$ is the mean value of the component of the spin in the $\hat{\eta}$ direction for each domain, and $(\hat{\tau} \cdot \hat{\eta})^2$ is averaged over all domains [77, p. 147]. If all directions are equally likely for $\hat{\eta}$, or if the easy axis of a ferromagnet has cubic symmetry, the value of $[1 - (\hat{\tau} \cdot \hat{\eta})_{\text{av}}^2]$ is $\frac{2}{3}$ [77, p. 147]. Antiferromagnets are further complex still, since, for a simple collinear bipartite lattice antiferromagnet, within each antiferromagnetic domain there are two interpenetrating ferromagnetic sublattices aligned antiparallel to one another. The coherent elastic cross-section for such an antiferromagnet looks similar to that for a ferromagnet

$$\frac{d\sigma}{d\Omega} = (\gamma r_0)^2 N \frac{(2\pi)^3}{v_0} \sum_{\tau} [S_M(\tau)]^2 e^{-2W} [1 - (\hat{\tau} \cdot \hat{\eta})_{\text{av}}^2] \delta(\mathbf{Q} - \tau) \quad (3.32)$$

except the sum is now over the reciprocal lattice vectors of the magnetic unit cell and

$$S_M(\boldsymbol{\tau}) = \frac{1}{2}g \langle S^\eta \rangle F(\boldsymbol{\tau}) \sum_d \sigma_d e^{i\boldsymbol{\tau} \cdot \mathbf{d}} \quad (3.33)$$

is the magnetic structure factor, where $\langle S^\eta \rangle$ is now the mean value of the sublattice magnetization and $\sigma_d = \pm 1$ has opposite sign for magnetic unit cell sites on different sublattices [77, p. 150].

More complex magnetic structures, such as helimagnets, exist; however, a more authoritative resource should be consulted for their neutron scattering cross-sections – e.g., Squires [77] and Lovesey [78].

3.1.2 Inelastic scattering

Excitations in condensed matter typically have energy scales similar to the energy of thermal neutrons. By exchanging energy with a system, a neutron is able to excite or extinguish an excitation by losing or gaining energy, respectively. As such, thermal neutron scattering is a useful tool to probe the momentum and energy dependence of various excitation in condensed matter systems.

3.1.2.1 Nuclear inelastic scattering

One type of crystalline excitation is the collective motion of nuclei in the lattice, dubbed a phonon. The displacement of the d^{th} nucleus in the l^{th} unit cell is given by the vector $\mathbf{u}(\mathbf{d}, l)$, which can be expressed as a sum over the displacements due to a set of normal modes

$$\mathbf{u} \begin{pmatrix} l \\ \mathbf{d} \end{pmatrix} = \sum_{\mathbf{q}} \sum_j \sqrt{\frac{\hbar}{2M_d N \omega_{qj}}} \left[\boldsymbol{\epsilon}_{d\mathbf{q}j} a_{\mathbf{q}j} e^{i\mathbf{q} \cdot \mathbf{d}} + \boldsymbol{\epsilon}_{d\mathbf{q}j}^* a_{\mathbf{q}j}^\dagger e^{-i\mathbf{q} \cdot \mathbf{d}} \right] \quad (3.34)$$

where M_d is the mass of the d^{th} nucleus, the energy of the j^{th} normal phonon mode at \mathbf{q} is $\hbar\omega_{qj}$, and the displacement eigenvector for the d^{th} nucleus in the unit-cell as a result of

the j^{th} normal mode is $\epsilon_{d\mathbf{q}j}$. If there are $r = \sum_{\mathbf{d}} r_{\mathbf{d}}$ atoms per unit cell, then there are $3r$ normal modes ($j = 1, \dots, 3r$) since each atom has three degrees of freedom [79, p. 105]. The displacement eigenvectors are orthonormal and behave the relations

$$\sum_{\mathbf{d}} \epsilon_{d\mathbf{q}j}^* \cdot \epsilon_{d\mathbf{q}j'} = \delta_{jj'} \quad \text{and} \quad \sum_j \epsilon_{d\mathbf{q}j}^{\alpha*} \epsilon_{d'\mathbf{q}j}^{\beta} = \delta_{\alpha\beta} \delta_{\mathbf{d}\mathbf{d}'}. \quad (3.35)$$

As given by Squires, the cross-section for the coherent creation of one phonon is given by [77, p. 46]

$$\begin{aligned} \frac{d^2\sigma}{d\Omega dE} &= \frac{k_f}{k_i} \frac{(2\pi)^3}{2v_0} \sum_{\mathbf{q}} \sum_j \sum_{\boldsymbol{\tau}} \frac{1}{\omega_{\mathbf{q}j}} \left| \sum_{\mathbf{d}} \frac{\bar{b}_{\mathbf{d}}}{\sqrt{M_{\mathbf{d}}}} e^{-W_{\mathbf{d}}} e^{i\mathbf{Q}\cdot\mathbf{d}} \mathbf{Q} \cdot \epsilon_{d\mathbf{q}j} \right|^2 \\ &\times \langle n_{\mathbf{q}j} + 1 \rangle \delta(\omega - \omega_{\mathbf{q}j}) \delta(\mathbf{Q} - \mathbf{q} - \boldsymbol{\tau}) \end{aligned} \quad (3.36)$$

and for the coherent annihilation of one phonon

$$\begin{aligned} \frac{d^2\sigma}{d\Omega dE} &= \frac{k_f}{k_i} \frac{(2\pi)^3}{2v_0} \sum_{\mathbf{q}} \sum_j \sum_{\boldsymbol{\tau}} \frac{1}{\omega_{\mathbf{q}j}} \left| \sum_{\mathbf{d}} \frac{\bar{b}_{\mathbf{d}}}{\sqrt{M_{\mathbf{d}}}} e^{-W_{\mathbf{d}}} e^{i\mathbf{Q}\cdot\mathbf{d}} \mathbf{Q} \cdot \epsilon_{d\mathbf{q}j} \right|^2 \\ &\times \langle n_{\mathbf{q}j} \rangle \delta(\omega + \omega_{\mathbf{q}j}) \delta(\mathbf{Q} + \mathbf{q} - \boldsymbol{\tau}) \end{aligned} \quad (3.37)$$

where the sums over $\boldsymbol{\tau}$ and \mathbf{d} are as in equation (3.25), $\langle n_{\mathbf{q}j} + 1 \rangle$ and $\langle n_{\mathbf{q}j} \rangle$ are the average thermal population factors for the creation and annihilation of a phonon of the j^{th} mode at \mathbf{q} , and the Dirac delta functions enforce conservation of energy and momentum.

3.1.2.2 Magnetic inelastic scattering

For a ferromagnetic system, if each atom has spin S the magnitude of its spin angular momentum is $\sqrt{S(S+1)}\hbar$ and any component of the spin angular momentum is given by $M\hbar$ ($M = S, S-1, \dots, -S$). At zero temperature all of the spins within a domain are aligned, and therefor $M = S$ for all atoms. Finite temperatures allow for the other values of

M due to thermal excitations, and the difference from $M = S$ is called a spin deviation. The spin deviations in a ferromagnetic domain can be represented by spin waves, which give the probability of a spin deviation when squared and are therefore continuous despite the spin deviations themselves being discrete [77, p. 156]. The spinwave is quantized, with an energy above the ground state of $n\hbar\omega$, where $n = 1, 2, \dots$ and ω is the spinwave angular frequency. The quanta of energy $\hbar\omega$ are known as magnons. By exchanging energy with a spinwave, a neutron is able to create or annihilate a magnon; therefore inelastic neutron scattering is able to directly probe the excitations of magnetic systems.

The general magnetic partial differential cross-section for neutron scattering is

$$\frac{d^2\sigma}{d\Omega dE} = \frac{N k_f}{\hbar k_i} (\gamma r_0)^2 \left[\frac{1}{2} g F(\mathbf{Q}) \right]^2 e^{-2W} \sum_{\alpha, \beta} (\delta_{\alpha\beta} - \hat{Q}_\alpha \hat{Q}_\beta) S^{\alpha\beta}(\mathbf{Q}, \omega) \quad (3.38)$$

where γ is the gyromagnetic ratio, $r_0 = e^2/m_e c^2$ is the classical electron radius, g is the Landé splitting factor ($g = 2$ for a spin-only moment), the sum over α and β is over directions of the spin-system, $(\delta_{\alpha\beta} - \hat{Q}_\alpha \hat{Q}_\beta)$ is a result of the neutron only interacting with the component of \mathbf{S} perpendicular to \mathbf{Q} given by

$$\mathbf{S}_\perp = \hat{\mathbf{Q}} \times \mathbf{S} \times \hat{\mathbf{Q}} \quad (3.39)$$

with squared magnitude

$$|\mathbf{S}_\perp|^2 = \sum_{\alpha, \beta} (\delta_{\alpha\beta} - \hat{Q}_\alpha \hat{Q}_\beta) S_\alpha^* S_\beta \quad (3.40)$$

and $S^{\alpha\beta}(\mathbf{Q}, \omega)$ is the spin-spin correlation function for the system.

For a small applied magnetic field, with Fourier transformed component $H_\beta(\mathbf{Q}, \omega)$, the magnetization of a system will respond in some way, $\Delta M_\alpha(\mathbf{Q}, \omega)$, which can be expanded in powers the applied field.

$$\Delta M_\alpha(\mathbf{Q}, \omega) = \chi_{\alpha\beta}(\mathbf{Q}, \omega) H_\beta(\mathbf{Q}, \omega) + \text{higher order terms} \quad (3.41)$$

The first term in such an expansion is linear in the applied field with a coefficient called the linear magnetic susceptibility, $\chi_{\alpha\beta}(\mathbf{Q}, \omega)$ which is a tensor that describes the magnetization response of a system along the α -direction to an applied magnetic field along the β -direction. The linear magnetic susceptibility of a material is, in general, a complex valued function with an imaginary component related to dissipation in response to the applied magnetic field,

$$\chi_{\alpha\beta}(\mathbf{Q}, \omega) = \chi'_{\alpha\beta}(\mathbf{Q}, \omega) + i\chi''_{\alpha\beta}(\mathbf{Q}, \omega). \quad (3.42)$$

The fluctuation-dissipation theorem relates the imaginary component of the magnetic susceptibility to the spin-spin correlation function

$$S^{\alpha\beta}(\mathbf{Q}, \omega) = \frac{1}{1 - e^{-\hbar\omega/k_B T}} \frac{1}{\pi(g\mu_B)^2} \chi''_{\alpha\beta}(\mathbf{Q}, \omega). \quad (3.43)$$

For magnon scattering, the general magnetic partial differential cross-section, equation (3.38), is modified by

$$\sum_{\alpha,\beta} (\delta_{\alpha\beta} - \hat{Q}_\alpha \hat{Q}_\beta) S^{\alpha\beta}(\mathbf{Q}, \omega) = \frac{1}{2} \left(1 + \langle \hat{Q}_z^2 \rangle_{\text{avg}} \right) S_{\text{sw}}(\mathbf{Q}, \omega). \quad (3.44)$$

For ferromagnetic spin waves, the spin wave function for small \mathbf{q} is

$$S_{\text{sw}}(\mathbf{Q}, \omega) = S \sum_{\tau, \mathbf{q}} [(n_q + 1)\delta(\mathbf{Q} - \mathbf{q} - \boldsymbol{\tau})\delta(\omega - \omega_q) + n_q\delta(\mathbf{Q} + \mathbf{q} - \boldsymbol{\tau})\delta(\omega + \omega_q)] \quad (3.45)$$

with quadratic dispersion relation $\hbar\omega_q = Dq^2$, and $D = 2Jsa^2$ where J is the exchange energy. While for antiferromagnetic spin waves, the spin wave function for small \mathbf{q} is

$$S_{\text{sw}}(\mathbf{Q}, \omega) = S \sum_{\tau, \mathbf{q}} \frac{\hbar\omega_0}{\hbar\omega_q} [(n_q + 1)\delta(\mathbf{Q} - \mathbf{q} - \boldsymbol{\tau})\delta(\omega - \omega_q) + n_q\delta(\mathbf{Q} + \mathbf{q} - \boldsymbol{\tau})\delta(\omega + \omega_q)] \quad (3.46)$$

where, as before, the $\boldsymbol{\tau}$ sum is over reciprocal lattice vectors of the magnetic unit cell and $\hbar\omega_0 = 2zJS$, with z nearest neighbors; and linear dispersion relation $\hbar\omega_q = \hbar cq$ with $c = zJSa/\hbar$.

3.2 Neutron Spectroscopy Techniques

In order to determine the partial differential cross-section for any scattering process one must know the energy of the scattering probe (e.g., the neutron) before and after allowing it to interact with the sample in order to be able to detect changes due to inelastic scattering processes. The name for the energy analysis of a scattering probe is spectroscopy, and the means by which it is accomplished is probe dependent.

All scattering probes have an energy-dependent wavelength, see e.g., figure 3.1. Bragg scattering from a crystal is dependent on the wavelength of a probe, and can therefore be used as a means of energy discrimination since different wavelengths are diffracted at different angles from the same set of crystal lattice planes. A device constructed of one or more crystals and aligned to diffract a wavelength (and energy) of interest upon a sample to be studied is called a monochromator. Monochromators are used extensively in x-ray and neutron diffraction. When a monochromator is placed after a sample and is used to select a single wavelength scattered by the sample for detection, it is conventionally referred to as an analyzer.

Scattering probes with finite mass have a kinetic energy dependent upon their velocity, and therefore measuring changes in their velocity is a way to analyze their kinetic energy. Since it is not too difficult to accurately measure fixed distances and times between events, most velocity based energy analysis measurements measure the time it takes for, e.g., a neutron to travel a known distance and from that calculate its velocity and energy.

Focusing on neutron spectroscopy, it is possible to measure the energy of a neutron via either its wavelength or its velocity. By measuring the energy of a neutron before and after

allowing it to interact with a sample, it is possible to determine the energy transferred to or from the sample and, ultimately, extract the partial differential cross-section for that interaction. In principle a neutron spectrometer, i.e., an instrument which allows for such a spectroscopy analysis, can consist of a combination of wavelength- and velocity-based energy analysis. However, the majority of neutron spectrometers utilize one or the other exclusively to analyze the energy of neutrons incident-on and scattered-from a sample. The most common neutron spectrometer which leverages the neutron wavelength to perform energy analysis is the triple-axis spectrometer, while the most common velocity-based neutron spectrometer is the direct-geometry time-of-flight spectrometer.

3.2.1 Triple-axis

The triple-axis neutron spectrometer uses Bragg scattering from monochromator and analyzer crystals in order to perform energy-analysis of neutron scattering. Illustrated in figure 3.4 is the triple-axis neutron spectrometer located on horizontal beamtube 3 (HB3) at the High Flux Isotope Reactor (HFIR) on the campus of Oak Ridge National Laboratory (ORNL), which is a typical triple-axis neutron spectrometer. The components of the HB3 spectrometer consist of a steady-state fission reactor neutron source, a variable-vertically-focusing monochromator comprised of pyrolytic graphite (PG) crystals arrayed to diffract neutrons from (002) planes, a sample table, a fixed-vertically-focusing analyzer also utilizing the (002) reflection of pyrolytic graphite, and a ^3He single detector — plus computer-controlled motors to enable scans through reciprocal space, and shielding to reduce measured background and personnel radiation risks. The three axes of the triple-axis spectrometer are the monochromator rotation (ψ_M), the sample rotation (ψ_S), and the analyzer rotation (ψ_A). It should be noted that, while the rotation angle of any of the three crystals, ψ_i , is half its scattering angle, $2\theta_i$, in the case of Bragg scattering, this relationship is not enforced

mechanically, nor strictly via software, and so the rotation angles (ψ_i) and scattering angles ($2\theta_i$) are typically treated as separate variables.

Since the energy of an incident neutron is selected via Bragg scattering from the monochromator, and the energy of a scattered neutron is determined via Bragg scattering from the analyzer, angular uncertainties are critically important for the correct determination of the energy transferred to (or from) a sample via inelastic scattering. Compared to synchrotron x-ray sources, neutron sources have orders-of-magnitude lower flux and, consequently, neutron beams are typically large in cross-section in order to increase the total-beam flux that can be directed upon a sample. Such broad beams contain neutrons with finite divergence due to the source and apertures defining them not being point-like. One way employed to reduce the divergence of a neutron beam is to place long and thin slats of neutron-absorbing material aligned-along and in the beam. Such devices are called Soller collimators, and they limit the divergence of the beam geometrically without significantly reducing the beam cross-sectional area. The HB3 triple-axis spectrometer has such Soller collimators (not shown in figure 3.4) between the monochromator and sample position, between the sample position and analyzer, and between the analyzer and detector. These collimators not only reduce the divergence of the beam, but also tend to reduce the background measured by the ^3He detector. Further details regarding the effect of Soller collimators and instrument components on the uncertainty of measurements are discussed in appendix C.

As illustrated in figure 3.3, any crystal which is aligned to diffract neutrons of wavelength λ (and wavenumber $k = 2\pi/\lambda$, and energy $E = h^2/2m\lambda^2$) will also diffract shorter-wavelength neutrons with $\lambda_n = \lambda/n$, $n = 2, 3, \dots$. These shorter-wavelength neutrons have higher energy than the primary neutrons, that goes like their order squared

$$E_n = \frac{h^2}{2m\lambda_n^2} = n^2 \frac{h^2}{2m\lambda^2} = n^2 E, \quad (3.47)$$

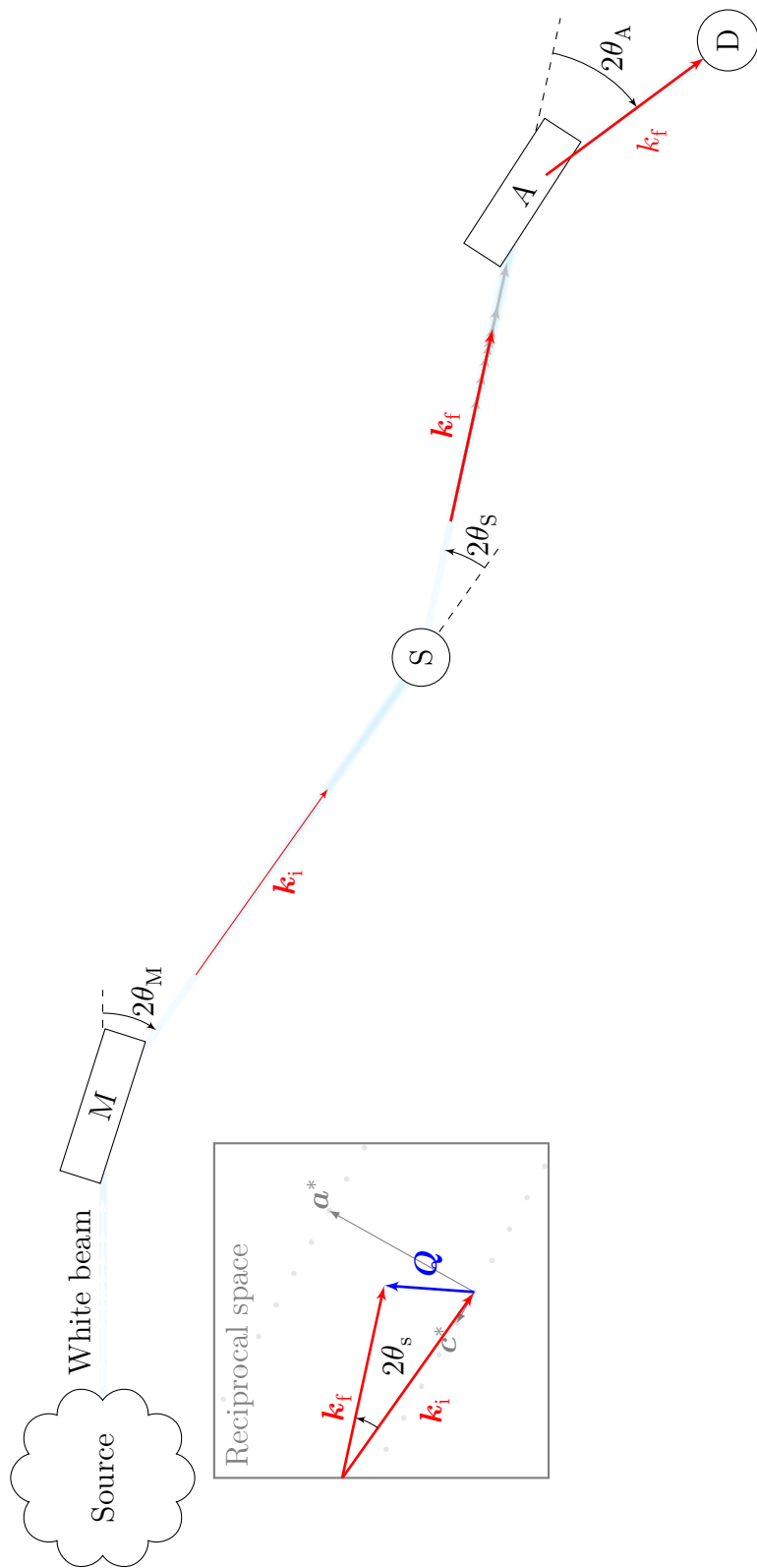


FIGURE 3.4. A simplified illustration of a triple-axis spectrometer, here modeled on the dimensions of the HB3 triple-axis spectrometer at the High Flux Isotope Reactor on the campus of Oak Ridge National Laboratory, Oak Ridge, Tennessee. Displayed here is the condition for inelastic scattering with $\mathbf{Q} = (0.5\ 0.5\ 1)_{\text{T}}$ and $E = 5\text{ meV}$ for a typical $\text{Ba}(\text{Fe}_{1-x}\text{Co}_x)_2\text{As}_2$ sample with final a neutron energy of 14.7 meV and a pyrolytic graphite monochromator and analyzer. Indicated are the monochromator (M), source (S), analyzer (A), and their scattering angles ($2\theta_i$, $i=M,S,A$); the reactor source (Source), the ^3He detector (D), the directions and proportional magnitudes of \mathbf{k}_i and \mathbf{k}_f , and an inset picture of reciprocal space. With the exception of the source-to-monochromator distance, all distances between elements are to scale.

and are called higher-order harmonics of the incident beam. If the monochromator, sample, and analyzer are all in the Bragg condition for some reflection, the detected neutrons will be some combination of the primary wavelength and high-order neutrons; dependent upon the exact energy-distribution of the neutron flux coming from the moderator. Because the sample is not in a Bragg condition during inelastic measurements such higher-order scattering might seem to be less problematic; however, higher-order scattering from either the monochromator or the analyzer that coincides with strong elastic scattering from the sample can produce sharp spurious peaks (spurious) in an inelastic scattering dataset, and can easily be misinterpreted as new and unexpected excitations. Therefore, it is important to reduce the percentage of higher-order neutrons in the neutron beam in order to avoid such deleterious effects. One often employed method by which to do so is to place a material with a highly energy-dependent neutron transmission probability in the beam and select a fixed incident or fixed final primary neutron energy to coincide with a high-transmission window that also gives low-transmission for higher-order neutrons. For convenience, due to the k_f term in the cross-section for inelastic neutron scattering, the HB3 triple-axis spectrometer is often operated with a fixed final neutron energy of 14.7 meV which coincides with a transmission window in a highly ordered pyrolytic graphite (HOPG) filter placed in the neutron beam between the sample and analyzer. HOPG filters also have useful primary transmission windows at 30.5 and 41.0 meV [80, p. 81]. As discussed in detail by Shirane et al. [80], there are other materials which can be used as high-pass and low-pass neutron filters. HB3 has such a filter, made of sapphire, before the monochromator to remove high-energy neutrons from the incident beam.

Working with a fixed final energy solves one problem while introducing another. With the final energy fixed, excitations can only be measured if the incident energy is varied – which also varies the incident neutron flux, making it difficult to measure absolute cross-sections. By placing a low-efficiency neutron detector (often a Geiger counter filled with mostly nitrogen

gas, called a beam monitor, that counts with an efficiency proportional to the neutron wavevector k) between the monochromator and sample, and then normalizing measured counts in the ^3He detector to measured counts in the monitor, it is possible to compare data measured with different incident energy neutrons; unfortunately this does not fully solve the issue of absolute cross-sections, which is discussed in detail in appendix D.

If one so chooses, the same HOPG filter can be placed between the monochromator and sample and the triple-axis instrument can be used with fixed incident neutron energy. The cross-section for inelastic neutron scattering is proportional to k_f/k_i , k_f (k_i) changes with energy transfer for fixed- E_i (fixed- E_f) and must be accounted for when comparing measured intensity to a theoretical model. Since interpreting data without correcting for varying k_f/k_i would be misleading, it is common to conduct triple-axis experiments with fixed- E_f (so that the k_f term remains constant and the remaining $1/k_i$ term is accounted for by the beam monitor efficiency) to minimize the possibility of misinterpreting data during the experiment.

With a single detector, the flexibility to easily define all components of (\mathbf{Q}, E) , and a steady-state source of neutrons, the triple-axis neutron spectrometer is a workhorse instrument for focused parametric studies of the effects of temperature, magnetic field, etc., on a condensed matter system and its excitations.

3.2.2 Time-of-flight

The time-of-flight neutron spectrometer takes advantage of the finite mass of the neutron to measure its energy via its velocity. In order to determine the velocity of a neutron one must define a path that the neutron can take and then measure the time for the neutron to travel through that path. This requires some time-structure to the neutron beam used the various time-of-flight techniques. While it is possible to take a steady-state neutron beam from a fission reactor and introduce a time-structure with, e.g., a series of disc choppers, it is far more advantageous to leverage the intrinsic time-structure of a pulsed neutron source for a

time-of-flight measurement. Time-of-flight neutron scattering instruments are typically large – with flight paths from a few to tens of meters – so measuring neutron path distances with high relative accuracy is possible (e.g., a relative uncertainty of 10^{-3} only requires millimeter precision for a meter long flight path, and commercial laser-based surveying equipment is available with sub-millimeter accuracy).

To measure the neutron velocity then, it is necessary to define a starting time and a stopping time. For pulsed sources, the starting time is typically taken to coincide with the pulse – the time of the proton beam hitting the target is used for pulsed spallation sources. Independent of the type of source, the stopping time is typically the time when a neutron is detected.

The energy of a neutron incident on a sample can be determined by opening a path through an otherwise-neutron-absorbing ‘chopper’ at some defined time after the pulse time. Knowing the distance between where the neutrons are produced at time-zero and the location of the chopper, allows for the energy of the incident neutron to be selected based on its velocity. Due to considerations of energy-resolution and transmitted flux there are different designs these beam choppers. Common beam choppers are: the disc chopper, which is made of neutron-absorbing material and aligns a neutron-transparent window with the beam at the appropriate time; and the Fermi chopper, which spins a pack of curved neutron absorbing blades around an axis perpendicular to the neutron beam thereby passing only those neutrons with the correct velocity (and phase) to pass through without touching, as illustrated in figure 3.5.

The ARCS direct-geometry time-of-flight of flight spectrometer, illustrated in figure 3.6, is located at beamline 18 of the Spallation Neutron Source on the campus of Oak Ridge National Laboratory, Oak Ridge, Tennessee. Beamline 18 makes use of thermally moderated neutrons and, due to the nature of accelerator-driven spallation sources, ARCS has access to incident neutrons with energies ranging from tens of meV to a few eV [82]. The first

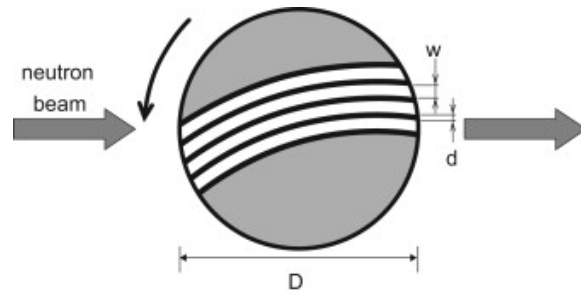


FIGURE 3.5. An illustration of a Fermi chopper, reproduced from [81].

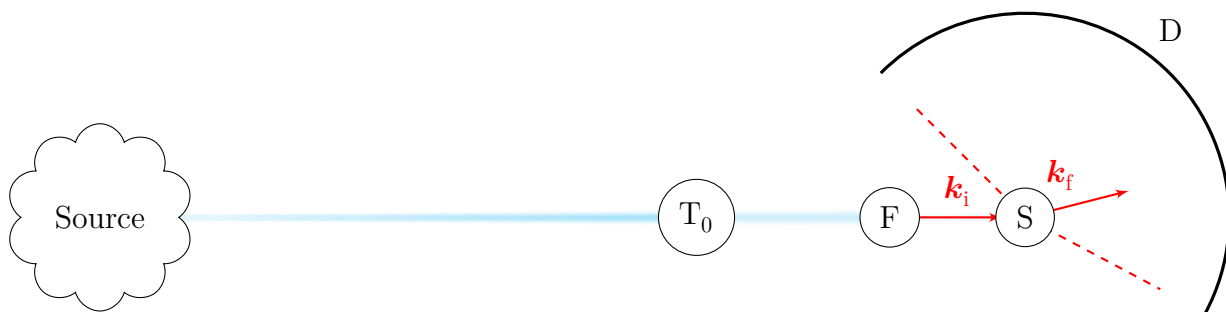


FIGURE 3.6. A simplified illustration of a time-of-flight spectrometer, here modeled on the dimensions of the ARCS time-of-flight spectrometer at the Spallation Neutron Source on the campus of Oak Ridge National Laboratory, Oak Ridge, Tennessee. Indicated are the T-zero chopper (T_0), Fermi chopper (F), sample (S), the intersection of the detector bank (D) with the instrumental horizontal plane, and the spallation source and thermal moderator (Source). All distances are to scale.

element along the beam path from the moderator at ARCS is a so-called T_0 chopper which is closed shortly-after each spallation event in order to prevent very-high-energy (unmoderated) neutrons and gamma rays produced in the spallation event from proceeding down the beam path and being detected. The T_0 chopper has a wide band-pass and lets through a large range of neutron energies, dependent upon its exact opening time after the spallation event. The next element along the ARCS beam path is one of two interchangeable Fermi choppers, which have different slit packages to allow coarse or fine energy resolution. Only neutrons with a selected energy are able to pass the Fermi chopper, at which point they travel towards the sample position thereby defining k_i .

Since total flight-time is used to analyze the energy of detected neutrons, there are no additional components between the sample and detector, which allows for a large-scale multiplexing through the use of an array of position-sensitive ^3He detector tubes. Such an array of detectors allows for a very efficient measurement of large swaths of reciprocal space at one sample setting; however, since each detector only measures three variables for each neutron (two angles describing its own position, and the detection time for each neutron) only a surface is measured in four-dimensional (\mathbf{Q}, E) space. This limitation can be overcome, if a sufficiently large sample (or cross-section) is to be measured, by rotating the sample angle while collecting data [83].

Having access to so much of reciprocal space in a single instrument and sample-environment setting makes it possible to accurately determine the background contribution to signals of interest; more details about how to determine and remove the background from a single-setting time-of-flight dataset are given in appendix E.

By accessing large regions of reciprocal space in a single measurement, direct-geometry time-of-flight spectrometers like ARCS can give a broad overview of the excitations in a system and are a fantastic complementary tool to the focused studies performed with triple-axis neutron spectrometers.

CHAPTER 4 METHODS AND PROCEDURES

Performing measurements with inelastic neutron scattering instruments employing the time of flight method creates data sets in the form of number of counted neutrons as a function of a number of instrument angles and time. This data is then converted to intensity, I , as a function of reciprocal space and energy transfer, (\mathbf{Q}, E) , typically before leaving the instrument computers and often before any real analysis. The measured intensity, $I(\mathbf{Q}, E)$, will contain information about static structures and excitations within a condensed matter system, and some details can typically be extracted without additional in-depth analysis, e.g., the peak position in a series of inelastic scan across a phonon branch can reveal the phonon dispersion, $\omega_s(\mathbf{q})$. However, in cases where the measured intensity is not obviously peaked or when there is a desire to extract additional information from a dataset, then a physical model must be fit to the dataset. If features of the physical model are as sharp or sharper than the instrumental resolution, it is further necessary to convolute the model intensity and resolution when fitting; details of this process are given in appendix C.

Expressions were given in chapter 3 for the small \mathbf{q} representation of the spin wave function, $S_{\text{sw}}(\mathbf{Q}, \omega)$, for a ferromagnet and an antiferromagnet. In both cases, the form given is a small \mathbf{q} expansion of the low-energy spin wave excitations of the Heisenberg Hamiltonian, which is itself an approximation to the Hamiltonian for a local moment system taking into account spin-spin interactions. As stated by Ashcroft and Mermin,

Extracting information even from the Heisenberg Hamiltonian is, in general, so difficult a task, that it by itself is taken as the starting point for many quite profound investigations of magnetism in solids. One must remember, however,

that much subtle physics and quite complex approximations must be delved into before one can even arrive at a Heisenberg Hamiltonian. [59, p. 681]

Despite the difficulties associated with deriving the Heisenberg Hamiltonian, it has been used with some success to fit spin fluctuations in the iron pnictides, as discussed below in section 4.1.1.

The challenges of deriving a local moment Heisenberg Hamiltonian for a system in which itinerant electrons are important for the magnetism, like the iron pnictides, are ample motivation to look elsewhere for simplified spin fluctuation models. One model, discussed in detail below in section 4.1.3, starts from a harmonic oscillator response function and adds features to better describe the iron pnictide spin fluctuations. Another relevant model for the spin fluctuations seen near optimal doping in the iron pnictides considers a system of antiferromagnetically coupled itinerant spins which lack long-range antiferromagnetic order, this diffusive model is detailed below in section 4.1.4.

Damping of the spin fluctuations in $\text{Ba}(\text{Fe}_{1-x}\text{Co}_x)_2\text{As}_2$ is in some cases dramatic and in all cases important, and gives an indication that itinerant electrons are at least partially responsible for the observed spin response. Similarly, the spin fluctuations in $\text{Ba}(\text{Fe}_{1-x}\text{Co}_x)_2\text{As}_2$ are always anisotropic and, in some cases, drastically so. The importance of damping and anisotropy has led to the development here of models including anisotropic parameters, wherever physically meaningful, and detailed in sections 4.1.3 to 4.1.5.

In contrast to the normal state spin fluctuations, where simple models with straightforward physical interpretations are available, the spin fluctuations in the superconducting state are more difficult to model. Described below are two developed models for the superconducting state spin fluctuations, including modeling the superconducting resonance. The two models differ in their physical interpretation, with one being a rescaling of the normal state spin fluctuations and the other being purely empirical; however they both allow for the extraction

of physically-relevant parameters, such as the resonance dispersion and spectral weight. These two models are discussed in sections 4.2.1 and 4.2.2, respectively.

4.1 Modeling Normal State Spin Excitations

4.1.1 Heisenberg model

4.1.1.1 A simple ferromagnet

Following the formalism laid out by Lovesey, a ferromagnetic system with localized spins can be described by the Heisenberg Hamiltonian [78, p. 57]

$$\hat{\mathcal{H}} = - \sum_{\mathbf{l}, \mathbf{l}'} \mathcal{J}(\mathbf{l} - \mathbf{l}') \hat{\mathbf{S}}_{\mathbf{l}} \cdot \hat{\mathbf{S}}_{\mathbf{l}'} - g\mu_{\text{B}}H \sum_{\mathbf{l}} \hat{S}_{\mathbf{l}}^z \quad (4.1)$$

with an applied external magnetic field H in the z direction, and an exchange parameter $\mathcal{J}(\mathbf{l} - \mathbf{l}')$ between spins located at sites \mathbf{l} and \mathbf{l}' defined such that $\mathcal{J}(0) = 0$. By introducing the spin angular momentum raising and lowering operators, $\hat{S}^{\pm} = \hat{S}^x \pm i\hat{S}^y$, the Hamiltonian can be recast as

$$\hat{\mathcal{H}} = - \sum_{\mathbf{l}, \mathbf{l}'} \mathcal{J}(\mathbf{l} - \mathbf{l}') [\hat{S}_{\mathbf{l}}^z \hat{S}_{\mathbf{l}'}^z + \hat{S}_{\mathbf{l}}^+ \hat{S}_{\mathbf{l}'}^-] - g\mu_{\text{B}}H \sum_{\mathbf{l}} \hat{S}_{\mathbf{l}}^z \quad (4.2)$$

and, by taking advantage of the commutation relations for the components of $\hat{\mathbf{S}}$, Lovesey derives the equation of motion for a Bravais lattice, where $\mathcal{J}(\mathbf{l} - \mathbf{l}') = \mathcal{J}(\mathbf{l}' - \mathbf{l})$, as

$$i\hbar\partial_t \hat{S}_{\mathbf{l}}^+ = g\mu_{\text{B}}H \hat{S}_{\mathbf{l}}^+ + 2 \sum_{\mathbf{l}'} \mathcal{J}(\mathbf{l} - \mathbf{l}') [\hat{S}_{\mathbf{l}'}^z \hat{S}_{\mathbf{l}}^+ - \hat{S}_{\mathbf{l}'}^+ \hat{S}_{\mathbf{l}}^z]. \quad (4.3)$$

Which, under the assumption that the spin is fully saturated and $\hat{S}^z \rightarrow S$ becomes

$$i\hbar\partial_t \hat{S}_{\mathbf{l}}^+ = g\mu_{\text{B}}H \hat{S}_{\mathbf{l}}^+ + 2S \sum_{\mathbf{l}'} \mathcal{J}(\mathbf{l} - \mathbf{l}') [\hat{S}_{\mathbf{l}}^+ - \hat{S}_{\mathbf{l}'}^+]. \quad (4.4)$$

By introducing the reciprocal space counterparts of \hat{S}_l^\pm and $\mathcal{J}(\mathbf{l})$ via

$$\hat{S}_l^\pm = \frac{1}{N} \sum_{\mathbf{q}} e^{\pm i\mathbf{q}\cdot\mathbf{l}} \hat{S}_{\mathbf{q}}^\pm \quad J(\mathbf{q}) = \sum_{\mathbf{l}} \mathcal{J}(\mathbf{l}) e^{-i\mathbf{q}\cdot\mathbf{l}} \quad (4.5)$$

the equation of motion can be replaced by

$$i\hbar\partial_t \hat{S}_{\mathbf{q}}^+ = g\mu_B H \hat{S}_{\mathbf{q}}^+ + 2S [J(0) - J(\mathbf{q})] \hat{S}_{\mathbf{q}}^+ \quad (4.6)$$

which can have time dependent solutions of the form $\hat{S}_{\mathbf{q}}^+(t) = \exp(-i\omega_{\mathbf{q}}t) \hat{S}_{\mathbf{q}}^+$ giving the dispersion relation

$$\hbar\omega_{\mathbf{q}} = g\mu_B H + 2S [J(0) - J(\mathbf{q})]. \quad (4.7)$$

If the exchange parameter is only finite between nearest-neighbors, with magnitude J , then

$$J(\mathbf{q}) = J \sum_{\boldsymbol{\rho}} e^{i\mathbf{q}\cdot\boldsymbol{\rho}} \quad (4.8)$$

where $\boldsymbol{\rho}$ is a vector pointing to each nearest-neighbor. In the limit of small \mathbf{q} , equation (4.8) can be expanded

$$J(\mathbf{q}) = J \sum_{\boldsymbol{\rho}} \left\{ 1 + i\mathbf{q}\cdot\boldsymbol{\rho} + \frac{1}{2}(i\mathbf{q}\cdot\boldsymbol{\rho})^2 + \dots \right\} \approx 1 - Jq^2 a^2 \quad (4.9)$$

where the approximation is only valid for cubic lattices with lattice parameter a . In such a case, it's clear to see that the dispersion relationship given for equation (3.45) is recovered in the case of no applied field

$$\hbar\omega_{\mathbf{q}} \approx g\mu_B H + 2JSa^2 q^2. \quad (4.10)$$

4.1.1.2 A simple antiferromagnet

Lovesey also derives the dispersion relationship for a simple collinear antiferromagnet as the limiting case of a ferrimagnet which is composed of two interpenetrating sublattices aligned antiferromagnetically with different spin magnitudes. Taking the limit of equal sublattice spin magnitudes early, and again following the formalism of Lovesey, one can write the Heisenberg Hamiltonian for a simple collinear antiferromagnet as

$$\begin{aligned}
\hat{\mathcal{H}} = & \sum_{l,r} \mathcal{J}(\mathbf{r}) \hat{\mathbf{S}}_l \cdot \hat{\mathbf{S}}_{l+r} + \sum_{m,r} \mathcal{J}(\mathbf{r}) \hat{\mathbf{S}}_m \cdot \hat{\mathbf{S}}_{m+r} \\
& + \sum_{l,r'} \mathcal{J}'(\mathbf{r}') \hat{\mathbf{S}}_l \cdot \hat{\mathbf{S}}_{l+r'} + \sum_{m,r'} \mathcal{J}'(\mathbf{r}') \hat{\mathbf{S}}_m \cdot \hat{\mathbf{S}}_{m+r'} \\
& - g\mu_B(H + H_A) \sum_l \hat{S}_l^z - g\mu_B(H - H_A) \sum_m \hat{S}_m^z
\end{aligned} \tag{4.11}$$

where \mathbf{r} connects sites on opposite sublattices and \mathbf{r}' connects sites on the same sublattice; similarly the exchange parameters \mathcal{J} and \mathcal{J}' represent magnetic exchange energy between inter- and intra-sublattice spins, respectively; and H_A is an effective magnetic field due to uniaxial anisotropy. To simplify the calculation of spin wave modes of this Hamiltonian, it is useful to rotate the spin operators associated with the \mathbf{m} sublattice via

$$\hat{T}_m^x = \hat{S}_m^x, \quad \hat{T}_m^y = -\hat{S}_m^y, \quad \text{and} \quad \hat{T}_m^z = -\hat{S}_m^z \tag{4.12}$$

which has the effect of reversing the spin raising and lowering operators for the \mathbf{m} sublattice ions, $\hat{T}_m^\mp = \hat{S}_m^\pm$. The Fourier transforms of \hat{T}_m^\pm and \hat{S}_l^\pm are defined by

$$\hat{S}_l^\pm = \frac{1}{N} \sum_{\mathbf{q}} e^{\pm i\mathbf{q}\cdot\mathbf{l}} \hat{S}_{\mathbf{q}}^\pm, \quad \text{and} \quad \hat{T}_m^\pm = \frac{1}{N} \sum_{\mathbf{q}} e^{\mp i\mathbf{q}\cdot\mathbf{m}} \hat{T}_{\mathbf{q}}^\pm, \tag{4.13}$$

where \mathbf{q} is restricted to the first Brillouin zone of one sublattice, and each sublattice has N sites [78, p. 111]. The linear equations of motion for each of the Fourier transformed operators

can be obtained by applying the operator commutation relations and ignoring terms with three or more raising or lowering operators; for $\hat{S}_{\mathbf{q}}^+$ and $\hat{T}_{\mathbf{q}}^-$ these are

$$i\hbar\partial_t\hat{S}_{\mathbf{q}}^+ = [2SJ(0) - 2S\{J'(0) - J'(\mathbf{q})\} + g\mu_{\text{B}}(H + H_{\text{A}})]\hat{S}_{\mathbf{q}}^+ - 2SJ(\mathbf{q})\hat{T}_{\mathbf{q}}^- \quad (4.14)$$

$$i\hbar\partial_t\hat{T}_{\mathbf{q}}^- = -[2SJ(0) - 2S\{J'(0) - J'(\mathbf{q})\} - g\mu_{\text{B}}(H - H_{\text{A}})]\hat{T}_{\mathbf{q}}^- + 2SJ(\mathbf{q})\hat{S}_{\mathbf{q}}^+. \quad (4.15)$$

The solution to these coupled linear equations of motion benefits from a second quantization, introduced by Lovesey, and ultimately yields two solutions with $a = 0, 1$ [78, p. 113]

$$\hbar\omega_{\mathbf{q},a} = (-1)^a g\mu_{\text{B}}H + \sqrt{[2SJ(0) - 2S\{J'(0) - J'(\mathbf{q})\} + g\mu_{\text{B}}H_{\text{A}}]^2 - [2SJ(\mathbf{q})]^2}. \quad (4.16)$$

As in the ferromagnetic case, the determination of $J(\mathbf{q})$ and $J'(\mathbf{q})$ is critically important for determining the dispersion relationship. If the antiferromagnetic system is simple and has exchange parameters similar to equation (4.8), i.e.,

$$\begin{aligned} J(\mathbf{q}) &= \sum_{\rho} \mathcal{J}(\rho)e^{i\mathbf{q}\cdot\rho} & J'(\mathbf{q}) &= \sum_{\rho'} \mathcal{J}'(\rho')e^{i\mathbf{q}\cdot\rho'} \\ &\approx J(0) - \frac{1}{6}q^2 \sum_{\rho} \mathcal{J}(\rho)\rho^2 & &\approx J'(0) - \frac{1}{6}q^2 \sum_{\rho'} \mathcal{J}'(\rho')\rho'^2 \\ &\equiv J(0) - \frac{1}{6}q^2 J^{(2)} & &\equiv J'(0) - \frac{1}{6}q^2 J'^{(2)} \end{aligned} \quad (4.17)$$

then equation (4.16) is approximately [78, p. 114]

$$\begin{aligned} \hbar\omega_{\mathbf{q},a} &\approx (-1)^a g\mu_{\text{B}}H \\ &+ \left\{ g\mu_{\text{B}}H_{\text{A}} [4SJ(0) + g\mu_{\text{B}}H_{\text{A}}] \right. \\ &+ \frac{1}{3}q^2 S [4SJ(0) (J^{(2)} - J'^{(2)}) - 2g\mu_{\text{B}}H_{\text{A}}J'^{(2)}] \\ &\left. + \frac{1}{9}q^4 S^2 [(J'^{(2)})^2 - (J^{(2)})^2] \right\}^{1/2}. \end{aligned} \quad (4.18)$$

It's clear that with no applied field, the dispersion relationship given by equation (4.18) remains finite at $\mathbf{q} = 0$ with a value determined by the effective anisotropy field H_A . If the anisotropy field is zero, the small \mathbf{q} behavior of equation (4.18), where the q^4 terms can be discarded, is linear in q .

4.1.2 BaFe₂As₂

Ewings et al. derived an approximate spin-only Heisenberg Hamiltonian for BaFe₂As₂ in an attempt to describe inelastic neutron scattering data from a powder sample [84]. Their form for the Hamiltonian has two nearest-neighbor exchange parameters, J_{1a} and J_{1b} , for interactions along the \mathbf{a} and \mathbf{b} orthorhombic lattice directions, a next-nearest-neighbor exchange, J_2 , for interactions along the diagonal directions of the \mathbf{a} - \mathbf{b} plane, and a fourth exchange parameter, J_c , for interactions between the iron-arsenic layers. Also included in their form for the Hamiltonian are two single-ion anisotropy constants for in-plane and out-of-plane spin rotations. The form given for the Hamiltonian is

$$\hat{\mathcal{H}} = \sum_{\langle jk \rangle} J_{jk} \hat{\mathbf{S}}_j \cdot \hat{\mathbf{S}}_k + \sum_j \left\{ K_c (\hat{S}_j^z)^2 + K_{ab} [(\hat{S}_j^y)^2 - (\hat{S}_j^x)^2] \right\} \quad (4.19)$$

where the first sum is over all nearest-neighbor and next-nearest-neighbor pairs, and J_{jk} takes on the appropriate exchange parameter value for the pair relationship.

Ewings et al. give the two resultant dispersion relationships

$$\hbar\omega_{\mathbf{Q},\pm} = \sqrt{A_{\mathbf{Q}}^2 - (C \pm D_{\mathbf{Q}})^2} \quad (4.20)$$

with

$$A_{\mathbf{Q}} = 2S \{ J_{1b} [\cos(\frac{1}{2}\mathbf{Q} \cdot \mathbf{b}) - 1] + J_{1a} + 2J_2 + J_c \} + S (3K_{ab} + K_c) \quad (4.21)$$

$$C = S (K_{ab} - K_c) \quad (4.22)$$

$$D_{\mathbf{Q}} = 2S \{ J_{1a} \cos(\frac{1}{2}\mathbf{Q} \cdot \mathbf{a}) + 2J_2 \cos(\frac{1}{2}\mathbf{Q} \cdot \mathbf{a}) \cos(\frac{1}{2}\mathbf{Q} \cdot \mathbf{b}) + J_c \cos(\mathbf{Q} \cdot \mathbf{c}) \} \quad (4.23)$$

as well as the non-zero elements of the spin-spin correlation tensor

$$S^{yy}(\mathbf{Q}, E) = S \frac{A_{\mathbf{Q}} - C - D_{\mathbf{Q}}}{\hbar\omega_{\mathbf{Q},+}} \langle n(\omega) + 1 \rangle \delta(\omega - \omega_{\mathbf{Q},+}) \quad (4.24)$$

$$S^{zz}(\mathbf{Q}, E) = S \frac{A_{\mathbf{Q}} + C - D_{\mathbf{Q}}}{\hbar\omega_{\mathbf{Q},-}} \langle n(\omega) + 1 \rangle \delta(\omega - \omega_{\mathbf{Q},-}) \quad (4.25)$$

from which, the cross section is defined by equation (3.38).

It's important to remember that this model of spin wave excitations for BaFe₂As₂ is an approximation and, more so, that it contains no energy damping or correlation length. As such, it can only reproduce the spin excitation spectra of a system with infinite spatial order and infinitely-lived spin wave excitations. Since itinerant electrons are at least partially responsible for the antiferromagnetism in Ba(Fe_{1-x}Co_x)₂As₂ and the substitution of cobalt for iron conceivably adds disorder to the system, it is desirable to add-in energy damping and finite correlation lengths. Therefore, it is worthwhile to develop other spin fluctuation models which incorporate these desirable features.

4.1.3 Spinwave model

The simplest case of modeling spin excitations emanating from an ordered antiferromagnetic state is that of the simple harmonic oscillator spin wave. In a completely isotropic system, the response function that defines the magnetic susceptibility is

$$\chi_s(\mathbf{Q}, E) = \chi_0 \Delta^2 [\Delta^2 + v^2 q^2 - E^2 - i\alpha E]^{-1}, \quad (4.26)$$

where $\chi_0 \equiv \chi_s(\mathbf{Q}_{\text{AFM}}, 0)$ is the staggered static susceptibility, Δ is the magnitude of the spin gap (if present) at \mathbf{Q}_{AFM} , the spin wave velocity v measures the dispersion away from \mathbf{Q}_{AFM} , $\mathbf{q} = \mathbf{Q} - \mathbf{Q}_{\text{AFM}}$, and α is responsible for the dissipation of energy due to damping. Inelastic neutron scattering measures the imaginary component of the magnetic susceptibility which, for equation (4.26) can be shown to be

$$\chi_s''(\mathbf{Q}, E) = \frac{\chi_0 \Delta^2 \alpha E}{(\Delta^2 + v^2 q^2 - E^2)^2 + \alpha^2 E^2}, \quad (4.27)$$

for the isotropic spin wave model (illustrated in figure 4.1).

Solid state systems only very rarely have truly isotropic properties and, one way to account for this is to include anisotropy in the spin wave velocity. Such a response function could be

$$\chi_{\text{as}}(\mathbf{Q}, E) = \chi_0 \Delta^2 [\Delta^2 + v_q^2 q^2 - E^2 - i\alpha E]^{-1}, \quad (4.28)$$

with imaginary component

$$\chi_{\text{as}}''(\mathbf{Q}, E) = \frac{\chi_0 \Delta^2 \alpha E}{(\Delta^2 + v_q^2 q^2 - E^2)^2 + \alpha^2 E^2} \quad (4.29)$$

where v_q is the, now anisotropic, spin wave velocity. Strictly speaking, $v_q^2 q^2$ is the product of four rank 2 tensors which depends strongly on the underlying symmetry of the system. For any orthonormal system the spin wave velocity tensor has, at most, three independent parameters – as is the case for an orthorhombic system; a tetragonal system has two independent parameters, and a cubic system one [85]. Since the low-temperature orthorhombic system is often indexed in terms of the tetragonal unit cell (and, therefore, \mathbf{q} is represented in tetragonal units), the three independent parameters chosen to represent the spin wave velocity tensor are not strictly the orthorhombic eigenvalues v_L , v_T , and v_z (with eigenvectors $[100]_O$, $[010]_O$, and $[001]_O$ which are along the ordered moment direction, within the Fe-*Ph* layer and

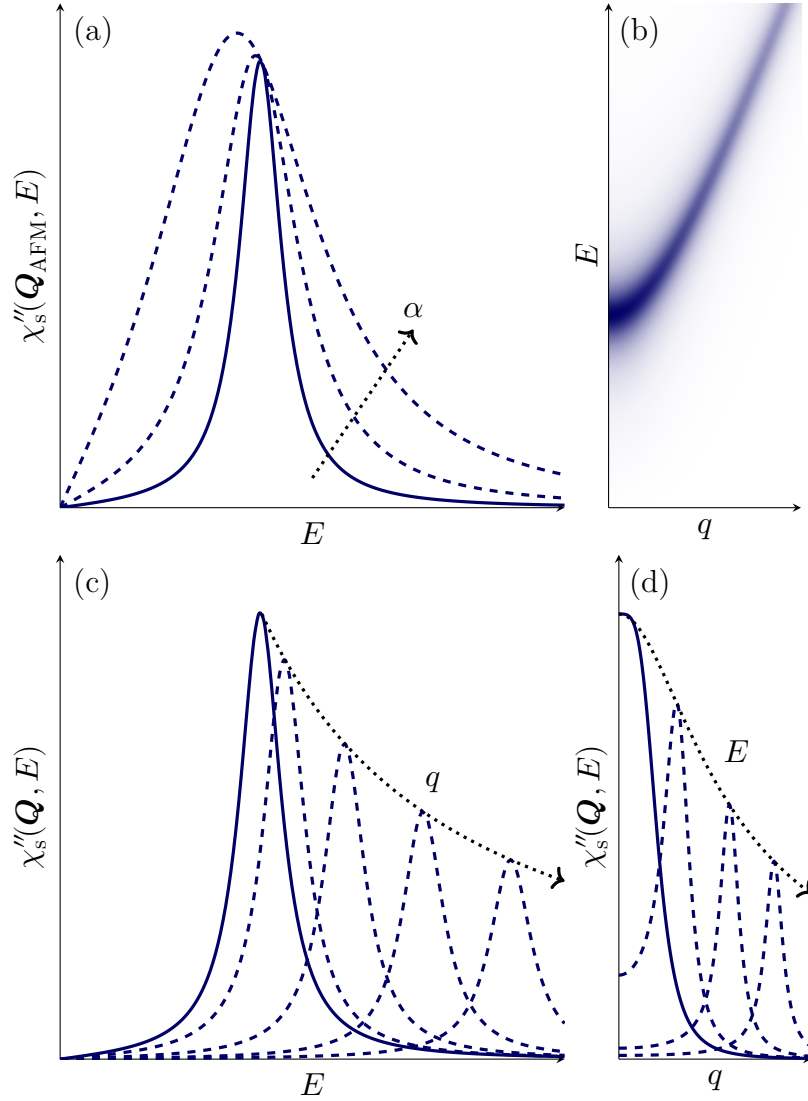


FIGURE 4.1. The spinwave model, equation (4.27), as a function of energy transfer, E , and reduced momentum transfer, q . Panel (a) shows $\chi_s''(\mathbf{Q}, E)$ at \mathbf{Q}_{AFM} as a function of E which is peaked at the spin gap magnitude, Δ , for small damping, α ; increasing damping has the effect of broadening the spinwave model response in energy, as shown by the nested dashed lines. Panel (b) shows an image plot of $\chi_s''(\mathbf{Q}, E)$ calculated for gridded points on the E - q plane, here white corresponds to zero and the darkest color is the maximum of $\chi_s''(\mathbf{Q}, E)$; the dispersion of the spinwave model is evident. Panel (c) reproduces the solid line from panel (a) and then shows the effect of increasing q on the position and magnitude of $\chi_s''(\mathbf{Q}, E)$ as dashed lines. Panel (d) shows $\chi_s''(\mathbf{Q}, \Delta)$ as a function of q as a solid line, and shows the effect of further increasing E as dashed lines.

perpendicular to the ordered moment direction, and along the inter-Fe-*Ph* layer direction, respectively). Instead, the non-linear combinations:

$$v_{xy} = \sqrt{\frac{v_L^2 + v_T^2}{2}} \quad \text{and} \quad \eta_v = 2 \frac{v_L^2 - v_T^2}{v_L^2 + v_T^2} \quad (4.30)$$

can be chosen. With these definitions, the product $v_q^2 q^2$ becomes

$$v_q^2 q^2 = v_{xy}^2 (q_x^2 + q_y^2 + 2\eta_v q_x q_y) + v_z^2 q_z^2, \quad (4.31)$$

where

$$q_x = \mathbf{q} \cdot [1\ 0\ 0]_T, \quad q_y = \mathbf{q} \cdot [0\ 1\ 0]_T, \quad \text{and} \quad q_z = \mathbf{q} \cdot [0\ 0\ 1]_T \quad (4.32)$$

4.1.4 Diffusive model

Between a well-ordered antiferromagnet and a fully-disordered paramagnet, is a system which has antiferromagnetic correlations between electrons and no long range antiferromagnetic order. In such a system it may be possible to have localized regions of antiferromagnetic order with a characteristic correlation length, ξ , which are able to diffuse through the crystal lattice. This type of system is akin to a liquid with antiferromagnetic correlations and is characterized by diffusive spin excitations in a long-wavelength limit approximation, with magnetic susceptibility

$$\chi_d(\mathbf{Q}, E) = \chi_0 a^2 \xi^{-2} [a^2 \xi^{-2} (1 + \xi^2 q^2) - i\gamma E]^{-1}, \quad (4.33)$$

where $\chi_0 \equiv \chi_d(\mathbf{Q}_{\text{AFM}}, 0)$, ξ is the bare magnetic correlation length, and the imaginary term is a consequence of the decay of spin excitations (paramagnons) into particle-hole pairs with the corresponding Landau damping γ . As discussed previously, inelastic neutron scattering

is only sensitive to the imaginary component of the magnetic susceptibility, which can be shown to be

$$\chi_d''(\mathbf{Q}, E) = \frac{\chi_0 a^2 \xi^{-2} \gamma E}{a^4 \xi^{-4} (1 + \xi^2 q^2)^2 + \gamma^2 E^2}, \quad (4.34)$$

which has no dispersion and is characterized only by a correlation length and characteristic energy, $\Gamma \equiv a^2/\gamma\xi^2$. Figure 4.2 illustrates the isotropic diffusive model.

Following the same path employed in section 4.1.3 for the spin wave model, one can introduce an anisotropic correlation length into this model of diffusive spin excitations, giving

$$\chi_{\text{ad}}(\mathbf{Q}, E) = \chi_0 a^2 \xi^{-2} [a^2 \xi^{-2} (1 + \xi_q^2 q^2) - i\gamma E]^{-1}, \quad (4.35)$$

where, similar to the definition of v_q in equation (4.31), the following nonlinear combinations of the orthorhombic correlation length eigenvalues (ξ_L, ξ_T , and ξ_z) have been defined

$$\xi = \sqrt{\frac{\xi_L^2 + \xi_T^2}{2}}, \quad \eta_\xi = \frac{\xi_L^2 - \xi_T^2}{\xi_L^2 - \xi_T^2}, \quad \text{and} \quad \eta_{\xi_z} = \frac{2\xi_z^2}{\xi_L^2 + \xi_T^2} \quad (4.36)$$

such that the anisotropic correlation length is defined as

$$\xi_q^2 q^2 = \xi^2 (q_x^2 + q_y^2 + 2\eta_\xi q_x q_y + \eta_{\xi_z} q_z^2). \quad (4.37)$$

Thus giving the imaginary component

$$\chi_{\text{ad}}''(\mathbf{Q}, E) = \frac{\chi_0 a^2 \xi^{-2} \gamma E}{a^4 \xi^{-4} (1 + \xi_q^2 q^2)^2 + \gamma^2 E^2}. \quad (4.38)$$

Rearranging the parameters in equation (4.38) and utilizing the definition of the characteristic energy $\Gamma \equiv a^2/\gamma\xi^2$ gives

$$\chi_{\text{ad}}''(\mathbf{Q}, E) = \frac{\chi_0 \Gamma E}{\Gamma^2 (1 + \xi_q^2 q^2)^2 + E^2}, \quad (4.39)$$

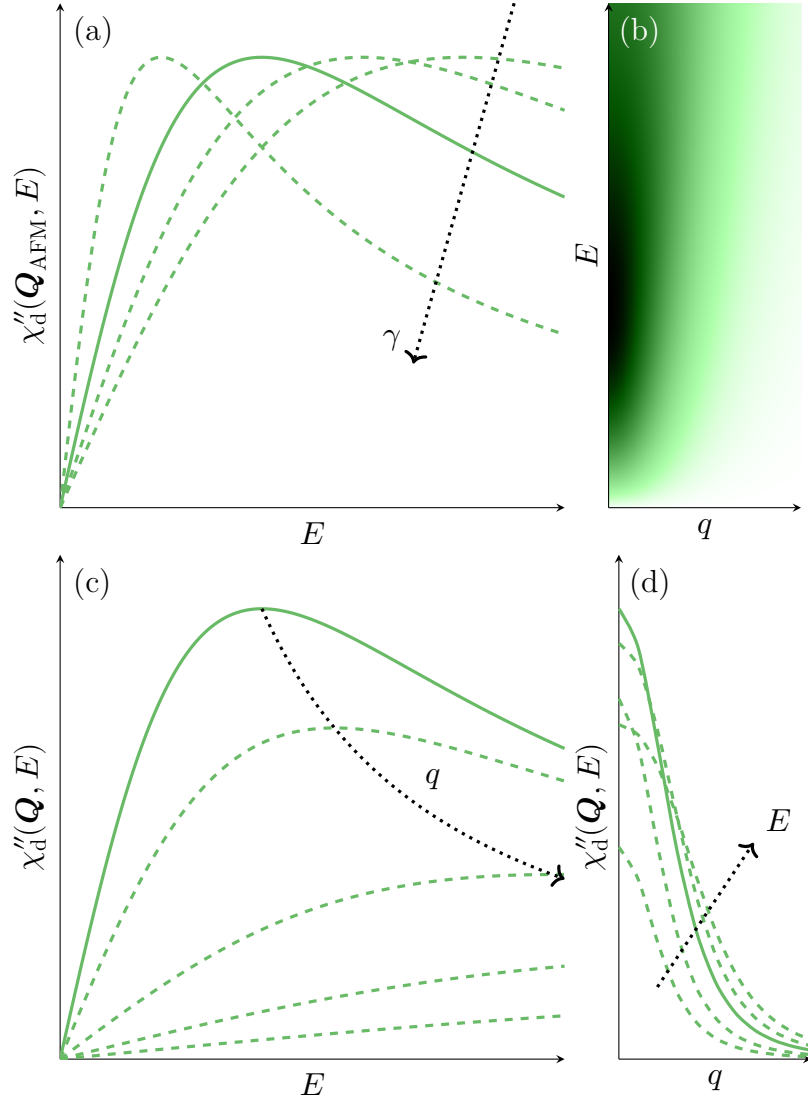


FIGURE 4.2. The diffusive model, equation (4.34), as a function of energy transfer, E , and reduced momentum transfer, q ; as shown by the dashed lines, increasing the Landau damping, γ , shifts the diffusive model response to lower energy transfers. Panel (a) shows $\chi_d''(\mathbf{Q}, E)$ at \mathbf{Q}_{AFM} as a function of E which is a maximum at the characteristic energy, Γ . Panel (b) shows an image plot of $\chi_d''(\mathbf{Q}, E)$ calculated for gridded points on the E - q plane, here white corresponds to zero and the darkest color is the maximum of $\chi_d''(\mathbf{Q}, E)$; the lack of any dispersion of the diffusive model is evident. Panel (c) reproduces the solid line from panel (a) and then shows the effect of increasing q on the position and magnitude of $\chi_d''(\mathbf{Q}, E)$ as dashed lines. Panel (d) shows $\chi_d''(\mathbf{Q}, \Gamma)$ as a function of q as a solid line, and shows the effect of changing E as dashed lines.

which takes the familiar form of a Lorentzian distribution multiplied by the energy transfer at \mathbf{Q}_{AFM} (where $\mathbf{q} = 0$).

As will be shown in chapter 5, the high-energy spin fluctuations in $\text{Ba}(\text{Fe}_{0.953}\text{Co}_{0.047})_2\text{As}_2$ are so anisotropic that they split in the direction perpendicular to the ordered moment. This extreme anisotropy can not be accounted for with only an anisotropic correlation length. An additional source of anisotropy is most-easily introduced by expanding the momentum-dependent Landau damping for small deviations from \mathbf{Q}_{AFM} and expressing the characteristic energy as

$$\Gamma_q = \frac{a^2}{\gamma_q \xi^2} = \frac{a^2}{\gamma \xi^2} [1 + \alpha^2 (q_x^2 + q_y^2 + 2\eta_{\Gamma} q_x q_y + \eta_{\Gamma z} q_z^2)], \quad (4.40)$$

where the anisotropy parameters η_{Γ} and $\eta_{\Gamma z}$ have been introduced. This gives the most-generally anisotropic form of the diffusive model

$$\chi''_{\text{gd}}(\mathbf{Q}, E) = \frac{\chi_0 \Gamma_q E}{\Gamma_q^2 (1 + \xi_q^2 q^2)^2 + E^2}. \quad (4.41)$$

The effect of this additional anisotropy is to cause the function to split along the three orthorhombic directions at higher energies. These energies can be determined by finding the energy at which the second derivative of the response function along a particular direction switches signs; i.e.,

$$\frac{\partial^2 \chi''_{\text{gd}}(\mathbf{Q}_{\text{AFM}}, E_{\text{L}})}{\partial [110]_{\text{T}}^2} = 0, \quad \frac{\partial^2 \chi''_{\text{gd}}(\mathbf{Q}_{\text{AFM}}, E_{\text{T}})}{\partial [\bar{1}10]_{\text{T}}^2} = 0, \quad \frac{\partial^2 \chi''_{\text{gd}}(\mathbf{Q}_{\text{AFM}}, E_z)}{\partial [001]_{\text{T}}^2} = 0 \quad (4.42)$$

this yields the values

$$E_{\text{L}} = \Gamma \sqrt{1 + 2 \frac{\xi^2}{\alpha^2} \frac{1 + \eta_{\xi}}{1 + \eta_{\Gamma}}}, \quad E_{\text{T}} = \Gamma \sqrt{1 + 2 \frac{\xi^2}{\alpha^2} \frac{1 - \eta_{\xi}}{1 - \eta_{\Gamma}}}, \quad E_z = \Gamma \sqrt{1 + 2 \frac{\xi^2}{\alpha^2} \frac{\eta_{\xi z}}{\eta_{\Gamma z}}} \quad (4.43)$$

which are typically on the order of hundreds of meV. An example of this anisotropy-induced dispersion is illustrated in figure 4.3.

4.1.5 Ballistic model

An alternative approach for modeling the observed high-energy transverse splitting in $\text{Ba}(\text{Fe}_{0.953}\text{Co}_{0.047})_2\text{As}_2$ is to replace the constant spin gap in equation (4.29) with an anisotropic spin gap

$$\Delta_q^2 = \frac{v_q^2}{\xi_q^2} \quad (4.44)$$

the resultant response function takes the form of propagating overdamped spinwaves in a disordered paramagnetic state, with

$$\chi_b''(\mathbf{Q}, E) = \frac{\chi_0 \frac{v_q^2}{\xi_q^2} \alpha E}{\left(\frac{v_q^2}{\xi_q^2} + v_q^2 q^2 - E^2 \right)^2 + \alpha^2 E^2}. \quad (4.45)$$

which can be also be written as

$$\chi_b''(\mathbf{Q}, E) = \frac{\chi_0 \Gamma_q E}{\Gamma_q^2 \left(1 + \xi_q^2 q^2 - \frac{\xi_q^2}{v_q^2} E^2 \right)^2 + E^2}. \quad (4.46)$$

where $\Gamma \equiv v_q^2/\alpha\xi_q^2$. By inspection, it is clear that for $E \ll v_q/\xi_q$ equation (4.46) is functionally identical to equation (4.39). Similarly, there are limits under which equations (4.29), (4.39) and (4.46) are functionally the same.

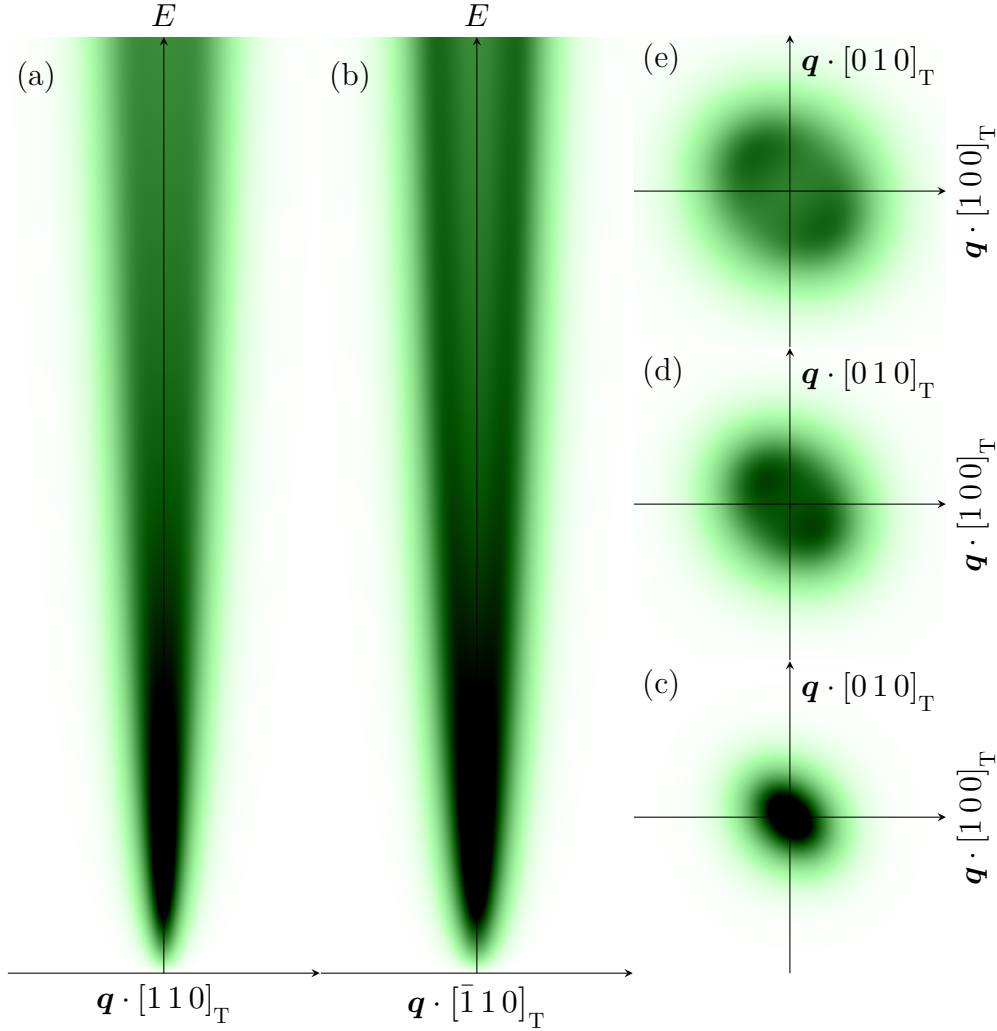


FIGURE 4.3. The diffusive model with anisotropic correlation length and Landau damping, equation (4.41), illustrated as a function of energy transfer, E , and reduced momentum transfer, \mathbf{q} . For a set of anisotropy parameters, panel (a) shows the longitudinal \mathbf{q} dependence versus E ; panel (b) shows the transverse \mathbf{q} versus E dependence; and panels (c), (d), and (e) show the in-plane \mathbf{q} dependence at $\frac{1}{6}$, $\frac{1}{2}$, and $\frac{5}{6}$ the maximum energy transfer shown in panels (a) and (b), respectively. At high energies, this anisotropic diffusive model can, as shown here, split in \mathbf{q} giving the appearance of a dispersion relationship.

4.2 Modeling Superconducting State Spin Excitations

4.2.1 Rescaled resonance model

It has been argued by Chubukov et al. that the superconducting state magnetic susceptibility should be of the form

$$\chi_{\text{sc}}(\mathbf{Q}, E) = \chi_0 a^2 \xi^{-2} [a^2 \xi^{-2} (1 + \xi_q^2 q^2) - \Pi_{\text{sc}}(\mathbf{Q}, E)]^{-1} \quad (4.47)$$

where $\Pi_{\text{sc}}(\mathbf{Q}, E)$ is the bosonic self energy [86]. As seen for the normal state, equation (4.35), the leading term for the bosonic self energy is typically due to the decay of spin fluctuations into electron-hole pairs and is purely imaginary. In the superconducting state, such Landau damping is gapped out for low energies and, instead, the leading term in the bosonic self energy is quadratic in energy, and real

$$\Pi_{\text{sc}}(\mathbf{Q}, E) \approx \frac{\gamma_q E^2}{\Delta_q} \quad (4.48)$$

where Δ_q is determined by the fermion gap at two points on the Fermi surface connected by $\mathbf{Q}_{\text{AFM}} + \mathbf{q}$, $2\Delta_q = |\Delta_{\mathbf{k}}| + |\Delta_{\mathbf{k}+\mathbf{Q}_{\text{AFM}}+\mathbf{q}}|$ [86]. As a result, the magnetic susceptibility as described by Chubukov et al. is purely real and can not describe inelastic neutron scattering data. However, as noted by Kim et al., equation (4.47) diverges when the term inside of the square brackets is zero; which defines the resonance energy dispersion observed via inelastic neutron scattering [87]. This leads to an expression for the dispersion relationship which has been successfully used to fit the $\text{Ba}(\text{Fe}_{1-x}\text{Ni}_x)_2\text{As}_2$ resonance dispersion,

$$\Omega_q = \sqrt{\Delta_q \Gamma_q (1 + \xi_q^2 q^2)}, \quad (4.49)$$

utilizing the definition of Γ_q given in equation (4.40).

Knowledge of the dispersion relationship alone is not sufficient to determine all properties of the superconducting resonance, e.g., its spectral weight. What is required is a model of the response function which is defined for all \mathbf{Q} and E , and that has the dispersion relation given by equation (4.49). One way to introduce such a dispersion relationship into a model related to the diffusive model of the normal-state response is

$$\begin{aligned} \chi_r(\mathbf{Q}, E) = & \frac{A}{E - \Omega_q} \left\{ 1 + \xi_q^2 q^2 - i \frac{E - \Omega_q}{\rho_q} \right\}^{-1} \\ & + \frac{A}{E + \Omega_q} \left\{ 1 + \xi_q^2 q^2 + i \frac{E + \Omega_q}{\rho_q} \right\}^{-1} \end{aligned} \quad (4.50)$$

where the sum of the two complex terms is due to the implicit \pm in equation (4.49), and in each case the energy term in equation (4.35) has been recentered to $\pm\Omega_q$ and rescaled by ρ_q , which is itself potentially anisotropic. This complex susceptibility can be shown to be

$$\begin{aligned} \chi_r(\mathbf{Q}, E) = & \left\{ \frac{\rho_q (1 + \xi_q^2 q^2) \left[\rho_q^2 (1 + \xi_q^2 q^2)^2 + E^2 + 3\Omega_q^2 \right]}{E^2 - \Omega_q^2} + i2\Omega_q \right\} \\ & \times \frac{2A\rho_q E}{\rho_q^4 (1 + \xi_q^2 q^2)^4 + 2\rho_q^2 (1 + \xi_q^2 q^2)^2 (E^2 + \Omega_q^2) + (E^2 - \Omega_q^2)^2}. \end{aligned} \quad (4.51)$$

Clearly, the real part of equation (4.51) diverges at $E = \pm\Omega_q$, just like equation (4.47), and is an odd function of E , unlike equation (4.47). The first property is desirable for our model spin resonance; the second property is not, but does not adversely affect the imaginary component of the model magnetic susceptibility, which is well behaved for all E and \mathbf{Q} , and an odd function of E — and therefore it preserves causality and energy conservation. The imaginary part of equation (4.51) is

$$\chi_r''(\mathbf{Q}, E) = \frac{4A\rho_q \Omega_q E}{\rho_q^4 (1 + \xi_q^2 q^2)^4 + 2\rho_q^2 (1 + \xi_q^2 q^2)^2 (E^2 + \Omega_q^2) + (E^2 - \Omega_q^2)^2}. \quad (4.52)$$

If the scaling parameter is a constant ($\rho_q \equiv \rho$) and the correlation length in the superconducting state is the same as in the normal state, then this model could be fit with as little as three free parameters.

The superconducting state response can then be modeled as a gapped normal state excitation plus this resonant mode given by equation (4.52)

$$\chi''_{\text{SC}}(\mathbf{Q}, E) = \chi''_{\text{r}}(\mathbf{Q}, E) + \begin{cases} 0 & |E| < \Delta_q \\ \chi''_{\text{NS}}(\mathbf{Q}, E) & |E| \geq \Delta_q \end{cases} \quad (4.53)$$

4.2.2 Empirical resonance model

As will be demonstrated, the diffusive model best reproduces the normal state spin fluctuations for compositions which also exhibit superconductivity. It may be possible then to employ a modified diffusive model to fit the superconducting data. The modifications employed to produce this empirical superconducting state model are built up from a number of step-approximating hyperbolic tangent functions to create (\mathbf{Q}, E) -dependent parameters and to add a low-energy superconducting gap. The imaginary part of this complex model is given by

$$\chi''_{\text{SC}}(\mathbf{Q}, E) = \frac{\chi_0 \xi_{\text{NS}}^2 \Gamma_{\text{NS}} E}{\Gamma^2(\mathbf{Q}, E) [1 + \xi^2(\mathbf{Q}, E) q^2]^2 + E^2} \Delta_{\text{gap}}(\mathbf{Q}, E) \quad (4.54)$$

where the superconducting gap is given by

$$\Delta_{\text{gap}}(\mathbf{Q}, E) = \frac{1}{2} \left(\tanh \frac{E - \zeta(\mathbf{Q})}{\kappa(\mathbf{Q})} + 2 - \tanh \frac{E + \zeta(\mathbf{Q})}{\kappa(\mathbf{Q})} \right) \quad (4.55)$$

with a mid-step energy given by $\zeta(\mathbf{Q})$ and step-width given by $\kappa(\mathbf{Q})$, the momentum and energy dependent characteristic energy is given by

$$\Gamma(\mathbf{Q}, E) = \Gamma_{\text{SC}} [\sigma(\mathbf{Q}, E) + \sigma(\mathbf{Q}, -E) - 1] + \Gamma_{\text{NS}} [2 - \sigma(\mathbf{Q}, E) - \sigma(\mathbf{Q}, -E)] \quad (4.56)$$

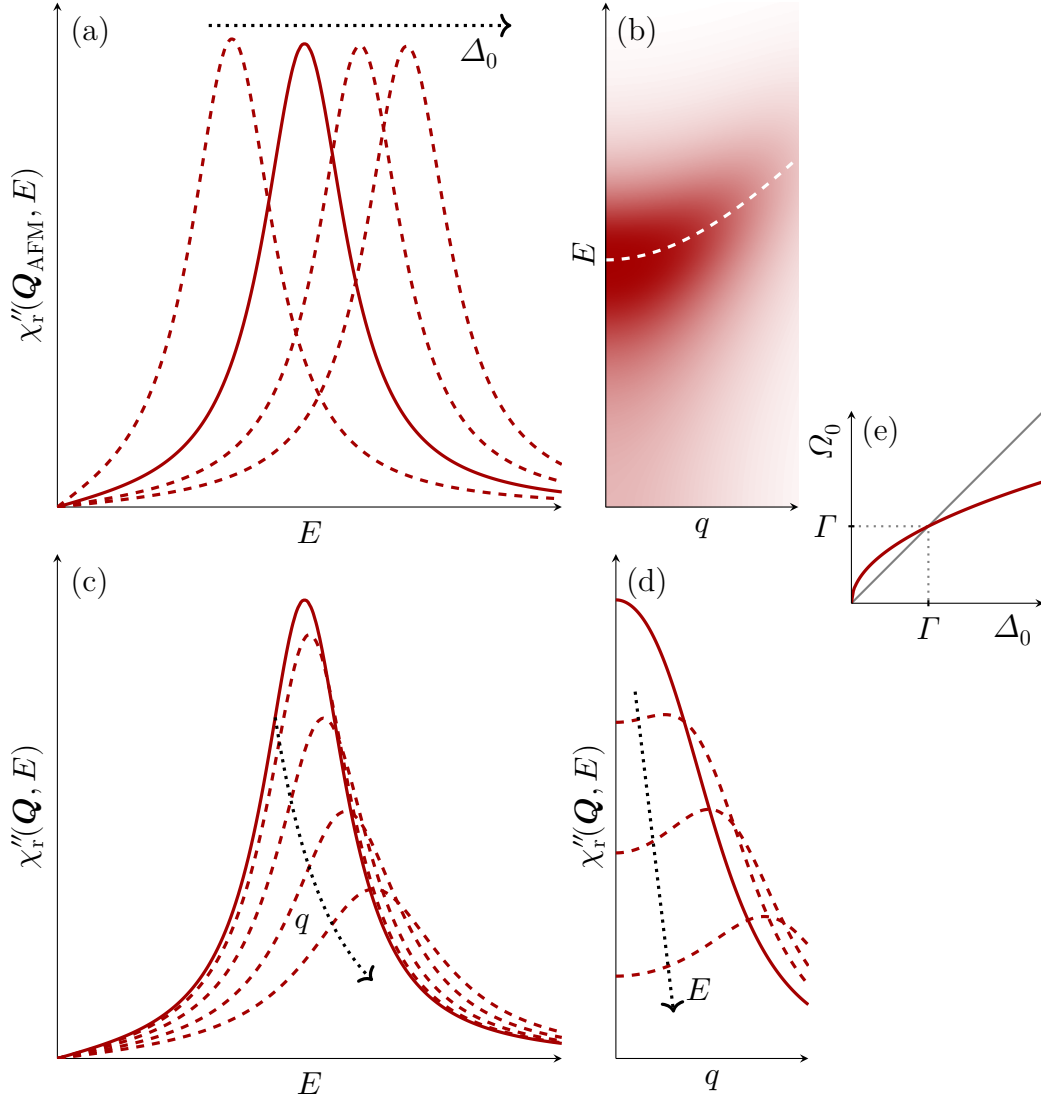


FIGURE 4.4. The resonance model, equation (4.52), as a function of energy transfer, E , and reduced momentum transfer, q . Panel (a) shows $\chi_r''(\mathbf{Q}, E)$ at \mathbf{Q}_{AFM} as a function of E which is a maximum at $\Omega_0 = \sqrt{\Delta_0 \Gamma}$. Panel (b) shows an image plot of $\chi_r''(\mathbf{Q}, E)$ calculated for gridded points on the E - q plane, here white corresponds to zero and the darkest color is the maximum of $\chi_r''(\mathbf{Q}, E)$. Panel (c) reproduces the solid line from panel (a) and then shows the effect of increasing q on the position and magnitude of $\chi_r''(\mathbf{Q}, E)$ as dashed lines. Panel (d) shows $\chi_r''(\mathbf{Q}, \Omega_0)$ as a function of q as a solid line, and shows the effect of changing E as dashed lines. Panel (e) shows the relationship between Δ_0 and Ω_0 for fixed Γ ; as long as $\Gamma < \Delta_0$ (which is typically the case) $\Omega_0 < \Delta_0$ as well.

the momentum and energy dependent correlation length by

$$\begin{aligned}\xi^2(\mathbf{Q}, E)q^2 &= \xi_{\text{SC}}^2(\mathbf{Q})q^2 [\sigma(\mathbf{Q}, E) + \sigma(\mathbf{Q}, -E) - 1] \\ &\quad - \xi_{\text{NS}}^2(\mathbf{Q})q^2 [\sigma(\mathbf{Q}, E) + \sigma(\mathbf{Q}, -E) - 2]\end{aligned}\quad (4.57)$$

where the rescaled hyperbolic tangent function which accomplishes the various steps is given by

$$\sigma(\mathbf{Q}, E) = \frac{1}{2} \left(1 + \tanh \frac{\frac{1}{2}[v(\mathbf{Q}) + \zeta(\mathbf{Q})] - E}{\frac{1}{6}[v(\mathbf{Q}) - \zeta(\mathbf{Q})]} \right) \quad (4.58)$$

and the three step-function momentum dependent characteristic energies, $\zeta(\mathbf{Q})$, $\kappa(\mathbf{Q})$, and $v(\mathbf{Q})$ are all defined in a similar fashion as

$$z(\mathbf{Q}) = z_1 + \frac{1}{2}(z_2 - z_1)(1 + \cos \pi L) \quad (4.59)$$

where $z = \zeta, \kappa, v$ and the $z_l = z(\mathbf{Q} = (\frac{1}{2} \frac{1}{2} l)_T)$. The subscripts NS and SC indicate normal state and superconducting state parameters, respectively. The normal state parameters are those determined from the diffusive model, equation (4.39), fit to the normal state data. Both $\Gamma(\mathbf{Q}, E)$, and $\xi^2(\mathbf{Q}, E)q^2$ utilize the same set of step functions to switch between free superconducting parameters at small energy transfers and fixed normal state parameters at large energy transfers, in order to remain consistent with the observation that the spectra are indistinguishable in the two states for large energy transfers. Figure 4.5 illustrates the energy dependence of this double step function. The form of the step function, equation (4.58), has been chosen such that $\Gamma(\mathbf{Q}, E)$, and $\xi^2(\mathbf{Q}, E)q^2$, collectively $p(\mathbf{Q}, E)$, are greater than 99.75% of their superconducting state value, $p_{\text{SC}}(\mathbf{Q})$, at $E = \zeta(\mathbf{Q})$ and greater than 99.75% of their normal state value, $p_{\text{NS}}(\mathbf{Q})$, at $E = v(\mathbf{Q})$ – therefore $\zeta(\mathbf{Q})$ and $v(\mathbf{Q})$ effectively defined the start and end of the step with increasing $|E|$. It is important to note that $\Delta_{\text{gap}}(\mathbf{Q}, E)$, $\Gamma(\mathbf{Q}, E)$, and $\xi^2(\mathbf{Q}, E)q^2$ are all even functions of energy which ensures that

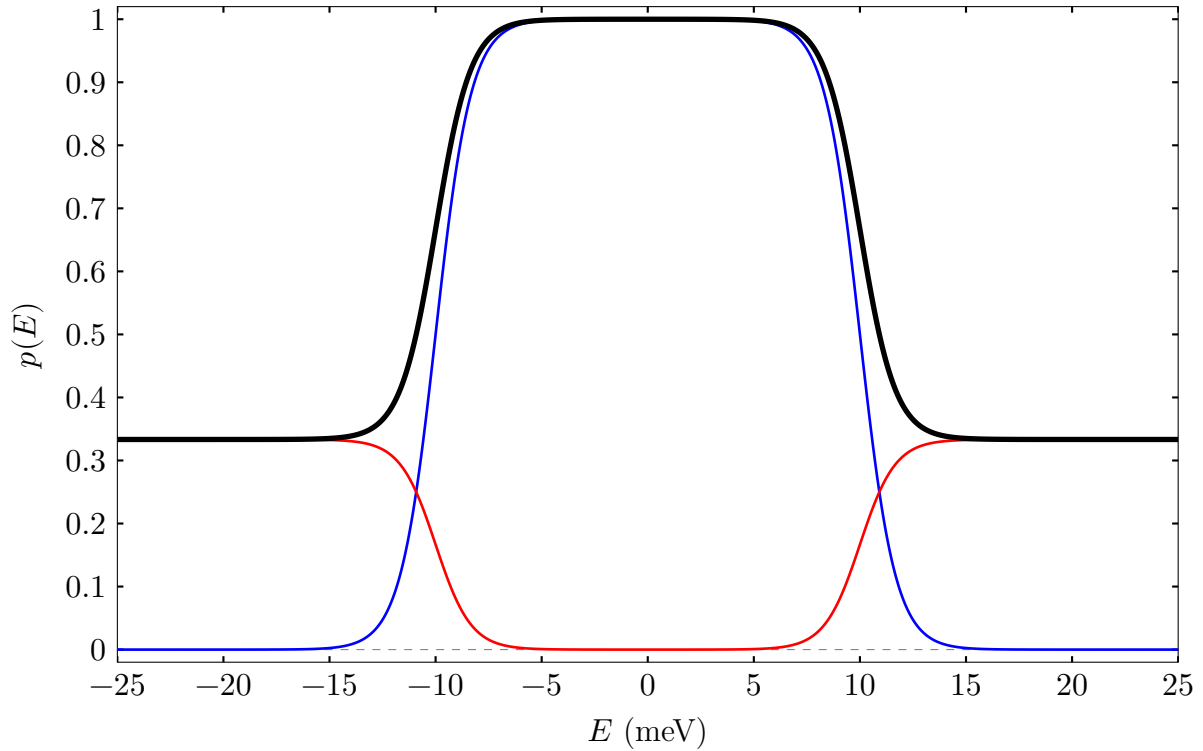


FIGURE 4.5. An illustration of the superconducting model double step function for an arbitrary parameter $p(E)$. The displayed lines are the superconducting parameter contribution, $p_{\text{SC}} [\sigma(E) + \sigma(-E) - 1]$ (—), the normal state parameter contribution, $p_{\text{NS}} [2 - \sigma(E) + \sigma(-E)]$ (—), and their sum, $p(E)$ (—). This arbitrary parameter has no momentum dependence, $p_{\text{SC}} = 1$, $p_{\text{NS}} = 1/3$, and the step functions are characterized by $\zeta = 5$ meV and $v = 15$ meV.

$\chi''_{\text{SC}}(\mathbf{Q}, E)$ remains an odd function in E and that energy conservation and causality are preserved.

4.3 Neutron Scattering Data Analysis

4.3.1 Analysis of time-of-flight neutron scattering data

Each scattered neutron collected at some modern time-of-flight spectrometers is recorded as an individual event, where the flight time, detector position, and any number of relevant environment variables are stored for each detected neutron. It is impossible to visualize the

data without first converting its format from a list of flight times and pixel positions to a spectrum for each detector pixel, this necessitates transforming the data into energy bins such that each spectrum is a histogram of the number of detected neutrons per unit energy transfer. This process is often referred to as data reduction and can be accomplished with the MANTID software package.^[88]

The observed inelastic neutron scattering intensity $I(\mathbf{Q}, E)$ includes contributions from various non-sample sources – primarily the sample holder and environment. If only magnetic scattering is to be studied, one might also consider non-magnetic scattering from the sample itself as a source of background. The collective intensity from these sources comprise the background function $B(\mathbf{Q}, E)$. The background function is generally estimated by averaging intensity from equal Q and E sections of the detector which are far from the magnetic intensity of interest.

$$B(Q_i, E_i) = \frac{\sum_j B(Q_j, E_j) \delta(Q_i - Q_j) \delta(E_i - E_j)}{\sum_j \delta(Q_i - Q_j) \delta(E_i - E_j)} \quad (4.60)$$

where the sum goes over all detectors far from magnetic intensity and the $Q_{i,j}, E_{i,j}$ correspond to bin centers. This simplest approximation to $B(\mathbf{Q}, E)$ can only properly account for contributions to the background which are isotropic about the incident beam direction and is, more accurately, $B(Q, E)$ — it may be possible to account for non-isotropic contributions to the background via a more involved estimation procedure, however such added complexity has thus far been unnecessary. An estimate of the sample-scattered intensity can be obtained by subtracting the averaged background estimate from the observed intensity.

$$S(\mathbf{Q}, E) = I(\mathbf{Q}, E) - B(Q, E) \quad (4.61)$$

Further details of this method of background estimation and subtraction are given in appendix [E](#).

4.3.2 Analysis of triple-axis neutron scattering data

Due to the inherently low flux and weak interactions involved in neutron scattering experiments the angular acceptances of triple-axis instrument components are often quite large, and are typically defined by the presence of Soller collimators. These angular uncertainties ultimately contribute to uncertainties in measured neutron momenta and energies, which increase the width of features in scans through momentum-energy-space.

If the dynamic structure factor of a sample is well described by a model, $S(\mathbf{Q}, E)$, and the instrumental uncertainties, $(\delta\mathbf{Q}, \delta E)$, are known precisely for all (\mathbf{Q}, E) , then it is possible to determine what scattering signal would be measured by that instrument by convoluting the instrumental uncertainties with $S(\mathbf{Q}, E)$. In practice the instrumental uncertainties in (\mathbf{Q}, E) are not known precisely for all (\mathbf{Q}, E) and are instead estimated from angular uncertainties. One popular approach, pioneered by Cooper and Nathans [89], assumes that the only sources for all uncertainties in (\mathbf{Q}, E) are Gaussian distributions of angular divergence defined by the maximum angular divergences allowed by Soller collimators and the mosaic of the monochromator and analyzer crystals. On modern instruments, with large monochromators and analyzers, this approximation can break down because, if the angle subtended by a sample as viewed from the monochromator or analyzer is smaller than the associated Soller collimator, the effective angular uncertainty will be significantly smaller than that defined by the collimator and the Cooper-Nathans approach will over-estimate resolution widths.

An extension to the Cooper-Nathans approach, proposed by Popovici [90], alleviates these issues by introducing size and shape (including curvature) effects into the angular uncertainty calculations.

Further details about the triple-axis resolution function and utilizing its approximation to convolute and fit model intensity to measured data are given in appendix C.

Equations for theoretical cross-sections are, as shown in section 3.1, given as a probability – however, neutron scattering experiments are often measured relative to a beam monitor and the absolute incident neutron flux on a sample is typically not known precisely. This experimental necessity makes the comparison of measured intensity to theoretical cross-sections require an arbitrary scaling factor, which is often not ideal. Methods exist for removing the arbitrary scale from measured intensity, such as normalizing to incoherent scattering from a vanadium standard sample or normalizing to a sample phonon of known intensity. Both of these methods and details of their implementation are given in appendix D.

It has been fruitful in the course of this work to define a common set of computer programs for the analysis of triple-axis neutron scattering data. The created collection of useful programs, a MATLAB class called `scandata.m` is fully described, including its typical use, in appendix B.

CHAPTER 5 RESULTS

5.1 Experiment Details and Data

Inelastic neutron scattering experiments were performed in order to better understand the evolution of spin fluctuations in $\text{Ba}(\text{Fe}_{1-x}\text{Co}_x)_2\text{As}_2$ from well-defined spin waves in the parent compound to diffusive spin excitations in the over-doped compounds and to determine if the change in character is due to disorder arising from the increased cobalt concentration or the loss of antiferromagnetic order. Inelastic neutron scattering measurements were performed on the HB3 triple-axis spectrometer at the High Flux Isotope Reactor at Oak Ridge National Laboratory on five $\text{Ba}(\text{Fe}_{1-x}\text{Co}_x)_2\text{As}_2$ samples spanning the Co concentration range from lightly- to nearly-optimally-doped. Furthermore, inelastic neutron scattering measurements were performed on one of these samples, an intermediate under-doped compound, on the ARCS [82] time-of-flight spectrometer at the Spallation Neutron Source at Oak Ridge National Laboratory. The results of these experiments have previously been reported separately in reference [91] and reference [92]. As detailed in table A.1, the samples each consist of co-aligned single-crystals grown from excess FeAs and CoAs, as outlined in reference [60], each with a total mass of ~ 2 grams and each mounted with a horizontal $[H H L]_{\text{T}}$ scattering plane.

5.1.1 ARCS time-of-flight spectrometer

5.1.1.1 $E_i = 250$ meV

The ARCS experiment was performed on $\text{Ba}(\text{Fe}_{0.953}\text{Co}_{0.047})_2\text{As}_2$; which similarly to other lightly- and under-doped $\text{Ba}(\text{Fe}_{1-x}\text{Co}_x)_2\text{As}_2$ compounds, and as discussed in section 2.3,

undergoes a tetragonal to orthorhombic structural transition at $T_S = 60$ K, orders antiferromagnetically at $T_N = 47$ K and magnetic long-range order coexists with superconductivity below $T_c = 17$ K. For the experiment at ARCS, the sample was aligned with the c -axis along the incident beam direction and measurements were performed with an incident neutron energy of $E_i = 250$ meV. The inelastic scattering spectra were measured at $T = 5$ K (i.e., in the orthorhombic, antiferromagnetic, and superconducting state) and $T = 70$ K (i.e., in the paramagnetic, tetragonal state). As described briefly in section 2.3, the orthorhombic distortion is too small to be resolved via most neutron scattering methods, including these measurements – as such, the ARCS neutron scattering data are described in the tetragonal $I4/mmm$ coordinate system with a rotated definition of H and K to better allow for indexing of the measured intensity $\mathbf{Q} = \frac{2\pi}{a}(H+K)\hat{i} + \frac{2\pi}{a}(H-K)\hat{j} + \frac{2\pi}{c}L\hat{k} = (H+K \ H-K \ L)_T$ where $a = 3.95$ Å and $c = 12.95$ Å are the tetragonal lattice constants. In tetragonal $I4/mmm$ notation, $\mathbf{Q}_{\text{AFM}} = (\frac{1}{2} \ \frac{1}{2} \ 1)$ [$H=\frac{1}{2}, K=0$]. With this definition of H and K it is convenient to describe diagonal cuts in the $I4/mmm$ basal plane; since varying H corresponds to a scan in the $[110]_T$ direction and varying K corresponds to a scan in the $[1\bar{1}0]_T$ direction which are the longitudinal and transverse directions, respectively, at $\mathbf{Q}_{\text{AFM}} = (\frac{1}{2} \ \frac{1}{2} \ 1)$.

ARCS, like other modern time-of-flight spectrometers, collects neutron data as individual events. The ARCS event data for each detector pixel were reduced to histograms with the DANSE software package [93] and subsequently analyzed in part by MSLICE [94].

The background subtracted ARCS spectra for detectors within the range $0.25 < H < 0.75$ r.l.u., $-0.5 < K < 0.45$ r.l.u. and $20 < E < 150$ meV were collectively fit with the Levenberg-Marquardt algorithm to model functions, described further in sections 5.2.1 and 5.3.1. In addition to a model function, a background was fit to account for an observed residual component of $B(\mathbf{Q}, E)$ caused by a detector bank top-to-bottom asymmetry of the measured intensity. The fit residual background function was

$$B_r(\mathbf{Q}, E) = -a_0 e^{-E/a_1} K \quad (5.1)$$

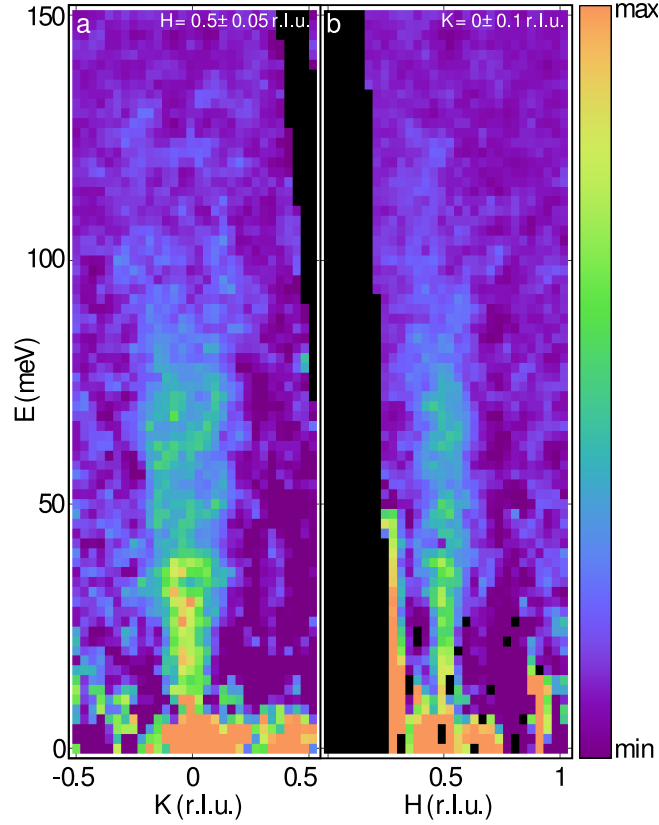


FIGURE 5.1. Inelastic neutron scattering data measured on $\text{Ba}(\text{Fe}_{0.953}\text{Co}_{0.047})_2\text{As}_2$ at $T = 5$ K using ARCS with $E_i = 250$ meV and the crystal aligned with the incident neutron beam along the $[001]_{\text{T}}$ direction. (a) Transverse slice of the data along the $[1\bar{1}0]_{\text{T}}$ direction through $\mathbf{Q}_{\text{AFM}} = (\frac{1}{2}, \frac{1}{2}, L)$ after averaging over $H = 0.5 \pm 0.05$ r.l.u. (b) Longitudinal slice of the data along the $[110]_{\text{T}}$ direction through $\mathbf{Q}_{\text{AFM}} = (\frac{1}{2}, \frac{1}{2}, L)$ after averaging over $K = 0 \pm 0.1$ r.l.u. In each panel, the color scale represents the intensity of scattered neutrons. This figure has been reproduce from reference [91].

where the a_i are positive model parameters and K (in r.l.u.) is a measure of the vertical displacement from the horizontal detector plane. Volumetric H, K, E data was fit in order to avoid artifacts introduced by binning which are inherent in 1-D cuts and 2-D slices.

Time-of-flight measurements from ARCS of the spin excitations at $T = 5$ K are shown in figure 5.1. The magnetic excitations are observed to emanate from \mathbf{Q}_{AFM} and are steeply dispersive, extending to energies approaching 150 meV. In contrast to CaFe_2As_2 [95] and BaFe_2As_2 [96] where long-lived collective modes are seen above ~ 50 meV and provide

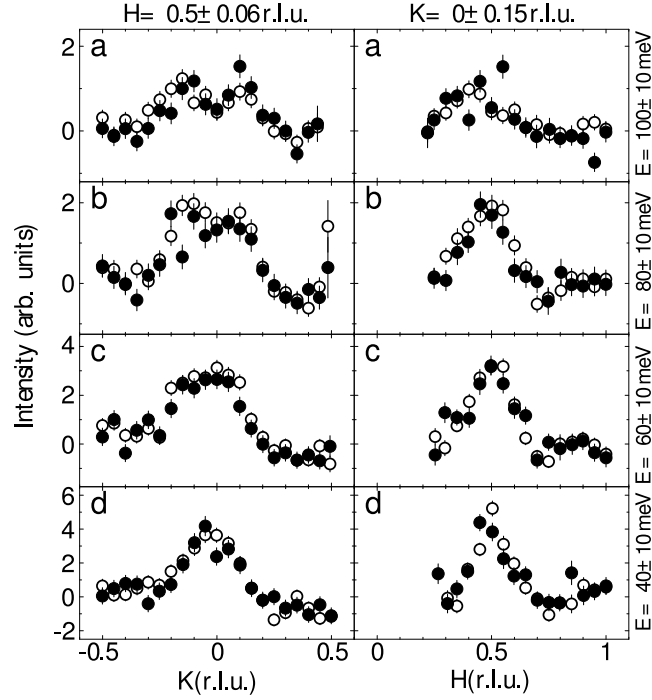


FIGURE 5.2. Comparison of inelastic neutron scattering data measured on $\text{Ba}(\text{Fe}_{0.953}\text{Co}_{0.047})_2\text{As}_2$ at $T = 5$ K (empty circles) and $T = 70$ K (filled circles). Transverse cuts of the data at (a') 100 ± 10 meV, (b') 80 ± 10 meV, (c') 60 ± 10 meV, (d') 40 ± 10 meV. Longitudinal cuts of the data at (a'') 100 ± 10 meV, (b'') 80 ± 10 meV, (c'') 60 ± 10 meV, (d'') 40 ± 10 meV. This figure has been reproduced from reference [91].

clear evidence of a conical spin wave dispersion (see, e.g., figure 2.23), the excitations here appear less well-defined and more diffusive. In addition a well-defined spin gap is also observed in CaFe_2As_2 and BaFe_2As_2 , which these ARCS measurements are insensitive to due to a large unaccounted for background near zero energy-transfer as a result of incoherent scattering from the aluminum sample holder. In this respect, the spin fluctuation spectrum for $\text{Ba}(\text{Fe}_{0.953}\text{Co}_{0.047})_2\text{As}_2$ is more like that measured in the optimally-doped and paramagnetic compositions of $\text{Ba}(\text{Fe}_{1-x}\text{Co}_x)_2\text{As}_2$, where the spin fluctuations are short-ranged and diffusive in character [70, 97].

Measurements in the paramagnetic state at $T = 70$ K above T_N and T_S , shown in figure 5.2, display a magnetic spectrum nearly identical to the one at $T = 5$ K. In addition, a comparison

of the transverse and longitudinal cuts shown in figure 5.2 panels (a')-(d') and (a'')-(d'') confirm a substantial anisotropy of the in-plane correlation lengths and a transverse splitting of the high energy spin fluctuations both above and below T_N . Similar features were reported previously for the $x = 0.074$ composition [97]. The similarity of the spin fluctuations at the two temperatures allows us to average the data taken at $T = 5$ K and 70 K in order to improve the counting statistics for subsequent analysis described below. Figure 5.3(a) and (b) show the temperature-averaged spectrum sliced in the transverse and longitudinal directions, respectively, while panels (c)-(h) show constant energy slices of the data in the (H, K) plane. In particular, the slices at 80 meV [Figure 5.3(e)] and 100 meV [Figure 5.3(f)] clearly display the transverse splitting of the spin excitations.

5.1.1.2 $E_i = 50$ meV

In addition to the high incident energy time of flight data shown previously, data was also collected at ARCS with an incident energy of $E_i = 50$ meV. Data was collected in the antiferromagnetic state at $T = 25$ K as well as in the combined antiferromagnetic and superconducting state at $T = 5$ K. Representative slices through the background subtracted datasets are shown in figure 5.4.

By taking the difference between identical slices through the two datasets, it's possible to see the effect of superconductivity on this medium incident energy data. Figure 5.5 shows the superconducting state data minus the normal state data for the same slices as displayed in figure 5.4, except that the sliced difference data has been convoluted with a Gaussian kernel in an attempt to smooth-out noise. The superconducting resonance is visible in these difference image plots, however it is not immediately evident. Integrating over a somewhat larger (Q, E) volume for each pixel and reducing the displayed data to one dimension produces a cut through the four dimensional datasets. Comparing cuts made at Q_{AFM} for the $T = 5$ and 25 K data, as in figure 5.6, is a clearer method of seeing the superconducting resonance which

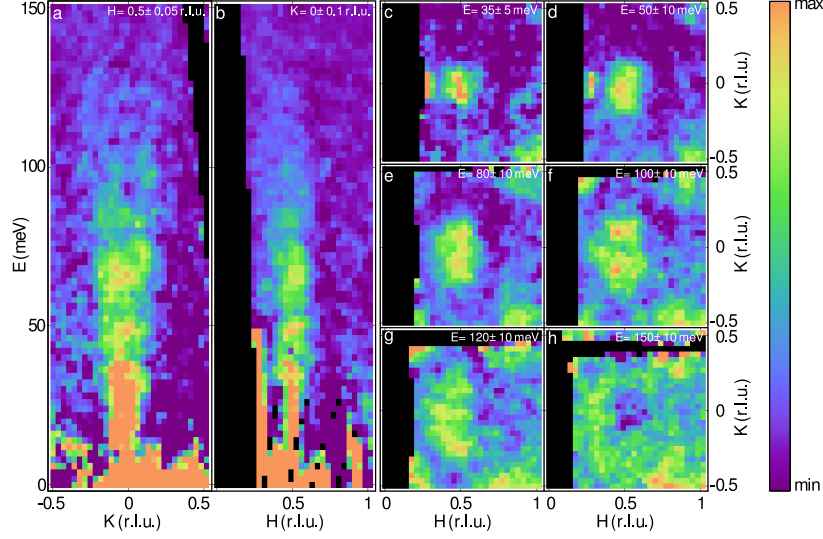


FIGURE 5.3. Inelastic neutron scattering data measured on $\text{Ba}(\text{Fe}_{0.953}\text{Co}_{0.047})_2\text{As}_2$ using ARCS with $E_i = 250$ meV and the crystal aligned with the incident neutron beam along the $[001]_{\text{T}}$ direction. Data at $T = 5$ K and 70 K are summed together to improve statistics. (a) Transverse slice of the data along the $[1\bar{1}0]_{\text{T}}$ direction through $\mathbf{Q}_{\text{AFM}} = (\frac{1}{2}, \frac{1}{2}, L)$ after averaging over $H = 0.5 \pm 0.05$ r.l.u. (b) Longitudinal slice of the data along the $[110]_{\text{T}}$ direction through $\mathbf{Q}_{\text{AFM}} = (\frac{1}{2}, \frac{1}{2}, L)$ after averaging over $K = 0 \pm 0.1$ r.l.u. Constant energy slices in the (H, K) -plane averaged over an energy range of (c) 35 ± 5 meV, (d) 50 ± 10 meV, (e) 80 ± 10 meV, (f) 100 ± 10 meV, (g) 120 ± 10 meV, and (h) 150 ± 10 meV. In each panel, the color scale represents the intensity of scattered neutrons, where the maximum intensity in each panel, in arbitrary units, is (a) 10, (b) 10, (c) 10, (d) 8, (e) 5, (f) 3, (g) 2, (h) 1; and the minimum intensity in all panels is -1 arbitrary units. This figure has been reproduced from reference [91].

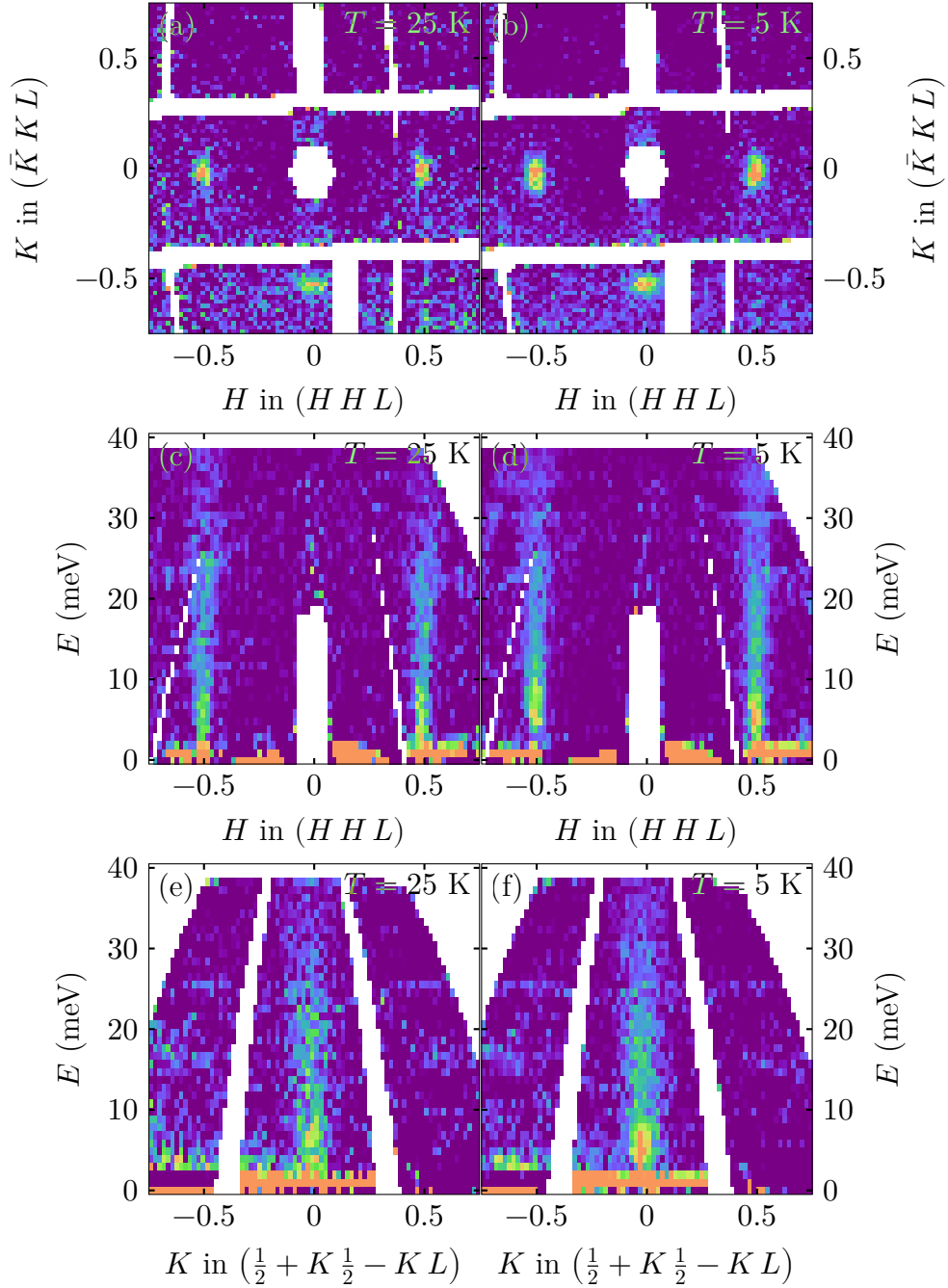


FIGURE 5.4. Background subtracted $\text{Ba}(\text{Fe}_{0.953}\text{Co}_{0.047})_2\text{As}_2$ time-of-flight data measured on ARCS with $E_i = 50$ meV. Panels (a) and (b) show constant-energy slices with an integration range $4 < E < 10$ meV such that $L \approx 1$ for $T = 25$ and 5 K, respectively. Panels (c) and (d) show $[H H 0]$ versus energy slices with an integration range $-0.1 < (\bar{K} K 0) < 0.1$ for $T = 25$ and 5 K, respectively. Panels (e) and (f) show $[\bar{K} K 0]$ versus energy slices with an integration range $0.45 < (H H 0) < 0.55$ for $T = 25$ and 5 K, respectively. White regions in each panel indicate a lack of data due to gaps between detector tubes or kinematic limitations.

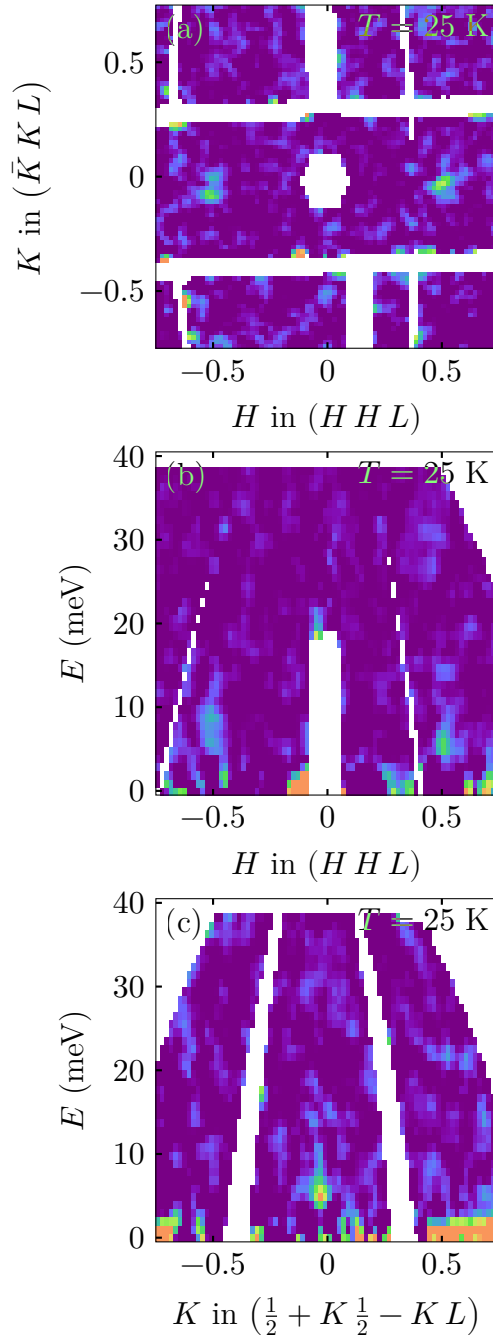


FIGURE 5.5. Data shown here is the smoothed difference between superconducting and normal state background subtracted $\text{Ba}(\text{Fe}_{0.953}\text{Co}_{0.047})_2\text{As}_2$ time-of-flight data measured on ARCS with $E_i = 50$ meV. Panel (a) shows a constant-energy slice with an integration range $4 < E < 10$ meV such that $L \approx 1$. Panel (b) shows a $[H H 0]$ versus energy slice with an integration range $-0.1 < (\bar{K} K 0) < 0.1$. Panel (c) shows a $[\bar{K} K 0]$ versus energy slice with an integration range $0.45 < (H H 0) < 0.55$. White regions in each panel indicate a lack of data due to gaps between detector tubes or kinematic limitations.

manifests as a peak in the superconducting data at $E \approx 5$ meV. Also shown in figure 5.6 is a lack of any significant difference between the $T = 5$ and 25 K data above $E \approx 15$ meV, providing further justification for the decision to combine the $E_i = 250$ meV $T = 5$ and 70 K data.

5.1.2 HB3 triple-axis spectrometer

Most of the compositions studied with the HB3 triple-axis spectrometer are under-doped, possessing both weak AFM ordering and superconductivity at low temperatures (i.e., small spin density wave and superconducting gaps). For the triple-axis data it is convenient to define $\mathbf{Q} = \frac{2\pi}{a}H\hat{i} + \frac{2\pi}{a}K\hat{j} + \frac{2\pi}{c}L\hat{k} = (H, K, L)$ in reciprocal lattice units as referenced to the tetragonal $I4/mmm$ unit cell. Data were collected with a fixed final energy of 14.7 meV and graphite filters between the sample and analyzer. HB3 utilizes a vertically focusing monochromator and analyzer, furthermore, all measured samples were sufficiently small compared to the monochromator and analyzer for finite-size effects to become important. As such, the Cooper-Nathans approximation to the resolution function was not appropriate for the analysis of this data and instead Popovici's method, as implemented in RESLIB [98], was used for resolution convolutions of model functions. Full details of the instrumental parameters for the Popovici approximation used are given in appendix C. Each scan has been reduced to the imaginary part of the dynamical susceptibility, $\chi''(\mathbf{Q}, E)$, after correcting for non-magnetic background, removing the temperature dependent Bose factor, and rescaling the intensity into absolute units of $\mu_B^2 \text{ meV}^{-1} \text{ f.u.}^{-1}$ by comparison to transverse acoustic phonons, as described in appendix D.

Figure 5.7 shows the spectrum at several different temperatures for $\text{Ba}(\text{Fe}_{0.985}\text{Co}_{0.015})_2\text{As}_2$ and $\text{Ba}(\text{Fe}_{0.967}\text{Co}_{0.033})_2\text{As}_2$, as measured by the HB3 triple-axis spectrometer. Each scan has been reduced to the imaginary part of the dynamical susceptibility, $\chi''(\mathbf{Q}, E)$, after correcting for non-magnetic background, removing the temperature-dependent Bose factor, and rescaling

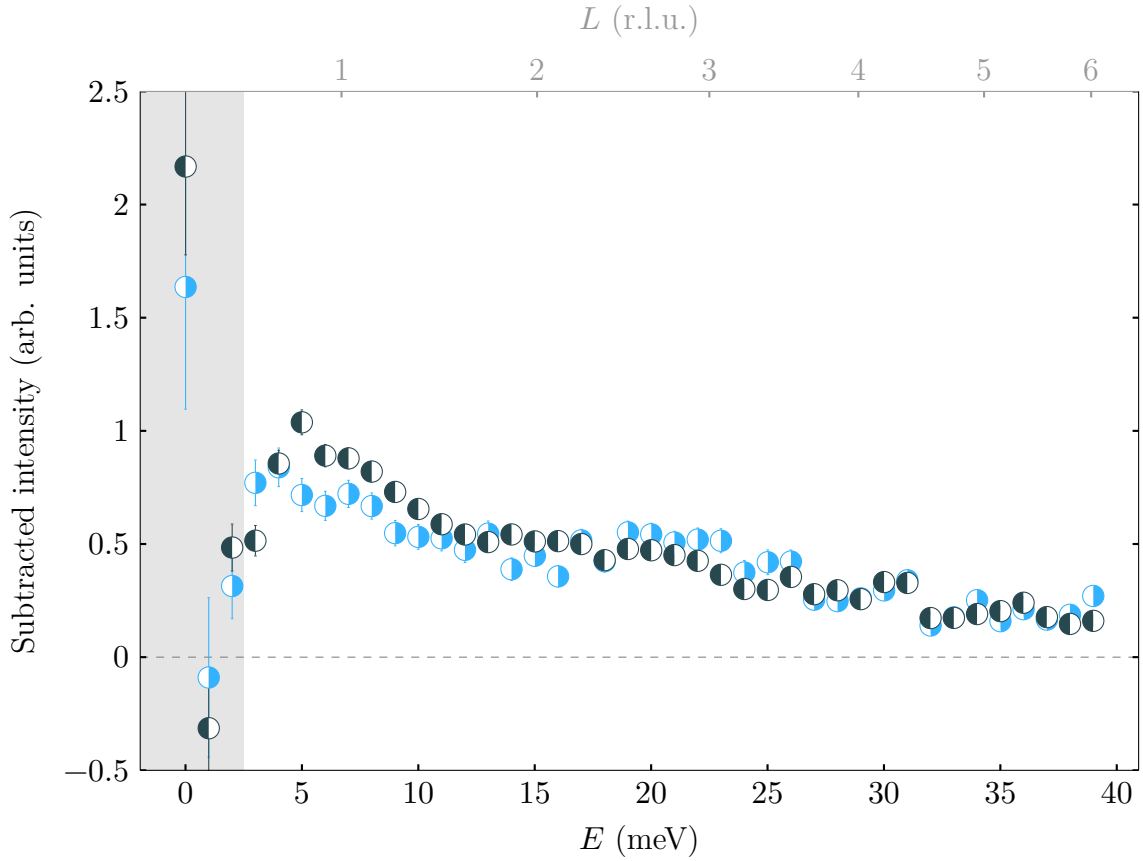


FIGURE 5.6. Background subtracted $\text{Ba}(\text{Fe}_{0.953}\text{Co}_{0.047})_2\text{As}_2$ time-of-flight data measured on ARCS with $E_i = 50$ meV. These cuts has been produced by averaging over $0.45 < (H H 0) < 0.55$, $-0.1 < (\bar{K} K 0) < 0.1$, and binning in energy with a bin-width of 1 meV for $T = 5$ K (●) and $T = 25$ K (●). The L component of \mathbf{Q} is fully determined by the other components of (\mathbf{Q}, E) and is indicated for bin centers by a second top horizontal scale. Data within the shaded gray region is likely too close to the elastic line for the subtracted background estimate to be accurate, due to the presence of strong incoherent scattering.

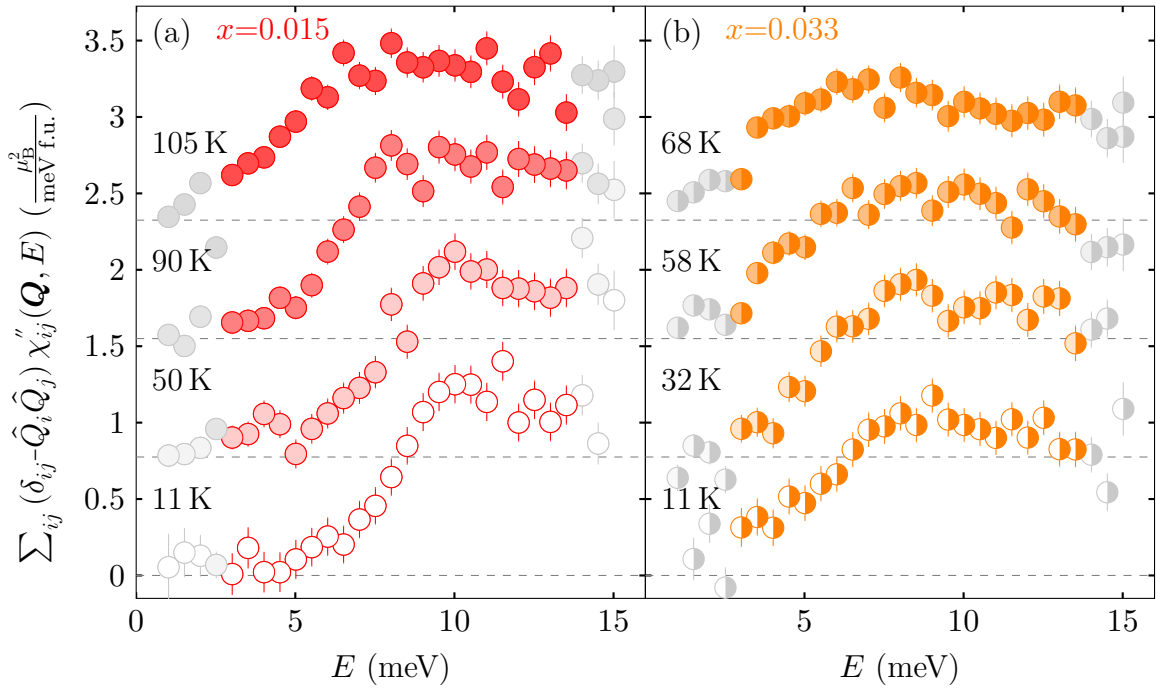


FIGURE 5.7. Temperature dependence of background subtracted $\text{Ba}(\text{Fe}_{0.985}\text{Co}_{0.015})_2\text{As}_2$ and $\text{Ba}(\text{Fe}_{0.967}\text{Co}_{0.033})_2\text{As}_2$ data measured at HB3. Panels (a,b) offset energy spectra at $\mathbf{Q}=(0.5\ 0.5\ 1)_{\text{T}}$ at the indicated temperatures for: (a) $x=0.015$; (b) $x=0.033$. Light gray symbols represent measured intensity which was excluded from fitting due to concerns with the validity of background estimates at those points.

the intensity into absolute units of $\mu_{\text{B}}^2 \text{ meV}^{-1} \text{ f.u.}^{-1}$ by comparison to transverse acoustic phonons [99].

In addition to the temperature dependent measurements, data for each of the five samples was collected in the antiferromagnetically ordered state at a number of (\mathbf{Q}, E) points via constant- \mathbf{Q} energy scans and constant- E momentum scans. All collected data are displayed in appendix A. Unfortunately, the range of data collected for each sample is not consistent across the range of samples and, in order to avoid over- or under-sampling effects, only a selection of the available scans were fit to model functions.

The subset of scans fit are shown in figure 5.8, which is a series of representative low-energy INS scans taken in the antiferromagnetic ordered and normal state ($T_{\text{c}} < T < T_{\text{N}}$) for each composition. Upon increased Co substitution, the spin gap appears to gradually close [figure 5.8(a)-(e)] and is completely absent at $x = 0.055$. One can also observe a gradual reciprocal space broadening of the longitudinal cut [figure 5.8(f)-(j)] with increasing Co composition. Finally, the modulations along $[\frac{1}{2} \frac{1}{2} 1]_{\text{T}}$ [figure 5.8(k)-(o)] are reduced, signaling a gradual evolution to two-dimensional spin dynamics.

5.2 $\text{Ba}(\text{Fe}_{1-x}\text{Co}_x)_2\text{As}_2$ and the Spinwave Model

5.2.1 High-energy time-of-flight analysis

In the so-called ballistic model, equation (4.46), the dynamics are governed by propagating over-damped spin-waves in the disordered paramagnetic state with anisotropic spin-wave velocity:

$$v_q^2 q^2 = v_{\text{xy}}^2 (q_x^2 + q_y^2 + \eta_v q_x q_y), \quad (5.2)$$

where, in contrast to equation (4.31), v_z has been omitted due to the ARCS measurement being insensitive to intensity modulations along the \mathbf{c}^* direction.

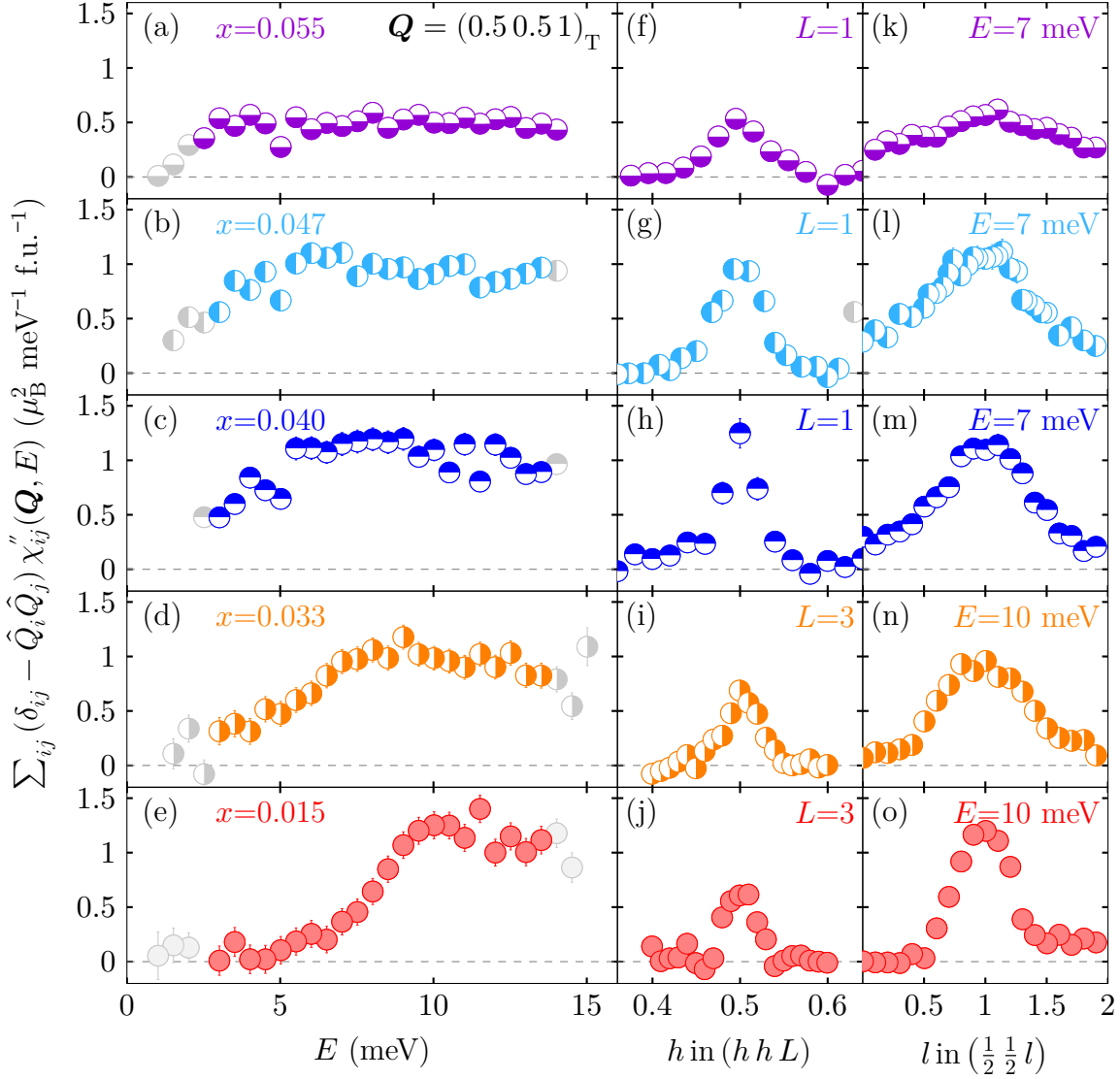


FIGURE 5.8. Background subtracted intensity corrected for the Bose thermal population factor and the single-ion magnetic form factor for Fe^{2+} for $\text{Ba}(\text{Fe}_{0.945}\text{Co}_{0.055})_2\text{As}_2$ (a,f,k), $\text{Ba}(\text{Fe}_{0.953}\text{Co}_{0.047})_2\text{As}_2$ (b,g,l), $\text{Ba}(\text{Fe}_{0.960}\text{Co}_{0.040})_2\text{As}_2$ (c,h,m), $\text{Ba}(\text{Fe}_{0.967}\text{Co}_{0.033})_2\text{As}_2$ (d,i,n), and $\text{Ba}(\text{Fe}_{0.985}\text{Co}_{0.015})_2\text{As}_2$ (e,j,o). (a-e) Constant- Q energy scans at $Q_{\text{AFM}} = (0.5\ 0.5\ 1)_{\text{T}}$ for the five compositions. (f-h) Constant- E Q scans in the $[1\ 1\ 0]_{\text{T}}$ -direction across $Q_{\text{AFM}} = (0.5\ 0.5\ 1)_{\text{T}}$ at $E = 7$ meV. (i-j) Constant- E Q scans in the $[1\ 1\ 0]_{\text{T}}$ -direction across $Q_{\text{AFM}} = (0.5\ 0.5\ 3)_{\text{T}}$ at $E = 10$ meV. (k-m) Constant- E Q scans in the $[0\ 0\ 1]_{\text{T}}$ -direction across $Q_{\text{AFM}} = (0.5\ 0.5\ 1)_{\text{T}}$ at $E = 7$ meV. (n-o) Constant- E Q scans in the $[0\ 0\ 1]_{\text{T}}$ -direction across $Q_{\text{AFM}} = (0.5\ 0.5\ 3)_{\text{T}}$ at $E = 10$ meV. Light gray symbols represent measured intensity which was excluded from fitting due to concerns with the validity of background estimates at those points.

TABLE 5.1. Best-fit parameter values and calculated η_ξ for the ballistic model, equation (4.46), fit to high-energy time-of-flight data for $\text{Ba}(\text{Fe}_{0.953}\text{Co}_{0.047})_2\text{As}_2$.

$\chi_0\xi^2/\text{a.u.}$	Γ/meV	$\xi_L/\text{\AA}$	$\xi_T/\text{\AA}$	$v_{xy}/\text{meV \AA}$	η_v	η_ξ
6.3(7)	8.5(11)	11.8(9)	8.2(6)	450(40)	0.37(3)	0.35(9)

Presumably, the spin wave velocities in the paramagnetic phase are comparable to those found deep in the AFM ordered state. The form of the susceptibility in equation (4.46) is diffusive in nature (consisting of relaxational dynamics and a single peak response) at low energies, where the spin-wave wavelength is longer than the correlation length (i.e., $E < v_q\xi^{-1}$). The renormalized spin-wave modes will appear in the form of a broad elliptical ring of scattering at constant E when $E > v_q\xi^{-1}$ is satisfied. The high-energy form of the scattering then represents a section of the damped, conical spin-wave dispersion. This approach was used to describe the anisotropic quasi-propagating mode postulated in by Li et al. in reference [97]. A similar approach was also used by Harriger et al. in reference [96], although in that case a local moment Heisenberg model was employed to describe the spin wave dispersion whereas here a linear dispersion is assumed.

Figure 5.9 shows calculations of the neutron scattering cross-section for the ballistic model using parameters determined from fits of the neutron data for the $x = 0.047$ compound to equation (4.46). The utilized fitting routine ensured that, for all cases, $|\eta| \leq 1$. Fit parameter values and their associated errors, plus values of η_ξ derived from the fit parameters are presented in table 5.1. The fits to the data are described in detail in section 5.4.1. The same slices through the neutron intensity are shown in figure 5.9 as the data in figure 5.3. The anisotropy of the spin wave velocity with $\eta_v > 0$ describes the elliptical shape of the scattering cross-section. At high energies, the scattering assumes the expected form of an elliptical ring.

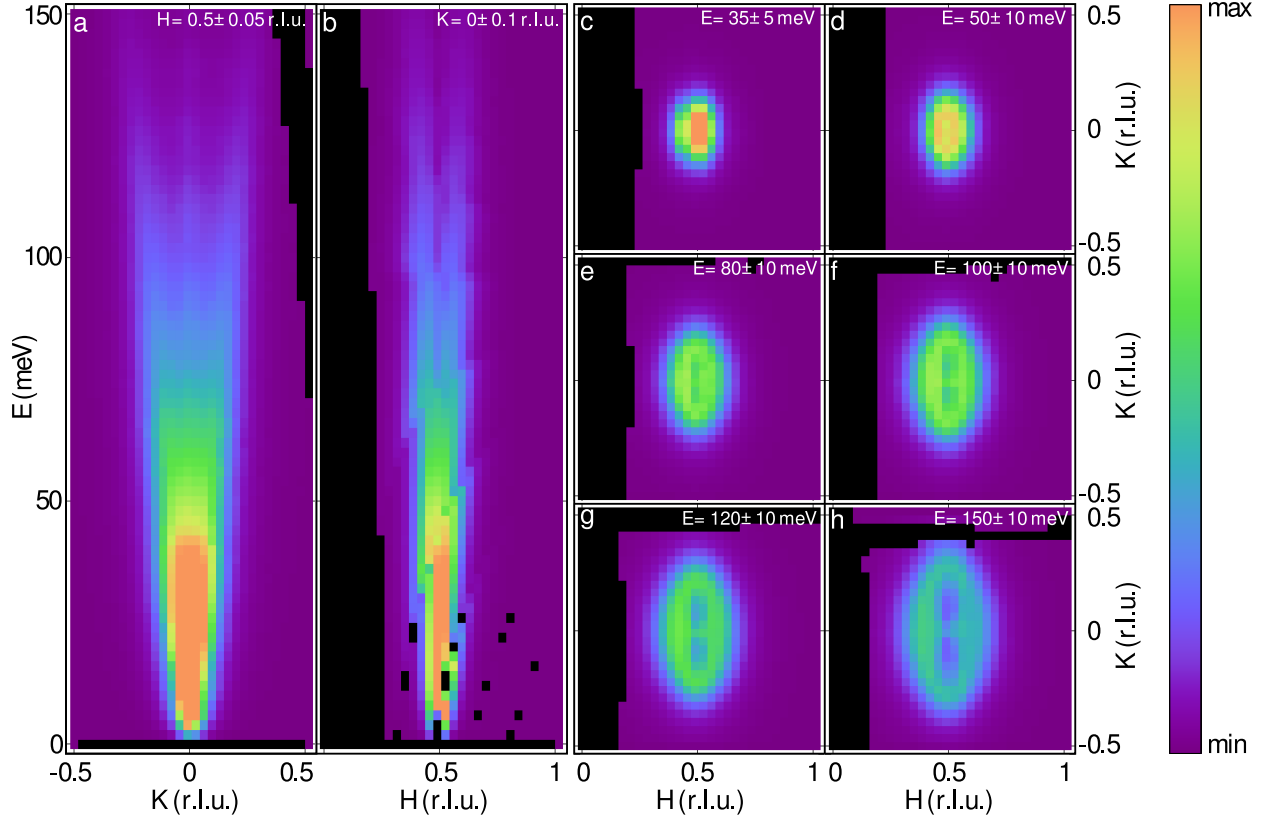


FIGURE 5.9. Calculations of the inelastic neutron scattering spectrum as obtained from a ballistic model of over-damped spin waves, as described by equation (4.46). The parameters of the model, reported in table 5.1, were obtained by fits to the neutron scattering data for $\text{Ba}(\text{Fe}_{0.953}\text{Co}_{0.047})_2\text{As}_2$ as shown in figures 5.15 and 5.16. (a) Transverse slice of the data along the $[K, -K]$ direction through $\mathbf{Q}_{\text{AFM}} = (\frac{1}{2}, \frac{1}{2}, L)$ after averaging over $H = 0.5 \pm 0.05$ r.l.u. (b) Longitudinal slice of the data along the $[H, H]$ direction through $\mathbf{Q}_{\text{AFM}} = (\frac{1}{2}, \frac{1}{2}, L)$ after averaging over $K = 0 \pm 0.1$ r.l.u. Constant energy slices in the (H, K) -plane averaged over an energy range of (c) 35 ± 5 meV, (d) 50 ± 10 meV, (e) 80 ± 10 meV, (f) 100 ± 10 meV, (g) 120 ± 10 meV, and (h) 150 ± 10 meV. In each panel, the color scale represents the intensity of scattered neutrons, where the maximum intensity in each panel, in arb. units, is (a) 10, (b) 10, (c) 10, (d) 8, (e) 5, (f) 3, (g) 2, (h) 1; and the minimum intensity in all panels is 0.

5.2.2 High-energy time-of-flight composition dependence

The high-energy spin fluctuations have been studied in several compositions of the $\text{Ba}(\text{Fe}_{1-x}\text{Co}_x)_2\text{As}_2$ series ($x = 0$ [96], 0.065 [100], 0.074 [97], 0.08 [70], and the $x = 0.047$ composition discussed here [91]) as well as in the parent compound CaFe_2As_2 [95, 101, 102]. In each composition, the spin excitations are seen to extend up to energies $> 100 - 150$ meV. In the paramagnetic phase, the spin fluctuations in momentum space display a pronounced elliptical anisotropy within the Fe layer, with softer magnetic excitations extending along the $[1\bar{1}0]_{\text{T}}$ -direction (transverse to the ordered moment direction) and stiffer excitations along the $[110]_{\text{T}}$ -direction (longitudinal to the ordered moment direction). In this regime, the anisotropy is defined in terms of the magnetic correlation lengths along antiferromagnetic (longitudinal correlation length, ξ_{L}) and ferromagnetic bonds (transverse correlation length, ξ_{T}) of the stripe magnetic structure:

$$\eta_{\xi} = \frac{\xi_{\text{L}}^2 - \xi_{\text{T}}^2}{\xi_{\text{L}}^2 + \xi_{\text{T}}^2}. \quad (5.3)$$

Anisotropy parameter $\eta_{\xi} = 0$ corresponds to isotropic spin fluctuations while $\eta_{\xi} = 1$ corresponds to the extreme limit where $\xi_{\text{L}} \gg \xi_{\text{T}}$ and ($\eta_{\xi} = -1$ to the other extreme where $\xi_{\text{L}} \ll \xi_{\text{T}}$). This two-fold anisotropy at $\mathbf{Q}_{\text{AFM}} = (\frac{1}{2}, \frac{1}{2}, 1)$ is allowed by the simple tetragonal symmetry of the Fe sublattice [103]. The origin of the anisotropy can be deduced from both localized [104] and itinerant descriptions of the magnetism in these materials. In the limit of local-moment magnetism, one can use the $J_1 - J_2$ model to show that $\eta_{\xi} = J_1/2J_2$ [102]. Within this approach, $\eta_{\xi} = 0$ corresponds to no coupling between the two interpenetrating Néel sublattices making up the stripe AFM structure ($J_1 = 0$), whereas $\eta_{\xi} = 1$ corresponds to the classical stability limit of the stripe ordered antiferromagnetic state, which gives way to G-type magnetic order for $J_1 > 2J_2$. In the itinerant approach, η_{ξ} is a consequence of the ellipticity of the electron pockets.

For those compositions having long-range AFM order, the spinwave dispersion is anisotropic within the Fe layer. To compare the anisotropy in the AFM and PM states, one can define the anisotropy of the spin wave velocity as

$$\eta_v = \frac{v_L^2 - v_T^2}{v_L^2 + v_T^2} \quad (5.4)$$

where v_L is the spin wave velocity along the longitudinal direction and v_T is the spin wave velocity along the transverse direction. If one uses a local-moment description for the spin wave dispersion, i.e., the $J_{1a} - J_{1b} - J_2$ model, and if the orthorhombic distortion is small ($a_O \approx b_O$, $\delta \approx 0$), then η_v is given by

$$\eta_v = \frac{J_{1a} + J_{1b}}{4J_2 + J_{1a} - J_{1b}} \quad (5.5)$$

When $J_{1a} \approx J_{1b} = J_1$, the spin-wave velocity anisotropy reduces to the same result as that obtained for the correlation lengths in the tetragonal paramagnetic phase, $\eta_v = \eta_\xi = J_1/2J_2$.

Using these expressions, one can compute experimental values for the correlation length and spin wave velocity anisotropies for several different iron arsenide compositions in both the ordered and paramagnetic phases, as shown in table 5.2. In those systems with long-range AFM order, the anisotropy of the low-energy spin fluctuations does not change strongly above T_N , i.e., between the AFM-orthorhombic and PM-tetragonal phases. This observation casts much doubt on the “nematic spin fluid” model proposed in reference [96]. In that model, local orthorhombic distortions are proposed to exist based on the analysis of short-wavelength zone boundary spin-waves at $\mathbf{Q} = (1\ 0\ L)$ using the $J_{1a} - J_{1b} - J_2$ model. The temperature independence of these zone boundary spin-waves suggests that J_{1a} and J_{1b} , which are very different in the orthorhombic phase, remain so even in the tetragonal paramagnetic phase. However, this local symmetry breaking cannot hold in the long-wavelength limit, where the crystallographic symmetry must be respected and an average nearest-neighbor exchange

$2J_1 = J_{1a} + J_{1b}$ must be assumed. Such a scenario would predict a sizable change in the momentum space anisotropy of low energy spin excitations above and below T_N , since the ratio of the velocity anisotropy in the tetragonal and orthorhombic states is given by

$$\frac{\eta_v^T}{\eta_v^O} = 1 + \frac{J_{1a} - J_{1b}}{4J_2}. \quad (5.6)$$

Using the values of the exchange constants J_{1a} and J_{1b} extracted from the spin-wave fitting of BaFe_2As_2 , gives $\eta_v^T/\eta_v^O \approx 1.7$. Thus, one would expect a change of the in-plane anisotropy by 70%, however, no change of the anisotropy is observed experimentally [96]. This temperature independence suggests that the $J_1 - J_2$ model is an appropriate parameterization of the spin dynamics in the long-wavelength limit (in either the tetragonal or orthorhombic phases). At shorter wavelengths/higher energies, the local-moment models clearly run into trouble [105] and a description that explicitly takes into account the itinerancy of the magnetic moments is needed [106]. It is interesting to note that spin fluctuations become more anisotropic with cobalt doping in the $\text{Ba}(\text{Fe}_{1-x}\text{Co}_x)_2\text{As}_2$ system, reaching values $\eta_\xi > \frac{1}{2}$ for $x > 0.065$.

At energies greater than 80 to 100 meV, the anisotropic spin fluctuations split along the transverse direction and seem to form separate counter-propagating branches. This splitting is unusual and not typical of propagating spin waves, where constant energy contours will form a ring of scattering from collective modes that propagate in all directions. This transverse splitting phenomenon was first noted in $\text{Ba}(\text{Fe}_{0.925}\text{Co}_{0.075})_2\text{As}_2$ composition [97] and has since been observed in the parent compound BaFe_2As_2 [96]. In $\text{Ba}(\text{Fe}_{0.953}\text{Co}_{0.047})_2\text{As}_2$, the transverse splitting is also observed, as shown in figure 5.2 and figure 5.3. The energy where this transverse splitting takes place and its intensity are temperature-independent (figure 5.2), i.e., the splitting is unmodified even deep in the AFM ordered state, a feature also observed in BaFe_2As_2 (figure 2.23) [96]. Viewed as a propagating mode where $v_T = E/\Delta q$, table 5.2 shows that the velocity of this mode is weakly dependent on composition within the

TABLE 5.2. Composition dependence of the transverse propagation velocity and anisotropy of spin fluctuations in $A(\text{Fe}_{1-x}\text{Co}_x)_2\text{As}_2$ ($A = \text{Ca}, \text{Sr}, \text{Ba}$). For undoped compounds in the antiferromagnetic ordered (AFM) phase, the transverse velocity and anisotropy parameters are obtained from a fit to a model of propagating spin waves. For paramagnetic (PM) compounds, the parameters are obtained from either damped spin wave or diffusive models. See references [91, 95–97, 100–103, 105] for further details. This table has been reproduced from reference [91].

A	x	T (K)	state	v_T (meV Å)	η_v	reference
Ca	0	5	AFM	370(10)	0.32(2)	[95]
Ca	0	10	AFM	350(40)	0.34(10)	[101]
Ca	0	180	PM		0.28(18)	[102]
Sr	0	6	AFM	335(20)	0.21(4)	[105]
Ba	0	7	AFM	316(11)	0.41(2)	[96]
Ba	0	150	PM	300	0.4	[96]
Ba	0.047	5	AFM	230(30)	0.35(9)	[91]
Ba	0.047	70	PM	230(30)	0.35(9)	[91]
Ba	0.065	7	PM	230(30)	0.70(2)	[100]
Ba	0.074	5	PM	245(10)	0.50(1)	[97]
Ba	0.075	200	PM		0.7	[103]

Ba($\text{Fe}_{1-x}\text{Co}_x$) $_2\text{As}_2$ series, with a value of 316 meV Å for BaFe $_2\text{As}_2$ that softens to ~ 240 meV Å for optimally-doped superconducting compositions. The weak dependence of this splitting on composition casts some doubt on its interpretation as an incipient incommensurability (i.e., a band nesting effect) which should be very sensitive to composition [103]. By plotting the magnitude of this velocity as a function of cobalt doping, see Figure 5.10 it becomes apparent that the velocity is nearly independent of cobalt concentration in Ba($\text{Fe}_{1-x}\text{Co}_x$) $_2\text{As}_2$, at least over the range covering the parent, lightly-doped, under-doped, and optimally-doped compounds – this fact is exceptionally important for the successful interpretation of the low-energy spin fluctuations in under-doped Ba($\text{Fe}_{1-x}\text{Co}_x$) $_2\text{As}_2$.

5.2.3 Low-energy triple-axis composition dependence

The data presented in figure 5.11 is reproduced from figure 5.7 and shows that for Ba($\text{Fe}_{0.985}\text{Co}_{0.015}$) $_2\text{As}_2$ and Ba($\text{Fe}_{0.967}\text{Co}_{0.033}$) $_2\text{As}_2$ the energy spectra are dominated by a

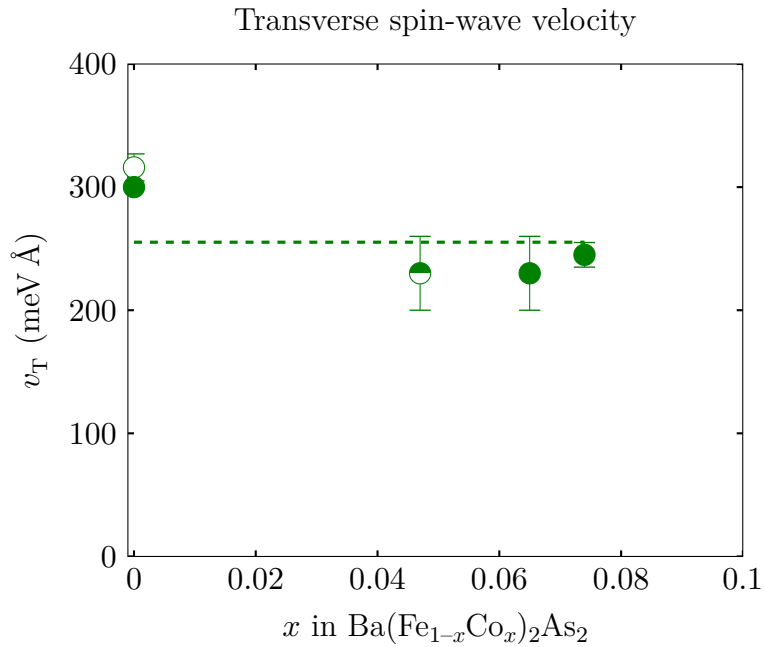


FIGURE 5.10. The transverse spin wave velocity in $\text{Ba}(\text{Fe}_{1-x}\text{Co}_x)_2\text{As}_2$ as a function of cobalt concentration compiled from references [91, 96, 97, 100]. The dashed horizontal line is an average of the presented data and, arguably, indicates that the velocity is nearly independent of composition. Filled symbols represent values obtained in the paramagnetic state, open symbols represent values obtained in the antiferromagnetic state, and the half-filled symbol represents that the value was obtained from data combined from both the antiferromagnetic and paramagnetic states.

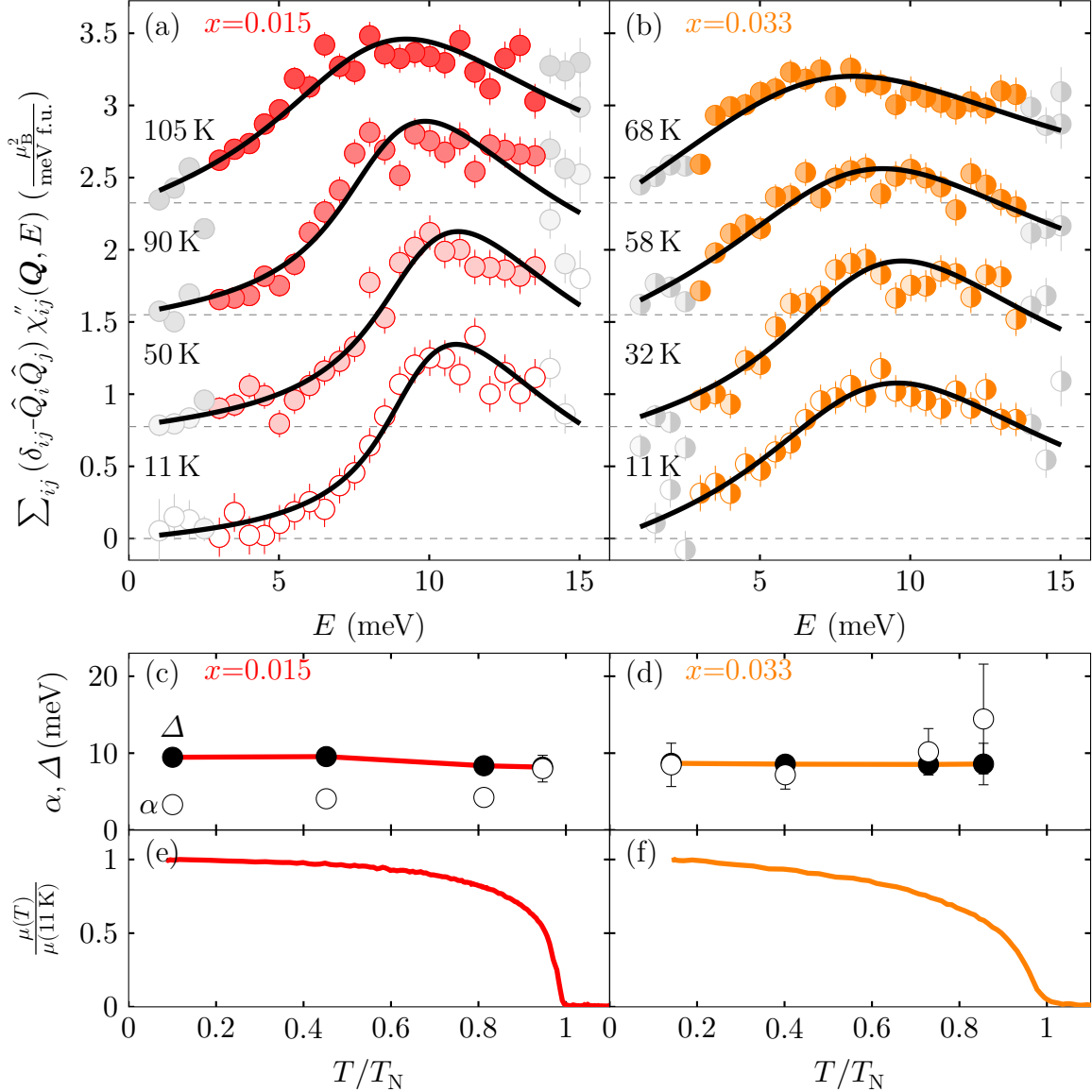


FIGURE 5.11. Temperature dependence of INS data for $\text{Ba}(\text{Fe}_{1-x}\text{Co}_x)_2\text{As}_2$ with $x = 0.015$ [(a, c, e)] and $x = 0.033$ [(b, d, f)] plus fits to the spinwave model, equation (4.29). (a, b) Energy scans at $\mathbf{Q}_{\text{AFM}} = (0.5, 0.5, 1)$ performed at the indicated temperatures are offset vertically. (c, d) Reduced temperature dependence of spinwave model parameters α (open symbols) and Δ (filled symbols). (e, f) Reduced temperature dependence of the ordered moment normalized to its low-temperature value. Light gray symbols in panels (a) and (b) represent measured intensity which was excluded from fitting due to concerns with the validity of background estimates at those points.

large spin gap at ~ 10 meV. These data can be fit to a damped spin wave form for $\chi''(\mathbf{Q}, E)$ which is related to the ballistic model used to fit the high-energy time-of-flight data in section 5.2.1. The full anisotropic form for the damped spin wave susceptibility is given earlier in equation (4.29). For $x = 0.015$ at 11 K, the damping parameter $\alpha = 3.6(4)$ meV is small in comparison to other energy scales and, in principle, can arise from a combination of different damping processes (such as Landau damping for energy scales larger than the spin density wave gap, or magnon-magnon interactions). The fit to the $x = 0.015$ 11 K data shows a large spin gap $\Delta = 9.73(14)$ meV characteristic of the parent AFM ordered state.

The solid lines in figure 5.11 (a) and (b) represent independent fits to the damped spin wave model where the gap and damping rate are allowed to vary freely. The magnitude of the spin gap is determined to be nearly constant with temperature up to a closest approach of $T/T_N = 0.95$ where $\mu(T)/\mu(11 \text{ K}) \approx 0.5$. Similar to the results described for NaFeAs [107], BaFe₂As₂ [107], and LaFeAsO [108], the spin gap energy scale is roughly 10 meV in the ordered state, regardless of size of the ordered moment and the dynamics become over-damped as T_N is approached.

Within the damped spin wave model of equation (4.29), the data at all compositions have been successfully fit by assuming that: in accordance with the temperature-dependent results, the spin gap remains constant; the damping increases dramatically with x ; and both the in-plane and inter-plane spin wave velocities are reduced with x . However, it is clear from high-energy INS investigations that the in-plane spin velocities are independent of composition (see figure 5.10) and constraining the in-plane velocity to this value leads to poorer and poorer agreement of the low-energy data with the damped spin wave model (as shown by the black lines in figure 5.12). Best-fit parameters for the spin wave model, equation (4.29), under these restrictions are given in table 5.3.

One major assumption of the data analysis using the spin wave model is that the spin gap is independent of composition. If the spin gap is due to single-ion anisotropy, then its

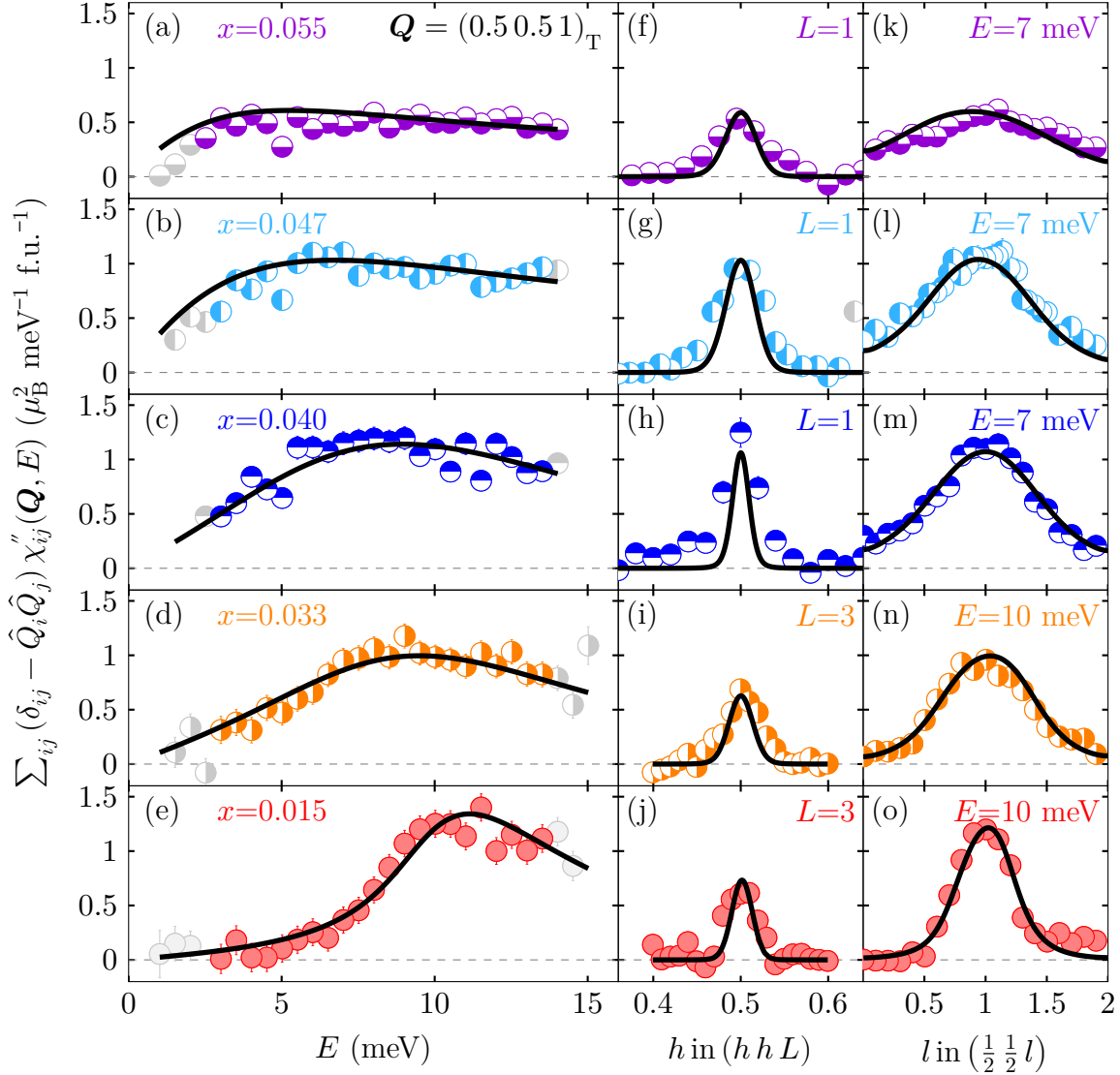


FIGURE 5.12. Background subtracted INS intensity of $\text{Ba}(\text{Fe}_{1-x}\text{Co}_x)_2\text{As}_2$ corrected for the Bose thermal population factor and the Fe^{2+} single-ion magnetic form factor plus best fit lines to the damped spin-wave (black lines) models. (a-e) Constant- \mathbf{Q} energy scans at $\mathbf{Q}_{\text{AFM}} = (0.5, 0.5, 1)$ for five compositions. (f-h) Constant- E \mathbf{Q} scans in the $[h, h, 0]$ -direction across $\mathbf{Q}_{\text{AFM}} = (0.5, 0.5, 1)$ at $E = 7$ meV. (i-j) Constant- E \mathbf{Q} scans in the $[h, h, 0]$ -direction across $\mathbf{Q}_{\text{AFM}} = (0.5, 0.5, 3)$ at $E = 10$ meV. (k-m) Constant- E \mathbf{Q} scans in the $[0, 0, l]$ -direction, perpendicular to the Fe layer, across $\mathbf{Q}_{\text{AFM}} = (0.5, 0.5, 1)$ at $E = 7$ meV. (n-o) Constant- E \mathbf{Q} scans in the $[0, 0, l]$ -direction across $\mathbf{Q}_{\text{AFM}} = (0.5, 0.5, 1)$ at $E = 10$ meV. Light gray symbols represent measured intensity which was excluded from fitting due to concerns with the validity of background estimates at those points.

TABLE 5.3. Fit parameter values for the spin wave model fit to low-energy triple-axis data, v_{xy} and η_v were fixed for all compositions by the high-energy time-of-flight best-fit parameters reported in table 5.1.

$x/\%$	$\chi_0/\frac{\mu_B^2}{\text{meV f.u.}}$	α/meV	Δ/meV	$v_{xy}/\text{meV}\text{\AA}$	η_v	$v_z/\text{meV}\text{\AA}$
1.5	1.27(8)	3.6(4)	9.73(14)	450	0.365	46(2)
3.3	1.61(6)	12.4(8)	9.73	450	0.365	47.3(16)
4.0	1.94(5)	15.3(7)	9.73	450	0.365	33.9(12)
4.7	3.32(8)	22.2(6)	9.73	450	0.365	44.7
5.5	1.96(5)	27.3(10)	9.73	450	0.365	35.8

magnitude should be proportional to some power of μ [109]. Data fitting in which the spin gap was allowed to freely vary resulted in an *increase* of the gap with composition, and fits in which the spin gap was constrained to be proportional to μ gave worse results.

5.3 Ba(Fe_{1-x}Co_x)₂As₂ and the Diffusive Model

5.3.1 High-energy time-of-flight analysis

To describe the magnetic spectrum in the paramagnetic state, one can consider an itinerant model that captures the diffusive character of the spin dynamics. One can perform a first-principles calculation for the spin dynamics by using the complete density functional theory (DFT) band structure and incorporating the electronic interaction via RPA[103, 105] or DMFT.[106] Indeed, such calculations provide a good description of the magnetic spectrum of different compounds, but their complexity makes it difficult to sort out the essential physics responsible for the behavior of the magnetic spectrum.

Here, instead of considering the full band structure input, a phenomenological approach described by the diffusive model, equation (4.41), is considered. The low-energy magnetic spectrum of this model has been discussed in references [62] and [110]. With the anisotropic correlation length

$$\xi_q^2 q^2 = \xi^2(q_x^2 + q_y^2 + 2\eta_\xi q_x q_y) \quad (5.7)$$

and characteristic energy

$$\Gamma_q = \frac{1}{\gamma_q \xi^2} = \Gamma [1 + \beta^2 (q_x^2 + q_y^2 + 2\eta_\Gamma q_x q_y)] \quad (5.8)$$

which both lack terms proportional to q_z^2 due to the insensitivity of the ARCS time-of-flight data to modulations along \mathbf{c}^* . In equation (5.8), the momentum-dependent damping Γ_q has been expanded for small deviations from \mathbf{Q}_{AFM} , introducing the anisotropy parameter η_Γ . And the analysis has been restricted to $|\eta_\Gamma| < 1$ in order to ensure that Γ_q^{-1} is maximum at $q = 0$. Similarly, to ensure that the magnetic correlation length in equation (5.7) is well-defined, $|\eta_\xi| < 1$ is assumed. Notice that equation (5.7) naturally gives rise to equation (5.3) considered before.

At low energies, this form of the susceptibility correctly captures the elliptical shape of $\chi''(\mathbf{q}, E)$ peaked at $\mathbf{q} = \mathbf{Q}_{\text{AFM}}(\mathbf{q} = 0)$, in agreement with the INS measurements on a variety of 122 compounds.[97, 102] The sign of the ellipticity depends on η_ξ ; for the parent and Co-doped BaFe₂As₂ compounds, such as the one shown in Fig. 5.3, the longitudinal correlation length [parallel to $\mathbf{Q}_{\text{AFM}} = (\frac{1}{2}, \frac{1}{2})$] $\xi_L = \xi\sqrt{1 + \eta_\xi}$ is longer than the transverse correlation length [perpendicular to $\mathbf{Q}_{\text{AFM}} = (\frac{1}{2}, \frac{1}{2})$] $\xi_T = \xi\sqrt{1 - \eta_\xi}$, implying that $\eta_\xi > 0$. On the other hand, the sign of η_ξ depends on the band structure (see, for instance Ref. [103]), and there is *a priori* no reason for it to be positive or negative. This is to be contrasted to the classical AFM $J_1 - J_2$ model, which always predicts $\eta \propto J_1/J_2 > 0$.

At high energies, as E increases, the momentum-dependence of the Landau damping eventually leads to the splitting of the single peak of $\chi''(\mathbf{Q}, E)$. Along the transverse direction, the low-energy peak splits into two symmetric peaks for energies $E > E_T$, as defined in equation (4.43). Similarly, along the longitudinal direction, the peak-splitting takes place for energies above E_L , as defined in equation (4.43).

Recalling that E_L and E_T are dependent on $\sqrt{1 \pm \eta_\xi/1 \pm \eta_\Gamma}$, respectively, if $\eta_\xi = \eta_\Gamma$ the elliptical shape of $\chi''(\mathbf{Q}, E)$ at low energies evolves in an elliptical-ring structure for

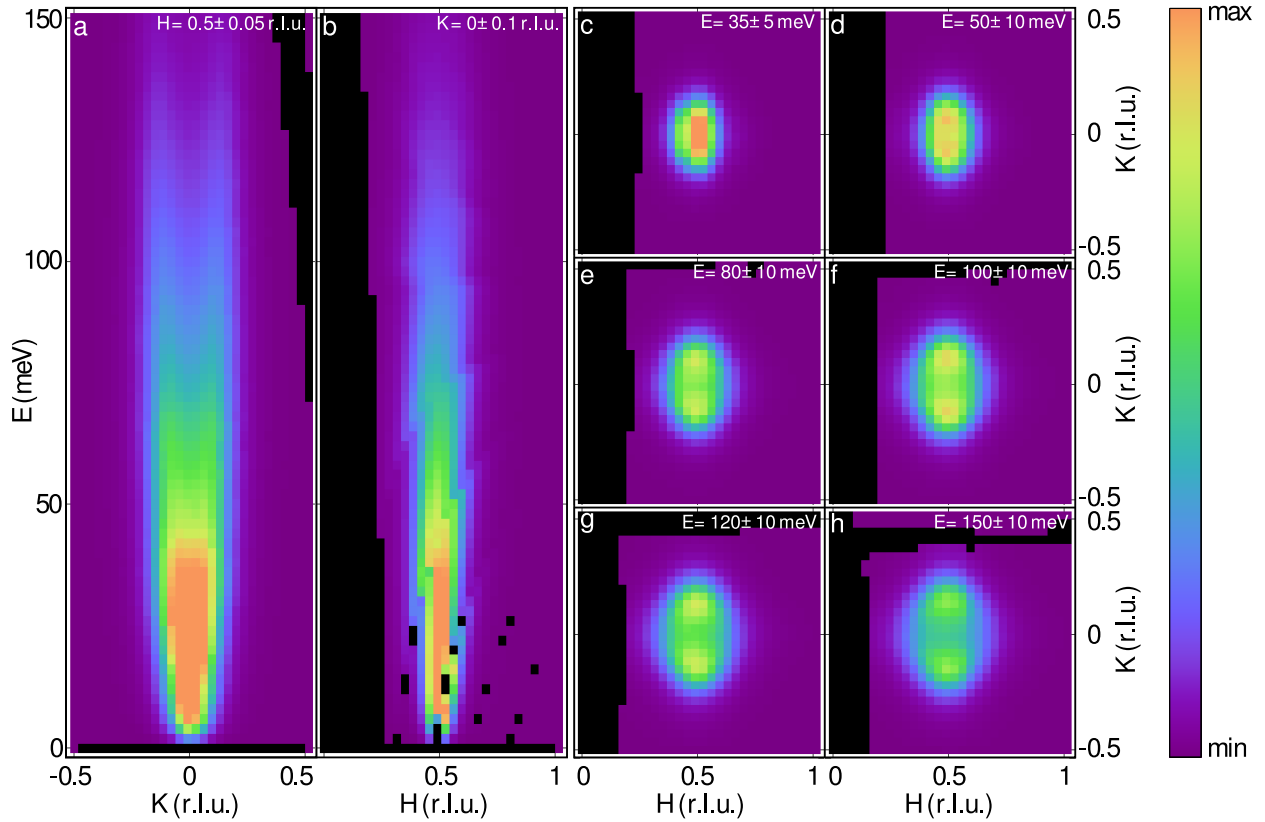


FIGURE 5.13. Calculations of the inelastic neutron scattering spectrum as obtained from a model of itinerant diffusive spin fluctuations, as described by equation (4.41). The parameters of the model, reported in table 5.4, were obtained by fits to the neutron scattering data for $\text{Ba}(\text{Fe}_{0.953}\text{Co}_{0.047})_2\text{As}_2$ as shown in figures 5.15 and 5.16. (a) Transverse slice of the data along the $[K, -K]$ direction through $\mathbf{Q}_{\text{AFM}} = (\frac{1}{2}, \frac{1}{2}, L)$ after averaging over $H = 0.5 \pm 0.05$ r.l.u. (b) Longitudinal slice of the data along the $[H, H]$ direction through $\mathbf{Q}_{\text{AFM}} = (\frac{1}{2}, \frac{1}{2}, L)$ after averaging over $K = 0 \pm 0.1$ r.l.u. Constant energy slices in the (H, K) -plane averaged over an energy range of (c) 35 ± 5 meV, (d) 50 ± 10 meV, (e) 80 ± 10 meV, (f) 100 ± 10 meV, (g) 120 ± 10 meV, and (h) 150 ± 10 meV. In each panel, the color scale represents the intensity of scattered neutrons, where the maximum intensity in each panel, in arbitrary units, is (a) 10, (b) 10, (c) 10, (d) 8, (e) 5, (f) 3, (g) 2, (h) 1; and the minimum intensity in all panels is 0.

TABLE 5.4. Fit parameter values and calculated η_ξ for the diffusive model, equation (4.41), fit to high-energy time-of-flight data for $\text{Ba}(\text{Fe}_{0.953}\text{Co}_{0.047})_2\text{As}_2$.

$\chi_0\xi^2$ /arb. units	Γ / meV	ξ_L / Å	ξ_T / Å	β / Å	η_Γ	η_ξ
5.0(4)	10.7(11)	9.4(5)	5.0(3)	2.0(2)	-1	0.57(6)

$E > E_T = E_L$. On the other hand, for $\eta_\xi > \eta_\Gamma$ ($\eta_\xi < \eta_\Gamma$) the splitting happens at a lower energy along the transverse (longitudinal) direction. Thus, depending on the magnitude of the difference $\Delta E \equiv E_T - E_L$, there can be a wide regime of energies where the low-energy single-peak response of $\chi''(\mathbf{Q}, E)$ at \mathbf{Q}_{AFM} splits into two peaks equidistant from \mathbf{Q}_{AFM} . For $\Delta E > 0$ (i.e., $\eta_\xi > \eta_\Gamma$), these two peaks split along the direction transverse to \mathbf{Q}_{AFM} , whereas for $\Delta E < 0$ (i.e., $\eta_\xi < \eta_\Gamma$), the two peaks split along the longitudinal direction to \mathbf{Q}_{AFM} . Therefore, the experimental data in the parent and Co-doped BaFe_2As_2 samples (figure 5.3) are compatible with $\eta_\xi > \eta_\Gamma$.

Figure 5.13 shows calculations of the neutron scattering cross-section for the diffusive model using parameters determined from fits of the neutron data for the $x = 0.047$ compound to equation (4.41). The fits to the data are described in detail below. This figure shows the same slices of the neutron intensity as in figure 5.3 and can be compared directly to the data. In general, the neutron data is best described with anisotropy parameters $\eta_\xi > 0$ and $\eta_\Gamma < 0$, resulting in anisotropic ellipsoids of scattering at low energies and a transverse splitting at higher energies.

Fit parameter values and their associated errors, plus values of η_ξ derived from the fit parameters are presented in table 5.4. Fits of the data were observed to be rather insensitive to changes in η_Γ , and subsequently η_Γ was fixed to -1 for the fitting. This limit gives q -independent (constant) damping in the longitudinal direction (Γ) and q -dependent damping in the transverse direction [$\Gamma_q = \Gamma(1 + 2\beta^2q^2)$].

5.3.2 Low-energy triple-axis composition dependence

Returning to the triple-axis results shown in figure 5.8. The increased reciprocal space broadening with x in the $[110]_{\text{T}}$ -direction suggests that another length scale must be introduced for low-energy magnetic fluctuations, such as a spin-spin correlation length. Considering also the gapless form of the magnetic excitations, the data at higher compositions resemble the low energy limit of the diffusive response used to describe the high-energy time-of-flight data in section 5.3.1 and also optimal and over-doped samples [97, 111].

Ignoring the Landau damping anisotropies of equation (4.41) which only significantly affect the form of the diffusive model above E_{T} , E_{L} and E_z [equations (4.43)] which are typically much higher than the energy scales probed by triple-axis measurements yields $\chi''_{\text{ad}}(\mathbf{Q}, E)$, equation (4.39). Here a special form of the correlation length anisotropy has been used

$$\xi_q^2 q^2 = \xi^2 (q_x^2 + q_y^2 + 2\eta_{\xi} q_x q_y + \eta_L (1 + \cos \pi L)) \quad (5.9)$$

to account for the exceptionally broad width of the excitation along the $[001]_{\text{T}}$ -direction. Fits to the diffusive form for $\chi''_{\text{ad}}(\mathbf{Q}, E)$ are shown as light green lines in figure 5.14. While the diffusive form does a poor job at the lowest compositions where the spin gap is sharp, it works exceptionally well at the higher compositions where the spectrum appears gapless and the increased reciprocal space broadening for longitudinal scans shown in figure 5.14 (f)-(j) is captured by a smaller correlation length. Best-fit parameters for resolution-convoluted fits to the data presented in figure 5.14 are reported in table 5.5.

5.4 A Comparison of the Spinwave and Diffusive Models

5.4.1 High-energy time-of-flight

In sections 5.2.1 and 5.3.1 the neutron intensity was used to test both the diffusive and the ballistic models, equations (4.41) and (4.46) respectively, and fitting results have thus

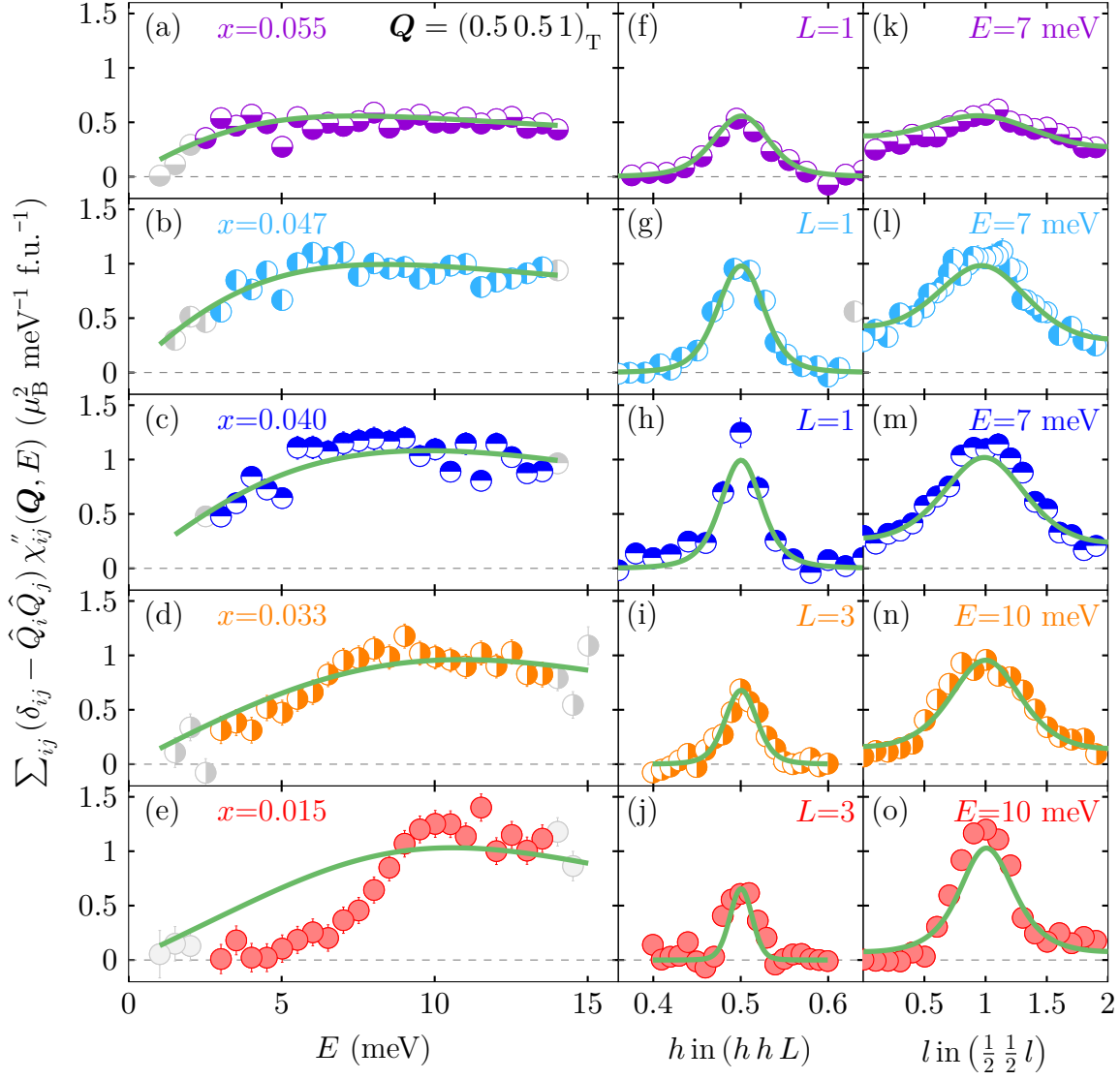


FIGURE 5.14. Background subtracted INS intensity of $\text{Ba}(\text{Fe}_{1-x}\text{Co}_x)_2\text{As}_2$ corrected for the Bose thermal population factor and the Fe^{2+} single-ion magnetic form factor plus best fit lines to the diffusive (light green lines) model. (a-e) Constant- \mathbf{Q} energy scans at $\mathbf{Q}_{\text{AFM}} = (0.5, 0.5, 1)$ for five compositions. (f-h) Constant- E \mathbf{Q} scans in the $[h, h, 0]$ -direction across $\mathbf{Q}_{\text{AFM}} = (0.5, 0.5, 1)$ at $E = 7$ meV. (i-j) Constant- E \mathbf{Q} scans in the $[h, h, 0]$ -direction across $\mathbf{Q}_{\text{AFM}} = (0.5, 0.5, 3)$ at $E = 10$ meV. (k-m) Constant- E \mathbf{Q} scans in the $[0, 0, l]$ -direction, perpendicular to the Fe layer, across $\mathbf{Q}_{\text{AFM}} = (0.5, 0.5, 1)$ at $E = 7$ meV. (n-o) Constant- E \mathbf{Q} scans in the $[0, 0, l]$ -direction across $\mathbf{Q}_{\text{AFM}} = (0.5, 0.5, 1)$ at $E = 10$ meV. Light gray symbols represent measured intensity which was excluded from fitting due to concerns with the validity of background estimates at those points.

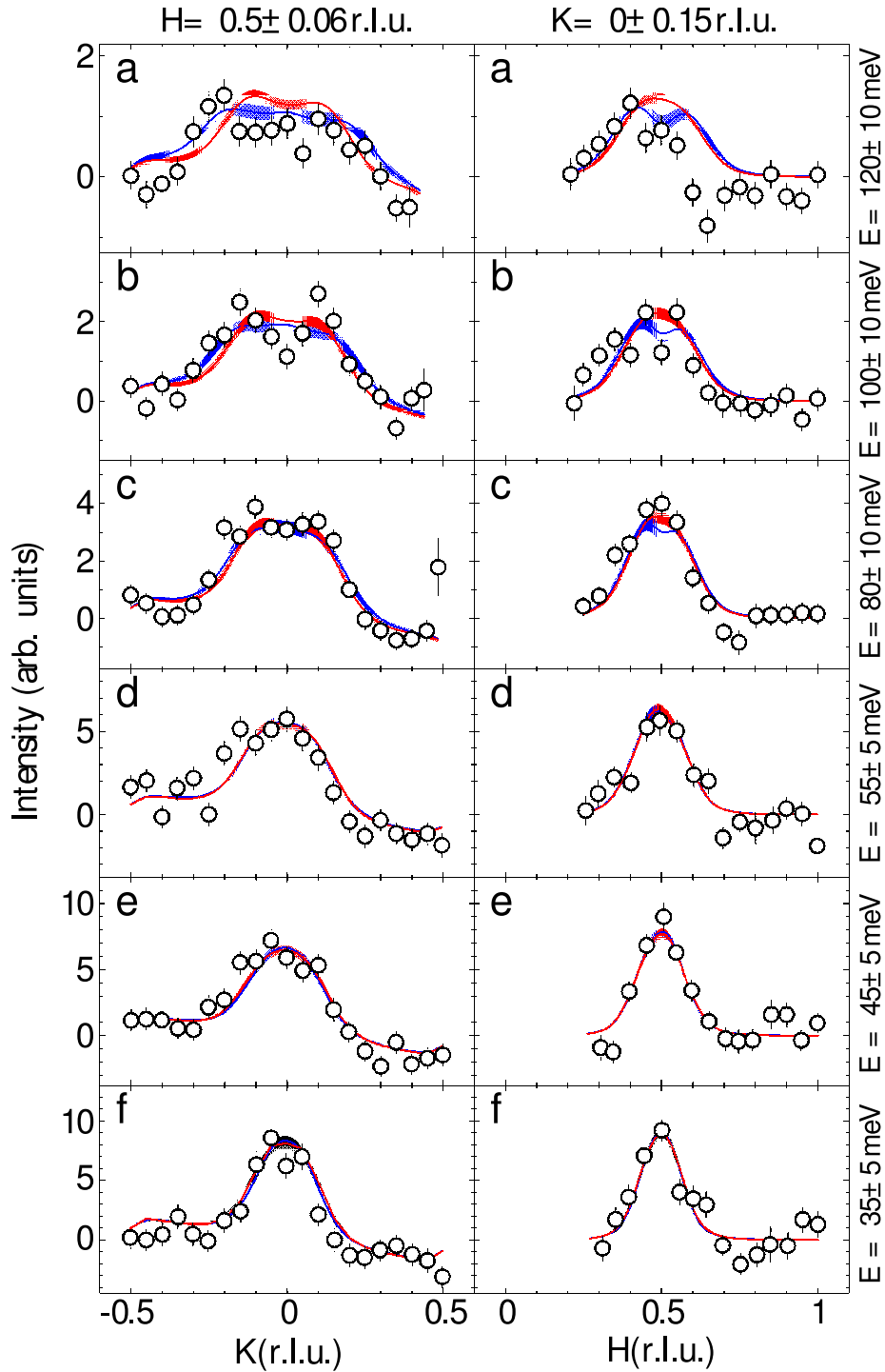


FIGURE 5.15. Fitting results for the diffusive (red lines) and ballistic (blue lines) models to the summed $T = 5$ K and 70 K data (open symbols). Transverse cuts (') and longitudinal cuts (") through $\mathbf{q} = (\frac{1}{2}, \frac{1}{2}, L)$ at (a) $E = 120 \pm 10$ meV, (b) $E = 100 \pm 10$ meV, (c) $E = 80 \pm 10$ meV, (d) $E = 55 \pm 5$ meV, (e) $E = 45 \pm 5$ meV, and (f) $E = 35 \pm 5$ meV. Shaded regions represent 95% confidence intervals for the fitting results.

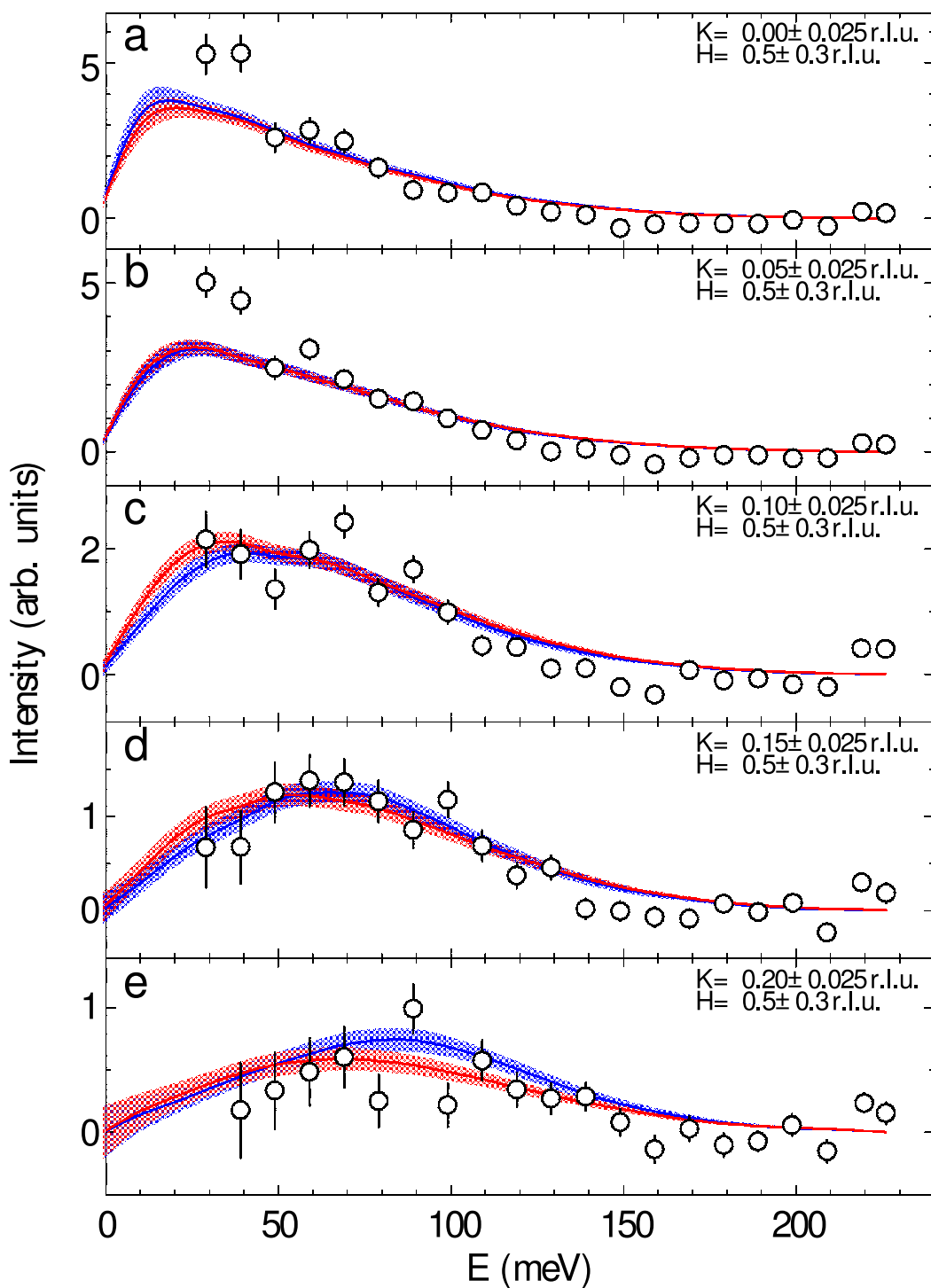


FIGURE 5.16. Fitting results for the diffusive (red lines) and ballistic (blue lines) models to the summed $T = 5$ K and 70 K data (open symbols). Spectra cuts centered at (a) $(0.5, 0.5, L)$, (b) $(0.55, 0.45, L)$, (c) $(0.6, 0.4, L)$, (d) $(0.65, 0.35, L)$, and (e) $(0.7, 0.3, L)$. Shaded regions represent 95% confidence intervals for the fitting results.

TABLE 5.5. Fit parameter values for the diffusive model, equation (4.39), fit to low-energy Ba(Fe_{1-x}Co_x)₂As₂ triple-axis data, η_ξ was fixed for all compositions by the high-energy time-of-flight best-fit parameters reported in table 5.4.

x	$\chi_0 / \mu_B^2 \text{ meV}^{-1} \text{ f.u.}^{-1}$	Γ / meV	$\xi / \text{\AA}$	η_ξ	η_L
0.015	7(5)	20	42(9)	0.57	0.0012(5)
0.033	1.9(4)	17(3)	17.1(14)	0.57	0.0035(5)
0.04	1.4(3)	10.4(6)	10.3(8)	0.57	0.0061(9)
0.047	1.61(13)	8.9(4)	11.5(3)	0.57	0.0039
0.055	0.82(12)	7.9(4)	9.2(5)	0.57	0.0033(4)

far been shown as slices through simulated data, figures 5.9 and 5.13. In order to make a quantitative comparison between the diffusive and ballistic models, cuts through the summed data and the best-fit simulated datasets are presented in figures 5.15 and 5.16 (red curves for the diffusive and blue curves for the ballistic model) for fixed energy and fixed momentum, respectively. For energies below 60 meV, the two models give nearly identical line shapes, which is not surprising, since both models reduce to an identical description of diffusive spin excitations at low energies. On the other hand, at higher energies, the purely diffusive model is in better agreement with the data, since the longitudinal cut has a maximum at $q = 0$ whereas the transverse cut has a minimum at $q = 0$. The ballistic model, on the other hand, gives the opposite: a minimum at $q = 0$ for the longitudinal cut and a maximum at $q = 0$ for the transverse cut.

These observations are also present in the sliced datasets. One should note that while the spectra in panels (a) and (b) of figures 5.3, 5.9 and 5.13 appear similar, there is a qualitative difference in the higher energy slices in panels (c)-(h). The diffusive model correctly reproduces the transverse splitting observed by experiment, whereas the ballistic model can only produce elliptical rings or, in the extreme case of $\eta_v \approx 1$, an elliptical ring that is pinched in the middle [see figure 5.9 (g) and (h)].

According to the fits of the INS data, neither the purely diffusive nor the ballistic model is strongly favored over the other. Mostly, this is due to the broad and overdamped nature

of the spin excitations and the convergence of the two models at low energies. Surprisingly, even though both models are low-energy descriptions of the magnetic excitation spectrum, the fitting to the data reveals that they are able to capture some of the intricate physics responsible for the high-energy behavior. Physically, the two models represent two different conceptual pictures for AFM fluctuations in the paramagnetic phase. The ballistic model would represent spin wave propagation in disordered AFM, whereas the diffusive model including Landau damping is based more closely on a quasiparticle description obtainable from either the simplified 3-band structure discussed here, or by first principles calculations in references [103] and [105]. However, the qualitative form of the scattering throughout the (H, K) -plane, and in particular the observation of the split transverse modes at high energies – visible in the presented data and previously published for other values of x [96, 97, 100]– seems to favor a description of the excitations in terms of the diffusive model, without the need to introduce propagating modes (compare figures 5.2, 5.3 and 5.13). In the diffusive model, the peak splitting is caused by the interplay between the momentum-space anisotropies associated with the Landau damping and the magnetic correlation length, both of which follow naturally from the band structure of the iron pnictides.

It is interesting to note that a similar discussion regarding the existence or not of propagating modes took place also in the context of a much simpler material, namely, bcc iron (see, for instance, references [112] and [113]). In that case, claims for the existence of propagating modes at low energies followed from observations of splitting in the constant-energy cuts of the INS data similar to the present case. It was subsequently shown that the nature of the damping in an itinerant ferromagnet, where $\Gamma_q \rightarrow 0$ as $q \rightarrow 0$, can result in a splitting that resembles a spin-wave dispersion [113]. In the ferromagnetic case, energy cuts at constant-momentum should show an inelastic peak in the ballistic model, whereas no such peak will be observed in the diffusive model. In the present case of paramagnetism in the stripe AFM ordered phase, one can see (figure 5.16) that both the ballistic and purely

diffusive models produce an inelastic peak in the constant-momentum energy scan. Thus, unlike the ferromagnetic case, the presence or absence of an inelastic peak in the spectrum cannot discern between the two models.

The excitations in the paramagnetic phase of the parent BaFe_2As_2 compound have been described using a $J_1 - J_2$ Heisenberg model combined with a phenomenological momentum-dependent damping function. This approach was able to describe the spin fluctuations close to the zone boundary only after allowing for tetragonal symmetry-breaking, as discussed in reference [96]. As described above, this “nematic spin fluid” model is called into question since the proposed model should lead to large changes in the low energy anisotropy of the spin fluctuations below T_N , which are not observed. In order to describe the peculiar transverse splitting, the authors chose a strongly anisotropic form for the Landau damping that resulted in large damping along the longitudinal direction and small damping in the transverse direction. This choice effectively washes out the longitudinal spin waves, leading to the split transverse modes. In my notation, the authors chose $\eta_r < -1$ meaning that the damping function has a saddle point around \mathbf{Q}_{AFM} , rather than a minimum, as one would expect. While similar in spirit to the approach considered here, the model used here does not require local symmetry breaking in the paramagnetic state. Note, however, that the analysis here does not preclude the existence of a nematic phase in the iron pnictides. To probe the nematic phase, it would be more appropriate to perform INS measurements in detwinned samples (see, for instance reference [114] and also [115, 116]).

Finally, I comment on the role of incommensuration of the SDW ordering vector. In reference [103], first principles calculations suggest that an incommensurability is present for the parent compound BaFe_2As_2 . It was then proposed that the high-energy peak splitting would be nothing but a manifestation of this incommensurability. If indeed the magnetism in the iron pnictides is of itinerant nature, then it is reasonable to expect, on general grounds, the development of incommensurability at some critical doping (see the seminal work of Rice [117]).

Subsequent to those predictions, static incommensurability was indeed observed in a narrow range of doping concentrations in the $\text{Ba}(\text{Fe}_{1-x}\text{Co}_x)_2\text{As}_2$ system.[63] The incommensurability is observed to develop in a first-order fashion with doping concentration.[63] However, in the INS data presented here for the under-doped $\text{Ba}(\text{Fe}_{0.953}\text{Co}_{0.047})_2\text{As}_2$, as well as in the previously presented data for the parent [96] and optimally doped $\text{Ba}(\text{Fe}_{0.926}\text{Co}_{0.074})_2\text{As}_2$ [97], the high-energy splitting of the inelastic peaks occurs at roughly the same energy $E_{\text{split}} \approx 80$ meV and momentum in both the commensurate AFM ordered state and the PM state. Thus, it is unlikely that the transverse splitting is associated with any instability towards incommensurate order.

5.4.2 Low-energy triple-axis

Figure 5.18 shows the locations in phase space of the triple-axis measurements, the fitting parameters for both the damped spin wave and diffusive models in equations (4.29) and (4.39), plus a χ^2 measure of the goodness-of-fit for these two models, and the composition-dependence of the low-energy spectral weight. For $x = 0.015$, the damped spin wave model is the best and $\alpha/\Delta = 0.37(8)$ is consistent with underdamped dynamics. For intermediate composition, $x = 0.033$, both models are of comparable quality. As shown in figure 5.18 (c), within the damped spin wave model $\alpha/\Delta > 1$ and the dynamics have become overdamped causing the spin gap to disappear. In the limit where $\alpha/\Delta \gg 1$, the overdamped spin wave model also takes on a relaxational form with $\Gamma_s = \Delta^2/\alpha$; as shown in figure 5.18 (c) and (d) Γ_s , Γ , and the effective magnetic energy, $E_{\text{SF}} = 1/\gamma$, decrease as the critical concentration for which the AFM order is fully suppressed is approached, as indicated by vanishing Δ_{SDW} . As seen in figure 5.17 (k-o) the excitation becomes increasingly two-dimensional with x as captured by the damped spin-wave model parameter v_z , figure 5.18 (e). For $x = 0.040, 0.047$, and 0.055 , the diffusive model becomes the better fit, as the smaller correlation length [figure 5.18 (f)] is able to capture the reciprocal space broadening of the in-plane spin fluctuations. A

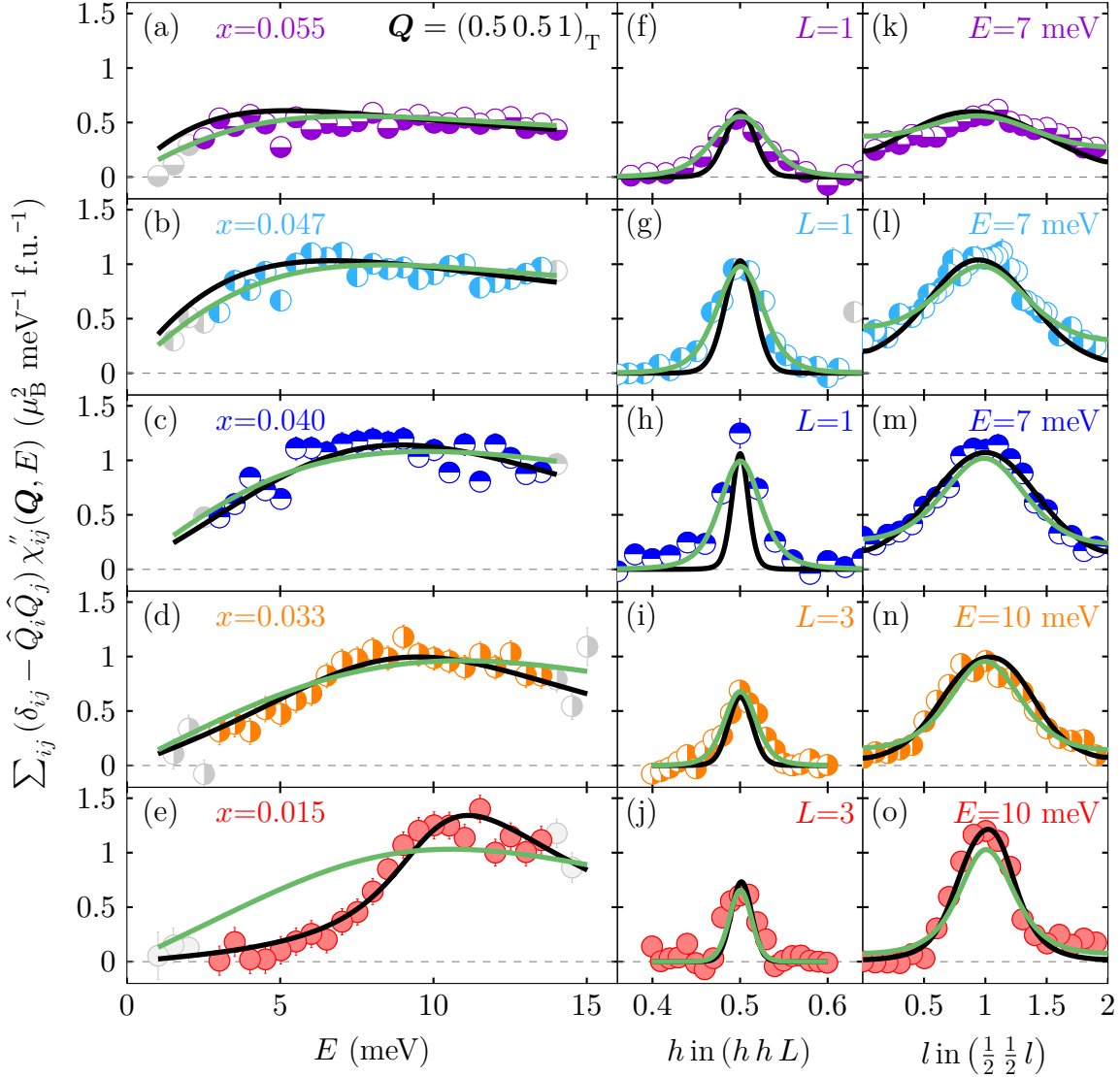


FIGURE 5.17. Background subtracted INS intensity of $\text{Ba}(\text{Fe}_{1-x}\text{Co}_x)_2\text{As}_2$ corrected for the Bose thermal population factor and the Fe^{2+} single-ion magnetic form factor plus best fit lines to the diffusive (light green lines) and the damped spin-wave (black lines) models. (a-e) Constant- \mathbf{Q} energy scans at $\mathbf{Q}_{\text{AFM}} = (0.5, 0.5, 1)$ for five compositions. (f-h) Constant- E \mathbf{Q} scans in the $[h, h, 0]$ -direction across $\mathbf{Q}_{\text{AFM}} = (0.5, 0.5, 1)$ at $E = 7$ meV. (i-j) Constant- E \mathbf{Q} scans in the $[h, h, 0]$ -direction across $\mathbf{Q}_{\text{AFM}} = (0.5, 0.5, 3)$ at $E = 10$ meV. (k-m) Constant- E \mathbf{Q} scans in the $[0, 0, l]$ -direction, perpendicular to the Fe layer, across $\mathbf{Q}_{\text{AFM}} = (0.5, 0.5, 1)$ at $E = 7$ meV. (n-o) Constant- E \mathbf{Q} scans in the $[0, 0, l]$ -direction across $\mathbf{Q}_{\text{AFM}} = (0.5, 0.5, 1)$ at $E = 10$ meV. Light gray symbols represent measured intensity which was excluded from fitting due to concerns with the validity of background estimates at those points.

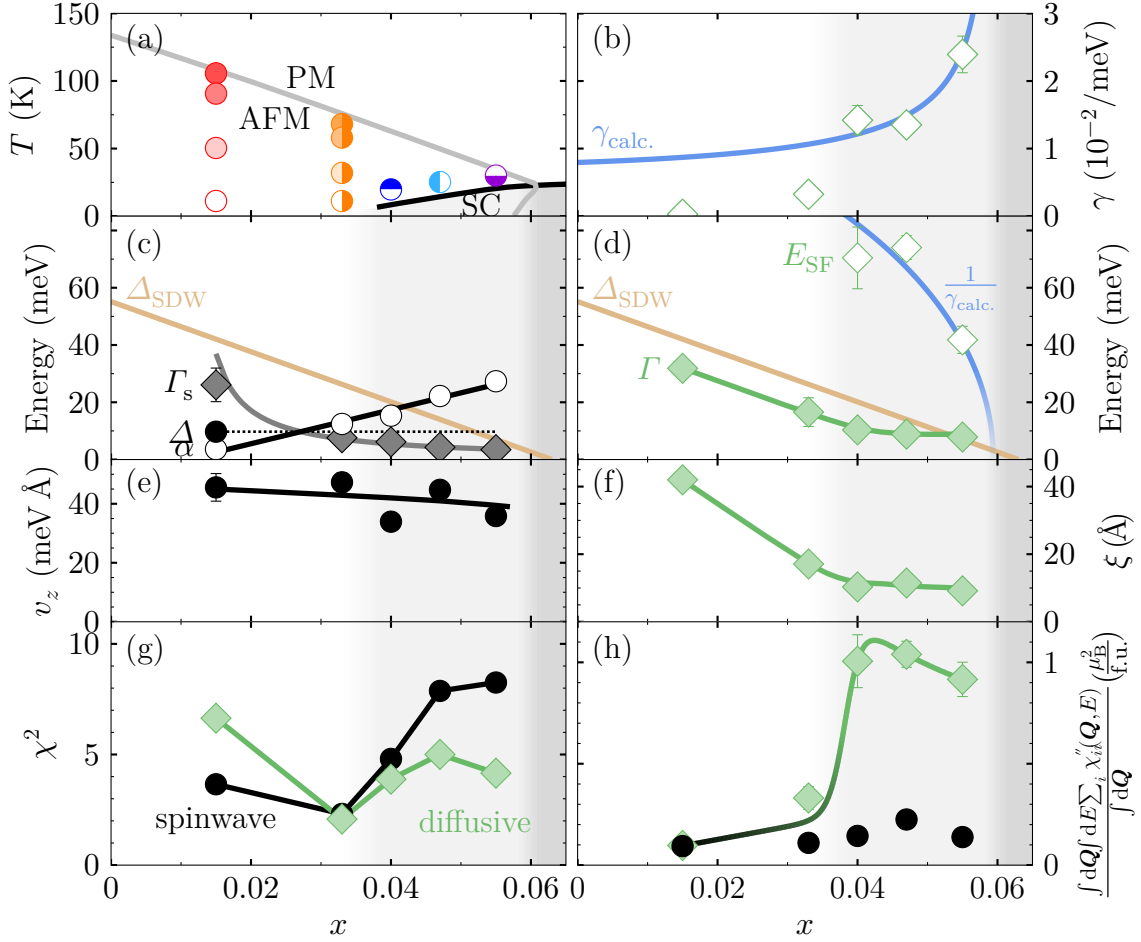


FIGURE 5.18. (a) Phase diagram of $\text{Ba}(\text{Fe}_{1-x}\text{Co}_x)_2\text{As}_2$ showing regions of AFM order, superconductivity, and their coexistence; colored symbols show the locations in phase-space of the measurements performed in this study. (b-f) Select model parameters as a function of composition for the diffusive (light green diamonds) and spin wave (black circles) models. All data points shown in (b-f) were determined at the lowest temperature indicated in (a), and the lightly shaded background indicates compositions which exhibit SC at low temperature. (b) Diffusive-model Landau damping γ and the corresponding theoretical prediction. (c) Spin-wave model parameters: spin gap Δ (filled circle), damping α (open circles), and $\Gamma_s = \Delta^2/\alpha$ (filled diamonds). (d) Spin relaxation characteristic energy Γ (filled), effective magnetic energy $E_{\text{SF}} = 1/\gamma$ (open) of the diffusive model, and an estimate for the SDW gap Δ_{SDW} (solid tan line). (e) Inter-plane spin wave velocity. (f) Diffusive model correlation length ξ . (g) Residual χ^2 for each fit model. (h) Spectral weight of the $(0.5, 0.5, 1)$ excitation. The spectral weight is the \mathbf{Q} -averaged energy integration of the trace of the imaginary component of the magnetic susceptibility tensor. The averaging-range in \mathbf{Q} here is $0 < H < 1$, $0 < K < 1$, $0 < L < 2$; the energy integration is over the range $0 < E < 35$ meV. All error bars represent the combined errors for all function parameters. The solid green and black lines in (c-h) are guides to the eye.

comparison of the residual for each fit model in figure 5.18 (g) clearly shows the crossover from spin-wave- to diffusive-like excitations. In figure 5.18 (h), a sharp increase in the low-energy spectral weight (< 35 meV) coincides with the appearance of superconductivity.

From figure 5.18, regardless of the model used to fit the triple-axis data, it is clear that upon approaching the optimally-doped composition, damping becomes stronger, the spin fluctuations acquire a more two-dimensional character, and the energy scale associated with these fluctuations (Γ or Γ_s) become smaller. These features, as well as the crossover from spin-wave to diffusive excitations, are consistent with a suppression of the spin density wave gap Δ_{SDW} upon doping. In figure 5.18 (c-d), the experimentally determined suppression of Δ_{SDW} obtained by combining the doping evolution of the zero-temperature ordered magnetic moment, μ , from reference [62] with the optical conductivity data of reference [118] is shown, using the fact that $\Delta_{\text{SDW}} \propto \mu$ [62, 71, 110, 119].

Based on this information, one can conclude that the presence of sub-gap spectral weight which appears with either an increase in temperature or cobalt composition is driven entirely by damping. For the temperature-driven transition, an increase of damping close to T_N is found. Given the similarities between the spin fluctuations above and below T_N near optimal doping and the smallness of the spin-wave gap Δ_{SDW} in this regime [see figure 5.18 (c)], the fitted damping rate γ and the calculated Landau damping γ_{calc} due to the decay of spin excitations into particle-hole pairs near the Fermi level are compared in figure 5.18 (b). Using a simplified two-band model, which was previously shown to successfully capture the coexistence of superconductivity and antiferromagnetism [71, 110, 119], the Landau damping is given by $\gamma_{\text{calc}}^{-1} \propto |\mathbf{v}_e \times \mathbf{v}_h|$ [120], where \mathbf{v}_e and \mathbf{v}_h are respectively the Fermi velocities of the electron and hole pockets at the hot spots (i.e., points connected by the AFM ordering vector \mathbf{Q}_{AFM}). Upon Co substitution, electrons are introduced into the system, making the hole pocket shrink and the electron pocket expand. As revealed by ARPES [65], this moves the hot spots, making their Fermi velocities become nearly parallel around optimal doping.

As a result, $\gamma_{\text{calc}}^{-1} \rightarrow 0$, as seen experimentally. Note that γ_{calc} describes well the data only in compositions near optimal doping, indicating that in slightly-doped compositions the damping comes from another mechanism, such as magnon-magnon interactions.

5.5 Ba(Fe_{1-x}Co_x)₂As₂ in the Superconducting State

In addition to the normal state data discussed in sections 5.1.2, 5.2.3 and 5.3.2, triple axis data were also collected for Ba(Fe_{0.960}Co_{0.040})₂As₂, Ba(Fe_{0.953}Co_{0.047})₂As₂, and Ba(Fe_{0.945}Co_{0.055})₂As₂ in their combined superconducting and antiferromagnetic states.

In previous discussions of the normal state data it was noted that convoluted fitting was performed on only a subset of the available data for each Ba(Fe_{1-x}Co_x)₂As₂ composition, namely that presented in figures 5.8, 5.12, 5.14 and 5.17. Despite this limitation, as shown by the green lines in figures 5.19 to 5.24, the best-fit normal state parameters for the diffusive model, equation (4.39), well describe the measured normal state intensity throughout the sampled volume of reciprocal space. The reason for this is a distinct lack of a dispersive mode in the normal state data and, therefore, a structurally simple model (i.e., the intensity varies smoothly and has few inflection points). The data for each composition in the superconducting state is decidedly more complex as is the empirical model, equation (4.54), and, as a result, the entirety of the collected data must be fit for each composition in order to capture the full complexity present. Simulated intensity based on the best-fit parameters for the empirical resonance model, equation (4.54), obtained by performing resolution convoluted Levenberg-Marquardt fitting to the entire measured dataset for each composition is shown as red lines in each of figures 5.19 to 5.24 for Ba(Fe_{0.960}Co_{0.040})₂As₂, Ba(Fe_{0.953}Co_{0.047})₂As₂, and Ba(Fe_{0.945}Co_{0.055})₂As₂, respectively. By comparing the best-fit simulated intensity in the normal and superconducting states the superconducting resonance is clear for each composition, as is its dispersion.

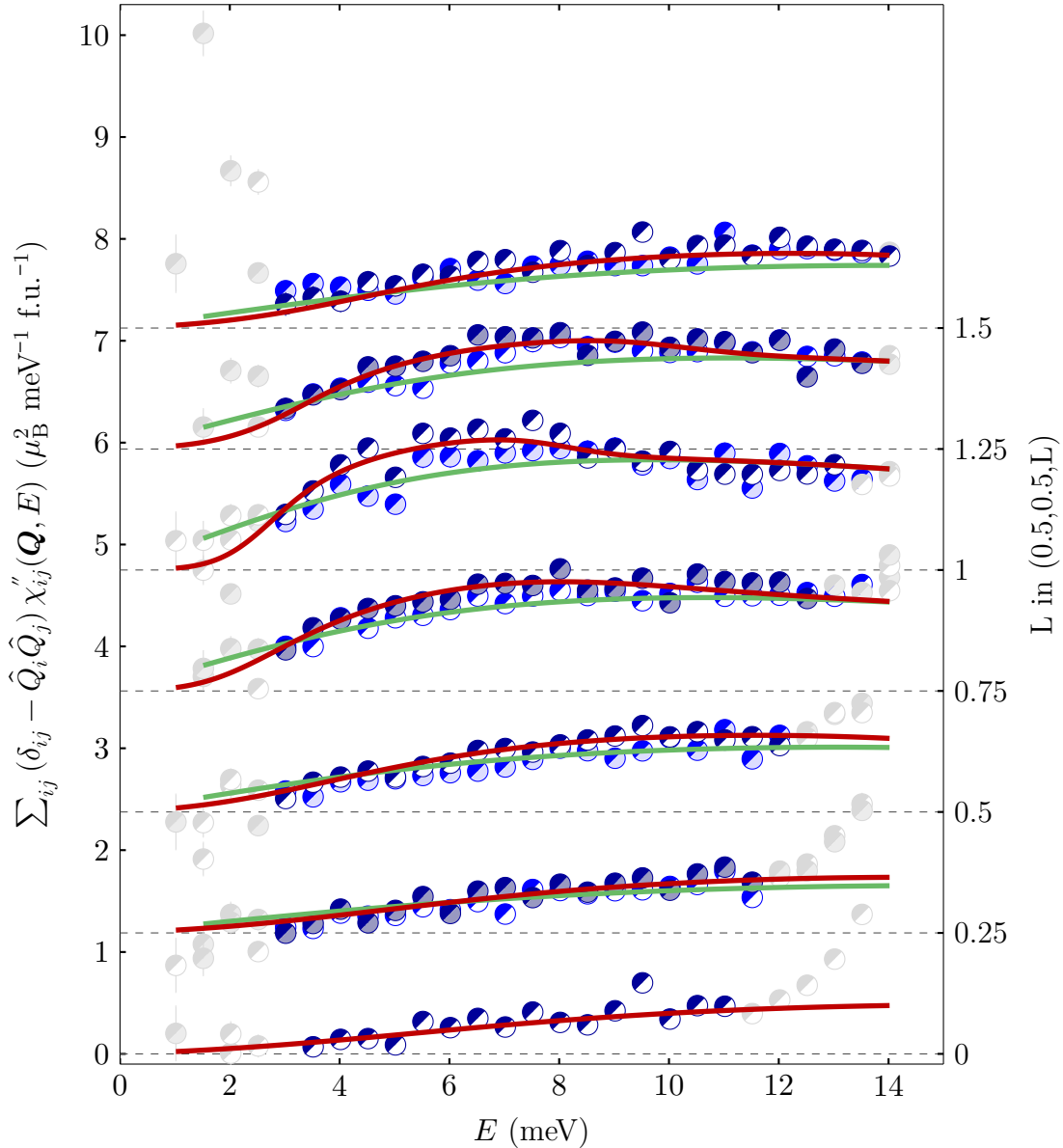


FIGURE 5.19. HB3 measured $\text{Ba}(\text{Fe}_{0.960}\text{Co}_{0.040})_2\text{As}_2$ triple-axis data after background subtraction and correction for the Bose thermal population factor. The data are energy spectra performed at $(\frac{1}{2}, \frac{1}{2}, L)$ with intensity offset by the L value, indicated by the right hand scale. Dark symbols are data collected at 2.62(16) K in the superconducting and antiferromagnetic state, light symbols are data collected at 19.8(2) K in the non-superconducting antiferromagnetic state. Green lines are global convoluted fits to the diffusive model to the normal state data, red lines are global convoluted fits to the modified superconducting diffusive model to the superconducting state data. Gray data correspond to measured intensity which has been excluded from fitting routines due to inadequate background estimation.

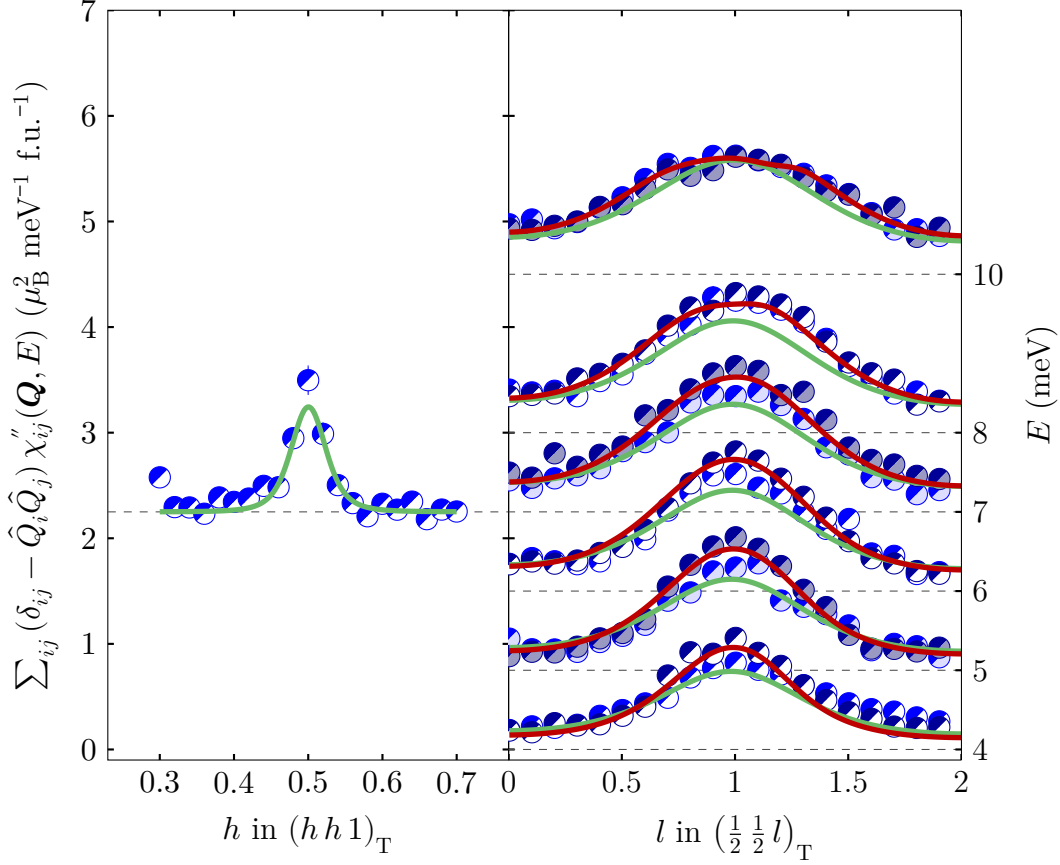


FIGURE 5.20. HB3 measured $\text{Ba}(\text{Fe}_{0.960}\text{Co}_{0.040})_2\text{As}_2$ triple-axis data after background subtraction and correction for the Bose thermal population factor. The data correspond to constant energy scans performed in the $[h h 1]$ and $[00 l]$ directions for the left and right panels, respectively, with intensity offset by the energy transfer, E , as indicated by the right hand scale. Dark symbols are data collected at 2.62(16) K in the superconducting and antiferromagnetic state, light symbols are data collected at 19.8(2) K in the non-superconducting antiferromagnetic state. Green lines are global convoluted fits to the diffusive model to the normal state data, red lines are global convoluted fits to the modified superconducting diffusive model to the superconducting state data.

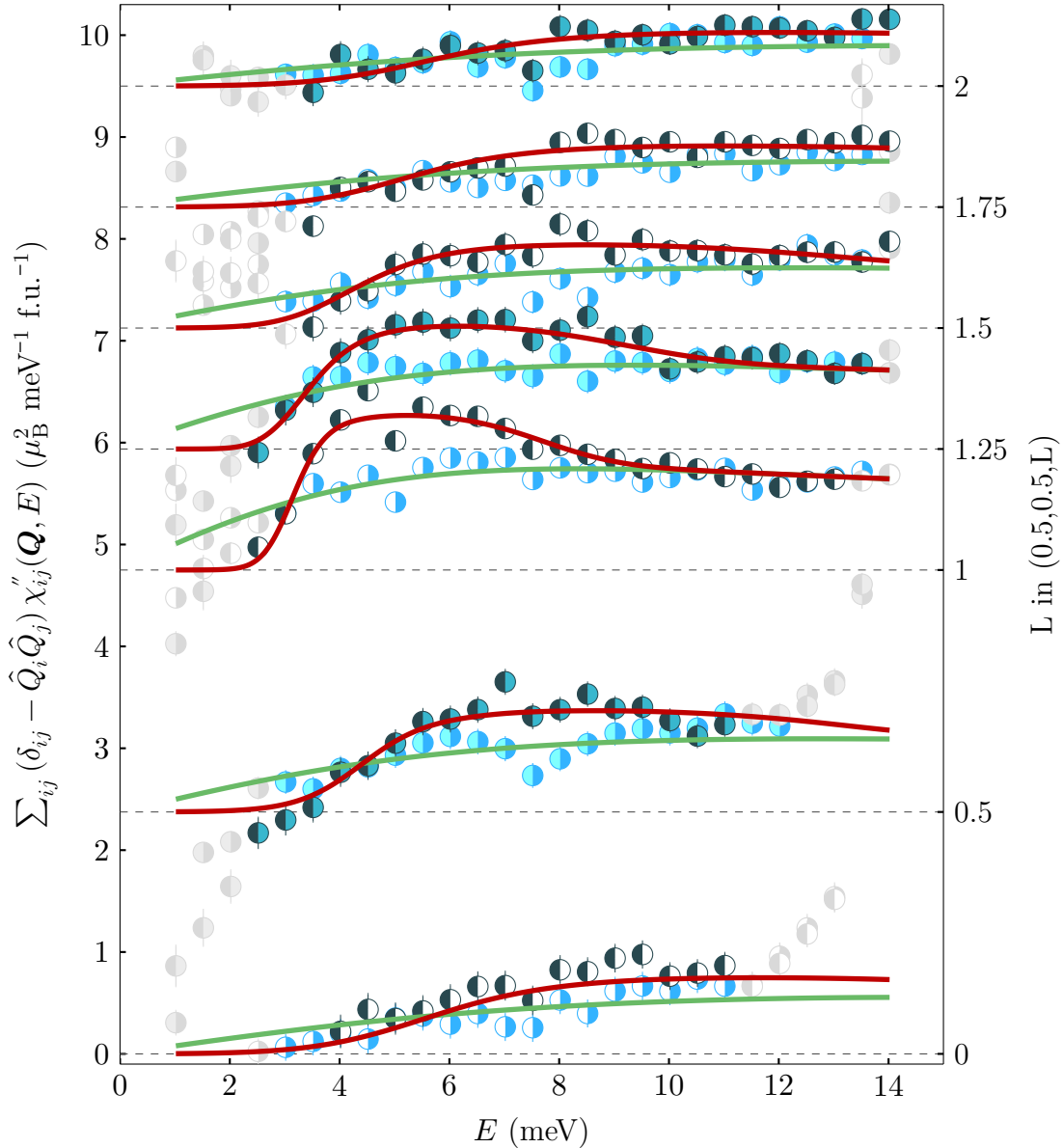


FIGURE 5.21. HB3 measured $\text{Ba}(\text{Fe}_{0.953}\text{Co}_{0.047})_2\text{As}_2$ triple-axis data after background subtraction and correction for the Bose thermal population factor. The data are energy spectra performed at $(\frac{1}{2}, \frac{1}{2}, L)$ with intensity offset by the L value, indicated by the right hand scale. Dark symbols are data collected at 4.30(2) K in the superconducting and antiferromagnetic state, light symbols are data collected at 25.3(4) K in the non-superconducting antiferromagnetic state. Green lines are global convoluted fits to the diffusive model to the normal state data, red lines are global convoluted fits to the modified superconducting diffusive model to the superconducting state data. Gray data correspond to measured intensity which has been excluded from fitting routines due to inadequate background estimation.

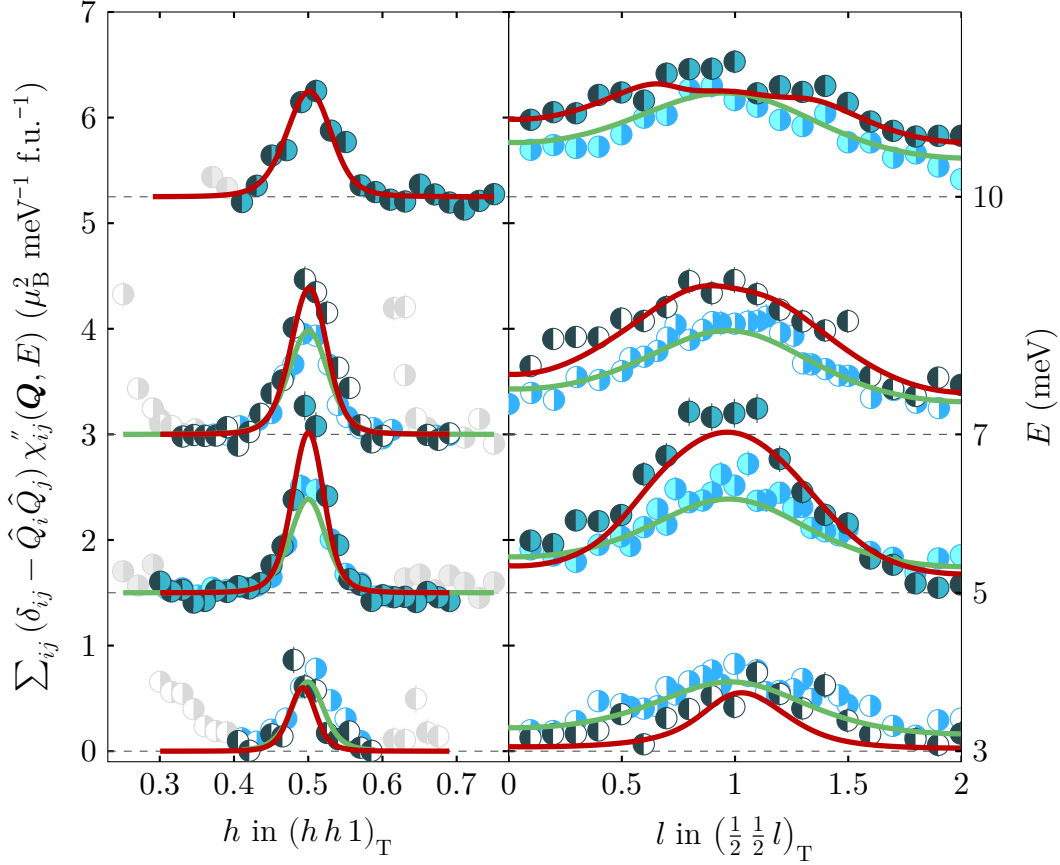


FIGURE 5.22. HB3 measured $\text{Ba}(\text{Fe}_{0.953}\text{Co}_{0.047})_2\text{As}_2$ triple-axis data after background subtraction and correction for the Bose thermal population factor. The data correspond to constant energy scans performed in the $[h h 1]$ and $[0 0 l]$ directions for the left and right panels, respectively, with intensity offset by the energy transfer, E , as indicated by the right hand scale. Dark symbols are data collected at 4.30(2) K in the superconducting and antiferromagnetic state, light symbols are data collected at 25.3(4) K in the non-superconducting antiferromagnetic state. Green lines are global convoluted fits to the diffusive model to the normal state data, red lines are global convoluted fits to the modified superconducting diffusive model to the superconducting state data. Gray data correspond to measured intensity which has been excluded from fitting routines due to inadequate background estimation.

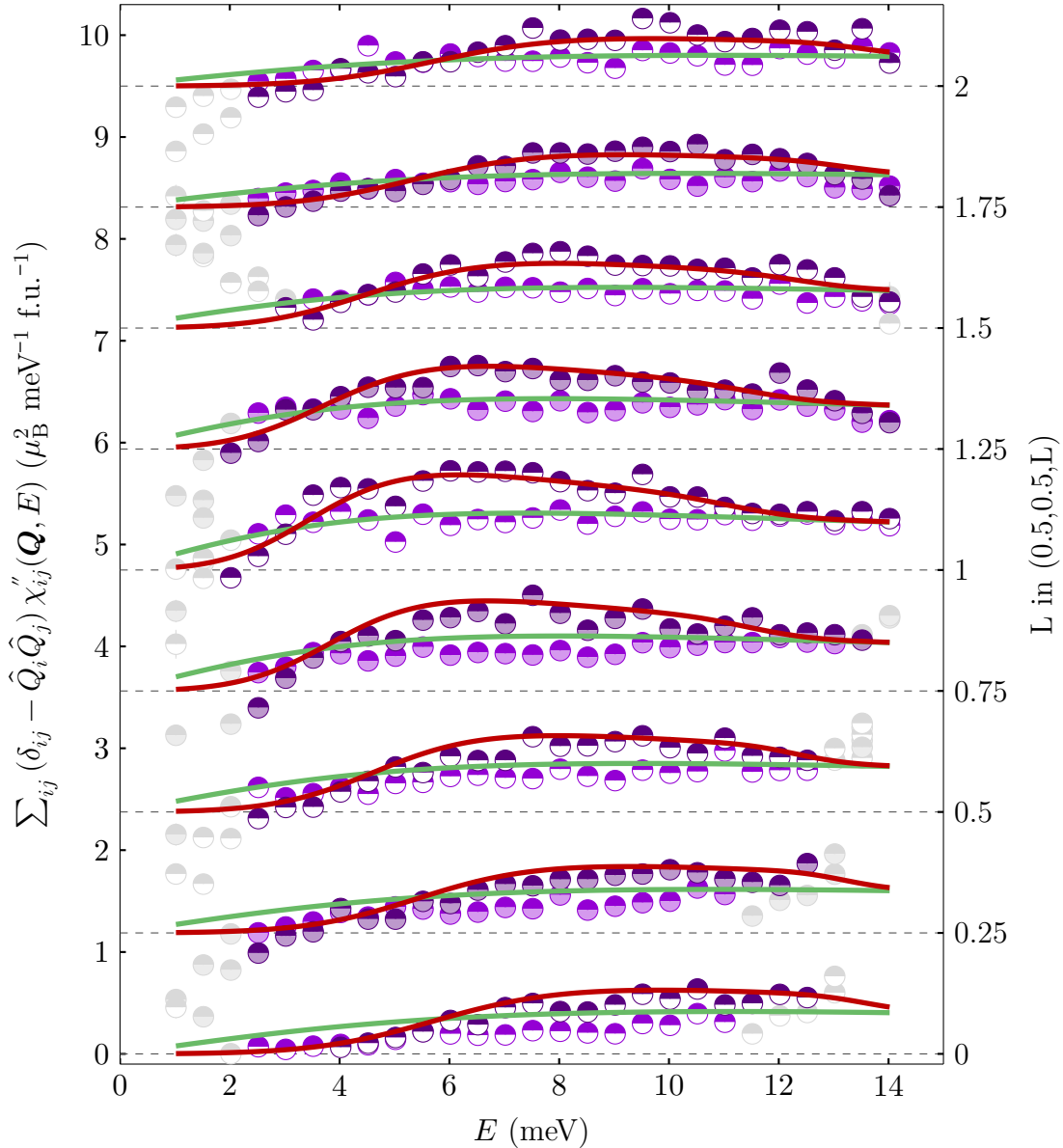


FIGURE 5.23. HB3 measured $\text{Ba}(\text{Fe}_{0.945}\text{Co}_{0.055})_2\text{As}_2$ triple-axis data after background subtraction and correction for the Bose thermal population factor. The data are energy spectra performed at $(\frac{1}{2}, \frac{1}{2}, L)$ with intensity offset by the L value, indicated by the right hand scale. Dark symbols are data collected at 7.97(3) K in the superconducting and antiferromagnetic state, light symbols are data collected at 30.0(3) K in the non-superconducting antiferromagnetic state. Green lines are global convoluted fits to the diffusive model to the normal state data, red lines are global convoluted fits to the modified superconducting diffusive model to the superconducting state data. Gray data correspond to measured intensity which has been excluded from fitting routines due to inadequate background estimation.

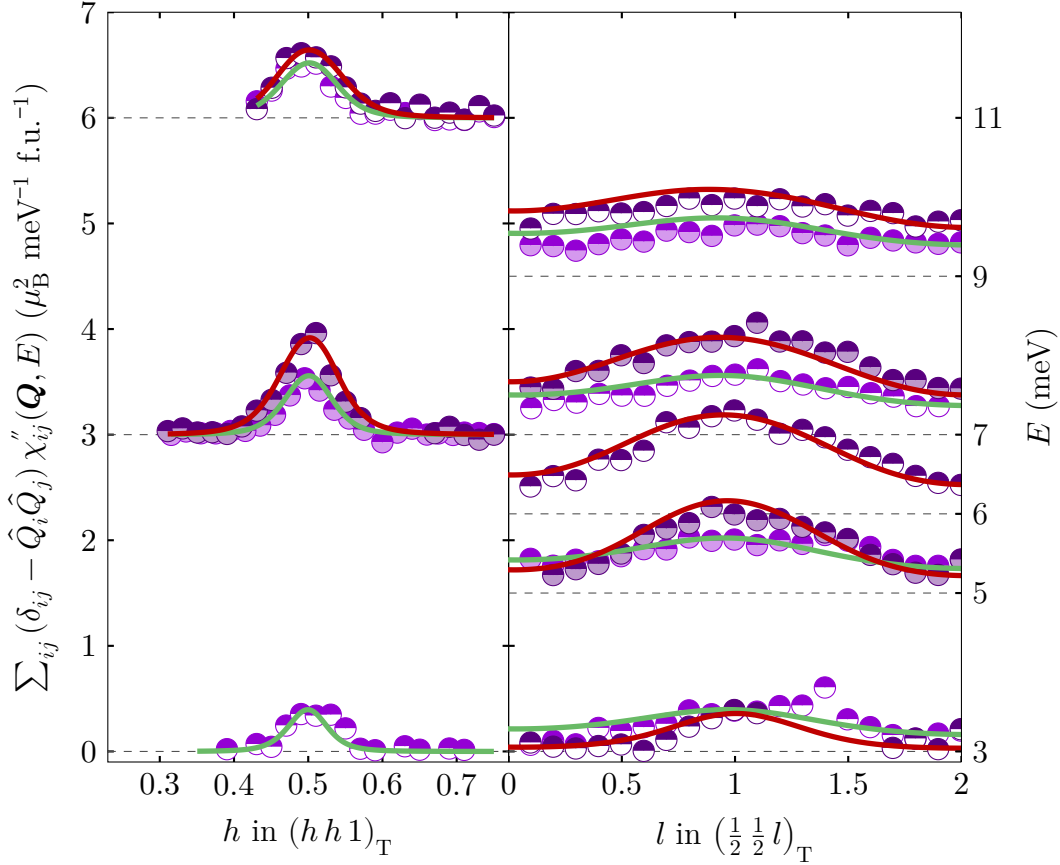


FIGURE 5.24. HB3 measured $\text{Ba}(\text{Fe}_{0.945}\text{Co}_{0.055})_2\text{As}_2$ triple-axis data after background subtraction and correction for the Bose thermal population factor. The data correspond to constant energy scans performed in the $[h h 1]$ and $[00 l]$ directions for the left and right panels, respectively, with intensity offset by the energy transfer, E , as indicated by the right hand scale. Dark symbols are data collected at $7.97(3)$ K in the superconducting and antiferromagnetic state, light symbols are data collected at $30.0(3)$ K in the non-superconducting antiferromagnetic state. Green lines are global convoluted fits to the diffusive model to the normal state data, red lines are global convoluted fits to the modified superconducting diffusive model to the superconducting state data.

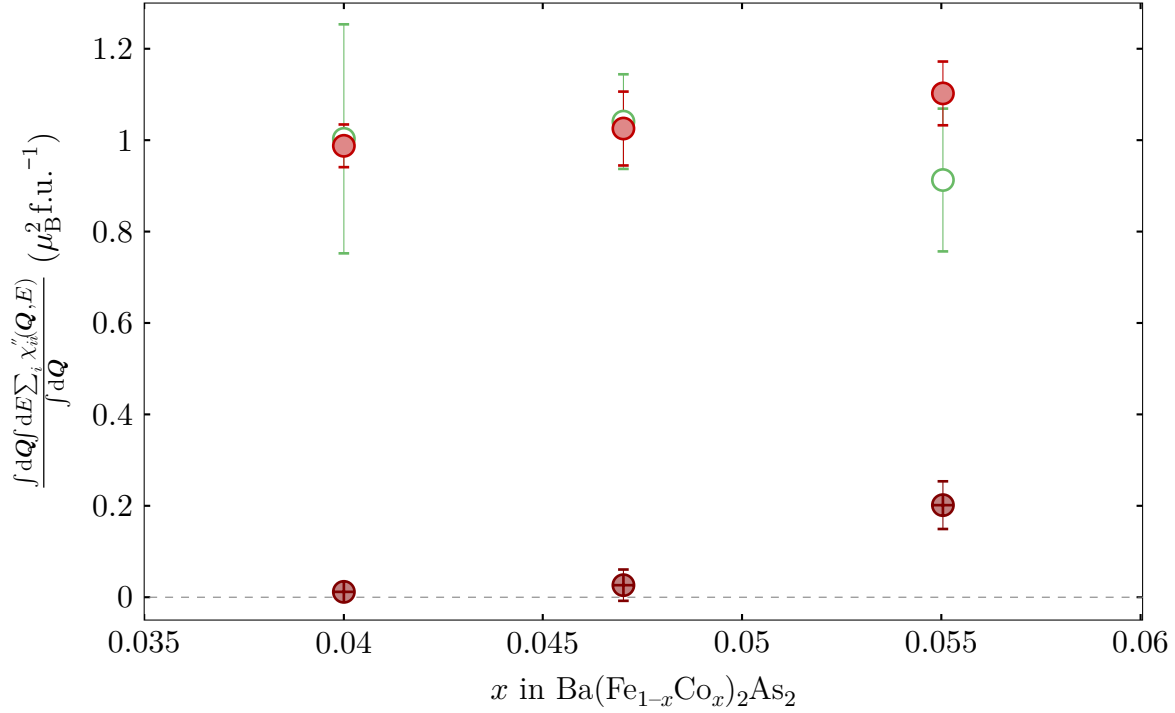


FIGURE 5.25. Integrated spectral weight as a function of x in $\text{Ba}(\text{Fe}_{1-x}\text{Co}_x)_2\text{As}_2$ for normal state data (○), superconducting state data (●), and their positive difference (⊕). While there is no statistically significant difference between the normal state and superconducting state spectral weight the spectral weight of their positive difference, which is a measure of the moving spectral weight due to the superconducting resonance, increases with x in $\text{Ba}(\text{Fe}_{1-x}\text{Co}_x)_2\text{As}_2$.

One open question about the $\text{Ba}(\text{Fe}_{1-x}\text{Co}_x)_2\text{As}_2$ superconducting resonance, and that found in and the other iron pnictides, is whether it is a redistribution of normal state spectral weight or is additional spectral weight due to a new excitation that only appears with superconductivity. One can address this open question by calculating the total spectral weight of the superconducting spin fluctuations. As shown in figure 5.25 there is no statistically significant difference in the fluctuating moment spectral weight between the normal state and superconducting state for the three compositions which exhibit a coexistence of superconductivity and antiferromagnetism. This is a clear indication that the superconducting resonance is a redistribution of the normal state spectral weight and not a new excitation that appears along with superconductivity.

The integrated spectral weight gives the energy-integrated total of the average intensity throughout the first Brillouin zone. The fact that the difference of the superconducting and normal state spectral weight is zero within statistical uncertainty does not necessarily indicate a featureless difference throughout the Brillouin zone. To look for, e.g., a dispersion in the resonance, it's helpful to look at the difference between superconducting and normal state data as well as best-fit models. Figure 5.26 has been constructed by binning collected data in the $(\frac{1}{2} \frac{1}{2} l)_T - E$ plane and taking the difference between the binned superconducting state data and the binned normal state data, it also contains simulated data on the same planes which is the difference between the superconducting model and normal state model. The black lines in figure 5.26 represent for each composition the maximum intensity in the simulated difference as a function of energy for each l value, and indicate the resonance dispersion. From the intensity and dispersion of the resonance, the resonance transitions from three dimensional (i.e., well localized in momentum-energy space) at $\text{Ba}(\text{Fe}_{0.960}\text{Co}_{0.040})_2\text{As}_2$ to nearly two dimensional at $\text{Ba}(\text{Fe}_{0.945}\text{Co}_{0.055})_2\text{As}_2$ which is reminiscent of the normal state excitation progression from three dimensional at $\text{Ba}(\text{Fe}_{1-x}\text{Co}_x)_2\text{As}_2$ to two dimensional at optimal-doped $\text{Ba}(\text{Fe}_{1-x}\text{Co}_x)_2\text{As}_2$.

Another way of examining the superconducting resonance is to find the magnitude of the spectral weight which moves as a result of the appearance of superconductivity. To do so, one can take the difference of the superconducting state model minus the normal state model and integrate only that part which is positive. This resonance spectral weight is shown in figure 5.25 and clearly increases as a function of cobalt concentration. Because the resonance spectral weight is a measure of the fluctuating moment which is affected by the appearance of superconductivity, it is interesting to compare it to the static moment lost to competition between antiferromagnetism and superconductivity. By examining neutron diffraction order parameter plots in references [62, 121, 122] it is possible to determine an estimate for the ordered moment lost due to the presence of superconductivity, $\Delta\mu$. Plotting the resonance

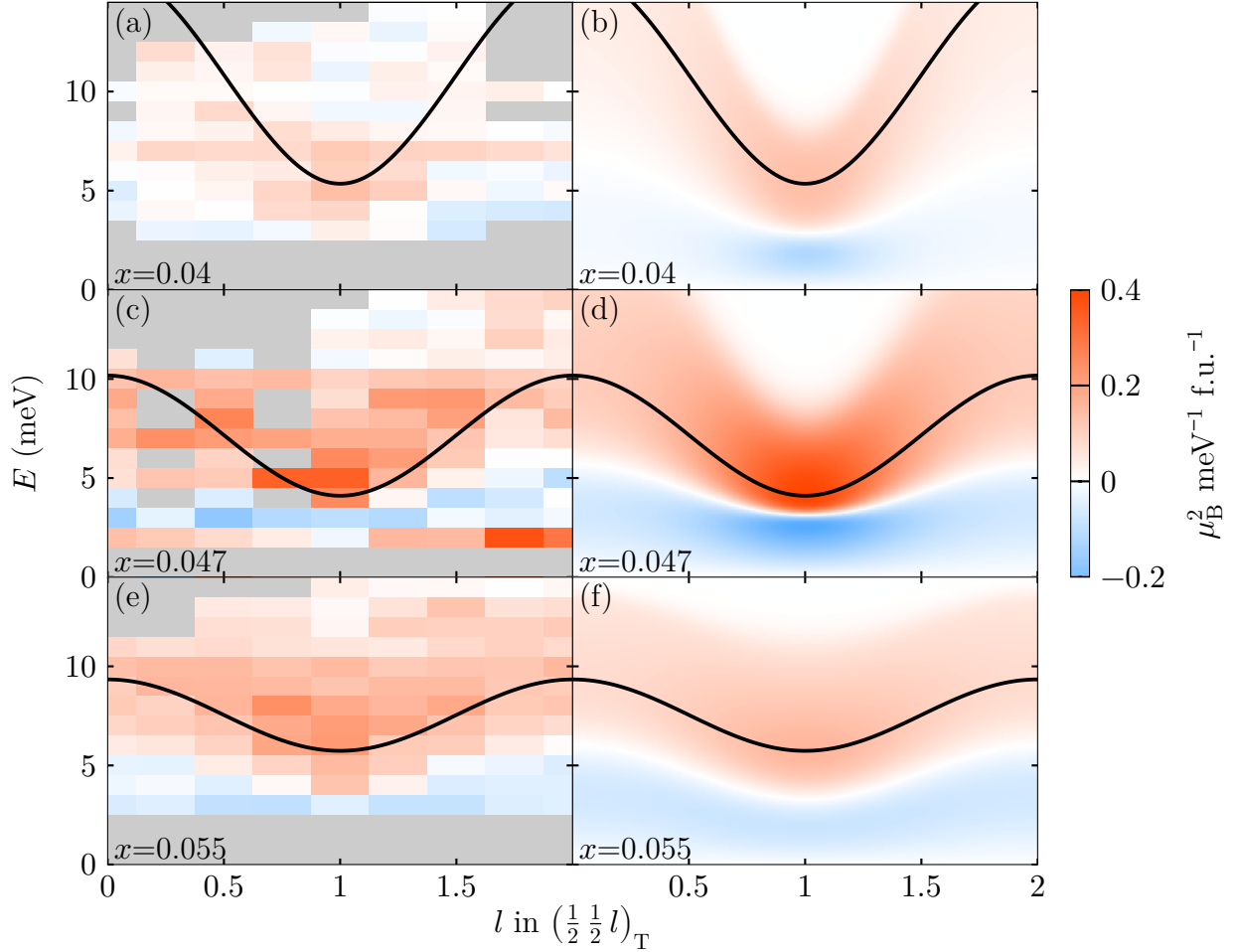


FIGURE 5.26. For each composition available superconducting state and normal state data was binned in the $(\frac{1}{2} \frac{1}{2} l)_T - E$ plane independently with bin centers and widths chosen to allow for subtraction of the two binned data sets. Panel (a) shows the subtracted binned data for $\text{Ba}(\text{Fe}_{0.960}\text{Co}_{0.040})_2\text{As}_2$ while (b) shows the difference between superconducting and normal state models for the $\text{Ba}(\text{Fe}_{0.960}\text{Co}_{0.040})_2\text{As}_2$ best-fit parameters. Panel (c) shows the subtracted binned data for $\text{Ba}(\text{Fe}_{0.953}\text{Co}_{0.047})_2\text{As}_2$ while (d) shows the difference between superconducting and normal state models for the $\text{Ba}(\text{Fe}_{0.953}\text{Co}_{0.047})_2\text{As}_2$ best-fit parameters. Panel (e) shows the subtracted binned data for $\text{Ba}(\text{Fe}_{0.945}\text{Co}_{0.055})_2\text{As}_2$ while (f) shows the difference between superconducting and normal state models for the $\text{Ba}(\text{Fe}_{0.945}\text{Co}_{0.055})_2\text{As}_2$ best-fit parameters. In each panel the color gray represents a lack of data to perform the subtraction and the black solid line represents the dispersion of the resonance derived from the difference between the best-fit models for each composition.

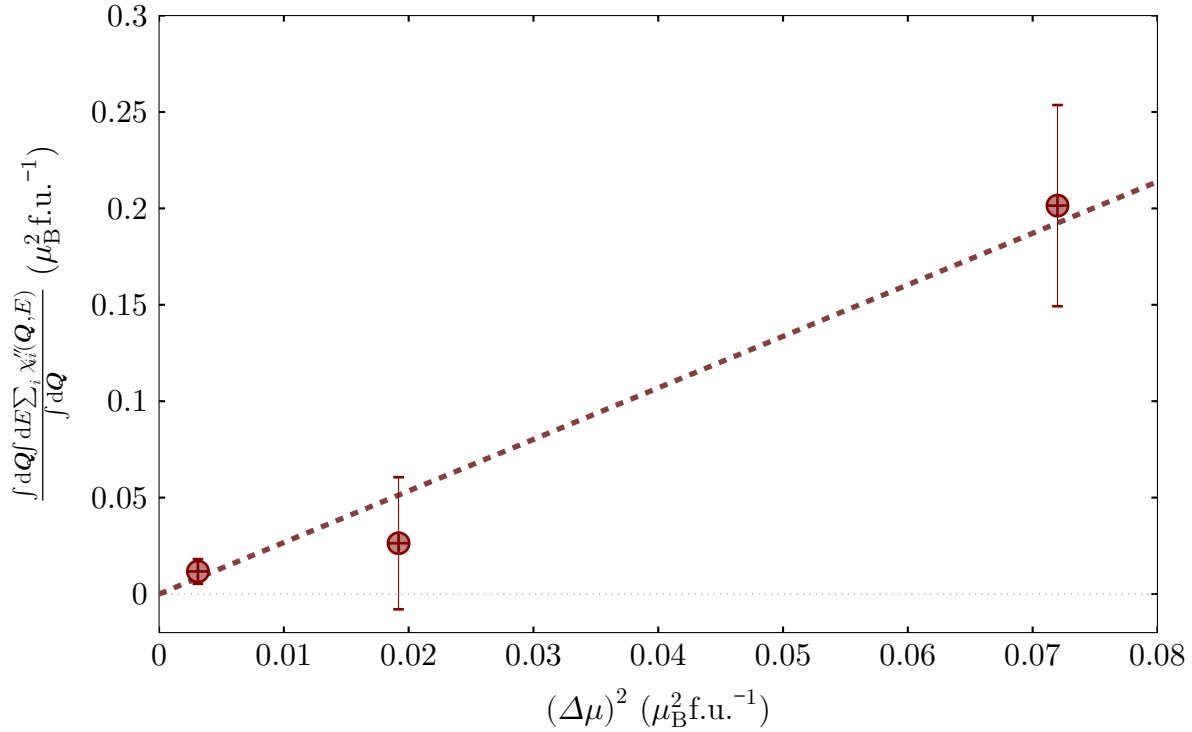


FIGURE 5.27. Integrated spectral weight as a function of $(\Delta\mu)^2$ for the moving intensity as a result of the superconducting resonance (\oplus). Clearly the fluctuating moment which moves to participate in the superconducting resonance is proportional to the missing ordered moment for $\text{Ba}(\text{Fe}_{0.960}\text{Co}_{0.040})_2\text{As}_2$, $\text{Ba}(\text{Fe}_{0.953}\text{Co}_{0.047})_2\text{As}_2$, and $\text{Ba}(\text{Fe}_{0.945}\text{Co}_{0.055})_2\text{As}_2$.

spectral weight versus the square of the lost ordered moment, as in figure 5.27, shows that the two quantities are linearly related to one another.

5.6 $\text{Ba}(\text{Fe}_{1-x}\text{TM}_x)_2\text{As}_2$

In addition to the $\text{Ba}(\text{Fe}_{0.953}\text{Co}_{0.047})_2\text{As}_2$ measurements discussed in section 5.1.1.2, time of flight inelastic neutron scattering measurements have been performed on a number of $\text{Ba}(\text{Fe}_{1-x}\text{TM}_x)_2\text{As}_2$ samples which are non-superconducting, with the ARCS spectrometer and an incident neutron energy of $E_i = 50$ meV. These measurements of representative samples for transition metal substitutions which do not produce bulk superconductivity provide information which may be vital to understanding superconductivity in the iron pnic-

oxide superconductors. Specifically, measurements were performed on $\text{Ba}(\text{Fe}_{0.939}\text{Cr}_{0.061})_2\text{As}_2$, $\text{Ba}(\text{Fe}_{0.925}\text{Mn}_{0.075})_2\text{As}_2$, and $\text{Ba}(\text{Fe}_{0.962}\text{Cu}_{0.028})_2\text{As}_2$ at $T = 5$ K which, for all three compounds, is deep within the stripe orthorhombic and antiferromagnetic phase. Like $\text{Ba}(\text{Fe}_{1-x}\text{Co}_x)_2\text{As}_2$, the orthorhombic distortion in these compounds is too small to be resolved in the ARCS data and the same tetragonal indexing scheme has been utilized.

Background subtracted data for the three non-superconducting compositions at $T = 5$ K as well as $\text{Ba}(\text{Fe}_{0.953}\text{Co}_{0.047})_2\text{As}_2$ at $T = 25$ K is shown in figure 5.28 arranged by the number of protons in the respective dopant atom. The data used to create the slices in each panel of figure 5.28 have been normalized such that the peak intensity in a representative cut across \mathbf{Q}_{AFM} is one, which is why the intensities in each panel in the vicinity of $K \approx 0$ and $5 < E < 10$ meV (where $\mathbf{Q} \approx (\frac{1}{2} \frac{1}{2} 1)$) are equivalent. In each panel $\mathbf{Q} \approx (\frac{1}{2} \frac{1}{2} 3)$ is where $K = 0$ and $20 \lesssim E \lesssim 25$ meV. Because of the coupled nature of E and L in this data, due to only collecting data with $\mathbf{c} \parallel \mathbf{k}_i$, the ratio of intensity at $\mathbf{Q} = (\frac{1}{2} \frac{1}{2} 1)$ to that at $\mathbf{Q} = (\frac{1}{2} \frac{1}{2} 3)$ is related to both the ordered moment direction, through the dipole polarization terms relating $\chi''(\mathbf{Q}, E)$ and $S(\mathbf{Q}, E)$, and purely energy-related properties, like damping. As such, separating the two effects is difficult at best; however, if one assumes that the ordered moment direction is the same for the four samples in figure 5.28 then the only explanation for the different ratio for $\text{Ba}(\text{Fe}_{0.925}\text{Mn}_{0.075})_2\text{As}_2$ is that the damping must be smaller than for $\text{Ba}(\text{Fe}_{0.939}\text{Cr}_{0.061})_2\text{As}_2$, $\text{Ba}(\text{Fe}_{0.953}\text{Co}_{0.047})_2\text{As}_2$, or $\text{Ba}(\text{Fe}_{0.962}\text{Cu}_{0.028})_2\text{As}_2$. Differences in the correlation length along \mathbf{c}^* would modify the ratio of intensity between $L = \text{odd}$ and $L = \text{even}$, and would not contribute to the ratio of $L = 1$ to $L = 3$.

Cuts through the three compositions with similar $L = 1$ to $L = 3$ intensity ratios are shown in figure 5.29. Comparing the intensity ratio of $L = 1$ to $L = 3$ for the three compounds shows that $\text{Ba}(\text{Fe}_{0.962}\text{Cu}_{0.028})_2\text{As}_2$ is very similar to $\text{Ba}(\text{Fe}_{0.953}\text{Co}_{0.047})_2\text{As}_2$, while $\text{Ba}(\text{Fe}_{0.939}\text{Cr}_{0.061})_2\text{As}_2$ is less so; which indicates that the damping in $\text{Ba}(\text{Fe}_{0.962}\text{Cu}_{0.028})_2\text{As}_2$ and $\text{Ba}(\text{Fe}_{0.953}\text{Co}_{0.047})_2\text{As}_2$ are likely similar. Looking at the overall shape of the measured in-

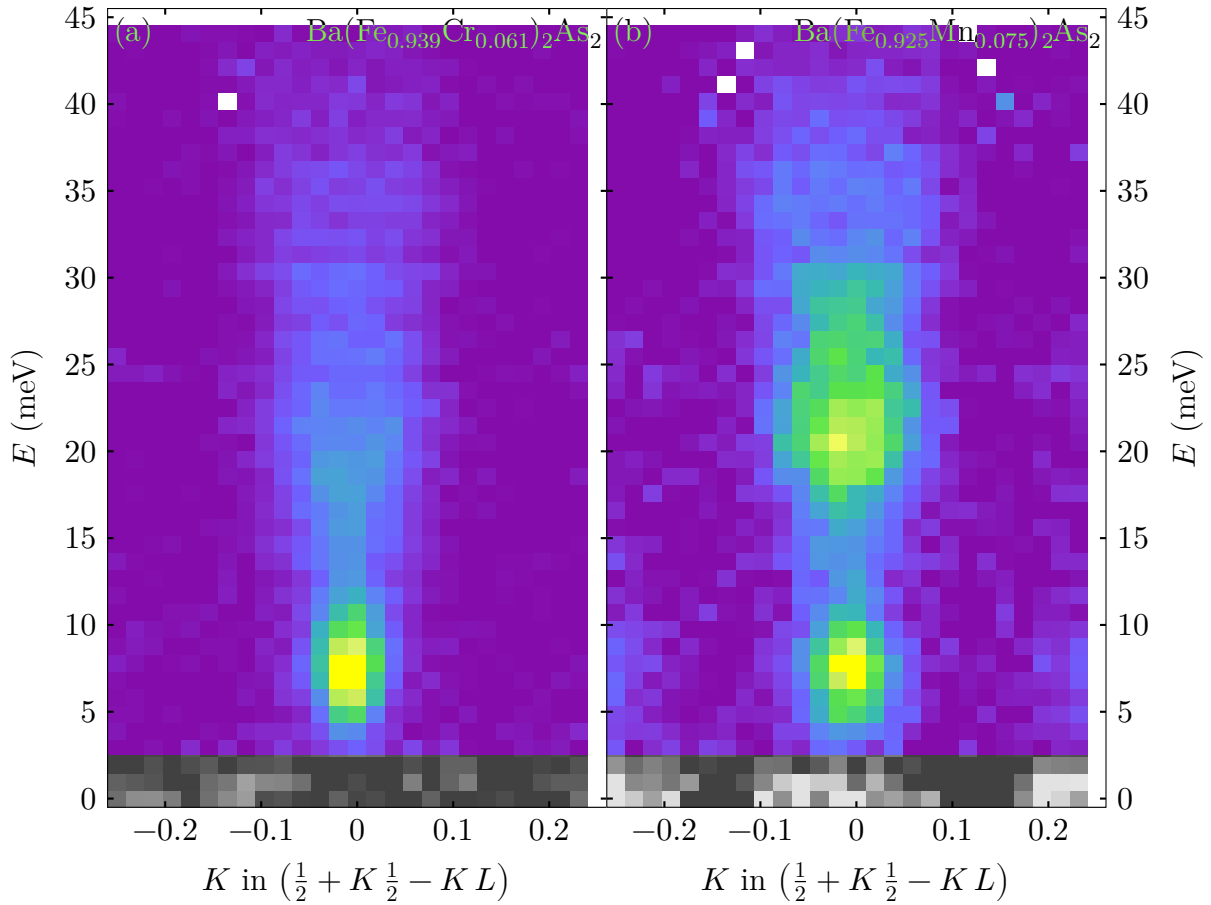


FIGURE 5.28. $[\bar{K} K 0]$ versus energy slices through background subtracted time-of-flight data measured on ARCS with $E_i = 50$ meV with integration range $0.45 < (H H 0) < 0.55$. The data in each panel is from a sample of the composition (a) $\text{Ba}(\text{Fe}_{0.939}\text{Cr}_{0.061})_2\text{As}_2$, (b) $\text{Ba}(\text{Fe}_{0.925}\text{Mn}_{0.075})_2\text{As}_2$, (c) $\text{Ba}(\text{Fe}_{0.953}\text{Co}_{0.047})_2\text{As}_2$, and (d) $\text{Ba}(\text{Fe}_{0.962}\text{Cu}_{0.028})_2\text{As}_2$. White regions in each panel indicate a lack of data due to gaps between detector tubes or kinematic limitations.

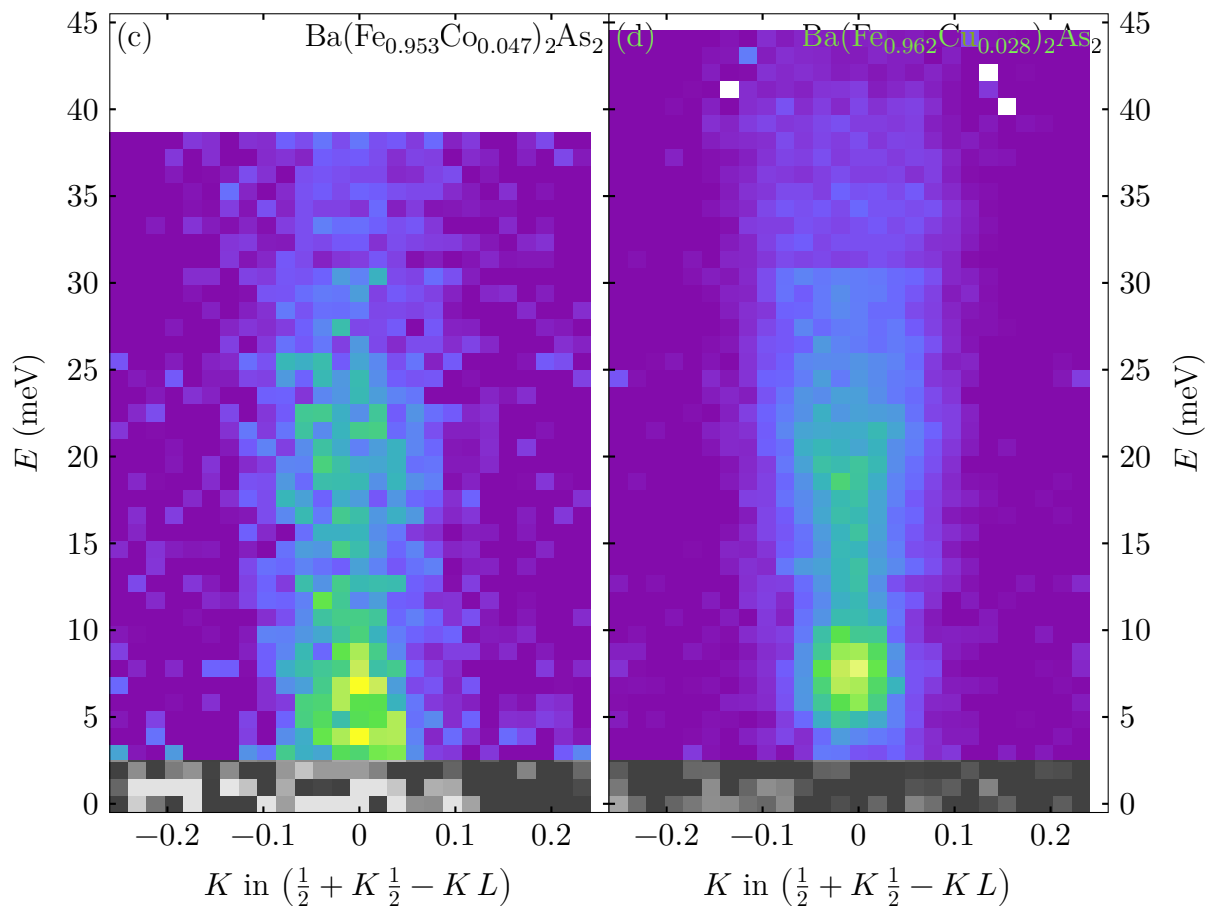


FIGURE 5.28. (Continued)

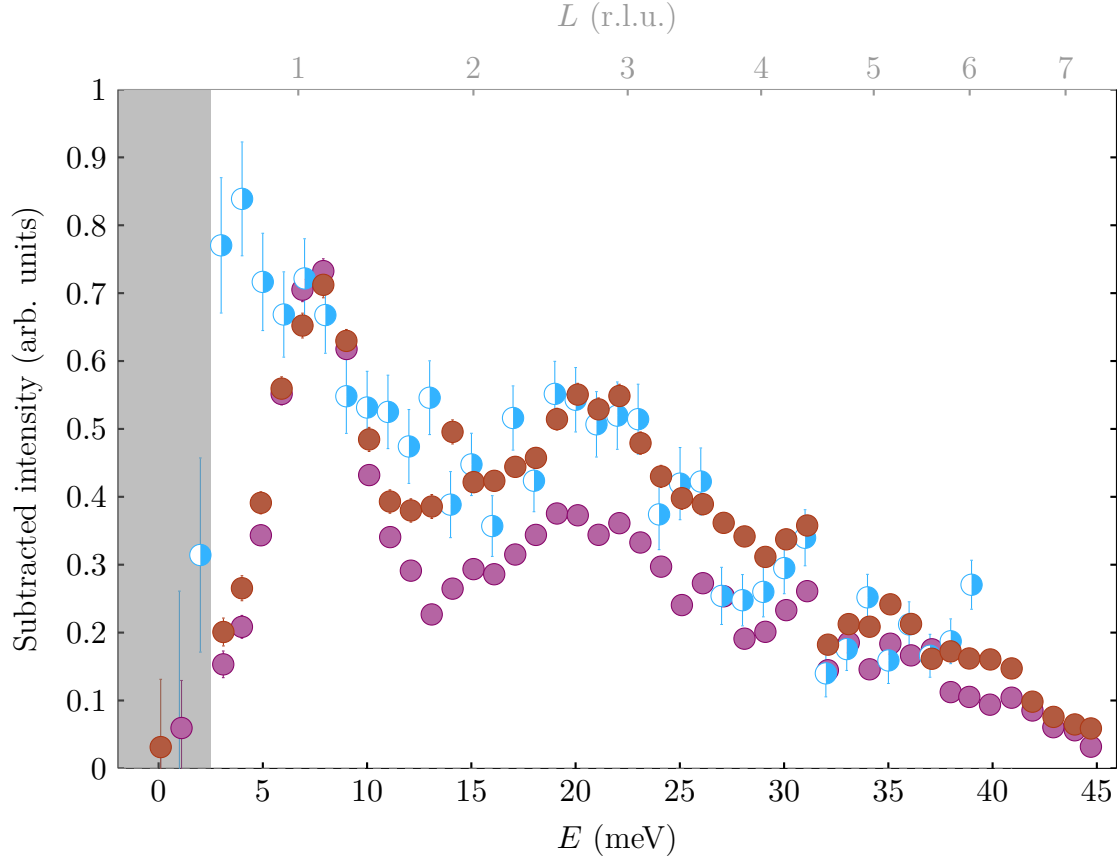


FIGURE 5.29. Background subtracted time-of-flight data measured on ARCS with $E_i = 50$ meV for $\text{Ba}(\text{Fe}_{0.939}\text{Cr}_{0.061})_2\text{As}_2$ at $T = 5$ K (\bullet), $\text{Ba}(\text{Fe}_{0.953}\text{Co}_{0.047})_2\text{As}_2$ at $T = 25$ K (\circ), and $\text{Ba}(\text{Fe}_{0.962}\text{Cu}_{0.028})_2\text{As}_2$ at $T = 5$ K (\bullet). These cuts have been produced by averaging over $0.45 < (H H 0) < 0.55$, $-0.1 < (\bar{K} K 0) < 0.1$, and binning in energy with a bin-width of 1 meV. The L component of \mathbf{Q} is fully determined by the other components of (\mathbf{Q}, E) and is indicated for bin centers by a second top horizontal scale. Data within the shaded gray region is likely too close to the elastic line for the subtracted background estimate to be accurate, due to the presence of strong incoherent scattering.

tensity, the $\text{Ba}(\text{Fe}_{0.953}\text{Co}_{0.047})_2\text{As}_2$ spectrum has less features than either $\text{Ba}(\text{Fe}_{0.939}\text{Cr}_{0.061})_2\text{As}_2$ or $\text{Ba}(\text{Fe}_{0.962}\text{Cu}_{0.028})_2\text{As}_2$ — though it also has much more statistical uncertainty — this indicates that the magnetic correlations along \mathbf{c}^* are likely much larger in $\text{Ba}(\text{Fe}_{0.939}\text{Cr}_{0.061})_2\text{As}_2$ and $\text{Ba}(\text{Fe}_{0.962}\text{Cu}_{0.028})_2\text{As}_2$ than in $\text{Ba}(\text{Fe}_{0.953}\text{Co}_{0.047})_2\text{As}_2$. Since the peak widths along $[\bar{K} K 0]$, shown in figure 5.28, are similar for the three compositions this indicates that the magnetic excitations in $\text{Ba}(\text{Fe}_{0.939}\text{Cr}_{0.061})_2\text{As}_2$ and $\text{Ba}(\text{Fe}_{0.962}\text{Cu}_{0.028})_2\text{As}_2$ are likely closer to three dimension than those in $\text{Ba}(\text{Fe}_{0.953}\text{Co}_{0.047})_2\text{As}_2$ — which are close to two dimensional, like those for optimally-doped $\text{Ba}(\text{Fe}_{1-x}\text{Co}_x)_2\text{As}_2$.

CHAPTER 6 SUMMARY

6.1 Discussion

As discussed in section 2.4, unconventional superconductivity and antiferromagnetism are often found in close proximity to one another. For the series of compounds $\text{Ba}(\text{Fe}_{1-x}\text{Co}_x)_2\text{As}_2$, which possesses both antiferromagnetism and superconductivity for the under-doped range of composition, this observation is certainly true. The close proximity, and in fact coexistence for under-doped $\text{Ba}(\text{Fe}_{1-x}\text{Co}_x)_2\text{As}_2$, of antiferromagnetism and superconductivity has encouraged speculation that antiferromagnetic spin fluctuations may mediate the electron pairing interaction in unconventional superconductors.

Previous studies indicated that the spin fluctuations at optimally-doped $\text{Ba}(\text{Fe}_{1-x}\text{Co}_x)_2\text{As}_2$ are diffusive, while those at BaFe_2As_2 are well defined spin wave excitations. It was therefore clear that the nature of spin fluctuation in $\text{Ba}(\text{Fe}_{1-x}\text{Co}_x)_2\text{As}_2$ change with the introduction of cobalt, but it remained unresolved if that change was merely a consequence of the loss of antiferromagnetic order, or a necessary ingredient for the appearance of superconductivity. To resolve this question, this work was undertaken to study the spin fluctuations of five $\text{Ba}(\text{Fe}_{1-x}\text{Co}_x)_2\text{As}_2$ compositions varying in cobalt concentration from lightly-doped to nearly optimally-doped. The spin fluctuations of these samples, in their antiferromagnetically ordered and (where possible) superconducting states have been studied via triple-axis and time-of-flight inelastic neutron scattering.

Via a time-of-flight spectroscopic study, I have shown that it is possible to capture the main features of the magnetic excitation spectra in $\text{Ba}(\text{Fe}_{0.953}\text{Co}_{0.047})_2\text{As}_2$ and related compounds with a simple model. The properties of the spin fluctuations, including the observed transverse

splitting of $\chi''(\mathbf{Q}, E)$ at high energy transfers, and the observed dispersion were shown to be attributable to the interplay between the anisotropies of the magnetic correlation length and of the Landau damping. Furthermore, due to the temperature- and state-independence of the high-energy spin fluctuations in $\text{Ba}(\text{Fe}_{0.953}\text{Co}_{0.047})_2\text{As}_2$, and the concentration-independence of the high-energy splitting, it is clear that such high-energy-transfer properties can not be responsible for superconductivity in $\text{Ba}(\text{Fe}_{1-x}\text{Co}_x)_2\text{As}_2$ and related compounds.

The low-energy study of the normal state $\text{Ba}(\text{Fe}_{1-x}\text{Co}_x)_2\text{As}_2$ spin dynamics via triple-axis neutron spectroscopy probed the spin fluctuations most strongly tied to the excitations in close proximity to the Fermi surface in these materials. This study clearly showed the crossover from gapped spin waves to a regime of strong damping and short correlation length, despite the continued presence of weak antiferromagnetic order. Furthermore, it was shown that the appearance of strong Landau damping near $x = 0.03$ – 0.04 coincides with the appearance of superconductivity in $\text{Ba}(\text{Fe}_{1-x}\text{Co}_x)_2\text{As}_2$; suggesting that the corresponding increase of low-energy spectral weight below the spin gap is a key ingredient for the development of superconductivity. Comparing these results with iron pnictide compositions on either side of the superconducting region — such as $\text{Ba}(\text{Fe}_{1-x}\text{Co}_x)_2\text{As}_2$ with $x = 0.015$ or $x = 0.14$, or $\text{Ba}(\text{Fe}_{0.85}\text{Ni}_{0.15})_2\text{As}_2$ [123, 124] — which all lack overdamped spin fluctuations, provides further evidence that overdamped spin fluctuations are a necessary component in the pairing mechanism for superconductivity in the iron pnictides.

The low-energy study of the superconducting state spin dynamics in $\text{Ba}(\text{Fe}_{1-x}\text{Co}_x)_2\text{As}_2$ via triple-axis neutron spectroscopy, has confirmed that the appearance of superconductivity in the under-doped $\text{Ba}(\text{Fe}_{1-x}\text{Co}_x)_2\text{As}_2$ compounds induces the appearance of a superconducting resonance, like other unconventional superconductors. The superconducting resonance was shown to be a redistribution of spectral weight present in the normal state and not a new excitation, as some have speculated. Furthermore, the spectral weight of the resonance, that is the spectral weight which moves as a result of the appearance of superconductivity, is directly

proportional to the ordered moment lost due to the competition between superconductivity and antiferromagnetism.

The time-of-flight inelastic neutron scattering measurements on stripe antiferromagnetically ordered $\text{Ba}(\text{Fe}_{1-x}\text{TM}_x)_2\text{As}_2$ samples further highlight the importance of low-energy spectral weight for superconductivity. The study clearly showed that three samples, all from doping-series which do not exhibit bulk superconductivity, all lack significant low energy spin fluctuations and are more three dimensional when compared to similar measurements performed on $\text{Ba}(\text{Fe}_{0.953}\text{Co}_{0.047})_2\text{As}_2$.

Taking in concert the results of these studies, it is clear that the change in character from spin wave excitations to diffusive excitations is indeed a necessary requirement for superconductivity in $\text{Ba}(\text{Fe}_{1-x}\text{Co}_x)_2\text{As}_2$; if only because it is an indication that large amounts of low-energy spin fluctuations exist in the system. The requisite presence of spin fluctuations in an energy scale similar to the superconducting transition temperature is highly indicative that they are participating in the superconducting pairing mechanism in the iron pnictide superconductors and, perhaps, other unconventional superconductors as well.

6.2 Outlook

As discussed in section 2.2.1 there are numerous members of the iron pnictide superconductor families. In the case of transition metal substituted BaFe_2As_2 , there are six additional known superconducting compounds beyond $\text{Ba}(\text{Fe}_{1-x}\text{Co}_x)_2\text{As}_2$. In order to verify that large amounts of low-energy spin fluctuations are important for the superconductivity in BaFe_2As_2 -based superconductors, inelastic neutron scattering experiments could be performed on one or more of the transition metal substituted, alkali substituted, or pnictogen substituted BaFe_2As_2 superconducting compounds. Such experiments, performed in absolute intensity units, could detect the presence or absence of significant low-energy spectral weight compared to non-superconducting compounds. The verification could be taken further by performing

similar experiments on representative members of other iron pnictide superconducting families and, ultimately, representative samples of other unconventional superconductors.

A side benefit to such a study would be the collection of data determining the superconducting resonance spectral weight for each of the studied compounds. Perhaps allowing for the determination of a universal relationship between the spectral weight of the superconducting resonance and other superconducting properties, e.g., the superconducting transition temperature.

APPENDIX A EXPERIMENTAL DATA AND DETAILS

Inelastic Neutron Scattering Data

Normal state HB3 data

In addition to the temperature dependent measurements for $\text{Ba}(\text{Fe}_{0.985}\text{Co}_{0.015})_2\text{As}_2$ and $\text{Ba}(\text{Fe}_{0.967}\text{Co}_{0.033})_2\text{As}_2$, data for each of the five samples was collected in the antiferromagnetically ordered state at a number of (\mathbf{Q}, E) points via constant- \mathbf{Q} energy scans and constant- E momentum scans. All collected data are displayed in figures A.1 to A.8 after correcting for non-magnetic background, removal of the temperature-dependent Bose factor, and rescaling the intensity into absolute units. By comparison, it is clear that the range of data collected for each sample is not consistent across the range of samples. In order to avoid over- or under-sampling effects, only a selection of the available scans were fit to model functions.

Superconducting state HB3 data

In addition to the normal state data discussed in sections 5.1.2, 5.2.3 and 5.3.2, triple axis data were also collected in the combined superconducting and antiferromagnetic states for $\text{Ba}(\text{Fe}_{0.960}\text{Co}_{0.040})_2\text{As}_2$, $\text{Ba}(\text{Fe}_{0.953}\text{Co}_{0.047})_2\text{As}_2$, and $\text{Ba}(\text{Fe}_{0.945}\text{Co}_{0.055})_2\text{As}_2$. This superconducting state triple axis data is displayed in figures A.9 to A.14 and, at first glance, may not look terribly different from the normal state data shown in figures A.3 to A.8.

By over plotting the normal state and superconducting state data, as shown in figures 5.19 to 5.24, it is clear that superconductivity modifies the spin excitation spectra. Furthermore, the superconducting resonance is indeed present in the under-doped coexisting regime of $\text{Ba}(\text{Fe}_{1-x}\text{Co}_x)_2\text{As}_2$, as in other unconventional superconductors (e.g., figure 2.24).

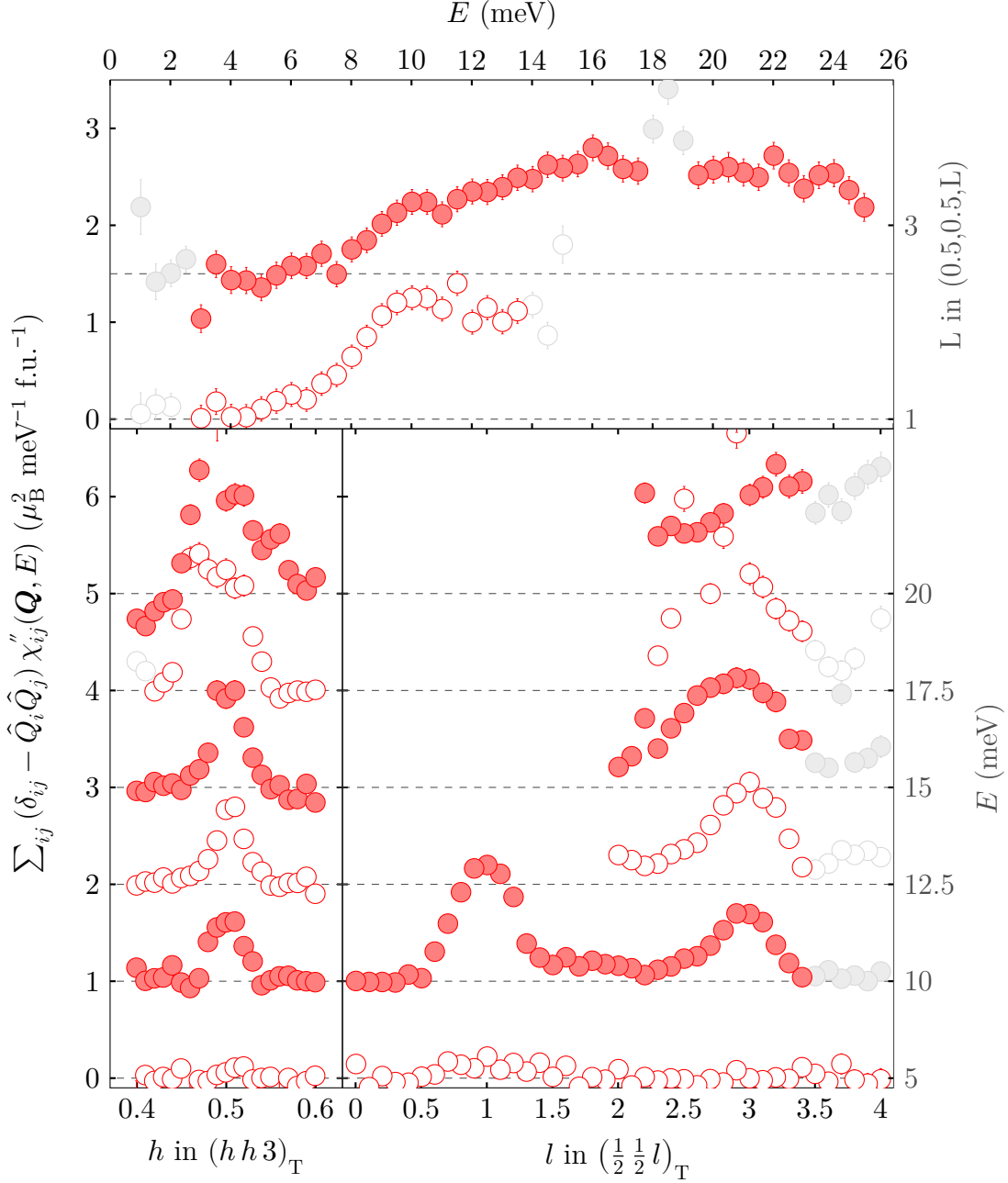


FIGURE A.1. All HB3 measured normal state [$T = 11.22(3)$ K] $\text{Ba}(\text{Fe}_{0.985}\text{Co}_{0.015})_2\text{As}_2$ triple-axis data after background subtraction and correction for the Bose thermal population factor. The top panel corresponds to energy spectra performed at $(\frac{1}{2} \frac{1}{2} L)$ with intensity offset by the L value, indicated by the right hand scale. The bottom panels correspond to constant energy scans performed in the $[hh3]$ and $[00l]$ directions with intensity offset by the energy transfer, E , as indicated by the right hand scale. In all panels gray data correspond to measured intensity which has been excluded from fitting routines due to inadequate background estimation.

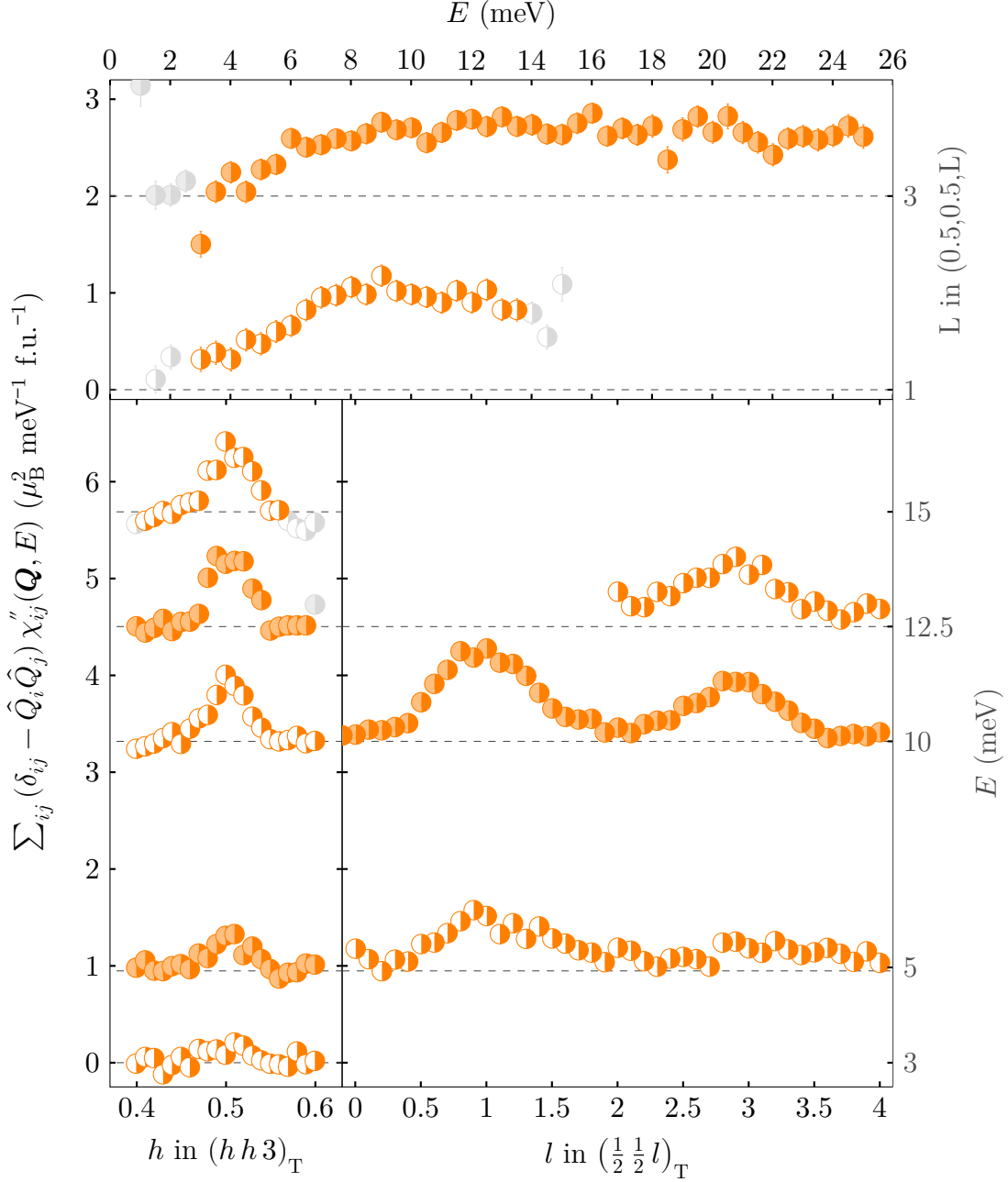


FIGURE A.2. All HB3 measured normal state [$T = 11.2(1)$ K] $\text{Ba}(\text{Fe}_{0.967}\text{Co}_{0.033})_2\text{As}_2$ triple-axis data after background subtraction and correction for the Bose thermal population factor. The top panel corresponds to energy spectra performed at $(\frac{1}{2} \frac{1}{2} L)$ with intensity offset by the L value, indicated by the right hand scale. The bottom panels correspond to constant energy scans performed in the $[h h 3]$ and $[00 l]$ directions with intensity offset by the energy transfer, E , as indicated by the right hand scale. In all panels gray data correspond to measured intensity which has been excluded from fitting routines due to inadequate background estimation.

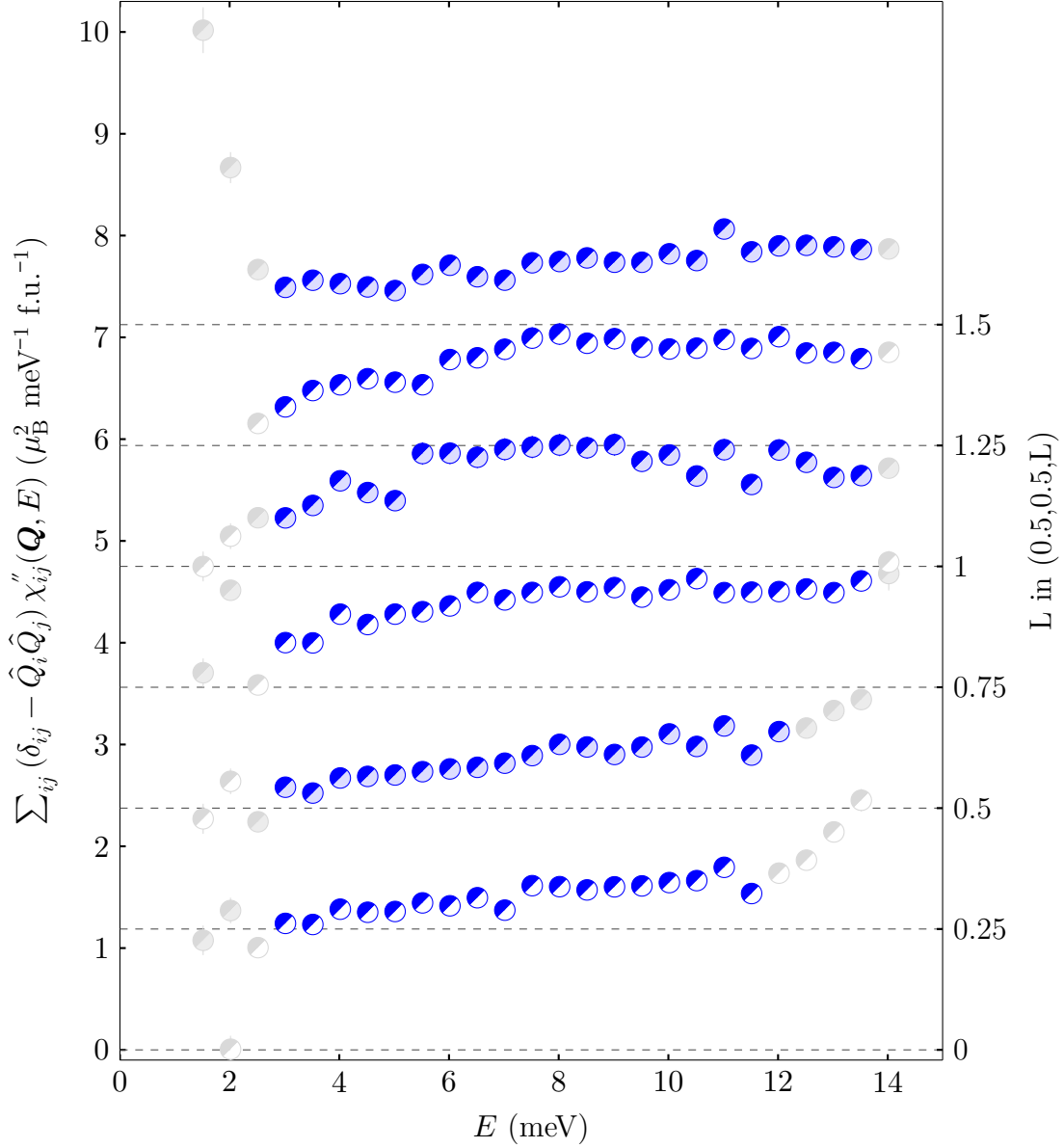


FIGURE A.3. HB3 measured normal state [$T = 19.8(2)$ K] $\text{Ba}(\text{Fe}_{0.960}\text{Co}_{0.040})_2\text{As}_2$ triple-axis energy spectra performed at $(\frac{1}{2} \frac{1}{2} L)$ with intensity offset by the L value, indicated by the right hand scale, after background subtraction and correction for the Bose thermal population factor. Gray data correspond to measured intensity which has been excluded from fitting routines due to inadequate background estimation.

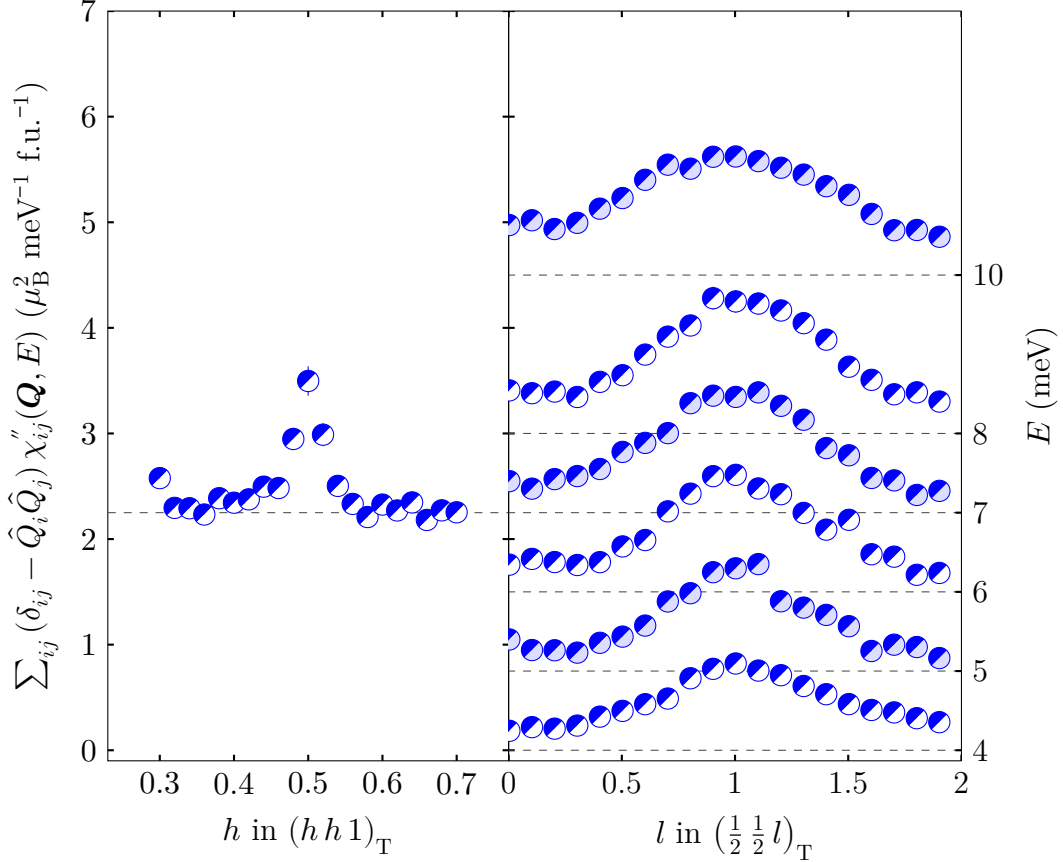


FIGURE A.4. HB3 measured normal state [$T = 19.8(2)$ K] $\text{Ba}(\text{Fe}_{0.960}\text{Co}_{0.040})_2\text{As}_2$ triple-axis data after background subtraction and correction for the Bose thermal population factor. The left panel corresponds to constant energy scans performed in the $[hh1]$ direction, where the right panel corresponds to the $[00l]$ direction, both with intensity offset by the energy transfer, E , as indicated by the right hand scale. Gray data correspond to measured intensity which has been excluded from fitting routines due to inadequate background estimation.

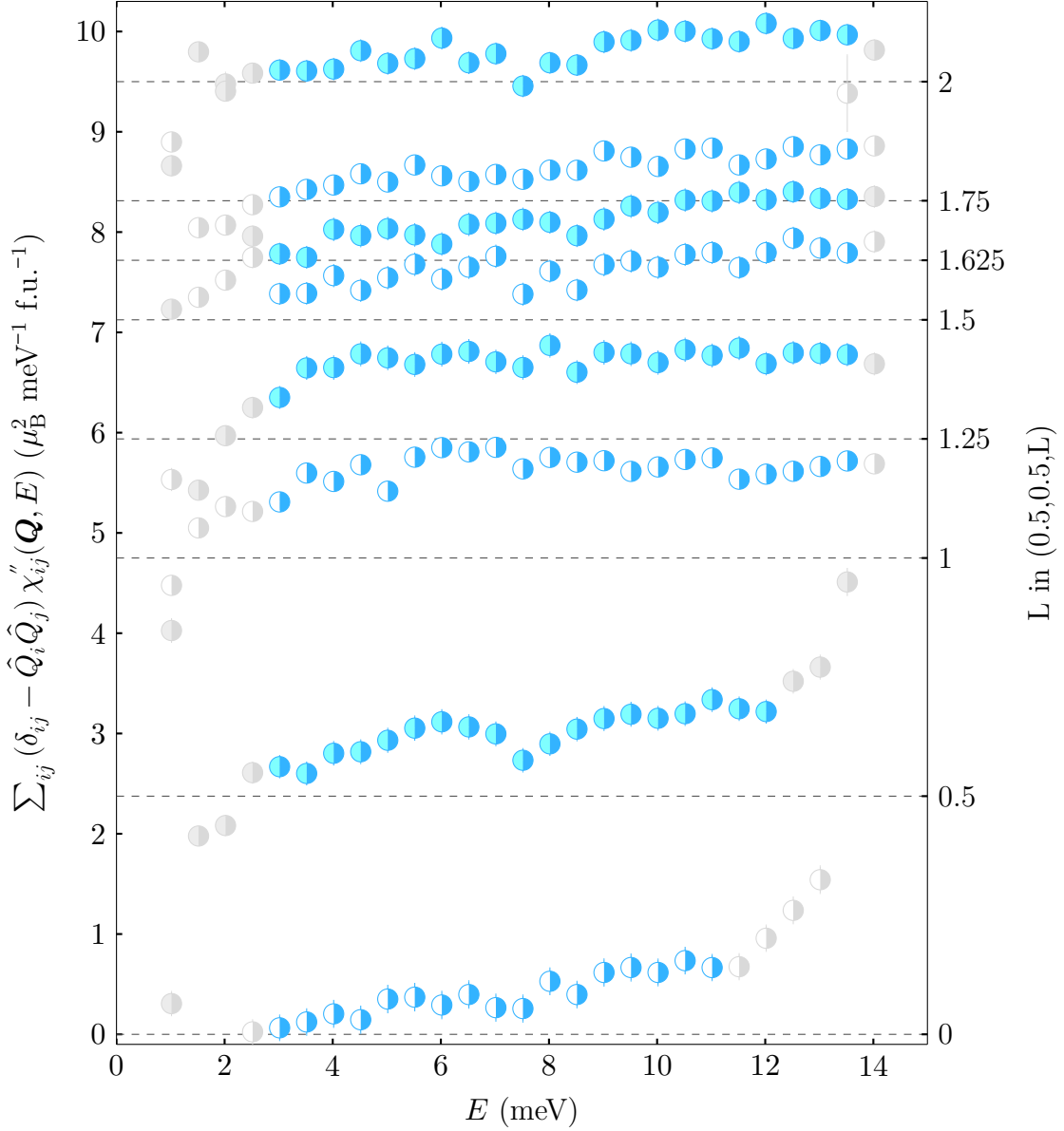


FIGURE A.5. HB3 measured normal state [$T = 25.3(4)$ K] $\text{Ba}(\text{Fe}_{0.953}\text{Co}_{0.047})_2\text{As}_2$ triple-axis energy spectra performed at $(\frac{1}{2} \frac{1}{2} L)$ with intensity offset by the L value, indicated by the right hand scale, after background subtraction and correction for the Bose thermal population factor. Gray data correspond to measured intensity which has been excluded from fitting routines due to inadequate background estimation.

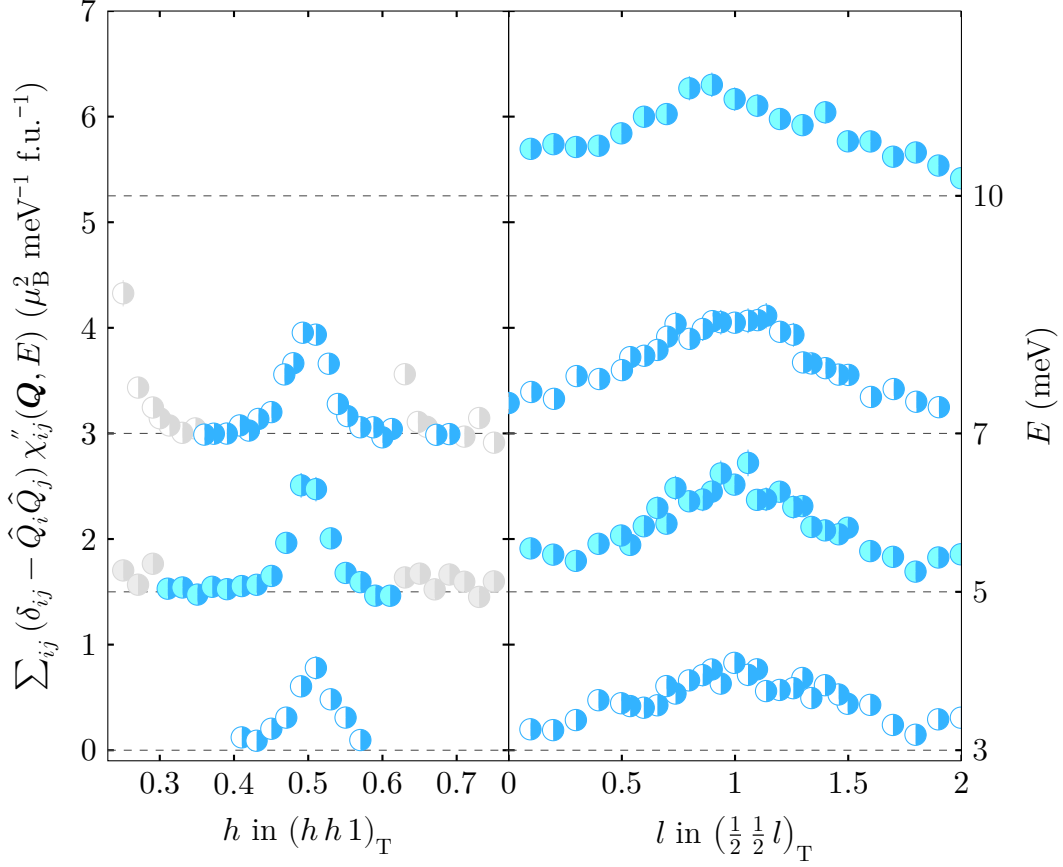


FIGURE A.6. HB3 measured normal state [$T = 25.3(4)$ K] $\text{Ba}(\text{Fe}_{0.953}\text{Co}_{0.047})_2\text{As}_2$ triple-axis data after background subtraction and correction for the Bose thermal population factor. The left panel corresponds to constant energy scans performed in the $[h h 1]$ direction, where the right panel corresponds to the $[00l]$ direction, both with intensity offset by the energy transfer, E , as indicated by the right hand scale. Gray data correspond to measured intensity which has been excluded from fitting routines due to inadequate background estimation.

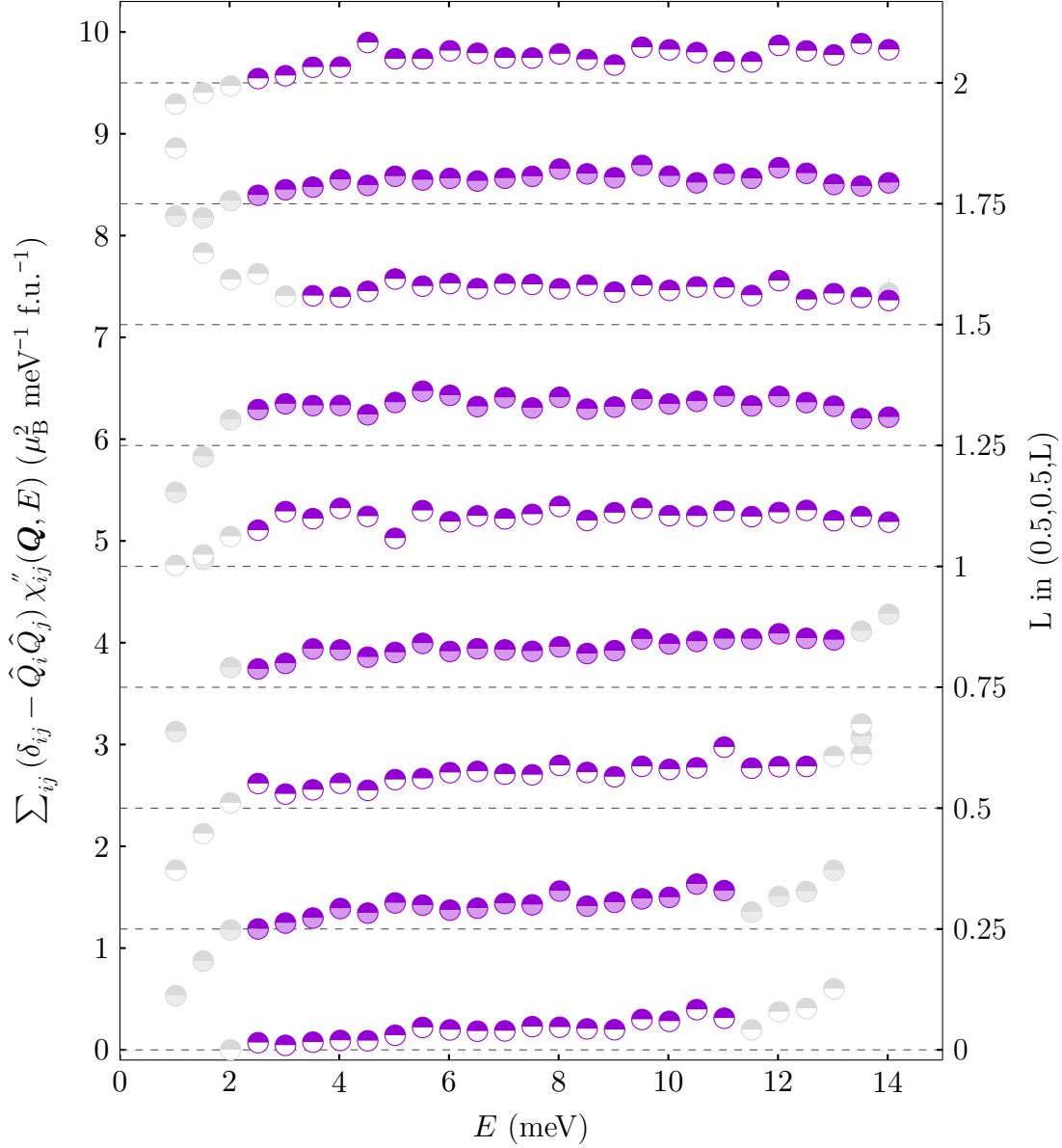


FIGURE A.7. HB3 measured normal state [$T = 30.0(3)$ K] $\text{Ba}(\text{Fe}_{0.945}\text{Co}_{0.055})_2\text{As}_2$ triple-axis energy spectra performed at $(\frac{1}{2} \frac{1}{2} L)$ with intensity offset by the L value, indicated by the right hand scale, after background subtraction and correction for the Bose thermal population factor. Gray data correspond to measured intensity which has been excluded from fitting routines due to inadequate background estimation.

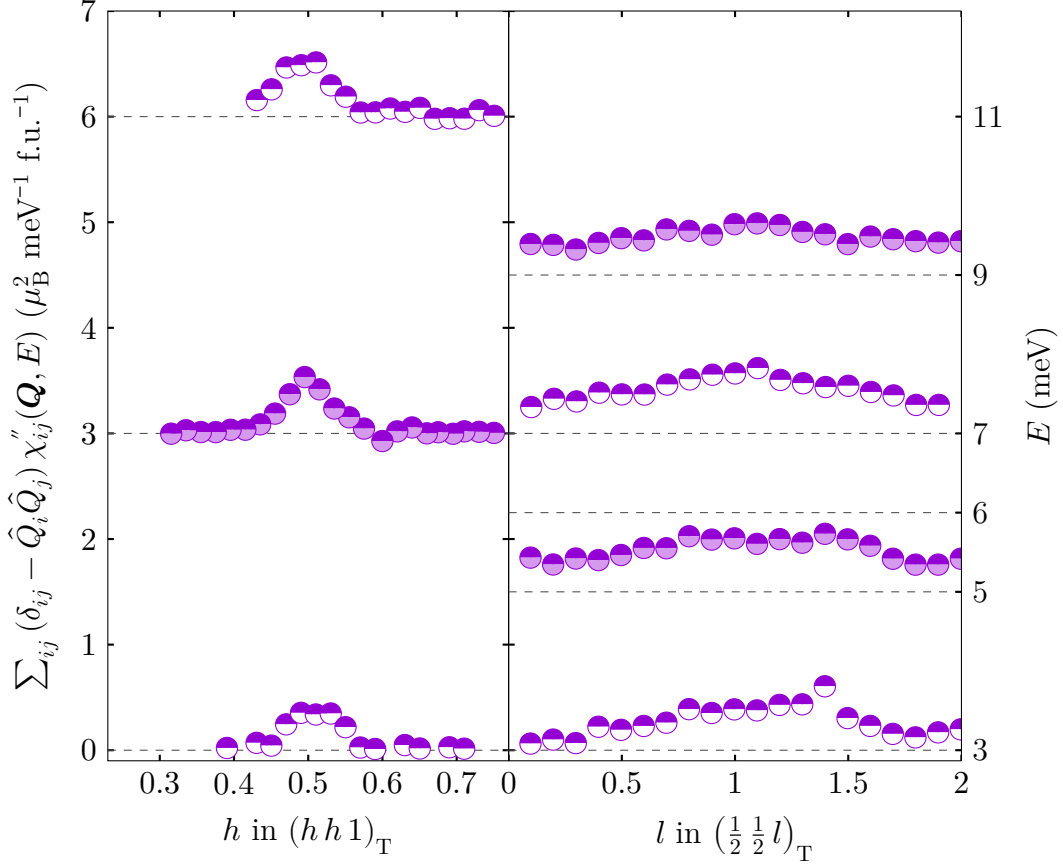


FIGURE A.8. HB3 measured normal state [$T = 30.0(3)$ K] $\text{Ba}(\text{Fe}_{0.945}\text{Co}_{0.055})_2\text{As}_2$ triple-axis data after background subtraction and correction for the Bose thermal population factor. The left panel corresponds to constant energy scans performed in the $[h h 1]$ direction, where the right panel corresponds to the $[0 0 l]$ direction, both with intensity offset by the energy transfer, E , as indicated by the right hand scale. Gray data correspond to measured intensity which has been excluded from fitting routines due to inadequate background estimation.

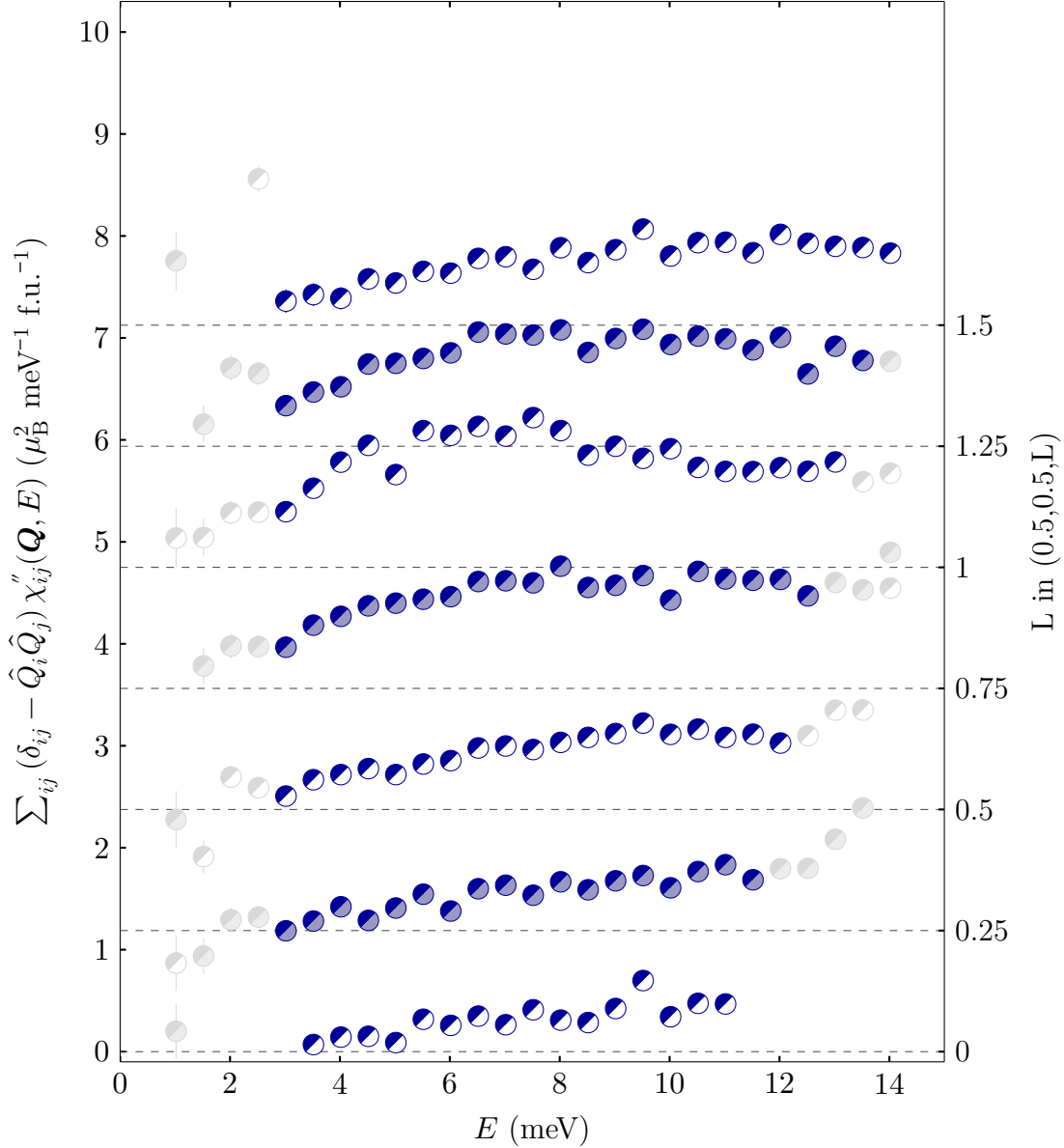


FIGURE A.9. HB3 measured superconducting state [$T = 2.62(16)$ K] $\text{Ba}(\text{Fe}_{0.960}\text{Co}_{0.040})_2\text{As}_2$ energy spectra after background subtraction and correction for the Bose thermal population factor. Data represent scans performed at $(\frac{1}{2}, \frac{1}{2}, L)$ with intensity offset by the L value, indicated by the right hand scale. Gray data correspond to measured intensity which has been excluded from fitting routines due to inadequate background estimation.

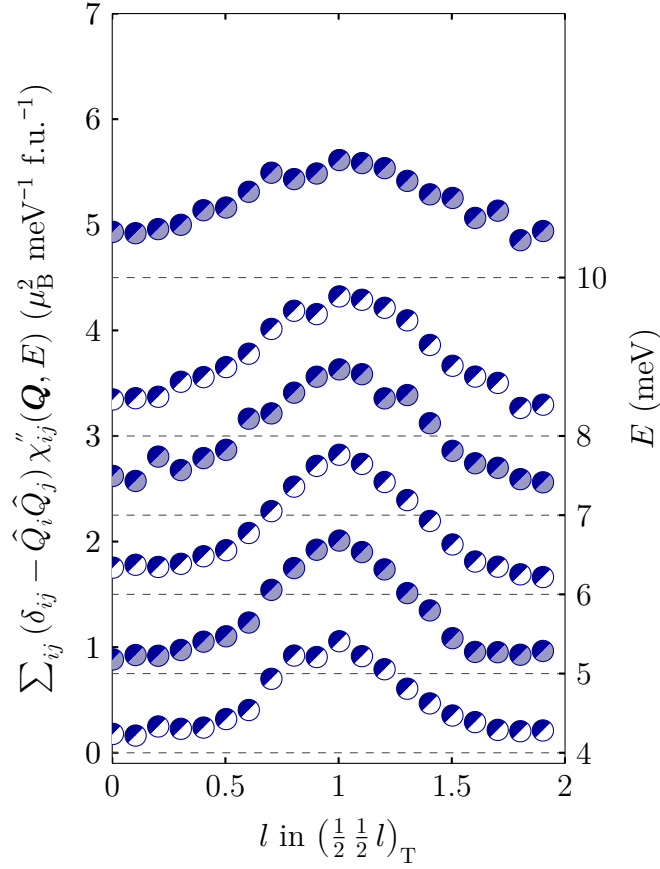


FIGURE A.10. HB3 measured superconducting state [$T = 2.62(16)$ K] $\text{Ba}(\text{Fe}_{0.960}\text{Co}_{0.040})_2\text{As}_2$ constant-energy $[00l]$ scans after background subtraction and correction for the Bose thermal population factor, with intensity offset by the energy transfer, E , as indicated by the right hand scale.

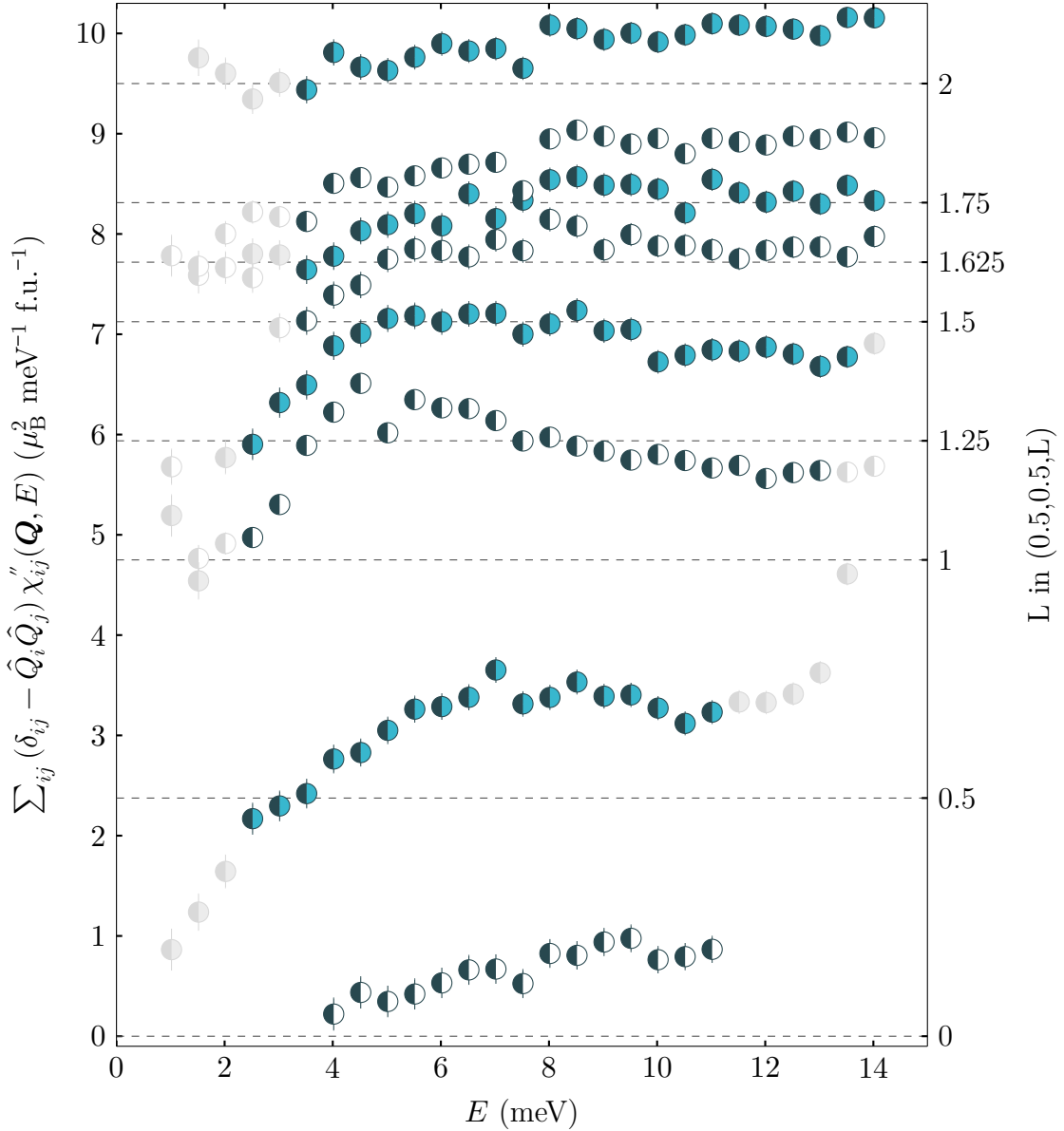


FIGURE A.11. HB3 measured superconducting state [$T = 4.30(2)$ K] $\text{Ba}(\text{Fe}_{0.953}\text{Co}_{0.047})_2\text{As}_2$ energy spectra after background subtraction and correction for the Bose thermal population factor. Data represent scans performed at $(\frac{1}{2}, \frac{1}{2}, L)$ with intensity offset by the L value, indicated by the right hand scale. Gray data correspond to measured intensity which has been excluded from fitting routines due to inadequate background estimation.

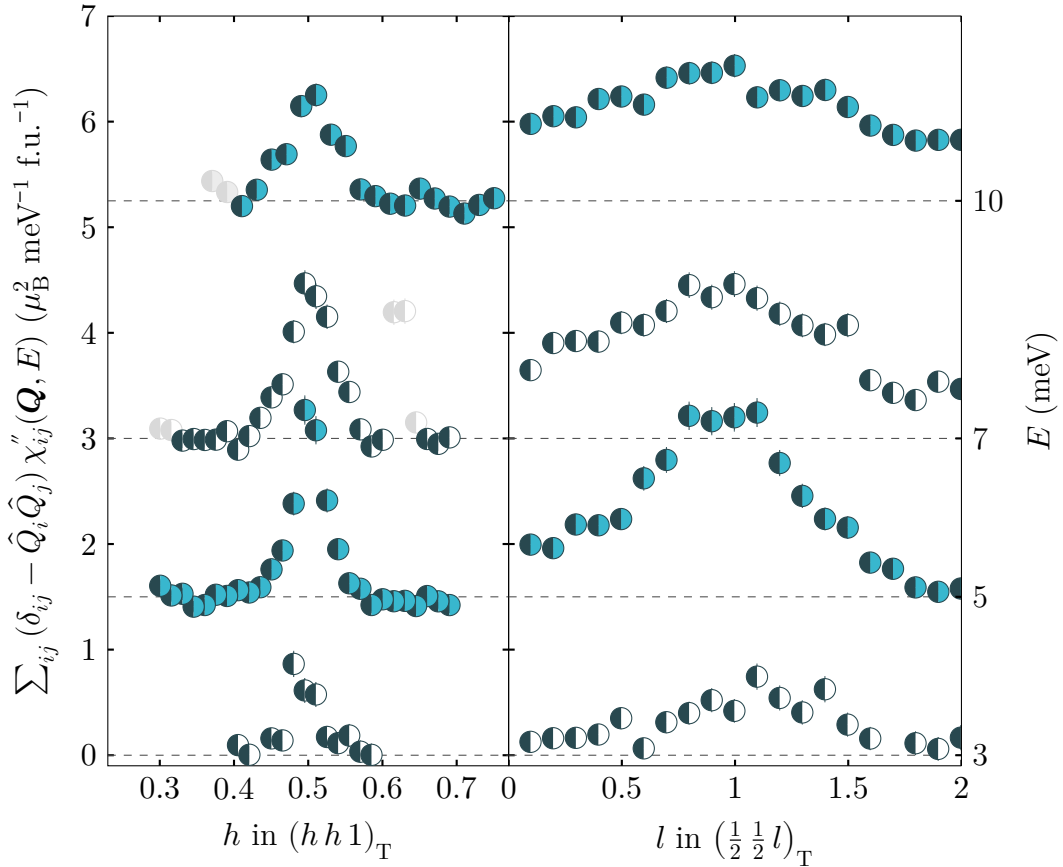


FIGURE A.12. All HB3 measured superconducting state [$T = 4.30(2)$ K] $\text{Ba}(\text{Fe}_{0.953}\text{Co}_{0.047})_2\text{As}_2$ constant-energy scans after background subtraction and correction for the Bose thermal population factor. The left (right) hand panel corresponds to constant energy scans performed in the $[h h 1]$ ($[0 0 l]$) direction with intensity offset by the energy transfer, E , as indicated by the right hand scale. Gray data correspond to measured intensity which has been excluded from fitting routines due to inadequate background estimation.

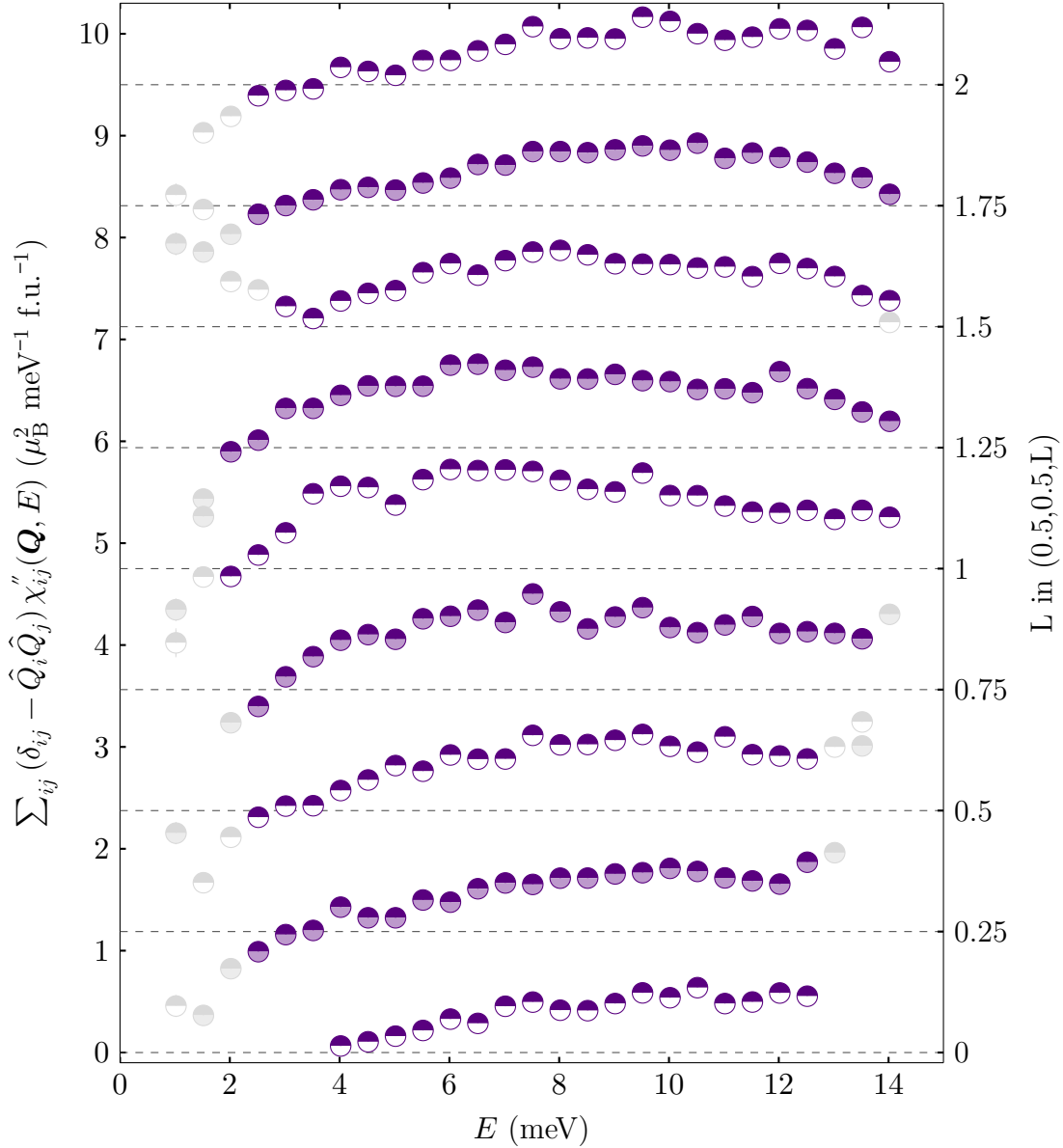


FIGURE A.13. HB3 measured superconducting state [$T = 7.97.2(3)$ K] $\text{Ba}(\text{Fe}_{0.945}\text{Co}_{0.055})_2\text{As}_2$ energy spectra after background subtraction and correction for the Bose thermal population factor. Data represent scans performed at $(\frac{1}{2} \frac{1}{2} L)$ with intensity offset by the L value, indicated by the right hand scale. Gray data correspond to measured intensity which has been excluded from fitting routines due to inadequate background estimation.

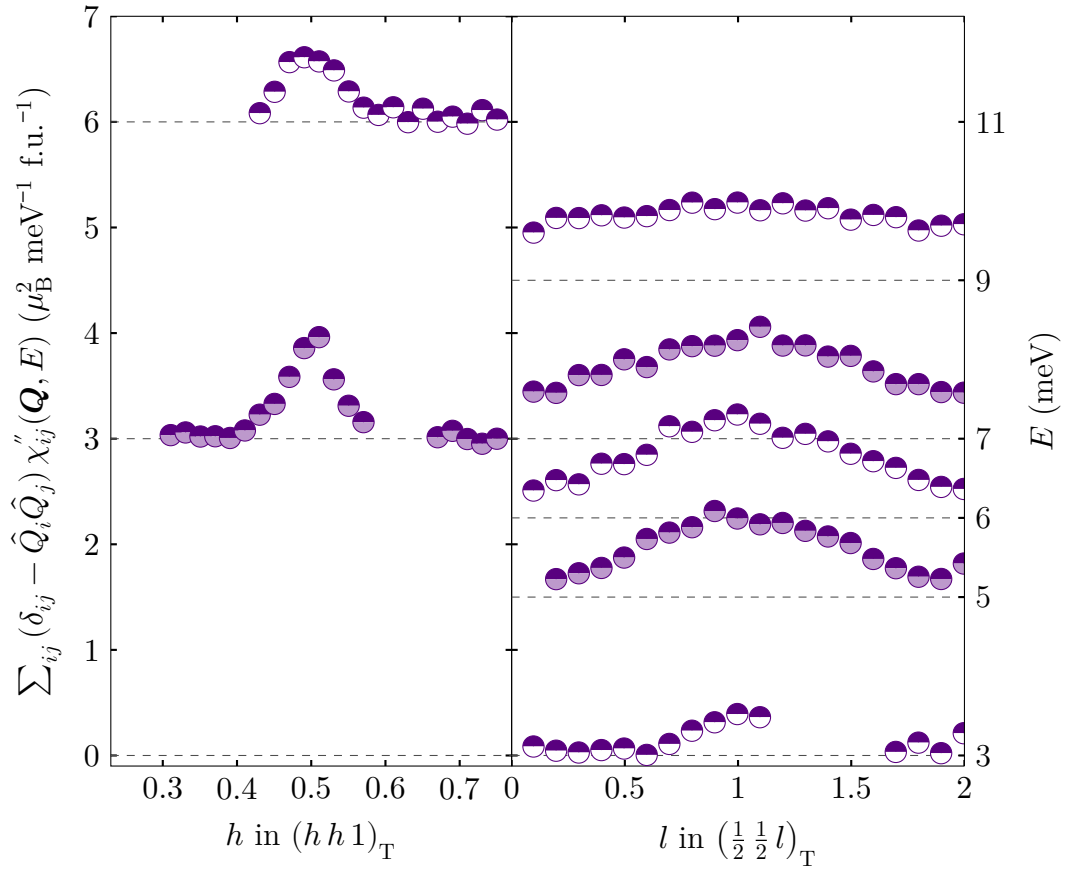


FIGURE A.14. All HB3 measured superconducting state [$T = 7.97.2(3)$ K] $\text{Ba}(\text{Fe}_{0.945}\text{Co}_{0.055})_2\text{As}_2$ constant-energy scans after background subtraction and correction for the Bose thermal population factor. The left (right) hand panel corresponds to constant energy scans performed in the $[h h 1]$ ($[0 0 l]$) direction with intensity offset by the energy transfer, E , as indicated by the right hand scale.

TABLE A.1. Details of the coaligned single-crystal samples used in this study. Given here are the transition metal dopant, average compositions, total masses, number of crystals coaligned in each set, antiferromagnetic transition temperatures, superconducting transition temperatures, who performed the crystal growth, who created the coalignment from individual single crystals, and a list of publications in which each coalignment has been used. The crystal growth column, g, is encoded with [‡]N. Ni, [‡]S. Ran, [†]A. S. Sefat, and ^{*}A. Thaler. The sample coalignment column, c, is encoded with [◊]A. D. Christianson, [‡]M. G. Kim, [•]D. K. Pratt, ^{*}G. S. Tucker. Values displayed here have been rounded to their last displayed digit and therefore have an uncertainty of no more than half in the last digit.

<i>TM</i>	<i>x</i> /%	Mass/g	No. xtals.	T_N /K	T_c /K	g	c	used in ref.
Cr	6.1	1.027	6	100		‡	*	
Mn	7.5	1.913	13	80		*‡	*	[125]
Co	1.5	1.803	14	114		*	*	[92]
Co	3.3	1.894	10	74		*	*	[92]
Co	4	2	4	58	11	†	◊	[92, 122]
Co	4.7	1.88	10	47	17	‡	•	[91, 92, 126]
Co	5.5	2.071	8	34	22	*	•*	[92]
Cu	2.8	1.52	2	64		*‡	‡	[127]

Sample Details

Five coaligned sets of $\text{Ba}(\text{Fe}_{1-x}\text{Co}_x)_2\text{As}_2$ single crystals each with a different cobalt concentration, as well as one sample each of chromium, manganese, and copper substituted $\text{Ba}(\text{Fe}_{1-x}\text{TM}_x)_2\text{As}_2$ coalignments were used in this study. Details of their properties are listed in table A.1, including transition metal dopant and concentration, coaligned mass, number of crystals in each coalignment, characteristic temperatures, who was responsible for the growth of the single crystals used, who was responsible for performing the coalignment process to create each sample, and a listing of publications in which data collected from each sample have been presented.

APPENDIX B SCANDATA.M

By standardizing the loading and manipulation of data from spectrometers, independent of the spectrometer control software (e.g., SPICE [128]), it becomes possible to efficiently analyze data in a repeatable and – hopefully – accurate way. In order to facilitate the analysis of data obtained from triple axis neutron spectrometers, I wrote a MATLAB class called SCANDATA. Through operator overloading, SCANDATA simplifies the processes of, e.g., adding and subtracting scans, binning scans, normalizing to a named monitor, and applying scale factors; all while keeping track of statistical-based uncertainties.

Basic Usage

The SCANDATA class has been written to be used in a UNIX-like environment. On WINDOWS systems, or other systems which do not use / as a directory separator, most of the functionality of SCANDATA should still work with the exception of the automatic creation of RESLIB configuration (EXP) structures.

A new SCANDATA object named `sdo` can be created in memory in one of three ways:

1. `sdo = scandata('path/to/filename');`
2. `sdo = scandata(pesdo);`
3. `sdo = scandata.empty();`

where the first calls the creation constructor and loads a scan data file from disk, the second calls the copy constructor to make a copy of a preexisting SCANDATA object named `pesdo`, and the third creates an empty SCANDATA object of size 0×0 . If passed a $1 \times N$ or $N \times 1$ cell

array of file names, the creation constructor will return a $N \times 1$ array of SCANDATA objects. Similarly, the copy constructor can be used to copy a preexisting SCANDATA object array. The utility in creating an empty SCANDATA object comes by adding size information to the empty function call, i.e., `scandata.empty([N,0])` will create an empty $N \times 0$ SCANDATA array which can then be filled one object at a time – which is how both the creation and copy constructors produce arrays of SCANDATA objects.

It is not uncommon for the same scan to be repeated multiple times in one or more experiments with the intention of adding together the repeated scans in order to increase counting statistics (and reduce relative statistical uncertainties). To add together two SCANDATA objects, or to add a constant intensity to a SCANDATA object, the `+` operator has been overloaded. Adding two scans, `s1` and `s2`, is as easy as `twoscans = s1 + s2`; similarly adding a constant, `c`, to `s1` is accomplished with `offsets1 = s1 + c`; . A series of repeated scans can be added by using the overloaded `sum` function on an array of SCANDATA objects. If a SCANDATA array is defined as `scans = vertcat(s1,s2,s3,...)`; from the repeated scans `s1`, `s2`, and `s3`, then the sum of those repeated scans is simply `sumofscans = sum(scans)`;

Another common operation is the subtraction of estimated background intensity. This can be accomplished by `i=s-b`; where `s` is the measured intensity and `b` is *either* a constant background estimate or a scan which is a direct measurement of the background. In the case the `b` is a SCANDATA object the overloaded `minus` function will interpolate, if necessary, between the points in `b` to ensure that intensity is subtracted from all points in `s`.

After adding repeated scans and subtracting a background estimate, it is typically useful to normalize the intensity in each point to another measured quantity (typically a counts in a beam monitor or elapsed time). The SCANDATA class is flexible in this manner, and can normalize intensity data to any named column contained in the original data file. The normalization routine in SCANDATA can be called in one of three ways: the first, e.g., `s.normalize('monitor')`, divides the number of counts for each point by the value of the

‘monitor’ column; the second, e.g., `s.normalize('monitor',c)`, would then multiply each intensity by the constant `c`; and the last, e.g., `s.normalize('monitor',c,dc)`, correctly folds-in the uncertainty of the normalization constant – this last form is useful when converting measured intensity to absolute units, as the conversion factor will undoubtedly have an associated statistical uncertainty. If the chosen normalization column has an associated uncertainty (currently SCANDATA knows how to calculate uncertainties for columns named `detector`, `monitor`, `time`, and `mcu`), then its uncertainty is also correctly propagated to the normalized intensity uncertainty.

After normalization, one often wants to fit a resolution convoluted model to measured data. To help in this endeavor, SCANDATA contains the methods to integrate with the RESLIB resolution estimation, convolution, and model fitting routines. If the data was measured with SPICE-driven spectrometer (and the analysis computer system is UNIX-like) then the method `createRLEXP` can be used to automatically populated the fields of a RESLIB `EXP` structure. Furthermore, if the data was measured on the instrument HB3, `createRLEXP` can automatically create the `EXP` fields necessary to perform a Popovici resolution approximation with RESLIB– a global structure, `RES_CONSTANTS`, needs to exist with a field named `method` set to 1 (i.e., execute `global RES_CONSTANTS`; and `RES_CONSTANTS.method=1`; before calling, e.g.s. `createRLEXP()`). `createRLEXP` looks through the scan header to find the name of the ‘UBConf’ file and then uses UNIX-like path information and the default SPICE directory layout to open the ‘UBConf’ and read in scattering plane and sample lattice information – this could be modified to be operating system independent. The `read4ResLib` method returns the RESLIB-appropriate vectors `H`, `K`, `L`, `W`, `Iobs`, `dIobs`, and `EXP` plus a vector of measured temperatures for each data point. The methods `ConvRes`, `ConvResSMA`, `FitConv`, and `FitConvSMA` are wrappers for the RESLIB functions of the same name; they take SCANDATA objects (or vectors) as inputs, create the appropriate `EXP` structures if necessary

through `createRLEXP`, assemble the appropriate data vectors through `read4ResLib`, and finally call the `RESLIB` function.

Finally, it is typical that one should want to plot measured and/or simulated data. The `plot` function is overloaded by `SCANDATA` to plot `SCANDATA` objects with relative ease, including plotting vectors of `SCANDATA` objects. The overloaded plotting routine automatically cycles through a list of color, symbol, and line specifications to help differentiate between over-plotted scans. `SCANDATA` objects which contain no uncertainty in their intensity are assumed to be simulations and are plotted as lines, otherwise the data is displayed as an `errorbar` plot. Points that have a zero weight value (stored in `s.w`, and initialized as `ones(size(s.y))`) are automatically ignored when using `scandata.FitConv` and `scandata.FitConvSMA`; the overloaded plotting routine plots these points as gray to indicate this fact. The `plot` method can display a scan as a function of a non-default variable – this can be useful when searching for the source of a spurious peak by, e.g., `plot(s, 's2')` to plot the intensity as a function of the sample scattering angle (at HB3).

There are many more functions defined as part of the `SCANDATA` class, some of which are internal and some of which are useful when analyzing unique data sets. The following pages contain a listing of the `SCANDATA` header, containing all of the method and property names of the `SCANDATA` class, as well as a complete listing of the `SCANDATA` class code, in order to help in your understanding of the contents of the class.

MATLAB Code

```

% The scandata class is a data container class for triple-axis scattering
% data stored in SpICE data files.
% To cut down on memory usage, all scandata objects inherit from the MATLAB
% handle class; as such the copy-constructor must be used in cases where
% passing a handle is not the intended action.
%
% Scandata uses spicedata.m to initialize itself and populate some of its
% properties. Inspiration for this class was also drawn from spiceload.m.
% Both spicedata and spiceload were written by Mark Lumsden.
%
% Public methods defined here-in:
% ConvRes                fillMillerVecs                normalize
% ConvResSMA            fillVectors                    plot
% Convert_mbpSr_uB2    findColumn                    plus
% CorrectBose           findEnergies                rdivide
% CorrectFormFactor    findInHeader                read4ResLib
% FitConv              findLatticeConstants        redefinex
% FitConvSMA          findScanTitle                redefiney
% Tcolor              findSum                    removeColumn
% ThermalAdjust       findTemperature                removePts
% Weight              fixedFinalEnergyCorrection    replacex
% WeightBounds        getColumn                    replacey
% avgColumn           getFromHeader                scandata
% bin                 hist                        setColumn
% checkStopped        horzcat                    times
% createHistogram     minus                        uminus
% createRLEXP         monitorHarmonic                vertcat
% crpoints            mrdivide
% emptyPointCheck     mtimes
%
% Static methods: (accessed by scandata.[method name])
% avgscans             decodeColor
%
% version 0.0, written by Gregory Tucker, 2010/03/01
% version 1.0, written by Gregory Tucker, 2013/09/04
%   + switched from spicedata.m to gentasload.m, which can load data from
%   multiple facilities, and is expandable.
% version 1.1, written by Gregory Tucker, 2014/08/06
classdef scandata < handle
    properties %(SetAccess=protected) % Protected Properties
        alat        % \
        blat        % } Lattice Vector lengths in Angstroms
        clat        % /
        alpha       % \
        beta        % } Lattice angles in degrees
        gamma       % /
        avgflg      % flag to tell if a data set is the result of averaging
        colnames    % array of data column names

```

```

data          % data matrix from datafile
defxname      % default independent quantity name
              % s1 for scanrel s1 1 -1 0.1, etc.
defyname      % default dependent quantity name (usually 'detector')
defxvalue     % column number for default independent quantity
defyvalue     % column number for default dependent quantity
e            % array of (ef - ei), energy transfer
ei           % array of incident neutron energy
ef           % array of final neutron energy
err          % array of error in independent quantity
monerr       % error in monitor counts
mcuerr       % error in mcu counts
timerr       % error in counting time
filename      % name of file from which data is imported
h            % vector for h Miller indicies data
k            % vector for k Miller indicies data
l            % vector for l Miller indicies data
header       % full header string from datafile
hstFlg       % flag          % \
hstX         % bin center vect % \\
hstEdg       % bin edge vector % \\
hstY         % averaged y vect % }+> Histogram variables
hstEr        % propagatd err  % ///
hstT         % averaged t vect % //
hstE         % averaged e vect % /
hstW         % weight vector
q            % magitude of q
stoppedFlag  % 1 if the scan was stopped, 0 if the scan finished
sumCounts    % total sum of all counts in scan; -1 if not defined
t            % vector of temperatures
x            % array of dependent quantity values
y            % array of independent quantity values
end % protected properties
properties % Public Properties
color        % color for plotting
EXP          % EXP parsed from datafile and UBConf, for ResLib
rl           % ResLib parameters,
samplename   % ideally a string containing the sample name, user set
scan_title   % user defined scantitle
UserData     % Unused by scandata, designated space for User Data
w            % weight vector, useful for knowing which datapoints
              % should be ignored, filled by Weight methods
end % public properties
properties (Constant) %constants that come up often, in useful units
hbar         = 6.58211899e-13; % meV s
kBoltzman    = 8.617343e-2;    % meV/K
neutronmass  = 1.045407672e-25;% meV s^2 A^-2
end % constant properties
methods % Initialization Methods
function obj = scandata(a)
    if ~ischar(a)&&length(a)>1
        obj = scandata.empty(length(a),0);
    end
end

```

```

    for i=1:length(a); obj(i)=scandata(a(i)); end
else
    if iscellstr(a) % in case the filename is in a cell
        a = char(a); %convert filename to string
    end
    if ischar(a)
        obj.filename = a;
        [obj.data,obj.header,obj.colnames,obj.defxname,...
        obj.defyname,obj.defxvalue,obj.defyvalue]=gentasload(a);
        obj.fillVectors % doesn't fill errors
        %check to see if the scan was stopped
        obj.stoppedFlag = obj.checkStopped;
        %find the total number of counts for the string
        obj.sumCounts = obj.findSum;
        obj.avgflg = false;
        obj.hstFlg = false;
        obj.scan_title = obj.findScanTitle;
        %calculate error for each dependent variable value
        obj.err =sqrt(obj.y);
        obj.monerr=sqrt(obj.getColumn('monitor'));
        obj.mcuerr=sqrt(obj.getColumn('mcu'));
        obj.timerr=sqrt(obj.getColumn('time'));
        %check for all-zero intensity points, and remove them
        obj.emptyPointCheck();
        %any remaining zero-intensity points shouldn't have
        %zero error associated with them:
        obj.err(~obj.y)=1;
        obj.monerr(~obj.getColumn('monitor'))=1;
        obj.mcuerr(~obj.getColumn('mcu'))=1;
        obj.timerr(~obj.getColumn('time'))=1;
    elseif isa(a,'scandata')
        pl=fieldnames(a);
        % we need to remove constant properties, which can't be
        % overwritten
        consts={'hbar','kBoltzman','neutronmass'};
        for i=1:length(consts);pl(strcmp(pl,consts(i)))=[];end
        for i=1:length(pl); obj.(pl{i})=a.(pl{i}); end
    end
end
end %initialization function
end % initialization methods
methods % Public Methods
function fillVectors(obj)
    % Any time that the data block is modified, through addition of
    % scans or binning of data, the various vector quantities need
    % to be pulled from the block. Since this happens in multiple
    % places, it should be standardized.
    if length(obj)>1;
        for i=1:length(obj);obj(i).fillVectors;end;
    else
        obj.x=obj.data(obj.defxvalue,:);
        obj.y=obj.data(obj.defyvalue,:);
    end
end

```

```

obj.findEnergies % obj.{ei,e,ef}
obj.findTemperature % obj.t
obj.q = obj.getColumn('q');
obj.h = obj.getColumn('h');
obj.k = obj.getColumn('k');
obj.l = obj.getColumn('l');
% Errors are always a special case and can't/shouldn't
% be handled in this function.
end
end % fillVectors
function normalize(obj, monname, norm, normerr)
%renormalize y to norm/monitor*y
if nargin<4 || isempty(normerr); normerr = 0; end
if nargin<3 || isempty(norm); norm=1; end
if length(obj)>1
    for i=1:length(obj);obj(i).normalize(monname,norm,normerr);end
else
    monitor=obj.data(obj.findColumn(monname),:);
    switch lower(monname)
        case 'monitor'; merr = obj.monerr;
        case 'mcu' ; merr = obj.mcuerr;
        case 'time' ; merr = obj.timerr;
        otherwise ; merr = 0;
    end
    [monzeros]=find(monitor==0);
    if ~isempty(monzeros);
        warning('scandata:normalize',...
            ['Selected monitor contains zeros! ',...
            'No Division performed!'])
        monitor=ones(size(obj.x));
    end
    if ~isnumeric(norm)
        warning('scandata:normalize',...
            'non-numeric normalization constant!')
    end
    % Calculate intensity error and possible-monitor errors,
    % including (possible) errors in norm, intensity and mon.
    u={obj.defyname,'monitor','mcu','time'}; % value col. names
    d={'err','monerr','mcuerr','timerr'}; % assos. error names
    for i=1:length(d)
        obj.(d{i})=sqrt( ...
            (obj.getColumn(u{i})*normerr./monitor).^2 ...
            +(norm.*obj.(d{i})./monitor).^2 ...
            +(norm.*obj.getColumn(u{i})*merr./monitor.^2).^2);
    end % this long equation should not be shortened in order
    % to avoid dividing by zero (intensity).
    switch lower(monname)
        case 'monitor';obj.monerr=normerr.*ones(size(monitor));
        case 'mcu' ;obj.mcuerr=normerr.*ones(size(monitor));
        case 'time' ;obj.timerr=normerr.*ones(size(monitor));
    end
    % Calculate normalized intensity/monitors

```

```

        for i = 1:length(u)
            obj.setColumn(u{i},norm.*obj.getColumn(u{i})./monitor);
        end
        obj.y=obj.getColumn(obj.defyname);
    end
end %normalize
function [location,expndhead]=findInHeader(obj,searchstring)
    expndhead = textscan(obj.header,'%s');
    expndhead = expndhead{:};
    location = strcmp(searchstring,expndhead);
    if sum(location)
        [~,location]=max(location);
    else %string not found
        location = -1;
    end
end %findInHeader
function val=getFromHeader(obj,name)
    if length(obj)>1
        val=cell(size(obj));
        for no=1:length(obj);val(no)=obj(no).getFromHeader(name);end
    else
        [lo,eh]=obj.findInHeader(name);
        if lo~-=-1
            val=eh(lo+2);
        else
            val=[];
        end
    end
end % getFromHeader
function scanTitle=findScanTitle(obj)
    if length(obj)>1
        scanTitle = cell(length(obj));
        for
            no=1:length(obj); scanTitle{no}=obj(no).findScanTitle();
        end
    else
        [loc, expndhd] = obj.findInHeader('scan_title');
        expndhd(1:loc+1)=[];
        loc = strcmp('#',expndhd); [~,loc]=max(loc);
        scanTitle = expndhd(1:loc-1);
        scanTitle = [scanTitle{:}];
        obj.scan_title=scanTitle;
    end
end % findScanTitle
function col=findColumn(obj,colname)
    col = strcmp(colname,obj.colnames);
    if any(col);[~,col]=max(col);else col=0;end
end % findColumn
function col=getColumn(obj,colname)
    col = obj.data(obj.findColumn(colname),:);
end %getColumn
function setColumn(obj,colname,colvals)

```

```

    obj.data(obj.findColumn(colname),:)=colvals;
end % setColumn
function stoppedFlag=checkStopped(obj)
    stoppedFlag = 0;
    loc = obj.findInHeader('stopped!!');
    if loc ~= -1
        stoppedFlag = 1;
    end
end % stoppedFlag
function sumCounts = findSum(obj)
    sumCounts = -1;
    [loc, expndhead]=obj.findInHeader('Counts');
    if loc ~= -1
        if size(loc,1)>1
            loc = loc(end);
        end
        sumCounts = str2double(char(expndhead(loc+2)));
    end
end % findSum
function avg = avgColumn(obj,colname)
    avg = mean(obj.getColumn(colname));
end % avgColumn
function tvec = findTemperature(obj,tcname)
    if nargin > 1 && ~isempty(tcname)
        if obj.findColumn(tcname)
            tvec = obj.getColumn(tcname);
        else
            tvec = -1;
        end
    else
        tcnames={'sample_[b]', 't_sample', 'tsample', 'tsample1', ...
            'sample', 'au-fe-tc', 'RTemp', 'tem', 'tt'};
        tvec=-1;
        for no=1:length(tcnames)
            if obj.findColumn(tcnames{no})
                tvec = obj.getColumn(tcnames{no});
            end
        end
    end
    if all(tvec~-1)
        obj.t = tvec;
    end
    if ~nargout; obj.t = tvec; clear('tvec'); end
end % findTemperature
function Weight(obj,cutoff,rel)
    if nargin < 3; rel = true;end
    if nargin < 2; cutoff = 1000;end
    obj.w = ones(1,length(obj.y));
    if obj.hstFlg
        obj.hstW=ones(1,length(obj.hstY));
    end
    if rel

```

```

    avgy = mean(obj.y);
    obj.w(abs(obj.y-avgy)>cutoff)=0;
    if obj.hstFlg
        avgy = mean(obj.hstY);
        obj.hstW(abs(obj.hstY-avgy)>cutoff)=0;
    end
else
    if cutoff > 0
        obj.w(obj.y>=cutoff)=0;
        if obj.hstFlg; obj.hstW(obj.hstY>=cutoff)=0;end
    else
        obj.w(obj.y<=cutoff)=0;
        if obj.hstFlg; obj.hstW(obj.hstY<=cutoff)=0;end
    end
end
end % Weight
function WeightBounds(obj,xbnds,ybnds,reset)
    %WeightBounds([Xmin,Xmax],[Ymin,Ymax],reset{true/false})
    %This function sets the weightvector entries to zero for all
    %points outside of the bounding box defined by [Xmin,Xmax] and
    %[Ymin,Ymax]. If reset is true the object's initial weight
    %vector is reinitialized to ones.
    if nargin<4; reset=false; end
    if nargin<3||isempty(ybnds);
        ybnds = [min(obj.y)-1,max(obj.y)+1];
    end
    if nargin<2||isempty(xbnds)
        xbnds=[min(obj.x)-1,max(obj.x)+1];
    end
    if isempty(obj.w)||reset; obj.w = ones(size(obj.x)); end
    obj.w(obj.x<min(xbnds))=0;
    obj.w(obj.x>max(xbnds))=0;
    obj.w(obj.y<min(ybnds))=0;
    obj.w(obj.y>max(ybnds))=0;
end % WeightBounds
function ThermalAdjust(obj)
    %kept only for backwards compatibility
    obj.CorrectBose()
end % ThermalAdjust
function CorrectBose(obj)
    if length(obj)>1
        for no=1:length(obj); obj(no).CorrectBose; end
    else
        if isempty(obj.e)
            obj.e = obj.data(obj.findColumn('e'),:);
        end
        % See Shirane, Shapiro, and Tranquada
        % page 26, eq. (2.31) and accompanying text.
        pmz = (1-exp(-obj.e ./ (obj.kBoltzman*obj.t)));
        obj.y = obj.y .* pmz;
        obj.data(obj.defyvalue,:)=obj.data(obj.defyvalue,:) .* pmz;
        obj.err = obj.err .* pmz;
    end
end

```

```

end
end % CorrectBose
function CorrectFormFactor(obj,ion)
% Magnetic Form Factor for various ions of 3d transition elements
%
% in the dipole approximation,
% 
$$F = \langle j_0(s) \rangle + (1 - \frac{2}{g}) \langle j_2(s) \rangle$$

% and in the case of spin-only scattering  $g = 2$ 
% 
$$\therefore F = \langle j_0(s) \rangle$$

%
% Values from the International Tables of Crystallography (2006),
% Vol. C, Chapter 4.4, Section 4.4.5, by P.J. Brown, pg 454-461.
%
%  $q = 4 * \pi \sin(\theta) / \lambda$ 
%  $s = \sin(\theta) / \lambda$ 
%  $\therefore q = 4 * \pi * s$  or  $s = \frac{q}{4 * \pi}$  q.e.d.
if length(obj)>1
    for no=1:length(obj); obj(no).CorrectFormFactor(ion); end
else
    switch ion
    case {'Fe', 'Fe0+'};
    C0=[0.0706,35.008,0.3589,15.358,0.5819,5.561,-0.0114];
    case {'Fe+', 'Fe1+'};
    C0=[0.1251,34.963,0.3629,15.514,0.5223,5.591,-0.0105];
    case 'Fe2+';
    C0=[0.0263,34.9597,0.3668,15.9435,0.6188,5.5935,-0.0119];
    case 'Fe3+';
    C0=[0.3972,13.244,0.6295,4.903,-0.0314,0.350,0.0044];
    case 'Fe4+';
    C0=[0.3782,11.380,0.6556,4.592,-0.0346,0.483,0.0005];
    case {'Co', 'Co0+'};
    C0=[0.4139,16.162,0.6013,4.780,-0.1518,0.021,0.1345];
    case {'Co+', 'Co1+'};
    C0=[0.0990,33.125,0.3645,15.177,0.5470,5.008,-0.0109];
    case 'Co2+';
    C0=[.4332,14.355,.5857,4.608,-.0382,.134,.0179,.0711];
    case 'Co3+';
    C0=[.3902,12.508,.6324,4.457,-.15,.034,.1272,.0515];
    case 'Co4+';
    C0=[0.3515,10.778,0.6778,4.234,-0.0389,0.241,0.0098];
    case {'Mn', 'Mn0+'};
    C0=[0.2438,24.963,0.1472,15.673,0.6189,6.540,-0.0105];
    case {'Mn+', 'Mn1+'};
    C0=[-0.0138,0.421,0.4231,24.668,0.5905,6.655,-0.0010];
    case 'Mn2+';
    C0=[0.4220,17.684,0.5948,6.0050,0.0043,-0.609,-0.0219];
    case 'Mn3+';
    C0=[0.4198,14.283,0.6054,5.469,0.9241,-0.009,-0.9498];
    case 'Mn4+';
    C0=[0.3760,12.566,0.6602,5.133,-0.0372,0.563,0.0011];
    case {'Cu', 'Cu0+'};
    C0=[0.0909,34.984,0.4088,11.443,0.5128,3.825,-0.0124];

```

```

case {'Cu+', 'Cu1+'};
C0=[0.0749,34.966,0.4147,11.754,0.5238,3.850,-0.0127];
case 'Cu2+';
C0=[0.0232,34.969,0.4023,11.567,0.5882,3.843,-0.0137,0.0532];
case 'Cu3+';
C0=[0.0031,34.907,0.3582,10.914,0.6531,3.828,-0.0147];
case 'Cu4+';
C0=[-0.0132,30.682,0.2801,11.163,0.7490,3.817,-0.0165];
otherwise; C0=[1,0,0,0,0,0,0];
warning('formfactor:ionSwitch',...
        ['I don''t know the parameters that',...
         ' describe the form factor for ',ion,',',...
         'Feel free to teach me something new.'])
end
%< j_0(s) > is really < j_0(s^2) > :
ss = (obj.q/4/pi).^2;
j0=C0(1)*exp(-C0(2).*ss)+C0(3)*exp(-C0(4).*ss)...
    +C0(5)*exp(-C0(6).*ss)+C0(7);
ff2=j0.^2;
obj.y=obj.y./ff2;
obj.err=obj.err./ff2;
obj.data(obj.defyvalue,:)=obj.data(obj.defyvalue,)./ff2;
end
end % CorrectFormFactor
function Convert_mbpSr_uB2(obj)
if length(obj)>1
for i=1:length(obj);obj(i).Convert_mbpSr_uB2; end
else
% Magnetic intensity should normally be cast in  $\mu_B^2$  (per eV?)
% The sole purpose of this routine is to unify this conversion
% in order to (hopefully) prevent errors due to typos.
r02= 290.6;% mb/Sr
cv = 4*pi/(r02); %  $\mu_B^2$ /(mb/Sr) %%% There may be factors
obj.y=obj.y*cv; % of  $\sum_{i,j} \chi_{i,j}$ 
obj.err=obj.err*cv; % multiplicity missing
obj.data(obj.defyvalue,:)=obj.data(obj.defyvalue,)*cv;
end
end % Convert_mbpSr_uB2
function removePts(obj,w)
% Data points with a weight of zero are removed.
% If w is empty, nothing happens to the data.
if nargin < 2; w = obj.w; end; lw=length(w);
if size(obj.data,2)==lw; obj.data(:,~w)=[]; end
if length(obj.err) ==lw; obj.err(~w) =[]; end
if length(obj.EXP) ==lw; obj.EXP(~w) =[]; end
if length(obj.monerr)==lw; obj.monerr(~w)=[]; end
if length(obj.mcuerr)==lw; obj.mcuerr(~w)=[]; end
if length(obj.timerr)==lw; obj.timerr(~w)=[]; end
if length(obj.w) ==lw; obj.w(~w) =[]; end
if obj.hstFlg;obj.hstY(~obj.hstW)=NaN;end
obj.fillVectors()
end % removePts

```

```

function Tcolor(obj,temperatures,colors)
    % This function is rarely used; remove?
    if nargin < 2; colors = 'b';end
    if nargin < 1; temperatures = 1 ;end
    if isempty(obj.t)
        obj.t = obj.findTemperature;
    end
    [~,b] = min(abs(mean(obj.t) - temperatures));
    obj.color = colors(b,:);
end % Tcolor
function [h,k,l,e,i,di,EXP,t]=read4ResLib(obj)
    if length(obj)>1
        np=0;
        for j=1:length(obj); np=np+length(obj(j).x); end
        h=zeros(np,1);k=h;l=h;e=h;i=h;di=h;t=h;EXP=[];
        p=0;
        for j=1:length(obj)
            np=length(obj(j).x);
            [h(1+p:np+p),k(1+p:np+p),l(1+p:np+p),e(1+p:np+p),...
                i(1+p:np+p),di(1+p:np+p),EXPt,t(1+p:np+p)]=...
                obj(j).read4ResLib();
            p=np+p;
            EXP=[EXP;EXPt];
        end
    else
        if isempty(obj.h)||isempty(obj.k)||isempty(obj.l)
            obj.fillMillerVecs()
        end
        h=obj.h(:);k=obj.k(:);l=obj.l(:);
        e=obj.e(:);i=obj.y(:);di=obj.err(:);t=obj.t(:);
        if isempty(obj.EXP)
            obj.createRLEXP
        end
        EXP=obj.EXP;
        if any(obj.w==0);
            h(obj.w==0)=[];k(obj.w==0)=[];l(obj.w==0)=[];
            e(obj.w==0)=[];i(obj.w==0)=[];di(obj.w==0)=[];
            t(obj.w==0)=[];EXP(obj.w==0)=[];
        end
    end
end % read4ResLib
function conv = ConvRes(obj,sfnc,bfnc,METHOD,ACCURACY,p)
    if nargin < 4 || isempty(METHOD);
        METHOD = 'mc';
        warning('scandata:ConvRes:METHOD','MonteCarlo method used');
    end
    if nargin<3; bfnc=[]; end

    if ~isfield(obj,'EXP')||isempty(obj.EXP)
        obj.createRLEXP();
    end
    aEXP = obj.EXP;

```

```

if any([isempty(obj.h),isempty(obj.k),isempty(obj.l)])
    obj.fillMillerVecs()
end
hh=obj.h(:);kk=obj.k(:);ll=obj.l(:);ee=obj.e(:);
obj.rl.conv = ConvRes(sfnc,bfnc,hh,kk,ll,ee,...
    aEXP,METHOD,ACCURACY,p);
if nargin>0; conv=obj.rl.conv; end
end % ConvRes
function conv = ConvResSMA(obj,sfnc,bfnc,METHOD,ACCURACY,p)
if nargin < 4 || isempty(METHOD);
    METHOD = 'mc';
    warning('scandata:ConvRes:METHOD','MonteCarlo method used');
end
if nargin < 3; bfnc = []; end

if ~isfield(obj,'EXP')||isempty(obj.EXP)
    obj.createRLEXP();
end
aEXP = obj.EXP;

if any([isempty(obj.h),isempty(obj.k),isempty(obj.l)])
    obj.fillMillerVecs()
end
hh=obj.h(:);kk=obj.k(:);ll=obj.l(:);ee=obj.e(:);
obj.rl.cE=ee;obj.rl.cH=hh;obj.rl.cK=kk;obj.rl.cL=ll;
obj.rl.conv = ConvResSMA(sfnc,bfnc,hh,kk,ll,ee,...
    aEXP,METHOD,ACCURACY,p);
if nargin>0; conv=obj.rl.conv; end
end % ConvResSMA
function [pa,dpa,chisqN,sim,CN,pQ,nit,kvg,details]=...
    FitConv(obj,sf,bf,MET,ACC,p,i,nmx,tol,dtol)
if nargin < 10; dtol=1e-5; end
if nargin < 9; tol = 0.001;end
if nargin < 8; nmx = 100; end
if nargin < 7; i = ones(size(p)); end
lv=zeros(size(obj));
for no=1:length(obj)
    lv(no)=length(obj(no).x);
end
hh=zeros(sum(lv),1);kk=hh;ll=hh;ee=hh;ii=hh;ie=hh;
xx=[];
j=1;
for no=1:length(obj)
    [ht,kt,lt,et,it,dt,xt]=obj(no).read4ResLib;
    hh(j:j+lv(no)-1)=ht;kk(j:j+lv(no)-1)=kt;ll(j:j+lv(no)-1)=lt;
    ee(j:j+lv(no)-1)=et;ii(j:j+lv(no)-1)=it;ie(j:j+lv(no)-1)=dt;
    xx=[xx;xt(:)]; j=j+lv(no);
end
[pa,dpa,chisqN,sim,CN,pQ,nit,kvg,details]=FitConv(...
    hh,kk,ll,ee,xx,ii,ie,sf,bf,p,i,MET,ACC,nmx,tol,dtol);
rp.pa=pa; rp.dpa=dpa; rp.chisqN=chisqN;
j=1;

```

```

for no=1:length(obj)
    rp.sim=sim(j:j+lv(no)-1);
    obj(no).rl=rp;
    j=j+lv(no);
end
if nargout < 9; clear('details');end
if nargout < 8; clear('kvg');end
if nargout < 7; clear('nit');end
if nargout < 6; clear('pQ');end
if nargout < 5; clear('CN');end
if nargout < 4; clear('sim');end
if nargout < 3; clear('chisqN');end
if nargout < 2; clear('dpa');end
if nargout < 1; clear('pa');end
end % FitConv
function [pa,dpa,chisqN,sim,CN,pQ,nit,kvg,details]=...
    FitConvSMA(obj,sf,bf,MET,ACC,p,i,nmx,tol,dtol)
if nargin < 10; dtol=1e-5; end
if nargin < 9; tol = 0.001;end
if nargin < 8; nmx = 100; end
if nargin < 7; i = ones(size(p)); end
lv=zeros(size(obj));
for no=1:length(obj)
    lv(no)=length(obj(no).x);
end
hh=zeros(sum(lv),1);kk=hh;ll=hh;ee=hh;ii=hh;ie=hh;
xx=[];
j=1;
for no=1:length(obj)
    [ht,kt,lt,et,it,dt,xt]=obj(no).read4ResLib;
    hh(j:j+lv(no)-1)=ht;kk(j:j+lv(no)-1)=kt;ll(j:j+lv(no)-1)=lt;
    ee(j:j+lv(no)-1)=et;ii(j:j+lv(no)-1)=it;ie(j:j+lv(no)-1)=dt;
    xx=[xx;xt(:)]; j=j+lv(no);
end
[pa,dpa,chisqN,sim,CN,pQ,nit,kvg,details]=FitConvSMA(...
    hh,kk,ll,ee,xx,ii,ie,sf,bf,p,i,MET,ACC,nmx,tol,dtol);
rp.pa=pa; rp.dpa=dpa; rp.chisqN=chisqN;
j=1;
for no=1:length(obj)
    rp.sim=sim(j:j+lv(no)-1);
    obj(no).rl=rp;
    j=j+lv(no);
end
if nargout < 9; clear('details');end
if nargout < 8; clear('kvg');end
if nargout < 7; clear('nit');end
if nargout < 6; clear('pQ');end
if nargout < 5; clear('CN');end
if nargout < 4; clear('sim');end
if nargout < 3; clear('chisqN');end
if nargout < 2; clear('dpa');end
if nargout < 1; clear('pa');end

```

```

end % FitConvSMA
function createRLEXP(obj)
    % % % Each datafile contains lattice parameters, and ubmatrix
    % (from which it should be possible to pull the orienting
    % vectors) in the header, plus all energies from which it
    % should be possible to determine which (if any) is fixed.
    [loc,eh]=obj.findInHeader('ubconf');
    expFile=[obj.filename(1:end-34) 'UBConf/' cell2mat(eh(loc+2))];
    %this will ultimately fail if we're not on a UNIX-like system
    %OR if the filename-length ever changes!!!!
    fid = fopen(expFile);
    lne = fgetl(fid);
    while ~strcmp(lne, '[UBMode]')
        lne = fgetl(fid);
    end
    mode = fgetl(fid);
    mode = str2double(mode(end));
    frewind(fid);
    switch mode
        case 1
            lne = fgetl(fid);
            while ~strncmp(lne, 'ScatteringPlaneVectors', 22)
                lne = fgetl(fid);
            end
            lne=lne(23:end);
            lne(lne==' ')=[]; lne(lne=='"')=[]; lne(lne=='=')=[];
            lne=str2num(lne);
            orient1=lne(1:3);
            orient2=lne(4:6);
            frewind(fid);
            lne = fgetl(fid);
            while ~strncmp(lne, 'LatticeParams', 13)
                lne = fgetl(fid);
            end
            lne=lne(14:end);
            lne(lne==' ')=[]; lne(lne=='"')=[]; lne(lne=='=')=[];
            lattice = str2num(lne);
            frewind(fid);
            lne = fgetl(fid);
            while ~strncmp(lne, 'Energy', 6)
                lne = fgetl(fid);
            end
            lne=lne(7:end);
            lne(lne==' ')=[]; lne(lne=='"')=[]; lne(lne=='=')=[];
            energy = str2double(lne);
            frewind(fid);
        case 2
            lne = fgetl(fid);
            while ~strncmp(lne, 'Peak1', 5)
                lne = fgetl(fid);
            end
            lne=lne(6:end);

```

```

lne(lne==' ')=[];lne(lne=='"')=[];lne(lne=='=')=[];
lne = str2num(lne);
orient1 = lne(1:3);
frewind(fid);
lne = fgetl(fid);
while ~strncmp(lne,'Peak2',5)
    lne = fgetl(fid);
end
lne=lne(6:end);
lne(lne==' ')=[];lne(lne=='"')=[];lne(lne=='=')=[];
lne = str2num(lne);
orient2 = lne(1:3);
frewind(fid);
lne = fgetl(fid);
while ~strncmp(lne,'LatticeParams',13)
    lne = fgetl(fid);
end
lne=lne(14:end);
lne(lne==' ')=[];lne(lne=='"')=[];lne(lne=='=')=[];
lattice = str2num(lne);
frewind(fid);
lne = fgetl(fid);
while ~strncmp(lne,'Energy',6)
    lne = fgetl(fid);
end
lne=lne(7:end);
lne(lne==' ')=[];lne(lne=='"')=[];lne(lne=='=')=[];
energy = str2double(lne);
frewind(fid);
otherwise
    warning('scandata:creatorLEXP',...
        'ResLib EXP structure not created, unknown UBMode')
    % Add extra cases for other UBModes when they come up.
end
fclose(fid);
[loc,eh]=obj.findInHeader('monochromator');
mon = cell2mat(eh(loc+2)); mon = [mon(1:2) '(' mon(3:end) ')'];
[loc,eh]=obj.findInHeader('analyzer');
ana = cell2mat(eh(loc+2)); ana = [ana(1:2) '(' ana(3:end) ')'];
[loc,eh]=obj.findInHeader('collimation');
hcol = cell2mat(eh(loc+2)); hcol(hcol=='-')=',';
hcol = str2num(hcol);

[loc,eh]=obj.findInHeader('sense');
sense = eh(loc+2); sense = sense{:};
switch sense
    case '+-';mondir=-1;dir1= 1;dir2= 1;
    case '+-+';mondir= 1;dir1= 1;dir2= 1;
    case '---';mondir=-1;dir1=-1;dir2=-1;
    case '---+';mondir=-1;dir1=-1;dir2= 1;
    case '-++';mondir=-1;dir1= 1;dir2=-1;
    case '+++';mondir= 1;dir1=-1;dir2=-1;

```

```

case '++-';mondir= 1;dir1=-1;dir2= 1;
case '+--';mondir= 1;dir1= 1;dir2=-1;
otherwise
    warning('scandata:createRLEXP',...
            'Unknown sense, using default values. ');
    mondir=1;dir1=1;dir2=1;
end

aEXP.mono.tau=mon;
aEXP.mono.mosaic=30;
aEXP.mono.vmosaic=45;
aEXP.ana.tau=ana;
aEXP.ana.mosaic=40;
aEXP.ana.vmosaic=25;
aEXP.sample.a=lattice(1);
aEXP.sample.b=lattice(2);
aEXP.sample.c=lattice(3);
aEXP.sample.alpha=lattice(4);
aEXP.sample.beta=lattice(5);
aEXP.sample.gamma=lattice(6);
aEXP.hcol = hcol;
aEXP.vcol=[180 300 300 600];
aEXP.efixed=energy;
aEXP.infin=-1; %default value, I think. fixed final energy
aEXP.orient1=orient1;
aEXP.orient2=orient2;
aEXP.dir1=dir1;
aEXP.dir2=dir2;
aEXP.mondir=mondir;

global RES_CONSTANTS
if isfield(RES_CONSTANTS,'method')&&RES_CONSTANTS.method==1
    % Set various parameters for Popovici method
    % defaulting to HB3 values and a typical coalignment
    if isfield(RES_CONSTANTS,'sample')
        if isfield(RES_CONSTANTS.sample,'mosaic')
            aEXP.sample.mosaic=RES_CONSTANTS.sample.mosaic;
        end
        if isfield(RES_CONSTANTS.sample,'shape')
            aEXP.sample.shape=RES_CONSTANTS.sample.shape;
        end
    end
    if isfield(RES_CONSTANTS,'beam')
        if isfield(RES_CONSTANTS.beam,'width')
            aEXP.beam.width=RES_CONSTANTS.beam.width;
        end
        if isfield(RES_CONSTANTS.beam,'height')
            aEXP.beam.height=RES_CONSTANTS.beam.height;
        end
    end
    if isfield(RES_CONSTANTS,'detector')
        if isfield(RES_CONSTANTS.detector,'width')

```

```

        aEXP.detector.width=RES_CONSTANTS.detector.width;
    end
    if isfield(RES_CONSTANTS.detector,'height')
        aEXP.detector.height=RES_CONSTANTS.detector.height;
    end
end
if isfield(RES_CONSTANTS,'mono')
    if isfield(RES_CONSTANTS.mono,'width')
        aEXP.mono.width=RES_CONSTANTS.mono.width;
    end
    if isfield(RES_CONSTANTS.mono,'height')
        aEXP.mono.height=RES_CONSTANTS.mono.height;
    end
    if isfield(RES_CONSTANTS.mono,'depth')
        aEXP.mono.depth=RES_CONSTANTS.mono.depth;
    end
    if isfield(RES_CONSTANTS.mono,'rv')
        aEXP.mono.rv=RES_CONSTANTS.mono.rv;
    end
    if isfield(RES_CONSTANTS.mono,'rh')
        aEXP.mono.rh=RES_CONSTANTS.mono.rh;
    end
end
if isfield(RES_CONSTANTS,'ana')
    if isfield(RES_CONSTANTS.ana,'width')
        aEXP.ana.width=RES_CONSTANTS.ana.width;
    end
    if isfield(RES_CONSTANTS.ana,'height')
        aEXP.ana.height=RES_CONSTANTS.ana.height;
    end
    if isfield(RES_CONSTANTS.ana,'depth')
        aEXP.ana.depth=RES_CONSTANTS.ana.depth;
    end
    if isfield(RES_CONSTANTS.ana,'rv')
        aEXP.ana.rv=RES_CONSTANTS.ana.rv;
    end
    if isfield(RES_CONSTANTS.ana,'rh')
        aEXP.ana.rh=RES_CONSTANTS.ana.rh;
    end
end
if isfield(RES_CONSTANTS,'monitor')
    if isfield(RES_CONSTANTS.monitor,'width')
        aEXP.monitor.width=RES_CONSTANTS.monitor.width;
    end
    if isfield(RES_CONSTANTS.monitor,'height')
        aEXP.monitor.height=RES_CONSTANTS.monitor.height;
    end
end
if isfield(RES_CONSTANTS,'arms')
    aEXP.arms=RES_CONSTANTS.arms;
end
end

```

```

if ~isfield(aEXP, 'sample') || ~isfield(aEXP.sample, 'mosaic')
    aEXP.sample.mosaic=32;
end
if ~isfield(aEXP, 'sample') || ~isfield(aEXP.sample, 'shape')
    %aEXP.sample.shape=sqrt(diag([4,2,3].^2/12));
    aEXP.sample.shape=diag([3,3,3].^2/12);
end
if ~isfield(aEXP, 'beam') || ~isfield(aEXP.beam, 'width')
    aEXP.beam.width=15/sqrt(12);
end
if ~isfield(aEXP, 'beam') || ~isfield(aEXP.beam, 'height')
    aEXP.beam.height=15/sqrt(12);
end
if ~isfield(aEXP, 'detector') || ~isfield(aEXP.detector, 'width')
    aEXP.detector.width=4/sqrt(12);
end
if ~isfield(aEXP, 'detector') || ~isfield(aEXP.detector, 'height')
    aEXP.detector.height=12/sqrt(12);
end
if ~isfield(aEXP, 'mono') || ~isfield(aEXP.mono, 'width')
    aEXP.mono.width=7.62/sqrt(12);
end
if ~isfield(aEXP, 'mono') || ~isfield(aEXP.mono, 'height')
    aEXP.mono.height=10.16/sqrt(12);
end
if ~isfield(aEXP, 'mono') || ~isfield(aEXP.mono, 'depth')
    aEXP.mono.depth=0.25/sqrt(12);
end
if ~isfield(aEXP, 'ana') || ~isfield(aEXP.ana, 'width')
    aEXP.ana.width=7.62/sqrt(12);
end
if ~isfield(aEXP, 'ana') || ~isfield(aEXP.ana, 'height')
    aEXP.ana.height=7/sqrt(12);
end
if ~isfield(aEXP, 'ana') || ~isfield(aEXP.ana, 'depth')
    aEXP.ana.depth=0.2/sqrt(12);
end
if ~isfield(aEXP, 'ana') || ~isfield(aEXP.ana, 'rv')
    aEXP.ana.rv=9.844*2.54;%cm,
end
if ~isfield(aEXP, 'monitor') || ~isfield(aEXP.monitor, 'width')
    aEXP.monitor.width=5/sqrt(12);
end
if ~isfield(aEXP, 'monitor') || ~isfield(aEXP.monitor, 'height')
    aEXP.monitor.height=12/sqrt(12);
end
if ~isfield(aEXP, 'arms')
    aEXP.arms=[650 190 160 86 60];
end
aEXP.method=1;
if ~isfield(aEXP, 'mono') || ~isfield(aEXP.mono, 'rv')
    %include HB3 varying monochromator focusing

```

```

        monorv=obj.getColumn('focal_length');
        aEXP= repmat(aEXP,size(obj.ei));
        for i=1:length(aEXP)
            %aEXP(i).mono.rv = ...
            %    obj.hbar/sqrt(2*obj.neutronmass) ...
            %    *GetTau(aEXP(i).mono.tau)/sqrt(obj.ei(i)) ...
            %    /(1/aEXP(i).arms(1) + 1/aEXP(i).arms(2));
            aEXP(i).mono.rv = 2*monorv(i);
        end
    end
end
% in case aEXP is not the length of obj.ei
aEXP=repmat(aEXP,size(obj.ei)./size(aEXP));
obj.EXP=aEXP(:);
end % createRLEXP
function fillMillerVecs(obj)
    if length(obj)>1
        for no=1:length(obj)
            obj(no).fillMillerVecs()
        end
    else
        obj.h = obj.getColumn('h');
        obj.k = obj.getColumn('k');
        obj.l = obj.getColumn('l');
    end
end % fillMillerVecs
function findLatticeConstants(obj)
    lcsstr=obj.getFromHeader('latticeconstants');lcsstr=lcsstr{:};
    lcsvec=str2num(lcsstr);
    obj.alat = lcsvec(1);
    obj.blat = lcsvec(2);
    obj.clat = lcsvec(3);
    obj.alpha = lcsvec(4);
    obj.beta = lcsvec(5);
    obj.gamma = lcsvec(6);
end % findLatticeConstants
function monitorHarmonic(obj,Tmoderator)
    %The Monitor overcounts at low energies due to higher-order
    %harmonics in the beam. This function accounts for the
    %overcounting by multiplying the observed intensity by a factor
    %that is always greater than 1 (approches 1 as  $E_i \gg k_b T_{moderator}$ )
    %See the Triple Axis book by Shirane, Shapiro & Tranquada
    %for a better explanation.
    if nargin < 2; Tmoderator = 350; end %Moderator temp. ~350K
    if length(obj) > 1
        for no=1:length(obj);
            obj(no).monitorHarmonic(Tmoderator);
        end
    return
end
if isempty(obj.ei); obj.ei = obj.getColumn('ei'); end
S = obj.ei/(obj.kBoltzman*Tmoderator); %  $\frac{E_i}{k_B T}$ 

```

```

S = 1+4*exp(-3*S)+ 9*exp(-8*S) +16*exp(-15*S)+...
    25*exp(-24*S)+36*exp(-25*S)+49*exp(-48*S)+...
    64*exp(-63*S)+81*exp(-80*S)+100*exp(-99*S);
obj.y = obj.y.*S;
obj.data(obj.defyvalue,:) = obj.data(obj.defyvalue,:).*S;
obj.err = obj.err.*S;
% An alternative approach would be to correct the monitor
% counts by dividing by S. It's unclear which approach is best.
end % monitorHarmonic
function [X,Y,Er,T,Edg,E]=createHistogram(obj,varargin)
eks = obj.x; why = obj.y; air = obj.err;
if ~isempty(obj.t); tee = obj.t; tF = true; else tF = false; end
if ~isempty(obj.e); eee = obj.e; eF = true; else eF = false; end
mult = false;
if ~isempty(varargin)
    Z = scandata.empty(size(varargin,2),0);
    for i = 1:length(varargin); Z(i) = varargin{i}; end
    z = cell(size(Z));
    [z{:}] = Z.x;   xvs = [{eks} z]; eks = [eks z{:}];
    [z{:}] = Z.y;   yvs = [{why} z]; why = [why z{:}];
    [z{:}] = Z.err; evs = [{air} z]; air = [air z{:}];
    if tF; [z{:}] = Z.t; tvs = [{tee} z]; tee = [tee z{:}]; end
    if eF; [z{:}] = Z.e; Evs = [{eee} z]; eee = [eee z{:}]; end
    nvs = cell(size(xvs)); cvs = nvs; bvs = nvs; mult = true;
end
xl = min(eks); xu = max(eks);
if mult
    eks = sort(eks);
    eks(diff(eks)<=1e-3)=[]; %remove repeated x's
    edges = [(3*eks(1)-eks(2))/2,... %lower edge
             eks(1:end-1)+diff(eks)/2,... %midpoint edges
             (3*eks(end)-eks(end-1))/2]; %upper edge
    for i=1:length(xvs)
        [nvs{i},bvs{i}] = histc(xvs{i},edges);
        cvs{i} = nvs{i}(1:end-1);
    end
    cond = ~all([cvs{:}]);

    xxx = cell2mat(xvs);
    while cond && length(edges)>2
        n = cell2mat(cvs{:});
        [~,least]=min(sum(n));
        bbb = cell2mat(bvs);
        if least == 1
            edges(least+1)=[];
        elseif least >= length(edges)-1
            edges(least)=[];
        else
            avgP = sum(xxx(bbb==least+1))/sum(bbb==least+1);
            avgM = sum(xxx(bbb==least-1))/sum(bbb==least-1);
            avgX = sum(xxx(bbb==least))/sum(bbb==least);
            avgv = [abs(avgM-avgX),abs(avgP-avgX)];
        end
    end
end

```

```

        [~,ccc]= min(avgv);
        switch ccc
            case 1
                edges(least)=[];
            case 2
                edges(least+1)=[];
        end
    end
    for i=1:length(xvs)
        [nvs{i},bvs{i}] = histc(xvs{i},edges);
        cvs{i} = nvs{i}(1:end-1);
    end
    cond = ~all([cvs{:}]);
end
yb = zeros(size(nvs{1}(1:end-1)));
eb = yb; tb=yb; Eb=yb;
for i = 1:length(yb)
    totpts = 0;
    for j = 1:length(nvs)
        v = bvs{j} == i;
        totpts = totpts + sum(v);
        yb(i) = yb(i) + sum(yvs{j}(v))/sum(v);
        eb(i) = eb(i) + sum(evs{j}(v).^2);
        if tF;tb(i) = tb(i) + sum(tvsv{j}(v));end
        if eF;Eb(i) = Eb(i) + sum(Evs{j}(v));end
    end
    eb(i) = sqrt(eb(i));
    tb(i) = tb(i)/totpts;
    Eb(i) = Eb(i)/totpts;
end
tb=tb/length(nvs);
Eb=Eb/length(nvs);
else
    %to avoid dividing by zero (or something close to it)
    d = diff(sort(eks)); d(abs(d)<=1e-3)=[];
    xs = min(abs(d));
    no = ceil((xu-xl)/xs)+1;
    edges = linspace(xl-xs/2,xu+xs/2,no);
    [n,b] = histc(eks,edges);
    cond = ~all(n(1:end-1));
    while cond && no>1 %if any bins have n=0 increase bin size
        no = no - 1;
        xs = (xu-xl)/(no-1);
        edges = linspace(xl-xs/2,xu+xs/2,no);
        [n,b] = histc(eks,edges);
        cond = ~all(n(1:end-1));
    end
    yb = zeros(size(n(1:end-1)));
    eb = yb;
    if tF; tb = eb; else tb=[];end
    if eF; Eb = eb; else Eb=[];end
    for i=1:length(yb)

```

```

        v = b==i;
        yb(i) = sum(why(v))/sum(v);
        eb(i) = sqrt(sum(air(v).^2)/sum(v));
        if tF; tb(i) = sum(tee(v))/sum(v);end
        if eF; Eb(i) = sum(eee(v))/sum(v);end
    end
end
xb = edges(1:end-1) + diff(edges)/2;
if ~nargout
    obj.hstX = xb;
    obj.hstY = yb;
    obj.hstEr = eb;
    obj.hstT = tb;
    obj.hstEdg = edges;
    obj.hstE = Eb;
    obj.hstFlg = true;
else
    X = xb;
    Y = yb;
    Er = eb;
    T = tb;
    Edg = edges;
    E = Eb;
end
end % createHistogram
function findEnergies(obj)
    if obj.findColumn('ei'); obj.ei = obj.getColumn('ei'); end
    if obj.findColumn('e'); obj.e = obj.getColumn('e'); end
    if obj.findColumn('ef'); obj.ef = obj.getColumn('ef'); end
end % findEnergies
function crpoints(obj,dontAvg,tol)
    % obj.crpoints(dontAvg,tol)
    % dontAvg is a cellstr of columns not to average, default value
    % is {time,detector,monitor,mcu} [pass empty set for default]
    % tol is the tolerance in x, default 0.0002
    % crpoints averages repeated points that are within some
    % tolerance in default-x value
    defdontAvg={'time','detector','monitor','mcu'};
    if nargin < 2||isempty(dontAvg);dontAvg = defdontAvg; end
    if nargin < 3 || isempty(tol); tol = 0.0005; end

    if length(obj)>1
        for i=1:length(obj); obj(i).crpoints(dontAvg,tol); end
    else
        %sort the data matrix and the point matrix. the advantage of
        %doing so is that repeated points end up next to each other in
        %the matrix
        tosort = [obj.data;obj.err;obj.monerr;obj.mcuerr;obj.timerr];
        sorted = sortrows(tosort',-obj.defxvalue); %WARNING: data^T
        dataT = sorted(:,1:end-4);
        errT = sorted(:,end-3);
        monerrT=sorted(:,end-2);
    end
end

```

```

mcuerrT=sorted(:,end-1);
timeerrT=sorted(:,end);

rpt = abs(diff(dataT(:,obj.defxvalue))) < tol;
drpt = diff(rpt); %diff(diff(x))
rid = 1; ron=false; % rid == repeat-ID
lrpt=zeros(size(rpt));
for i=1:length(drpt);
    if drpt(i)==1; ron=true; drpt(i)=rid; lrpt(i+1)=rid;
    elseif drpt(i)==-1;
        drpt(i)=rid;lrpt(i+1)=-rid; ron=false; rid = rid+1;
    elseif ron;
        drpt(i)=rid; lrpt(i+1)=-rid;
    end
end
rpt1 = rpt(1);
if rpt1==1;
    drpt(1)=1;
    lrpt(1)=1;lrpt(2)=-1;
end
rpt = [rpt1;drpt]; %tested working for rpt(1)=0, and rpt(1)=1.

xcol = dataT(:,obj.defxvalue);
if abs(xcol(end)-xcol(end-1))<tol
    rpt=[rpt;max(rpt)];
    lrpt=[lrpt;-abs(lrpt(end))]; %% fixed 20120414
    % abs() added 2013-03-12 to account for the situation of
    % multiple points at the end being combined into one, i.e.
    % [... 5 -5] should become [... 5 -5 -5] not [... 5 -5 5]!
else
    rpt=[rpt;0];
    lrpt=[lrpt;0];
end

%dontAvg = {'time','detector','monitor','mcu'};
xxx=length(obj.colnames);yyy=length(dontAvg);
damat = repmat(dontAvg,xxx,1);
hdmat = repmat(obj.colnames,1,yyy);
mtchmat = strcmp(damat,hdmat);
avgFlag = ~logical(sum(mtchmat,2));

avgcts = ~any(strcmp('detector',dontAvg));
avgmon = ~any(strcmp('monitor',dontAvg));
avgmcu = ~any(strcmp('mcu',dontAvg));
avgtme = ~any(strcmp('time',dontAvg));
for i=1:max(rpt)
    if any(size(sum(dataT(rpt==i,:),1))~=size(dataT(lrpt==i,:)))
        warning('scandata:crpoints','dimension mismatch')
    end
    dataT(lrpt==i,:)=sum(dataT(rpt==i,:));
    errT(lrpt==i)=sqrt(sum(errT(rpt==i).^2));
end

```

```

monerrT(lrpt==i)=sqrt(sum(monerrT(rpt==i).^2));
mceuerrT(lrpt==i)=sqrt(sum(mceuerrT(rpt==i).^2));
timeerrT(lrpt==i)=sqrt(sum(timeerrT(rpt==i).^2));
if avgcts
    errT(lrpt==i)=errT(lrpt==i)/sum(rpt==i);
end
if avgmon
    monerrT(lrpt==i)=monerrT(lrpt==i)/sum(rpt==i);
end
if avgmcu
    mceuerrT(lrpt==i)=mceuerrT(lrpt==i)/sum(rpt==i);
end
if avgtme
    timeerrT(lrpt==i)=timeerrT(lrpt==i)/sum(rpt==i);
end
try
    dataT(lrpt==i,avgFlag)=dataT(lrpt==i,avgFlag)/sum(rpt==i);
catch problem
    disp('More colnames than columns.')
    disp(' Does one have a space?')
    rethrow(problem)
end
end
dataT(lrpt<0,:)=[];errT(lrpt<0)=[];
monerrT(lrpt<0)=[];mceuerrT(lrpt<0)=[];timeerrT(lrpt<0)=[];

obj.data=dataT'; %transpose back
obj.err=errT';
obj.monerr=monerrT';
obj.mceuerr=mceuerrT';
obj.timerr=timeerrT';
obj.x = obj.data(obj.defxvalue,:);
obj.y = obj.data(obj.defyvalue,:);
obj.q = obj.data(obj.findColumn('q'),:);

if ~isempty(obj.w); obj.Weight(); end
if ~isempty(obj.h); obj.fillMillerVecs;end
if ~isempty(obj.alat); obj.findLatticeConstants;end
obj.findEnergies
obj.findTemperature
if obj.hstFlg
    [obj.hstX,obj.hstY,obj.hstEr,obj.hstT,...
    obj.hstEdg,obj.hstE] = obj.createHistogram();
end
end
end % crpoints
function bin(obj,binsec)
if nargin<2; binsec=[];end
if length(obj)>1
for i=1:length(obj)
    obj(i).bin(binsec)
end
end

```

```

else
    if isempty(binspec);
        binspec=[min(obj.x),...
                 mode(abs(diff(unique(sort(obj.x))))),max(obj.x)];
    elseif length(binspec)==1
        binspec=[min(obj.x),binspec,max(obj.x)];
    end
    sx=min(binspec([1,3]));
    dx=abs(binspec(2));
    lx=max(binspec([1,3]));
    if (lx-sx)<dx %guarantee at least one bin
        bc=(lx+sx)/2;
        %be=bc+dx*0.5*[-1,1]; % uncomment for bin edges
    else
        bc=sx:dx:lx;
        %be=[bc-0.5*dx,lx+0.5*dx]; % uncomment for bin edges
    end
    dbe=[obj.data;obj.err.^2;obj.monerr.^2;...
         obj.mcuerr.^2;obj.timerr.^2];
    [hno,pno]=size(dbe);

    bindbe=zeros(hno,length(bc));
    binno=bindbe;
    for i=1:pno
        [~,b]=min(abs(obj.x(i)-bc));
        bindbe(:,b)=bindbe(:,b)+dbe(:,i);
        binno(:,b)=binno(:,b)+1;
    end
    bindbe=bindbe./binno;
    bindbe(:,~sum(binno))=[];
    obj.data=bindbe(1:end-4,:);
    obj.fillVectors
    % We're missing a factor of 1/binno for the errors, since
    % the error in x=sum(y) is dx=sqrt(sum(dy.^2))/numel(y)
    binno(:,~sum(binno))=[];
    bindbe=bindbe./binno;
    obj.err =sqrt(bindbe(end-3,:));
    obj.monerr=sqrt(bindbe(end-2,:));
    obj.mcuerr=sqrt(bindbe(end-1,:));
    obj.timerr=sqrt(bindbe(end ,:));
end
end % bin
function fixedFinalEnergyCorrection(obj)
    %  $E = \frac{\hbar k^2}{2m}$  so  $\frac{k_f}{k_i} = \sqrt{\frac{E_f}{E_i}}$ 
    % the energy vectors were filled at object creation
    kfk_i = sqrt(obj.ef ./ obj.ei);
    obj.y = obj.y ./ kfk_i;
    obj.data(obj.defyvalue,:)=obj.data(obj.defyvalue,:)./kfk_i;
    obj.err=obj.err ./ kfk_i;
end % fixedFinalEnergyCorrection
function replacedata(obj,data)

```

```

    obj.data=data;
    obj.fillVectors
end
function replaceerror(obj,err,monerr,mcuerr,timerr)
    if (nargin>4&&~isempty(timerr)); obj.timerr=timerr; end
    if (nargin>3&&~isempty(mcuerr)); obj.monerr=monerr; end
    if (nargin>2&&~isempty(monerr)); obj.mcuerr=mcuerr; end
    if (nargin>1&&~isempty(err)); obj.err = err; end
end
function replaceprop(obj,prop,val)
    obj.(prop)=val;
end
function redefinex(obj,newname)
    for i=1:length(obj)
        if obj(i).findColumn(newname)
            obj(i).defxname=newname;
            obj(i).defxvalue=obj(i).findColumn(newname);
            obj(i).x=obj(i).getColumn(newname);
        end
    end
end % redefinex
function replacex(obj,newx)
    obj.x=newx;
    obj.data(obj.defxvalue,:)=newx;
end % replacex
function redefiney(obj,newname)
    for i=1:length(obj)
        if obj(i).findColumn(newname)
            obj(i).defyname=newname;
            obj(i).defyvalue=obj(i).findColumn(newname);
            obj(i).y=obj(i).getColumn(newname);
            obj(i).err=sqrt(obj(i).y);
        end
    end
end % redefiney
function replacey(obj,newy)
    obj.y=newy;
    obj.data(obj.defyvalue,:)=newy;
    obj.err=sqrt(obj.y);
end % replacey
function removeColumn(obj,list)
    if ~iscell(list); list={list}; end
    if length(obj)>1;
        for i=1:length(obj); obj.removeColumn(list); end
        return
    end
    for i=1:length(list)
        lno=obj.findColumn(list{i});
        if lno
            obj.data(lno,:)=[];
            obj.colnames(lno)=[];
        end
    end
end

```

```

    end
end % removeColumn
function addColumn(obj,named,values)
    if ~iscell(named); named={named}; end
    if ~iscell(values); values={values}; end
    if length(obj)>1;
        for i=1:length(obj); obj.addColumn(named,values); end
    return
end
for i=1:length(named)
    if ~obj.findColumn(named{i}) % column doesn't exist yet
        lx=length(obj.x); lv=length(values{i});
        if lv==lx || lv==1
            obj.colnames(end+1)=named(i);
            if lv==1
                obj.data(end+1,:)=values{i}*ones(size(obj.x));
            else
                obj.data(end+1,:)=values{i};
            end
        end
    end
end
end % addColumn
function emptyPointCheck(obj)
    az = ~( obj.getColumn('detector')|obj.getColumn('monitor')...
            |obj.getColumn('mcu')      |obj.getColumn('time')  );
    obj.data(:,az)=[]; obj.fillVectors% re-fill all but errors
    errlist={'err','monerr','mcuerr','timerr'};
    for i=1:length(errlist); obj.(errlist{i})(az)=[]; end
end % emptyPointCheck
end % public methods
methods % Overloaded Methods
function comb = horzcat(sd1,sd2) %[a,b]
    %if both objects are scandata object
    if isa(sd1,'scandata')&&isa(sd2,'scandata')
        comb = scandata(sd1);
        comb.filename = [sd1.filename;sd2.filename];
        comb.data = [sd1.data,sd2.data];
        comb.header = [sd1.header,sd2.header];
        if strcmp([sd1.colnames{:}],[sd2.colnames{:}])
            comb.colnames = sd1.colnames;
        else
            comb.colnames = {'Added scans with different colnames'};
        end
        if strcmp([sd1.defxname{:}],[sd2.defxname{:}])
            comb.defxname = sd1.defxname;
        else
            comb.defxname = [sd1.defxname;sd2.defxname];
        end
        if strcmp([sd1.defyname{:}],[sd2.defyname{:}])
            comb.defyname = sd1.defyname;
        else

```

```

        comb.defyname = [sd1.defyname;sd2.defyname];
    end
    if sd1.defxvalue==sd2.defxvalue;comb.defxvalue=sd1.defxvalue;
    else comb.defxvalue=[sd1.defxvalue;sd2.defxvalue];end
    if sd1.defyvalue==sd2.defyvalue;comb.defyvalue=sd1.defyvalue;
    else comb.defyvalue=[sd1.defyvalue;sd2.defyvalue];end
    comb.x = [sd1.x,sd2.x];
    comb.y = [sd1.y,sd2.y];
    comb.err = [sd1.err,sd2.err];
    comb.stoppedFlag = sd1.stoppedFlag + sd2.stoppedFlag;
    comb.ei = [sd1.ei,sd2.ei];
    comb.e = [sd1.e,sd2.e];
    comb.ef = [sd1.ef,sd2.ef];
    comb.w = [sd1.w,sd2.w];
    comb.q = [sd1.q,sd2.q];
    comb.monerr=[sd1.monerr,sd2.monerr];
    comb.mcuerr=[sd1.mcuerr,sd2.mcuerr];
    comb.timerr=[sd1.timerr,sd2.timerr];

    if ~(isempty(sd1.sumCounts)||isempty(sd2.sumCounts))
        comb.sumCounts = sd1.sumCounts+sd2.sumCounts;
    end
    if ~isempty(sd1.color) && strcmp(sd1.color,sd2.color)
        comb.color = sd1.color;
    end

    if ~isempty(sd1.h) || ~isempty(sd2.h)
        comb.fillMillerVecs;
    end
    if ~isempty(sd1.alat) || ~isempty(sd2.alat)
        if ~isempty(sd1.alat)
            comb.alat = sd1.alat; comb.blat = sd1.blat;
            comb.clat = sd1.clat;
            comb.alpha = sd1.alpha; comb.beta = sd1.beta;
            comb.gamma = sd1.gamma;
        else
            comb.alat = sd2.alat; comb.blat = sd2.blat;
            comb.clat = sd2.clat;
            comb.alpha = sd2.alpha; comb.beta = sd2.beta;
            comb.gamma = sd2.gamma;
        end
    end
end
%if there is one scandata object and one double object
elseif (isa(sd1,'scandata')&&isa(sd2,'double'))...
    ||(isa(sd2,'scandata')&&isa(sd1,'double'))
    if isa(sd2,'scandata')
        tmp = sd1; %if the scandata object is sd2, rename
        sd1 = sd2; %it to sd1 and rename the double object
        sd2 = tmp; %to sd2.
    end
    %now sd1 is guaranteed to be a scandata object
    comb = scandata(sd1);

```

```

        comb.y = sd1.y + sd2.y;
    end
end %horzcat
function comb = vertcat(varargin) %[a;b]
    %original functionality of mapping vertcat to horzcat wasn't
    %particularly useful, instead vertcat will now create an empty
    %scandata vector object the size of a plus the size of b and
    %then place the elements of a and b into the empty vector
    ww = 0;
    for i=1:length(varargin)
        z = varargin{i};
        z = z(:);
        ww = ww + size(z,1);
        varargin{i}=z;
    end
    comb = scandata.empty(ww,0);
    p=1;
    for i=1:length(varargin)
        z = varargin{i};
        ww = size(z,1);
        for j=1:ww; comb(p)=z(j); p=p+1; end
    end
end % vertcat
function sm = sum(a)
    if isa(a,'scandata')
        sm=scandata(a(1));
        for no=2:length(a)
            sm=sm+a(no);
        end
    end
end

function pls = plus(a,b) % a+b
    if isa(a,'scandata')&&isa(b,'scandata')
        la=length(a); lb=length(b);
        if la>1&&lb>1&&la~=lb
            error('scandata:plus','No addition performed')
        end
        if la==1;         for i=1:lb; pls(i)=plus_sdsd(a,b(i));         end
        elseif lb==1;    for i=1:la; pls(i)=plus_sdsd(a(i),b);         end
        else              for i=1:la; pls(i)=plus_sdsd(a(i),b(i));     end
        end
    else
        if isa(b,'scandata')&&isa(a,'double')
            tmp=a;a=scandata(b);b=tmp;
            end %now a is a scandata and b a double
        la=length(a); lay=length(a(1).y); lb=length(b);
        if la>1&&lb>1&&la~=lb&&lay~=lb
            error('scandata:plus','No addition performed')
        elseif la==1&&lay==lb
            pls=plus_sddb(a,b);
        elseif la==lb

```

```

        for i=1:la; pls(i)=plus_sddb(a(i),b(i)); end
    elseif lb==1
        for i=1:la; pls(i)=plus_sddb(a(i),b); end
    elseif la==1
        for i=1:lb; pls(i)=plus_sddb(a,b(i)); end
    else
        error('scandata:plus','No additon performed')
    end
end
end % plus
function mult = times(a,b) % a .* b
% vectorization overloading:
la=length(a);lb=length(b);
if la>1&&lb>1&&la~=lb
    warning('scandata:times','No multiplication performed')
    return
end
if la==1
    for i=1:lb; mult(i)=timeshelper(a,b(i));end
elseif lb==1
    for i=1:la; mult(i)=timeshelper(a(i),b);end
else
    for i=1:la; mult(i)=timeshelper(a(i),b(i));end
end
end % times
function mult = mtimes(a,b) % a*b
mult = a .* b;
end % mtimes
function div = rdivide(a,b) % a ./ b
%rdivide, this whole function needs quite a lot of work.
if isa(a,'scandata')&&isa(b,'scandata')
    div = scandata(a);
elseif isa(a,'scandata')&&isa(b,'double')
    div = scandata(a) .* (1./b);
elseif isa(a,'double')&&isa(b,'scandata')
    div = scandata(b);
end
end % rdivide
function div = mrdivide(a,b) % a/b
div = a ./ b;
end % mrdivide
function c = uminus(b) % -a
if isa(b,'scandata')
    c = scandata.empty(0,length(b));
    for i=1:length(b)
        c(i) = scandata(b(i));
        c(i).y = -c(i).y;
        c(i).data(c(i).defyvalue,:) = -c(i).data(c(i).defyvalue,:);
    end
else
    c = -b;
end
end

```

```

end % uminus
function sub = minus(a,b)
    if isa(a,'scandata') && isa(b,'scandata')
        la=length(a);lb=length(b);
        if la>1&&lb>1&&la~=lb
            warning('scandata:minus','No subtraction performed')
            return
        end
        if la==1
            sub = scandata.empty(0,lb);
            for i=1:lb; sub(i)=minushelper(a,b(i));end
        elseif lb==1
            sub = scandata.empty(0,la);
            for i=1:la; sub(i)=minushelper(a(i),b);end
        else
            sub = scandata.empty(0,la);
            for i=1:la; sub(i)=minushelper(a(i),b(i));end
        end
    else
        sub = a + (-b);
    end
end % minus
function h = plot(a,xc,co,ln,sm)
    % Hint for specifying precise color, line, and symbol
    % combinations: pass all specifications in via co (i.e., pass
    % in {'ro','os','yd','g>','b^'}) and pass {''} for each of ln
    % and sm -- thus overriding their default values.
    if nargin < 5||isempty(sm); sm={'o';'d';'^';'<';'>';'s'}; end
    if nargin < 4||isempty(ln);
        ln={'-';'--';'-.';':'}; % must be -. not .- !!!!
    end
    if nargin < 3||isempty(co);
        co={'r';'o';'y';'g';'b';'i';'v';'k'};
    end
    if nargin < 2||isempty(xc); xc=a(1).defxname; end
    lc=length(co);ll=length(ln);ls=length(sm);
    cls = cell(lc*ll*ls,1);
    for i=1:ll
        for j=1:ls
            for m=1:lc
                cls(sub2ind([lc,ls,ll],m,j,i))...
                    =[{co{m},ln{i},sm{j}}];
            end
        end
    end
    mult=ceil(length(a)/size(cls,1));
    cls = repmat(cls,mult,1);
    h=zeros(size(a));
    %if cls is only one element this prevents an error
    if ~iscell(cls); cls = {cls}; end
    if ishold; prehold=true; else prehold=false;hold on;end
    for i=1:length(a)

```

```

clr=cls{i};
if ~isempty(a(i).color); clr(1)=a(i).color; end
if sum(a(i).err) %only plot errorbars if one+ is non-0
    zw = ~a(i).w; % logical zero weight vector will be
                % empty if a(i).w is empty!
if isempty(zw); zw = false(size(a(i).y)); end
if any(zw)
    fc='m';if mod(i,2); fc='w'; end
    %any points with a weight of zero should be gray
    [markercolor,fc]=scandata.decodeColor('gray',fc);
    hi = errorbar(...
        a(i).data(a(i).findColumn(xc),zw),...
        a(i).y(zw),a(i).err(zw),clr(2:end),...
        'color',markercolor);
    set(hi, 'MarkerSize',6, 'MarkerFaceColor',fc)
    ud.zeroWeight=1;
    set(hi, 'userdata',ud)
    hi=get(hi, 'Children');ebxd=get(hi(2), 'XData');
    ebxd(4:9:end)=ebxd(1:9:end);
    ebxd(5:9:end)=ebxd(1:9:end);
    ebxd(7:9:end)=ebxd(1:9:end);
    ebxd(8:9:end)=ebxd(1:9:end);
    set(hi(2), 'XData', ebxd)
end
if any(~zw)
    fc='m';if mod(i,2); fc='w'; end
    [markercolor,fc]=scandata.decodeColor(clr(1),fc);
    h(i) = errorbar(...
        a(i).data(a(i).findColumn(xc),~zw),...
        a(i).y(~zw),a(i).err(~zw),clr(2:end),...
        'color',markercolor); hold on
    %increase the marker size and fill in their faces
    %with a lighter version of the line color
    set(h(i), 'MarkerSize',6, 'MarkerFaceColor',fc)
    %remove the ends of the error bars since they
    %aren't representative of any actual error
    %and only clutter the plot
    hc=get(h(i), 'Children');ebxd=get(hc(2), 'XData');
    ebxd(4:9:end)=ebxd(1:9:end);
    ebxd(5:9:end)=ebxd(1:9:end);
    ebxd(7:9:end)=ebxd(1:9:end);
    ebxd(8:9:end)=ebxd(1:9:end);
    set(hc(2), 'XData', ebxd)
end
else
% If sum(a(i).err) ==0, the data likely represents a
% simulation. The following only plots the line
% segments connecting points not the points themselves.
switch length(clr)
    case 2, lns = '-';
    case 3, lns = clr(2);
    case 4, lns = clr(2:3);

```

```

        otherwise, lns = 'o'; %this shouldn't be chosen
    end
    markercolor=scandata.decodeColor(clr(1));
    if any(isnan(a(i).y))
        ynn = a(i).y;
        xnn = a(i).data(a(i).findColumn(xc),:);
        ynn(isnan(ynn)) = interp1(...
            xnn(~isnan(ynn)),ynn(~isnan(ynn)),...
            xnn(isnan(ynn)), 'linear', 'extrap');
        plot(xnn,ynn,lns, 'color',markercolor/2),hold on
    end
    % It's possible to get to this point with empty y and
    % err vectors, so do some error checking before plot
    if ~(isempty(a(i).data(a(i).findColumn(xc),:))...
        ||isempty(a(i).y))
        h(i) = plot(a(i).data(a(i).findColumn(xc),:),...
            a(i).y,lns, 'color',markercolor); hold on
    end
end
end
if ~prehold; hold off; end
if ~nargout; clear('h'); else h(h==0)=[]; end
end % plot
function h = hist(a,co,ln,sm)
    if nargin < 4; sm={'o';'d';'^';'<';'>';'s'}; end
    if nargin < 3; ln={'-';'-';'.-';':'}; end
    if nargin < 2; co={'r';'o';'g';'b';'i';'v';'k'}; end
    lc=length(co);ll=length(ln);ls=length(sm);
    cls = cell(lc*ll*ls,1);
    for i=1:ll
        for j=1:ls
            for m=1:lc
                cls(sub2ind([lc,ls,ll],m,j,i))...
                    =[co{m},ln{i},sm{j}];
            end
        end
    end
end
mult=ceil(length(a)/size(cls,1));
cls = repmat(cls,mult,1);
h=zeros(size(a));
%if cls is only one element this prevents an error
if ~iscell(cls); cls = {cls}; end
if ishld; prehold=true; else prehold=false;hold on;end
for i=1:length(a)
    clr=cls{i};
    if ~isempty(a(i).color); clr(1)=a(i).color; end
    fc='w';if mod(i,2); fc='m'; end
    [markercolor,facecolor]=scandata.decodeColor(clr(1),fc);
    if ~a(i).hstFlg; a(i).createHistogram; end
    h(i) = errorbar(a(i).hstX,...
        a(i).hstY,a(i).hstEr,clr(2:end),...
        'color',markercolor); hold on
end

```

```

%increase the marker size and fill in their faces with a
%lighter version of the line color
set(h(i), 'MarkerSize',6, 'MarkerFaceColor',facecolor)
%remove the ends of the error bars since they aren't
%representative of any actual error and clutter the plot
hc=get(h(i), 'Children');ebxd=get(hc(2), 'XData');
ebxd(4:9:end)=ebxd(1:9:end);ebxd(5:9:end)=ebxd(1:9:end);
ebxd(7:9:end)=ebxd(1:9:end);ebxd(8:9:end)=ebxd(1:9:end);
set(hc(2), 'XData',ebxd)
end
if ~prehold; hold off; end
if ~nargout; clear('h');end
end % hist
end % overloaded methods
methods (Access=private) % Private Methods
function sub = minushelper(a,b,cList) % a-b
if nargin<3; cList=[]; end
b = -b;
abswitch=false;
if length(a.x)<length(b.x)
abswitch=true;
tmp = scandata(a);
a = scandata(b);
b = scandata(tmp);
clear('tmp')
end %now b is guaranteed to have <= points than a
sub = scandata(b);

[ax,p]=sort(a.x);
%ay = a.y(p);
%aerr = a.err(p);

ih=diff(ax);
[~,ik]=histc(b.x,ax);
ik(b.x<ax(1))=1;
ik(b.x>=ax(end))=length(ax)-1;
is = (b.x - ax(ik))./ih(ik);

%u={b.defyname,'monitor','mcu','time'};
%d={'err','monerr','mcuerr','timerr'};
% Combining normalization-intensity columns is wrong for
% point-subtractions!
u={b.defyname};
d={'err'};
iy=cell(size(d));ie=iy;
for i=1:length(d)
ay=a.getColumn(u{i});ay=ay(p);
ae=a.(d{i});ae=ae(p);
iy{i}=ay(ik) + is .* (ay(ik+1)-ay(ik));
ie{i}=sqrt((ax(ik+1)-b.x).^2 .* ae(ik).^2 ...
+(ax(ik)-b.x).^2 .* ae(ik+1).^2)/(ax(ik+1)-ax(ik));
end

```

```

for i = 1:size(a.data,1)
    sub.data(i,:) = ...
        interp1(a.x,a.data(i,:),b.x,'linear','extrap');
end

%if a and b were switched, b contains the (probably) more
%important motor positions. So switch the data blocks back.
if abswitch
    datatemp=sub.data;
    sub.data=b.data;
    b.data=datatemp;
    if iscell(b.defyname)
        defy=b.defyname{:};
    elseif ischar(b.defyname)
        defy=b.defyname;
    end
else
    if iscell(a.defyname)
        defy=a.defyname{:};
    elseif ischar(a.defyname)
        defy=a.defyname;
    end
end

%combine only intensity related columns
for i=1:length(d)
    sub.(d{i})=sqrt(ie{i}.^2+b.(d{i}).^2);
    sub.setColumn(u{i},iy{i}+b.getColumn(u{i}));
end
sub.fillVectors
sub.x = b.x;

%since the data columns have been manipulated, let's fill in
%any vectors with their proper (new) values
if ~isempty(a.w) || ~isempty(b.w)
    sub.Weight();
end
if ~isempty(a.alat) || ~isempty(b.alat)
    sub.findLatticeConstants;
end

if a.hstFlg||b.hstFlg
    [sub.hstX,sub.hstY,sub.hstEr,sub.hstT,...
    sub.hstEdg,sub.hstE]=a.createHistogram(b);
    sub.hstFlg = true;
end
end % minus-helper
function mult = timeshelper(a,b)
    if isa(a,'scandata')&&isa(b,'scandata')
        ua={a.defyname,'monitor','mcu','time'};
        ub={b.defyname,'monitor','mcu','time'};
        d={'err','monerr','mcuerr','timerr'};
    end
end

```

```

if length(a.y)==length(b.y)
    mult = scandata(a);
    for i=1:length(d)
        mult.(d{i})=sqrt(...
            (a.getColumn(ua{i})*b.(d{i})).^2 ...
            +(b.getColumn(ub{i})*a.(d{i})).^2 );
        mult.setColumn(ua{i},...
            a.getColumn(ua{i})*b.getColumn(ub{i}));
    end
else
    %ensure that a is shorter than b
    if length(a.y)>length(b.y)
        tmp=scandata(b);b=scandata(a);a=tmp;
    end
    mult = scandata(a); lv=1:length(a.y);
    for i=1:length(d)
        bv=b.getColumn(ub{i});be=b.(d{i});
        mult.(d{i})=sqrt(...
            (a.getColumn(ua{i})*be(lv)).^2 ...
            +(bv(lv)*a.(d{i})).^2 );
        mult.setColumn(ua{i},a.getColumn(ua{i})*bv(lv));
    end
end
elseif (isa(a,'scandata')&&isa(b,'double'))...
    ||(isa(b,'scandata')&&isa(a,'double'))
    if isa(b,'scandata')
        tmp=a; a=b; b=tmp;
    end
    ua={a.defyname};%,'monitor','mcu','time'};
    d={'err'};%,'monerr','mcuerr','timerr'};
    mult = scandata(a);
    for i=1:length(d)
        mult.setColumn(ua{i},b.*mult.getColumn(ua{i}))
        mult.(d{i})=b.*mult.(d{i});
    end
end
mult.fillVectors % most importantly mult.y
end % timeshelper
function pls = plus_sdsd(a,b)
    pls = scandata(a);
    pls.data = [a.data b.data];
    pls.err = [a.err b.err];
    pls.monerr=[a.monerr b.monerr];
    pls.mcuerr=[a.mcuerr b.mcuerr];
    pls.timerr=[a.timerr b.timerr];

    dontavg = {'time' 'detector' 'monitor' 'mcu'};
    pls.crpoints(dontavg);
end % plus_sdsd
function pls = plus_sddb(a,b)
    pls = scandata(a);
    pls.y = a.y + b;

```

```

pls.data(pls.defyvalue, :)=pls.data(pls.defyvalue, :)+b;
if a.hstFlg
    pls.hstY=pls.hstY+b;
end
end % plus_sddb
end % private methods
methods (Static=true) % Static Methods
function avg = avgscans(varargin)
    % varargin is assumed to be a cellarray of scandata objects to
    % be averaged

    %copy the first scandata object to a new handle
    avg = scandata(varargin{1});
    if length(varargin) > 1
        avg.avgflg = true;
        divby = length(varargin);
        lengths = zeros(1,divby);
        for i = 1:divby
            lengths(i)=length(varargin{i}.y);
        end
        maxlen = max(lengths);
        xmat = NaN*ones(divby,maxlen);
        ymat = xmat; emat = xmat; mnet=xmat; mcet=xmat; tmet=xmat;
        dmat = NaN*ones(size(avg.data,1),maxlen,divby);
        for i = 1:divby
            xmat(i,1:lengths(i))=varargin{i}.x;
            ymat(i,1:lengths(i))=varargin{i}.y;
            emat(i,1:lengths(i))=varargin{i}.err;
            mnet(i,1:lengths(i))=varargin{i}.monerr;
            mcet(i,1:lengths(i))=varargin{i}.mcuerr;
            tmet(i,1:lengths(i))=varargin{i}.timerr;
            [b,c]=size(varargin{i}.data);
            dmat(1:b,1:c,i)=varargin{i}.data;
        end
        sortmat = [lengths ', (1:divby)', xmat, ymat, emat, mnet, mcet, tmet];
        sortmat = sortrows(sortmat, -1);
        %lengths = sortmat(:,1);
        posi = sortmat(:,2);
        xmat = sortmat(:,3:maxlen+2);
        ymat = sortmat(:,maxlen+3:2*maxlen+2);
        emat = sortmat(:,2*maxlen+3:3*maxlen+2);
        mnet = sortmat(:,3*maxlen+3:4*maxlen+2);
        mcet = sortmat(:,4*maxlen+3:5*maxlen+2);
        tmet = sortmat(:,5*maxlen+3:6*maxlen+2);

        if xmat(1,1)<xmat(2,1); %check to see if x increases or
            tol = 0.02; %decreases. set tol accordingly
        else
            tol = -0.02;
        end
    end
end

```

```

done = false;
while ~done
    extra = 0;
    rulemat = [xmat(1,:);ymat(1,:);...
               emat(1,:);mnet(1,:);mcet(1,:);tmet(1,:);...
               dmat(:, :, posi(1))];
    for i=2:divby
        matchmt = [xmat(i,:);ymat(i,:);...
                   emat(i,:);mnet(i,:);mcet(i,:);tmet(i,:);...
                   dmat(:, :, posi(i))];
        [rulemat,matchmt] = ...
            rec2match(rulemat',matchmt',tol,0);
        rulemat=rulemat';matchmt=matchmt';
        if size(rulemat,2) > maxlen
            extra = size(rulemat,2)-maxlen;
            xmat = [xmat,NaN*ones(divby,extra)];
            ymat = [ymat,NaN*ones(divby,extra)];
            emat = [emat,NaN*ones(divby,extra)];
            mnet = [mnet,NaN*ones(divby,extra)];
            mcet = [mcet,NaN*ones(divby,extra)];
            tmet = [tmet,NaN*ones(divby,extra)];
            dmat(:,end+1:end+extra,:)=NaN;
            xmat(1,:)=rulemat(1,:);
            ymat(1,:)=rulemat(2,:);
            emat(1,:)=rulemat(3,:);
            mnet(1,:)=rulemat(4,:);
            mcet(1,:)=rulemat(5,:);
            tmet(1,:)=rulemat(6,:);
            dmat(:, :, posi(1))=rulemat(7:end,:);
            maxlen = maxlen + extra;
        end
        xmat(i,:) = matchmt(1,:);
        ymat(i,:) = matchmt(2,:);
        emat(i,:) = matchmt(3,:);
        mnet(i,:) = matchmt(4,:);
        mcet(i,:) = matchmt(5,:);
        tmet(i,:) = matchmt(6,:);
        dmat(:, :, posi(i))=matchmt(7:end,:);

    end
    if ~extra; done = true; end
end
%need to write changes to rule-dmat
dmat(:, :, posi(1))=rulemat(7:end,:);

X = zeros(1,maxlen);
Y = X; ERR = X; MNR=X;MCR=X;TMR=X;
for i = 1:maxlen
    xcol = xmat(:,i);
    ycol = ymat(:,i);
    ecol = emat(:,i);
    mnel = mnet(:,i);

```

```

mcel = mcet(:,i);
tmel = tmet(:,i);

xcol(isnan(xcol))=[];
ycol(isnan(ycol))=[];
ecol(isnan(ecol))=[];
mnel(isnan(mnel))=[];
mcel(isnan(mcel))=[];
tmel(isnan(tmel))=[];

X(i) = sum(xcol)/length(xcol);
Y(i) = sum(ycol)/length(ycol);
ERR(i) = sqrt(sum(ecol.^2)/length(ecol));
MNR(i) = sqrt(sum(mnel.^2)/length(mnel));
MCR(i) = sqrt(sum(mcel.^2)/length(mcel));
TMR(i) = sqrt(sum(tmel.^2)/length(tmel));
end

[a,b,~]=size(dmat);
adata = zeros(a,b);
for i=1:a;
    for j=1:b;
        pages = dmat(i,j,:);
        pages(isnan(pages))=[];
        adata(i,j) = sum(pages)/length(pages);
    end
end

avg.y = Y;
avg.x = X;
avg.err = ERR;
avg.monerr=MNR;
avg.mcuerr=MCR;
avg.timerr=TMR;
avg.data = adata;

avg.findTemperature;
avg.findEnergies;

Q = scandata.empty(size(varargin,2),0);
for i=1:length(varargin); Q(i) = varargin{i}; end
qq = cell(size(Q)); [qq{:}]=Q.hstFlg;
qq = cell2mat(qq);
if any(qq) %then at least one input file has hstFlg == true
    avg.createHistogram(varargin{2:end});
    %since avg = varargin(1), this creates the averaged
    %histogram of varargin

    %since createHistogram ensures that at least one point
    %from each varargin is included in each histogram point
    %it's easy to find the average Y and Err
    avg.hstY = avg.hstY/length(varargin);
end

```

```

        avg.hstEr = avg.hstEr/length(varargin);
    end
end
end % avgscans
function [markercolor,facecolor]=decodeColor(clr,face)
if nargin<2||isempty(face); face='c';end
if nargin<1||isempty(clr);   clr='k';end
if ischar(clr) % allow for a special color to be passed in.
    switch lower(clr)
        case {'r','red'},      markercolor=[1,0,0];
        case {'o','orange'},   markercolor=[1,0.5,0];
        case {'y','yellow'},   markercolor=[1,0.75,0];
        case {'g','green'},    markercolor=[0,1,0];
        case {'b','blue'},     markercolor=[0,0,1];
        case {'darkindigo'},   markercolor=[0,0.5,1];
        case {'i','indigo'},   markercolor=[0.2,0.7,1];
        case {'v','violet'},   markercolor=[0.58,0,0.83];
        case {'k','black'},    markercolor=[0,0,0];
        case {'w','white'},    markercolor=[1,1,1];
        case {'c','cyan'},     markercolor=[0,1,1];
        case {'m','magenta'},  markercolor=[1,0,1];
        case {'a','gray'},     markercolor=0.85*[1,1,1];
        otherwise,markercolor=[0,0,0];
    end
elseif isnumeric(clr)&&length(clr)==3&&max(clr)<=1&&min(clr)>=0
    markercolor=clr;
end
if ischar(face) % allow for a special facecolor to be passed in.
switch lower(face)
    case {'c','clear','empty','none'}, facecolor='none';
    case {'l','light'}, facecolor=0.2*markercolor+0.8*[1,1,1];
    case {'m','medium'},facecolor=0.5*markercolor+0.5*[1,1,1];
    case {'d','dark'},  facecolor=0.7*markercolor+0.3*[1,1,1];
    case {'f','full','filled'}, facecolor=markercolor;
    case {'w','white'}, facecolor=[1,1,1];
end
elseif isnumeric(face) && max(face)<=1 && min(face)>=0
    if length(face)==3 %face is a color specification
        facecolor=face;
    elseif length(face)==1 % face is a shading specification
        facecolor=(1-face)*markercolor+face*[1,1,1];
    end
end
end
end % static methods
end %classdef

```

APPENDIX C INSTRUMENT RESOLUTION

As neutron scattering experiments are flux-limited, experimental setups typically relax momentum-defining elements in exchange for increased neutron flux. This relaxed momentum-resolution can have drastic effects on the lineshape of peaks in neutron scattering experiments, especially in peaks corresponding to inelastic processes. This is especially true for triple-axis neutron spectrometers. Figure C.1 shows how finite instrumental resolution modifies line shapes of measured scans due to the partial inclusion of intensity at other momentum-energy points.

Over time, two leading methods have been developed in an attempt to account for resolution effects when fitting triple-axis neutron scattering data. The older of the two methods, the Cooper-Nathans approximation, is arguably more-popular due in part to its primacy but more importantly to its simplicity. The approximation which has been named for Cooper and Nathans is to assume that the only source of uncertainty in the momentum of a neutron is due to maximally accepted angular divergences of Soller collimators placed between elements of a triple-axis spectrometer and the mosaic spreads of crystal elements, and that all angular divergences of a neutron beam follow a Gaussian distribution [89]. A more complex alternative, the Popovici approximation, improves upon the Cooper-Nathans method by including effects due to the finite-size of instrument components and the size and shape of the sample [90].

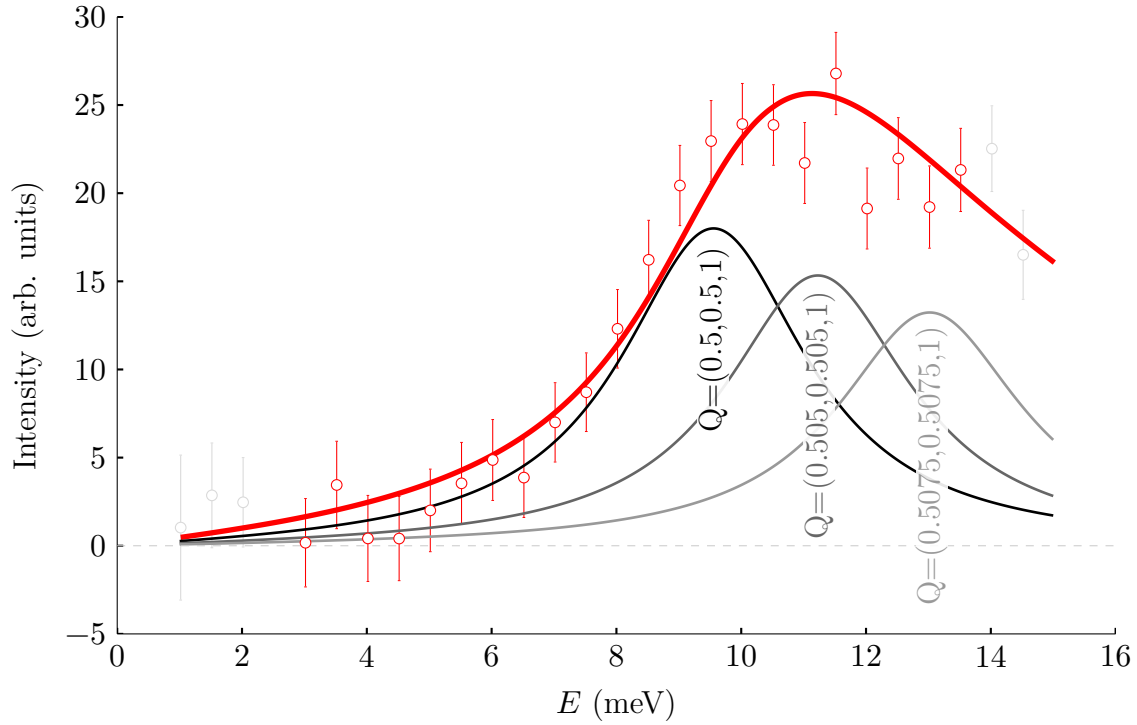


FIGURE C.1. Background subtracted INS intensity of $\text{Ba}(\text{Fe}_{0.985}\text{Co}_{0.015})_2\text{As}_2$ corrected for the Bose thermal population factor and the Fe^{2+} single-ion magnetic form factor plus best fit line to the damped spin-wave model. The remaining progressively lighter solid lines are the rescaled unconvoluted spin wave model and are representative of the spin wave dispersion along $[1\ 1\ 0]_{\text{T}}$ which is partially included in the measured scan due to the finite instrumental resolution.

Convolved Fitting With RESLIB

Convoluting either resolution approximation with a theoretical model is not a trivial task; thankfully, there is a MATLAB-based program, RESLIB, readily available to do most of the heavy-lifting for us. When used in concert with the wrapper methods of the SCANDATA class, the difficulties involved in performing convoluted fitting are minimized. Some issues that remain are:

- the to-be-convoluted function must be defined for all momentum-energy space,
- the RESLIB fixed integration method should be used when fitting in order to avoid fluctuations in the residual inherent to Monte Carlo integration,
- and the fixed integration grid size should be finer than features in the model function.

The last point is likely the largest issue, as the grid spacing (in angle space) is given by π/n for $(2n + 1)^4$ grid points (with a RESLIB grid specification of $[n, n]$), so halving the grid spacing leads to an approximately sixteen-fold increase in the total number of integration grid points. The memory requirements for this 4D grid can quickly get out of hand and care should be taken to avoid exhausting physical memory, as the use of virtual memory (in the form of temporary files or swap space) is typically orders of magnitude slower. Please refer to the RESLIB manual written by Zheludev [98] for further details regarding its implementation.

Figure C.2 shows transverse acoustic phonons measured near $(220)_T$ and the results of convolution of a model transverse phonon branch with the Popovici and Cooper-Nathans approximations to the instrumental resolution. This shows that, by ignoring finite size effects, the Cooper-Nathans approximation over-estimates the energy-width of the resolution. The increased accuracy of Popovici's method comes at the price of a large number of instrument- and sample-dependent parameters, without a significant increase in computational time. The appropriate parameters for the experimental setup at HB3 and for a typical sample are given in table C.1.

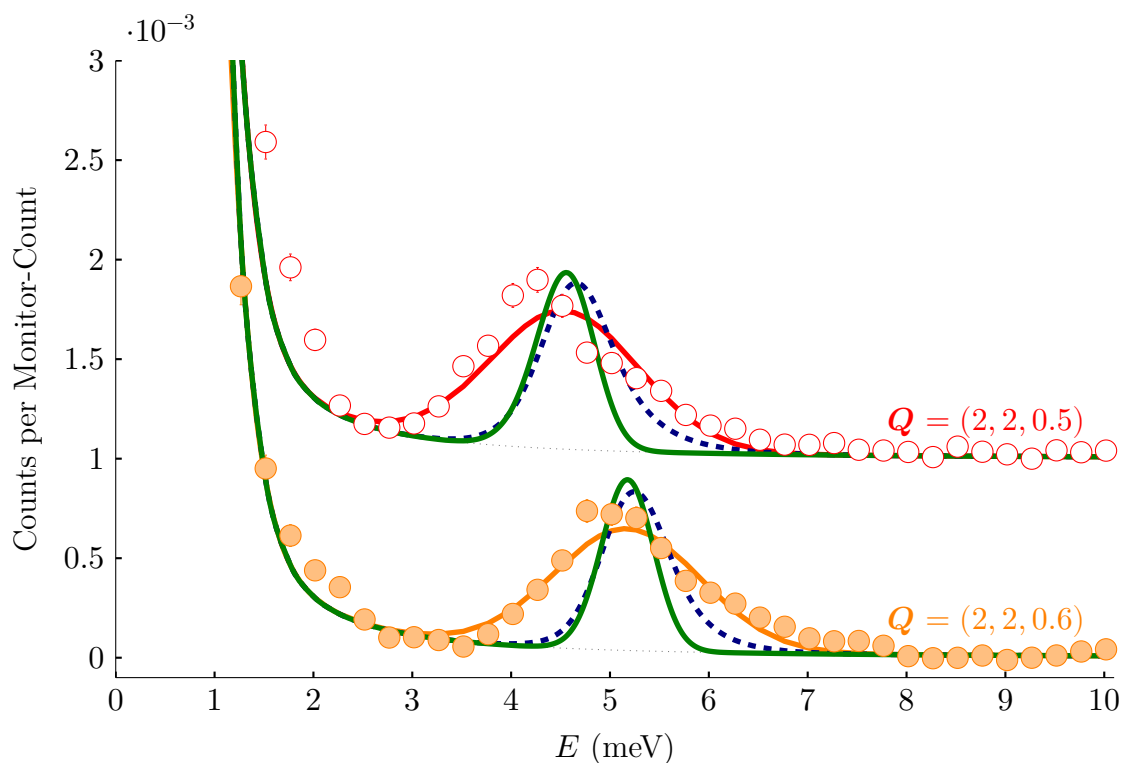


FIGURE C.2. Offset constant- Q measurements of the transverse acoustic phonon branch near (220). Circles are neutrons counted by the detector normalized to beam monitor counts after correcting for monitor over-counting due to the presence of higher-order neutrons in the incident neutron beam. The dotted gray lines represent an estimate to the incoherent elastic background. Solid thick lines are the result of a Popovici approximation resolution-convoluted fitting of the intensity to a model of a dispersing transverse acoustic phonon plus the incoherent elastic background. Green solid and blue dashed lines are a convolution of the same phonon model with the intrinsic line-width set to zero (and the intensity arbitrarily rescaled); green lines are derived from the Popovici approximation and blue lines from the Cooper-Nathans approximation — this highlights that the Cooper-Nathans approach estimates a larger resolution energy width.

TABLE C.1. Instrument and sample parameters for the experimental setup at HB3 and a typical sample. All components are assumed to be rectangular prisms prior to being bent for focussing – this leads to an additional factor of $1/\sqrt{12}$ in the square root of the variance for each dimension, which RESLIB takes as input.

Component	Property	Value
beam	width	15 cm
	height	15 cm
monochromator	width	7.62 cm
	height	10.16 cm
	depth	0.25 cm
	vertical radius of curvature	variable
	horizontal mosaic	30′
	vertical mosaic	45′
	τ_{mono}	1.873 Å ⁻¹
beam monitor	width	5 cm
	height	12 cm
sample	width	4 cm
	height	2 cm
	depth	3 cm
	horizontal mosaic	30′
	vertical mosaic	30′
analyzer	width	7.62 cm
	height	7 cm
	depth	0.2 cm
	vertical radius of curvature	25 cm
	horizontal mosaic	40′
	vertical mosaic	25′
detector	τ_{ana}	1.873 Å ⁻¹
	width	4 cm
	height	12 cm

TABLE C.1. (Continued)

Component	Property	Value
horizontal divergence	source to monochromator	48'
	monochromator to sample	60'
	sample to analyzer	80'
	analyzer to detector	120'
vertical divergence	source to monochromator	180'
	monochromator to sample	300'
	sample to analyzer	300'
	analyzer to detector	600'
Distances	source to monochromator	650 cm
	monochromator to sample	190 cm
	sample to analyzer	160 cm
	analyzer to detector	86 cm
	monochromator to monitor	60 cm

APPENDIX D NORMALIZATION

Normalizing measured neutron scattering data into absolute cross-section units is often desirable, as it allows for the direct comparison of experimental data to theoretical models. There are two methods which are routinely applied to normalize measured triple-axis neutron scattering data into absolute units. One relies upon the known incoherent scattering cross-section of Vanadium, and the other utilizes an easily-calculated approximation for the cross-section of one (or more) sample phonon. In either case, the data to be normalized must be treated properly before normalization.

What is measured with any neutron scattering instrument is a combination of a scattering function, $S(\mathbf{Q}, E)$, and a background function, $B(\mathbf{Q}, E)$, which is the collective intensity of all sources of background such as incoherent scattering from the sample itself, counted neutrons due to inadequate shielding of the source or the detector, or purely stochastic, e.g., due to noise in the detector electronics. As such, for comparison to any theoretical model for the cross-section the measured data, $I(\mathbf{Q}, E)$ must first have an estimate for the background removed,

$$S(\mathbf{Q}, E) = I(\mathbf{Q}, E) - B(\mathbf{Q}, E) \quad (\text{D.1})$$

where the background estimate is typically determined from measurements near the intensity of interest or by repeating measurements after changing sample environment conditions to suppress the scattering of interest.

If intensity is measured as the ratio of counts in a detector to counts in a beam monitor, as is typically the case for triple-axis neutron spectrometers, the measured intensity must also be corrected for monitor over counting due to the presence of higher-order neutrons in

the beam – especially if more than one energy transfer is to be compared with a fixed final neutron energy. This topic is discussed in detail by Shirane et al. [80, pp. 117-121] with the conclusion that the total monitor signal is

$$M \sim CE_1 e^{-E_1/k_B T} \quad (\text{D.2})$$

where E_1 is the fundamental neutron energy, T is the neutron moderator temperature, and

$$C = \sum_{n=1}^{\infty} n^2 e^{-(n^2-1)E_1/k_B T}. \quad (\text{D.3})$$

As noted by Shirane et al., “The measured intensities for the scattered beam can be corrected by multiplying by C ” [80, p. 121]. As part of the SCANDATA class, I’ve written a method called `monitorHarmonic` which takes the moderator temperature as input and performs this correction, with C calculated up to $n = 10$.

After removing an estimated background and correcting for monitor over counting, it is possible to compare (corrected) measured intensity of a well-defined feature to an easily-calculable and well-verified theoretical cross section to determine a scaling factor which will convert all measured arbitrary intensity, with typical units of detector counts per monitor counts per meV, to absolute cross-section, with units of mb sr^{-1} per meV per mole (or atom, or formula unit).

Calculating Vanadium Intensity

The partial-differential cross-section for elemental vanadium is nearly-entirely incoherent and, for N atoms, is given by

$$\frac{d^2\sigma}{d\Omega dE} = Nb^2 e^{-2W} \delta(E) \quad (\text{D.4})$$

where the square of the incoherent scattering length is $b^2 = 405.8 \text{ mbsr}^{-1}$, and the Debye–Waller exponent is a temperature-dependent measure of the mean-squared displacement of each vanadium atom $2W = Q^2 \langle u^2 \rangle$. At room temperature $\langle u^2 \rangle \approx 0.038 \text{ \AA}^2$, and the Debye–Waller factor is a Gaussian with $\text{FWHM} = 2.35\sqrt{2\langle u^2 \rangle} \approx 27 \text{ \AA}^{-1}$. The energy-integration of the partial-differential cross-section yields the differential cross section and is straight-forward in this case due to the delta function. In practice, the finite energy resolution of a triple-axis spectrometer will act to broaden the measured intensity (while, of course, preserving the total intensity) and so either a simple Gaussian-fit or a numerical integration of the measured intensity must be performed for comparison to the known incoherent cross section for vanadium.

Since the intensity of incoherent scattering depends on the number of vanadium atoms present in a sample, the accuracy of any conversion factor determined from incoherent vanadium scattering will depend strongly on the accuracy with which the number of vanadium atoms is known. Furthermore, as most theoretical cross-sections are expressed in terms of mbsr^{-1} per atom (or per formula unit), the accuracy with which the number of atoms (or formula units) in the studied sample is known can also drastically effect the accuracy with which the absolute intensity is known.

Calculating Phonon Intensities

For the superposition of any number of phonons in a crystalline system, the displacement of the d^{th} nucleus in the l^{th} unit cell is given by the vector $\mathbf{u} \begin{pmatrix} l \\ d \end{pmatrix}$, which can be expressed as a sum over the displacements due to a set of normal modes

$$\mathbf{u} \begin{pmatrix} l \\ d \end{pmatrix} = \sum_q \sum_j \sqrt{\frac{\hbar}{2M_d N \omega_{qj}}} [\epsilon_{dqj} a_{qj} e^{iq \cdot l} + \epsilon_{dqj}^* a_{qj}^\dagger e^{-iq \cdot l}] \quad (\text{D.5})$$

where M_d is the mass of the d^{th} nucleus, the energy of the j^{th} normal phonon mode at \mathbf{q} is $\hbar\omega_{\mathbf{q}j}$, and the displacement eigenvector for the d^{th} nucleus in the unit-cell as a result of the j^{th} normal mode is $\boldsymbol{\epsilon}_{d\mathbf{q}j}$. If there are $r = \sum_d$ atoms per unit cell, then there are $3r$ normal modes ($j = 1, \dots, 3r$) since each atom has three degrees of freedom [79, p. 105]. The displacement eigenvectors are orthonormal and behave the relations

$$\sum_d \boldsymbol{\epsilon}_{d\mathbf{q}j}^* \cdot \boldsymbol{\epsilon}_{d\mathbf{q}j'} = \delta_{jj'} \quad \text{and} \quad \sum_j \epsilon_{d\mathbf{q}j}^{\alpha*} \epsilon_{d'\mathbf{q}j}^{\beta} = \delta_{\alpha\beta} \delta_{dd'}. \quad (\text{D.6})$$

As given by Squires, the cross-section for the coherent creation of one phonon is given by [77, p. 46]

$$\begin{aligned} \frac{d^2\sigma}{d\Omega dE} &= \frac{k_f}{k_i} \frac{(2\pi)^3}{2v_0} \sum_{\mathbf{q}} \sum_j \sum_{\boldsymbol{\tau}} \frac{1}{\omega_{\mathbf{q}j}} \left| \sum_d \frac{\bar{b}_d}{\sqrt{M_d}} e^{-W_d} e^{i\mathbf{Q}\cdot d} \mathbf{Q} \cdot \boldsymbol{\epsilon}_{d\mathbf{q}j} \right|^2 \\ &\times \langle n_{\mathbf{q}j} + 1 \rangle \delta(\omega - \omega_{\mathbf{q}j}) \delta(\mathbf{Q} - \mathbf{q} - \boldsymbol{\tau}) \end{aligned} \quad (\text{D.7})$$

where $(2\pi)^3/v_0$ comes from pre-evaluating a sum over all unit cells and is the volume of the reciprocal lattice unit cell, the sum over \mathbf{d} is over all of the nuclei in the unit cell, $\langle n_{\mathbf{q}j} + 1 \rangle$ is the average thermal population factors for the creation of a phonon of the j^{th} mode at \mathbf{q} , and the Dirac delta functions enforce conservation of energy and momentum.

In order to calculate the phonon cross section for a transverse acoustic mode in absolute units one must make the approximation that the eigenvector of the branch is perpendicular to \mathbf{q} and is parallel to the reciprocal lattice vector $\boldsymbol{\tau}$, such that

$$\mathbf{Q} \cdot \boldsymbol{\epsilon}_{d\mathbf{q}j} = \mathbf{Q} \cdot \hat{\boldsymbol{\tau}} \sqrt{\frac{M_d}{\sum_{d'} M_{d'}}} \quad (\text{D.8})$$

where the eigenvector is normalized such that each atom in the acoustic mode has an equal displacement vector \mathbf{u}_d . In the limit of small \mathbf{q} , where $\mathbf{Q} \approx \boldsymbol{\tau}$, the coherent one phonon cross

section for such a transverse acoustic (TA) mode is

$$\left(\frac{d^2\sigma}{d\Omega dE}\right)_{\text{TA}} = \frac{k_f}{k_i} \frac{(2\pi)^3}{v_0} \frac{\hbar^2 (\mathbf{Q} \cdot \hat{\boldsymbol{\tau}})^2}{2\hbar\omega_{\mathbf{q}} \sum_{d'} M_{d'}} \left| \sum_d \bar{b}_d e^{-W_d} e^{i\boldsymbol{\tau} \cdot \mathbf{d}} \right|^2 \frac{\delta(\hbar\omega - \hbar\omega_{\mathbf{q}})}{1 - e^{-\hbar\omega_{\mathbf{q}}/k_B T}} \quad (\text{D.9})$$

and the energy-integrated intensity of the phonon partial-differential cross-section is

$$\left(\frac{d\sigma}{d\Omega}\right)_{\text{TA}} = \frac{k_f}{k_i} \frac{(2\pi)^3}{v_0} \frac{\hbar^2 (\mathbf{Q} \cdot \hat{\boldsymbol{\tau}})^2}{2\hbar\omega_{\mathbf{q}} \sum_{d'} M_{d'}} \left| \sum_d \bar{b}_d e^{-W_d} e^{i\boldsymbol{\tau} \cdot \mathbf{d}} \right|^2 \frac{1}{1 - e^{-\hbar\omega_{\mathbf{q}}/k_B T}} \quad (\text{D.10})$$

where the quantity in vertical brackets is just the static structure factor for the associated Bragg reflection. The k_f/k_i factor is implicitly corrected for in E_f -fixed mode due to analyzer reflectivity and beam monitor efficiency effects.

While equation (D.10) is true for any transverse acoustic phonon with sufficiently small \mathbf{q} , in the case of the 122 iron pnictides the presence of the static structure factor is problematic for any TA phonons near a reciprocal lattice point that fulfills the condition $\boldsymbol{\tau} \cdot [001]_{\text{T}} \neq 0$ due to the poorly-defined arsenic z-position in $\text{Ba}(\text{Fe}_{1-x}\text{TM}_x)_2\text{As}_2$. Therefore in normalizing the triple-axis data presented above, focus was placed on fitting measured TA phonons near $(220)_{\text{T}}$.

By determining the integrated intensity of a TA phonon, either by fitting a Gaussian function or performing a numerical integration, it is then possible to determine an appropriate scale factor to convert measured intensity from normalized counts to $\text{mb sr}^{-1} \text{ meV}^{-1} \text{ f.u.}^{-1}$. This conversion factor has an advantage over the vanadium-determined conversion, since both the phonon and other scattering-of-interest come from the same sample, there is no need to determine the number of formula units in the sample if the theoretical cross section to be compared is expressed in $\text{mb sr}^{-1} \text{ meV}^{-1} \text{ f.u.}^{-1}$.

Resolution considerations

The methods that RESLIB employs were designed to normalize intensity to the incident neutron flux. Since most triple-axis neutron spectrometers do not have a well-defined incident flux and instead normalize intensity to a beam monitor this leads to a discrepancy between absolute cross-section and RESLIB intensity (i.e., the intensity reported when fitting a theoretical model to measured intensity in absolute units via a RESLIB convolution).

If we consider the convolution, f , of a well-normalized function $\int g(\mathcal{Q}) d^4\mathcal{Q} = 1$ (where, for brevity, $\mathcal{Q} \equiv (\mathbf{Q}, E)$ and $\int d^4\mathcal{Q} \equiv \int d^3\mathbf{Q} \int dE$). The discrepancy constant is given by ϕ in

$$\phi \int f[g(\mathcal{Q})] d^4\mathcal{Q} = \int g(\mathcal{Q}) d^4\mathcal{Q}. \quad (\text{D.11})$$

When a dataset, $\mathcal{S}(\mathcal{Q})$, is fit to a convoluted theoretical function, $S(p, \mathcal{Q})$, the model parameters, p , are modified such that the residual,

$$R = \sum_{i=1}^N \{f[S(p, \mathcal{Q}_i)] - \mathcal{S}(\mathcal{Q}_i)\}^2, \quad (\text{D.12})$$

(for N discrete measurements) is minimized. In an ideal situation $R = 0$ which would imply that, for all i ,

$$f[S(p, \mathcal{Q}_i)] - \mathcal{S}(\mathcal{Q}_i) = 0, \quad (\text{D.13})$$

and, in general,

$$\mathcal{S}(\mathcal{Q}) = f[S(p, \mathcal{Q})], \quad (\text{D.14})$$

i.e., the convoluted function and the measured intensity are identical. What we are interested in determining is which parameters of S best represent our data, where instead p are the best-fit parameters for $f[S]$. From equation (D.11) it is clear that $f[g(\mathcal{Q})] = \frac{1}{\phi}g(\mathcal{Q})$, by extension it is evident that the best-fit function to $\mathcal{S}(\mathcal{Q})$ is $S(p, \mathcal{Q})/\phi$. Typically, model functions have only one parameter which determines intensity; if that one parameter is modified such

that $S(p', \mathcal{Q}) = S(p, \mathcal{Q})/\phi$ then the parameters p' are the true best-fit parameters for the theoretical model function S and data \mathcal{S} .

Fortunately, the discrepancy is constant for a particular instrument in one configuration and can be determined by comparing arbitrary-to-absolute scaling factors determined with and without RESLIB convolution of a theoretical model.

Convoluting fitting of measured vanadium

Since equation (D.4) contains a Dirac δ -function, a standard 4D numerical convolution of the resolution function and vanadium cross section is not possible, due to a numerical limitation that the integration grid-size remain finite. Instead, the vanadium cross section must be artificially broadened in order to be fit, yielding the fitting function

$$S(\mathbf{Q}, E) = A_v b^2 e^{Q^2 \langle u^2 \rangle} \frac{1}{\pi} \frac{\Gamma}{\Gamma^2 + E^2} \quad (\text{D.15})$$

which yields the RESLIB arbitrary-to-absolute scaling factor, A_v , when convoluted and fit to vanadium incoherent scattering data.

Convoluting fitting of measured phonons

As with the vanadium case, since equation (D.9) contains a Dirac δ -function a standard 4D numerical convolution of the resolution function and phonon cross section is not possible. Instead, to remove the δ -function analytically, equation (D.9) can be replaced by the function

$$S(\mathbf{Q}, \omega) = \frac{1}{\pi} s(\mathbf{Q}) \frac{\Gamma}{\Gamma^2 + (\omega - \omega_q)^2} \quad (\text{D.16})$$

where an intrinsic Lorentzian energy-width Γ has been introduced, and the transverse acoustic mode intensity and dispersion relation are given by

$$s(Q) = A_p \frac{\hbar^2 (\mathbf{Q} \cdot \hat{\boldsymbol{\tau}})^2}{2\hbar\omega_q \sum_{d'} M_{d'}} \left| \sum_d \bar{b}_d e^{-W_d} e^{i\boldsymbol{\tau} \cdot \mathbf{d}} \right|^2 \frac{1}{1 - e^{-\hbar\omega_q/k_B T}} \quad (\text{D.17})$$

and

$$\omega_q = A_d \sin\left(\frac{c}{4}q\right) \quad (\text{D.18})$$

respectively. This substitution allows for a very quick approximation to the energy convolution and a standard 3D numerical convolution of the momentum space resolution function and equation (D.17) by using RESLIB's `ConvResSMA` function. And allowed for the determination of the variables A_p , A_d , and Γ by fitting the resolution convoluted equation (D.16) to measured TA $(220)_T$ phonon intensity utilizing the RESLIB function `FitConvSMA`. A representative simultaneous best-convoluted-fit is shown for two TA phonons in figure C.2 as the solid red and orange lines.

APPENDIX E NEUTRON SCATTERING BACKGROUND

Neutron scattering experiments always measure a combination of a scattering function, $S(\mathbf{Q}, E)$, and a background function, $B(\mathbf{Q}, E)$, which is the collective intensity of all sources of background such as incoherent scattering from the sample itself, counted neutrons due to inadequate shielding of the source or the detector, or purely stochastic in origin, e.g., due to noise in the detector electronics. As such, for comparison to any theoretical model for the cross-section the measured data, $I(\mathbf{Q}, E)$ must first have an estimate for the background removed,

$$S(\mathbf{Q}, E) = I(\mathbf{Q}, E) - B(\mathbf{Q}, E). \quad (\text{E.1})$$

Triple-axis background estimation

For triple-axis instruments it is common to estimate the background intensity by remeasuring a scan with the sample in a condition to not scatter to the detector. One way to achieve such a condition could be to change the sample temperature above or below an ordering temperature. Another often used method is to rotate the sample angle until a minimum in the measured intensity is found and then repeat the scan, since the background for any neutron spectrometer is independent upon the direction of \mathbf{Q} . The shape of a sample can invalidate the last statement due to sample incoherent scattering and/or sample neutron absorption if it is not isotropic. However, for most cases it is a good approximation to assume that $B(\mathbf{Q}, E) = B(Q, E)$.

Time-of-flight background estimation

Time-of-flight instruments typically have large arrays of position sensitive detectors in order to make efficient use of the low average neutron flux available from pulsed sources. For a direct-geometry time-of-flight neutron spectrometer and a fixed sample orientation, a large position-sensitive detector array measures intensity on a kinematically-defined three-dimensional surface in four-dimensional momentum-energy space. For measurements which intensity-of-interest relatively well localized in momentum, like the magnetic excitations in $\text{Ba}(\text{Fe}_{1-x}\text{TM}_x)_2\text{As}_2$, there are ample detectors in the position sensitive array that measure only background. If one creates a masked dataset, $I_m(\mathbf{Q}, E)$, from the measured intensity, $I(\mathbf{Q}, E)$, in such a way that I_m does not contain any of $S(\mathbf{Q}, E)$ it is possible to estimate $B(Q, E)$ with a high degree of accuracy. In practice, it is easiest to create the background estimate by creating a binned dataset in scattering angle, 2θ , and energy, E , from I_m and then use the result to repopulate intensity into a ‘blank’ detector array. Specifically, by creating bins in the scattering angle that each contain an approximately equal number of detectors (e.g., by selecting bin-boundaries, $2\theta_n \propto n^2$ with $n = 0, 1, 2, \dots$ and using the intrinsic energy-bins) it is possible to create approximately equal-statistics background-estimate bins.

Figure E.1 (a) shows a constant-energy slice through a $\text{Ba}(\text{Fe}_{0.953}\text{Co}_{0.047})_2\text{As}_2$ dataset, $I(\mathbf{Q}, E)$, collected at the time-of-flight spectrometer ARCS. Panel (b) in the same figure shows the same slice through the dataset modified to have all magnetic intensity removed, $I_m(\mathbf{Q}, E)$. Panel (c) shows the same slice through a repopulated ‘blank’ detector where the intensity for every (\mathbf{Q}, E) point has been determined from $B(Q, E)$. Finally, panel (d) shows the same slice through $S(\mathbf{Q}, E) = I(\mathbf{Q}, E) - B(Q, E)$. A different slice, with intensity displayed perpendicular to the $[K \bar{K} 0]$ direction, is shown in figure E.2 for the same datasets. In both figures E.1 and E.2 there are prominent features in the as-measured datasets [panels (a)] that are entirely separate from the magnetic scattering of interest, as evident by their appearance in the background estimates [panels (c)] and absence in the

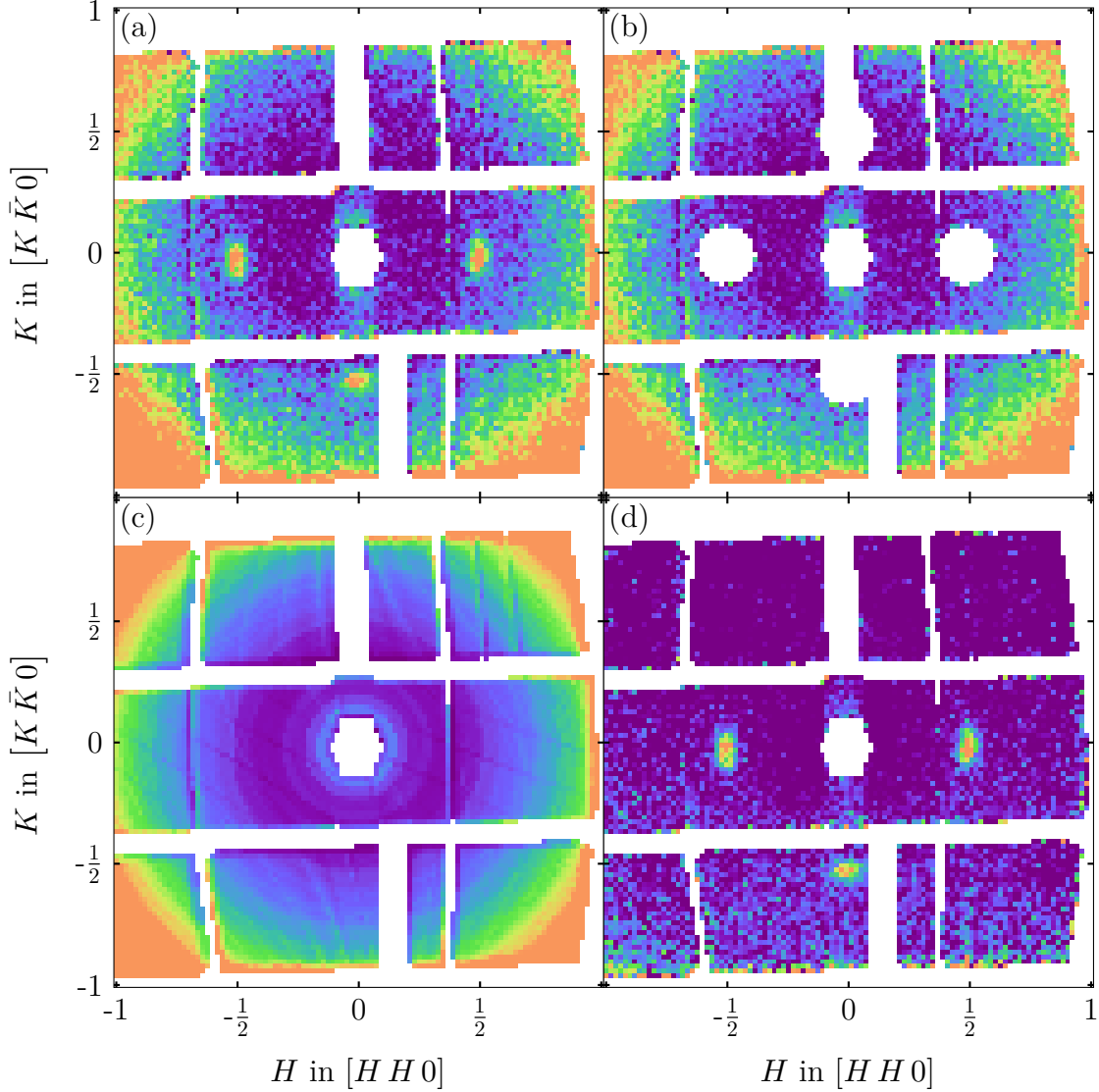


FIGURE E.1. Each panel in this figure shows an identical slice with $4 < E < 10$ meV for data collected on the ARCS spectrometer from the $\text{Ba}(\text{Fe}_{0.953}\text{Co}_{0.047})_2\text{As}_2$ sample, $E_i = 50$ meV and $T = 5$ K. (a) $I(\mathbf{Q}, E)$, the measured intensity. (b) $I_m(\mathbf{Q}, E)$, the measured intensity with all of-interest magnetic intensity removed; leaving only background. (c) A visualization of $B(\mathbf{Q}, E)$, the equal-scattering-angle averaged background estimate made from the masked dataset. (d) $S(\mathbf{Q}, E)$, the difference between panels (a) and (c), is mostly-devoid of background scattering.

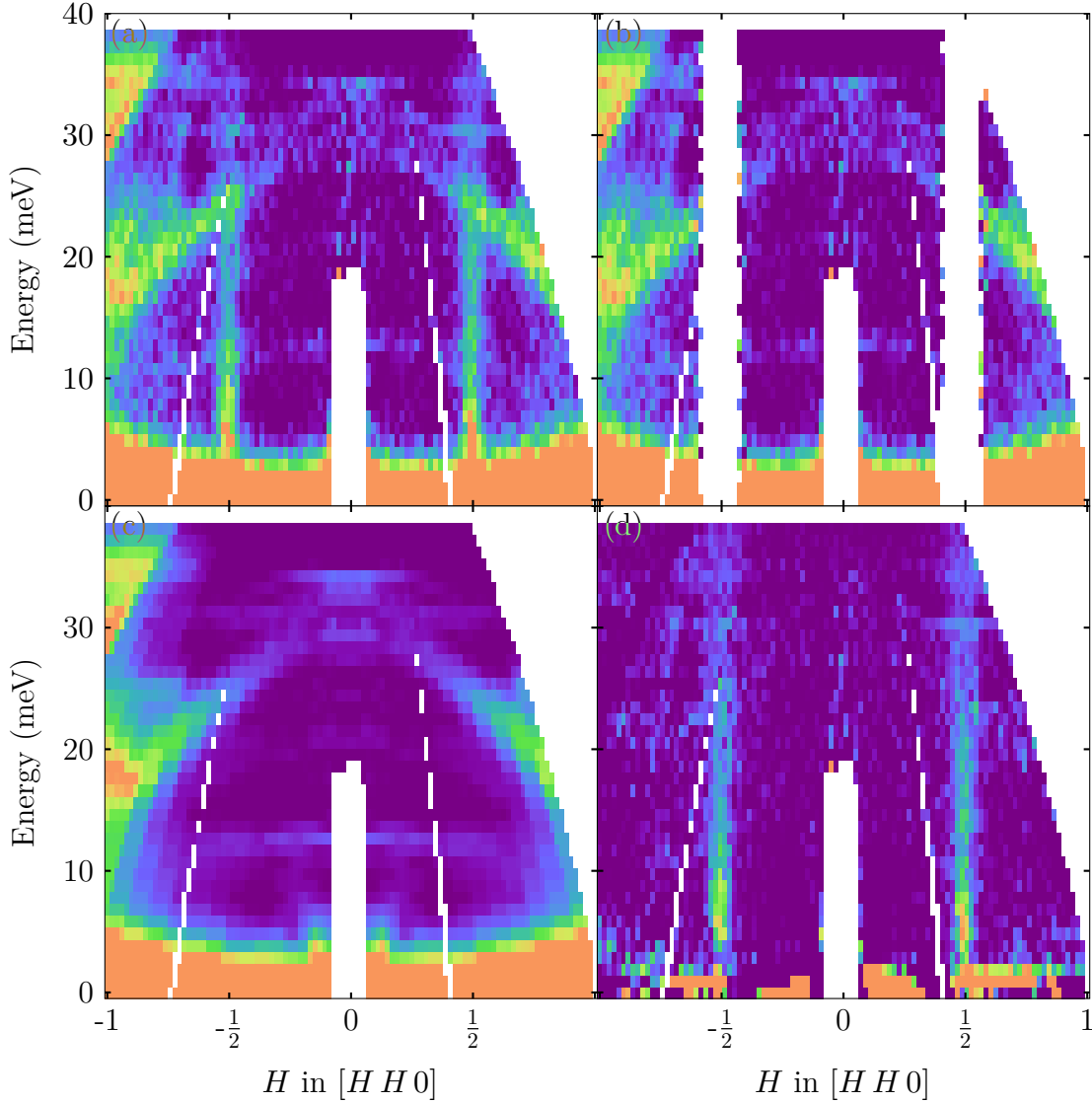


FIGURE E.2. Each panel in this figure shows an identical slice with $-0.1 < [K \bar{K} 0] < 0.1$ r.l.u. for data collected on the ARCS spectrometer from the $\text{Ba}(\text{Fe}_{0.953}\text{Co}_{0.047})_2\text{As}_2$ sample, $E_i = 50$ meV and $T = 5$ K. (a) $I(\mathbf{Q}, E)$, the measured intensity. (b) $I_m(\mathbf{Q}, E)$, the measured intensity with all of-interest magnetic intensity removed; leaving only background. (c) A visualization of, $B(\mathbf{Q}, E)$, the equal-scattering-angle averaged background estimate made from the masked dataset. (d) $S(\mathbf{Q}, E)$, the difference between panels (a) and (c), is mostly-devoid of background scattering.

subtracted datasets [panels (d)]. These background features are common to inelastic neutron scattering datasets collected with aluminum in the beam (typically in the form of a sample holder and/or components of the sample environment) and show aluminum phonons and incoherent scattering. While trained experts likely ignore such features, their presence can be a distraction for novices and such background features inhibit scientific communication. Therefore, it is certainly worth the effort to remove such artifacts when discussion of your data is targeted at the larger physics community.

BIBLIOGRAPHY

- [1] H. Kamerlingh Onnes, “Further experiments with liquid helium. C. On the change of electric resistance of pure metals at very low temperatures etc. IV. The resistance of pure mercury at helium temperatures”, [Proceedings of the Royal Netherlands Academy of Arts and Sciences](#) **13**, 1274 (1911).
- [2] D. v. Delft and P. Kes, “The discovery of superconductivity”, [Physics Today](#) **63**, 38 (2010).
- [3] H. Kamerlingh Onnes, “Further experiments with Liquid Helium G. On the electrical resistance of Pure Metals etc. VI. On the Sudden Change in the Rate at which the Resistance of Mercury Disappears”, [Proceedings of the Royal Netherlands Academy of Arts and Sciences](#) **14**, 818 (1912).
- [4] B. T. Matthias, T. H. Geballe, and V. B. Compton, “Superconductivity”, [Reviews of Modern Physics](#) **35**, 1 (1963).
- [5] J. Schmalian, “Unkonventionell und komplex”, [Physik Journal](#) **10**, 37 (2011).
- [6] A. A. Abrikosov, “Magnetic Properties of Superconductors of the Second Group”, [Soviet Physics – Journal of Experimental and Theoretical Physics](#) **5:6** (1957).
- [7] L. D. Landau, *Electrodynamics of continuous media*, in collab. with L. P. Pitaevskii and E. M. Lifshitz, trans. by J. B. Sykes, J. S. Bell, and M. J. Kearsley (Pergamon, Oxford; New York, 1984), 460 pp.
- [8] H. Fröhlich, “Theory of the Superconducting State. I. The Ground State at the Absolute Zero of Temperature”, [Physical Review](#) **79**, 845 (1950).
- [9] H. Fröhlich, “Isotope Effect in Superconductivity”, [Proceedings of the Physical Society. Section A](#) **63**, 778 (1950).
- [10] J. Bardeen, “Zero-Point Vibrations and Superconductivity”, [Physical Review](#) **79**, 167 (1950).
- [11] J. Bardeen and D. Pines, “Electron-Phonon Interaction in Metals”, [Physical Review](#) **99**, 1140 (1955).
- [12] L. N. Cooper, “Bound Electron Pairs in a Degenerate Fermi Gas”, [Physical Review](#) **104**, 1189 (1956).
- [13] J. Bardeen, L. N. Cooper, and J. R. Schrieffer, “Microscopic Theory of Superconductivity”, [Physical Review](#) **106**, 162 (1957).
- [14] J. Bardeen, L. N. Cooper, and J. R. Schrieffer, “Theory of Superconductivity”, [Physical Review](#) **108**, 1175 (1957).

- [15] K. Burnett, M. Edwards, and C. W. Clark, eds., *Special Issue, Journal of Research of the National Institute of Standards and Technology* 101.4 (1996): *Bose-Einstein Condensation*.
- [16] I. I. Mazin, “Superconductivity gets an iron boost”, [Nature](#) **464**, 183 (2010).
- [17] L. H. Greene, H. Z. Arham, C. R. Hunt, and W. K. Park, “Design of New Superconducting Materials, and Point-Contact Spectroscopy as a Probe of Strong Electron Correlations”, [Journal of Superconductivity and Novel Magnetism](#) **25**, 2121 (2012).
- [18] K. H. Bennemann and J. B. Ketterson, eds., *Superconductivity: Conventional and Unconventional Superconductors* (Springer, Berlin; Heidelberg, DE, 2008).
- [19] G. R. Stewart, “Heavy-fermion systems”, [Reviews of Modern Physics](#) **56**, 755 (1984).
- [20] P. A. Lee, N. Nagaosa, and X.-G. Wen, “Doping a Mott insulator: Physics of high-temperature superconductivity”, [Reviews of Modern Physics](#) **78**, 17 (2006).
- [21] D. Jérôme and H. Schulz, “Organic conductors and superconductors”, [Advances in Physics](#) **31**, 299 (1982).
- [22] J. Singleton and C. Mielke, “Quasi-two-dimensional organic superconductors: A review”, [Contemporary Physics](#) **43**, 63 (2002).
- [23] K. Miyake, S. Schmitt-Rink, and C. M. Varma, “Spin-fluctuation-mediated even-parity pairing in heavy-fermion superconductors”, [Physical Review B](#) **34**, 6554 (1986).
- [24] P. Monthoux and D. Pines, “YBa₂Cu₃O₇: A nearly antiferromagnetic Fermi liquid”, [Physical Review B](#) **47**, 6069 (1993).
- [25] V. J. Emery, “Some basic questions in organic superconductivity”, [Le Journal de Physique Colloques](#) **44**, C3 (1983).
- [26] V. J. Emery, “The mechanisms of organic superconductivity”, [Synthetic Metals](#) **13**, 21 (1986).
- [27] G. Knebel, J. Buhot, D. Aoki, G. Lapertot, S. Raymond, E. Ressouche, and J. Flouquet, “Antiferromagnetism and Superconductivity in CeRhIn₅”, [Journal of the Physical Society of Japan](#) **80**, SA001 (2011).
- [28] N. P. Armitage, P. Fournier, and R. L. Greene, “Progress and perspectives on electron-doped cuprates”, [Reviews of Modern Physics](#) **82**, 2421 (2010).
- [29] G. R. Stewart, “Superconductivity in iron compounds”, [Reviews of Modern Physics](#) **83**, 1589 (2011).
- [30] A. V. Balatsky, I. Vekhter, and J.-X. Zhu, “Impurity-induced states in conventional and unconventional superconductors”, [Reviews of Modern Physics](#) **78**, 373 (2006).
- [31] B. S. Chandrasekhar and J. K. Hulm, “The electrical resistivity and superconductivity of some uranium alloys and compounds”, [Journal of Physics and Chemistry of Solids](#) **7**, 259 (1958).
- [32] B. T. Matthias, V. B. Compton, and E. Corenzwit, “Some new superconducting compounds”, [Journal of Physics and Chemistry of Solids](#) **19**, 130 (1961).

- [33] H. F. Braun, “Superconductivity of rare earth-iron silicides”, *Physics Letters A* **75**, 386 (1980).
- [34] G. P. Meisner, “Superconductivity and magnetic order in ternary rare earth transition metal phosphides”, *Physica B+C* **108**, 763 (1981).
- [35] A. W. Graham, M. Kurmoo, and P. Day, “ β'' -(bedt-ttf)₄[(H₂O)Fe(C₂O₄)₃] · PhCN: the first molecular superconductor containing paramagnetic metal ions”, *Journal of the Chemical Society, Chemical Communications*, 2061 (1995).
- [36] I. Shirotni, Y. Shimaya, K. Kihou, C. Sekine, N. Takeda, M. Ishikawa, and T. Yagi, “Superconductivity of new filled skutterudite YFe₄P₁₂ prepared at high pressure”, *Journal of Physics: Condensed Matter* **15**, S2201 (2003).
- [37] Y. Kamihara, H. Hiramatsu, M. Hirano, R. Kawamura, H. Yanagi, T. Kamiya, and H. Hosono, “Iron-Based Layered Superconductor: LaOFeP”, *Journal of the American Chemical Society* **128**, 10012 (2006).
- [38] Y. Kamihara, T. Watanabe, M. Hirano, and H. Hosono, “Iron-Based Layered Superconductor LaO_{1-x}F_xFeAs ($x = 0.05 - 0.12$) with $T_c = 26$ K”, *Journal of the American Chemical Society* **130**, 3296 (2008).
- [39] D. C. Johnston, “The puzzle of high temperature superconductivity in layered iron pnictides and chalcogenides”, *Advances in Physics* **59**, 803 (2010).
- [40] H. Takahashi, K. Igawa, K. Arii, Y. Kamihara, M. Hirano, and H. Hosono, “Superconductivity at 43 K in an iron-based layered compound LaO_{1-x}F_xFeAs”, *Nature* **453**, 376 (2008).
- [41] Z.-A. Ren, J. Yang, W. Lu, W. Yi, X.-L. Shen, Z.-C. Li, G.-C. Che, X.-L. Dong, L.-L. Sun, F. Zhou, and Z.-X. Zhao, “Superconductivity in the iron-based F-doped layered quaternary compound NdO_{1-x}F_xFeAs”, *Europhysics Letters* **82**, 57002 (2008).
- [42] H. Kito, H. Eisaki, and A. Iyo, “Superconductivity at 54 K in F-Free NdFeAsO_{1-y}”, *Journal of the Physical Society of Japan* **77**, 063707 (2008).
- [43] R. Zhi-An, L. Wei, Y. Jie, Y. Wei, S. Xiao-Li, Zheng-Cai, C. Guang-Can, D. Xiao-Li, S. Li-Ling, Z. Fang, and Z. Zhong-Xian, “Superconductivity at 55 K in Iron-Based F-Doped Layered Quaternary Compound Sm(O_{1-x}F_x)FeAs”, *Chinese Physics Letters* **25**, 2215 (2008).
- [44] C. Wang, L. Li, S. Chi, Z. Zhu, Z. Ren, Y. Li, Y. Wang, X. Lin, Y. Luo, S. Jiang, X. Xu, G. Cao, and Z. Xu, “Thorium-doping-induced superconductivity up to 56 K in Gd_{1-x}Th_xFeAsO”, *Europhysics Letters* **83**, 67006 (2008).
- [45] N. Takeshita, A. Iyo, H. Eisaki, H. Kito, and T. Ito, “Remarkable Suppression of T_c by Pressure in NdFeAsO_{1-y} ($y = 0.4$)”, *Journal of the Physical Society of Japan* **77**, 075003 (2008).
- [46] G. Wu, R. H. Liu, H. Chen, Y. J. Yan, T. Wu, Y. L. Xie, J. J. Ying, X. F. Wang, D. F. Fang, and X. H. Chen, “Transport properties and superconductivity in Ba_{1-x}M_xFe₂As₂ ($M=La$ and K) with double FeAs layers”, *EPL (Europhysics Letters)* **84**, 27010 (2008).

- [47] C. Krellner, N. Caroca-Canales, A. Jesche, H. Rosner, A. Ormeci, and C. Geibel, “Magnetic and structural transitions in layered iron arsenide systems: $A\text{Fe}_2\text{As}_2$ versus $R\text{FeAsO}$ ”, *Physical Review B* **78**, 100504 (2008).
- [48] K. Sasmal, B. Lv, B. Lorenz, A. M. Guloy, F. Chen, Y.-Y. Xue, and C.-W. Chu, “Superconducting Fe-Based Compounds ($A_{1-x}\text{Sr}_x$) Fe_2As_2 with $A=\text{K}$ and Cs with Transition Temperatures up to 37 K”, *Physical Review Letters* **101**, 107007 (2008).
- [49] X. C. Wang, Q. Q. Liu, Y. X. Lv, W. B. Gao, L. X. Yang, R. C. Yu, F. Y. Li, and C. Q. Jin, “The superconductivity at 18 K in LiFeAs system”, *Solid State Communications* **148**, 538 (2008).
- [50] M. J. Pitcher, D. R. Parker, P. Adamson, S. J. C. Herkelrath, A. T. Boothroyd, R. M. Ibberson, M. Brunelli, and S. J. Clarke, “Structure and superconductivity of LiFeAs ”, *Chemical Communications*, 5918 (2008).
- [51] Z. Deng, X. C. Wang, Q. Q. Liu, S. J. Zhang, Y. X. Lv, J. L. Zhu, R. C. Yu, and C. Q. Jin, “A new ‘111’ type iron pnictide superconductor LiFeP ”, *EPL (Europhysics Letters)* **87**, 37004 (2009).
- [52] F.-C. Hsu, J.-Y. Luo, K.-W. Yeh, T.-K. Chen, T.-W. Huang, P. M. Wu, Y.-C. Lee, Y.-L. Huang, Y.-Y. Chu, D.-C. Yan, and M.-K. Wu, “Superconductivity in the PbO -type structure $\alpha\text{-FeSe}$ ”, *Proceedings of the National Academy of Sciences* **105**, 14262 (2008).
- [53] E. Colombier, S. L. Bud’ko, N. Ni, and P. C. Canfield, “Complete pressure-dependent phase diagrams for SrFe_2As_2 and BaFe_2As_2 ”, *Physical Review B* **79**, 224518 (2009).
- [54] M. Rotter, M. Tegel, and D. Johrendt, “Superconductivity at 38 K in the Iron Arsenide ($\text{Ba}_{1-x}\text{K}_x$) Fe_2As_2 ”, *Physical Review Letters* **101**, 107006 (2008).
- [55] S. Jiang, H. Xing, G. Xuan, C. Wang, Z. Ren, C. Feng, J. Dai, Z. Xu, and G. Cao, “Superconductivity up to 30 K in the vicinity of the quantum critical point in $\text{BaFe}_2(\text{As}_{1-x}\text{P}_x)_2$ ”, *Journal of Physics: Condensed Matter* **21**, 382203 (2009).
- [56] N. Ni, A. Thaler, J. Q. Yan, A. Kracher, E. Colombier, S. L. Bud’ko, P. C. Canfield, and S. T. Hannahs, “Temperature versus doping phase diagrams for $\text{Ba}(\text{Fe}_{1-x}\text{TM}_x)_2\text{As}_2$ ($\text{TM}=\text{Ni}, \text{Cu}, \text{Cu/Co}$) single crystals”, *Physical Review B* **82**, 024519 (2010).
- [57] M. G. Kim, R. M. Fernandes, A. Kreyssig, J. W. Kim, A. Thaler, S. L. Bud’ko, P. C. Canfield, R. J. McQueeney, J. Schmalian, and A. I. Goldman, “Character of the structural and magnetic phase transitions in the parent and electron-doped BaFe_2As_2 compounds”, *Physical Review B* **83**, 134522 (2011).
- [58] A. S. Sefat, R. Jin, M. A. McGuire, B. C. Sales, D. J. Singh, and D. Mandrus, “Superconductivity at 22 K in Co-Doped BaFe_2As_2 Crystals”, *Physical Review Letters* **101**, 117004 (2008).
- [59] N. W. Ashcroft and N. D. Mermin, *Solid State Physics* (Holt, Rinehart and Winston, 1976), 856 pp.

- [60] N. Ni, M. E. Tillman, J.-Q. Yan, A. Kracher, S. T. Hannahs, S. L. Bud'ko, and P. C. Canfield, "Effects of Co substitution on thermodynamic and transport properties and anisotropic H_{c2} in $\text{Be}(\text{Fe}_{1-x}\text{Co}_x)_2\text{As}_2$ single crystals", [Physical Review B **78**, 214515 \(2008\)](#).
- [61] S. Nandi, M. G. Kim, A. Kreyssig, R. M. Fernandes, D. K. Pratt, A. Thaler, N. Ni, S. L. Bud'ko, P. C. Canfield, J. Schmalian, R. J. McQueeney, and A. I. Goldman, "Anomalous Suppression of the Orthorhombic Lattice Distortion in Superconducting $\text{Be}(\text{Fe}_{1-x}\text{Co}_x)_2\text{As}_2$ Single Crystals", [Physical Review Letters **104**, 057006 \(2010\)](#).
- [62] R. M. Fernandes, D. K. Pratt, W. Tian, J. Zarestky, A. Kreyssig, S. Nandi, M. G. Kim, A. Thaler, N. Ni, P. C. Canfield, R. J. McQueeney, J. Schmalian, and A. I. Goldman, "Unconventional pairing in the iron arsenide superconductors", [Physical Review B **81**, 140501 \(2010\)](#).
- [63] D. K. Pratt, M. G. Kim, A. Kreyssig, Y. B. Lee, G. S. Tucker, A. Thaler, W. Tian, J. L. Zarestky, S. L. Bud'ko, P. C. Canfield, B. N. Harmon, A. I. Goldman, and R. J. McQueeney, "Incommensurate Spin-Density Wave Order in Electron-Doped BaFe_2As_2 Superconductors", [Physical Review Letters **106**, 257001 \(2011\)](#).
- [64] J. Fink, S. Thirupathaiah, R. Ovsyannikov, H. A. Dürr, R. Follath, Y. Huang, S. de Jong, M. S. Golden, Y.-Z. Zhang, H. O. Jeschke, R. Valentí, C. Felser, S. Dastjani Farahani, M. Rotter, and D. Johrendt, "Electronic structure studies of BaFe_2As_2 by angle-resolved photoemission spectroscopy", [Physical Review B **79**, 155118 \(2009\)](#).
- [65] C. Liu, T. Kondo, R. M. Fernandes, A. D. Palczewski, E. D. Mun, N. Ni, A. N. Thaler, A. Bostwick, E. Rotenberg, J. Schmalian, S. L. Bud'ko, P. C. Canfield, and A. Kaminski, "Evidence for a Lifshitz transition in electron-doped iron arsenic superconductors at the onset of superconductivity", [Nature Physics **6**, 419 \(2010\)](#).
- [66] M. Yi, D. Lu, J.-H. Chu, J. G. Analytis, A. P. Sorini, A. F. Kemper, B. Moritz, S.-K. Mo, R. G. Moore, M. Hashimoto, W.-S. Lee, Z. Hussain, T. P. Devereaux, I. R. Fisher, and Z.-X. Shen, "Symmetry-breaking orbital anisotropy observed for detwinned $\text{Be}(\text{Fe}_{1-x}\text{Co}_x)_2\text{As}_2$ above the spin density wave transition", [Proceedings of the National Academy of Sciences **108**, 6878 \(2011\)](#).
- [67] M. G. Kim, D. K. Pratt, G. E. Rustan, W. Tian, J. L. Zarestky, A. Thaler, S. L. Bud'ko, P. C. Canfield, R. J. McQueeney, A. Kreyssig, and A. I. Goldman, "Magnetic ordering and structural distortion in Ru-doped BaFe_2As_2 single crystals studied by neutron and x-ray diffraction", [Physical Review B **83**, 054514 \(2011\)](#).
- [68] A. D. Christianson, M. D. Lumsden, O. Delaire, M. B. Stone, D. L. Abernathy, M. A. McGuire, A. S. Sefat, R. Jin, B. C. Sales, D. Mandrus, E. D. Mun, P. C. Canfield, J. Y. Y. Lin, M. Lucas, M. Kresch, J. B. Keith, B. Fultz, E. A. Goremychkin, and R. J. McQueeney, "Phonon Density of States of $\text{LaFeAsO}_{1-x}\text{F}_x$ ", [Physical Review Letters **101**, 157004 \(2008\)](#).
- [69] L. W. Harriger, M. Liu, H. Luo, R. A. Ewings, C. D. Frost, T. G. Perring, and P. Dai, "Temperature dependence of the paramagnetic spin excitations in BaFe_2As_2 ", [Physical Review B **86**, 140403 \(2012\)](#).

- [70] D. S. Inosov, J. T. Park, P. Bourges, D. L. Sun, Y. Sidis, A. Schneidewind, K. Hradil, D. Haug, C. T. Lin, B. Keimer, and V. Hinkov, “Normal-state spin dynamics and temperature-dependent spin-resonance energy in optimally doped $\text{BaFe}_{1.85}\text{Co}_{0.15}\text{As}_2$ ”, [Nature Physics](#) **6**, 178 (2010).
- [71] R. M. Fernandes and J. Schmalian, “Competing order and nature of the pairing state in the iron pnictides”, [Physical Review B](#) **82**, 014521 (2010).
- [72] S. Maiti, J. Knolle, I. Eremin, and A. Chubukov, “Effect of nodes, ellipticity, and impurities on the spin resonance in iron-based superconductors”, [Physical Review B](#) **84**, 144524 (2011).
- [73] S. Onari and H. Kontani, “Neutron inelastic scattering peak by dissipationless mechanism in the s_{++} -wave state in iron-based superconductors”, [Physical Review B](#) **84**, 144518 (2011).
- [74] C. Kittel, *Introduction to Solid State Physics*, 8th edition (Wiley, Hoboken, NJ, 2004), 704 pp.
- [75] K. Nakamura and P. D. Group, “Review of Particle Physics”, [Journal of Physics G: Nuclear and Particle Physics](#) **37**, 075021 (2010).
- [76] J. Chadwick, “Possible Existence of a Neutron”, [Nature](#) **129**, 312 (1932).
- [77] G. L. Squires, *Introduction to the Theory of Thermal Neutron Scattering*, 3rd edition (Cambridge University Press, Cambridge; New York, 2012), 272 pp.
- [78] S. W. Lovesey, *The Theory of Neutron Scattering from Condensed Matter: Volume II* (Oxford University Press, Oxford, 1986), 310 pp.
- [79] S. W. Lovesey, *The Theory of Neutron Scattering from Condensed Matter: Volume I* (Oxford University Press, Oxford, 1986), 270 pp.
- [80] G. Shirane, S. M. Shapiro, and J. M. Tranquada, *Neutron Scattering with a Triple-Axis Spectrometer: Basic Techniques* (Cambridge University Press, New York, 2002), 284 pp.
- [81] S. Itoh, K. Ueno, and T. Yokoo, “Fermi chopper developed at KEK”, [Nuclear Instruments and Methods in Physics Research Section A: Accelerators, Spectrometers, Detectors and Associated Equipment](#) **661**, 58 (2012).
- [82] D. L. Abernathy, M. B. Stone, M. J. Loguillo, M. S. Lucas, O. Delaire, X. Tang, J. Y. Y. Lin, and B. Fultz, “Design and operation of the wide angular-range chopper spectrometer ARCS at the Spallation Neutron Source”, [Review of Scientific Instruments](#) **83**, 015114 (2012).
- [83] F. Weber, S. Rosenkranz, L. Pintschovius, J.-P. Castellan, R. Osborn, W. Reichardt, R. Heid, K.-P. Bohnen, E. A. Goremychkin, A. Kreyssig, K. Hradil, and D. L. Abernathy, “Electron-Phonon Coupling in the Conventional Superconductor $\text{YNi}_2\text{B}_2\text{C}$ at High Phonon Energies Studied by Time-of-Flight Neutron Spectroscopy”, [Physical Review Letters](#) **109**, 057001 (2012).

- [84] R. A. Ewings, T. G. Perring, R. I. Bewley, T. Guidi, M. J. Pitcher, D. R. Parker, S. J. Clarke, and A. T. Boothroyd, “High-energy spin excitations in BaFe_2As_2 observed by inelastic neutron scattering”, [Physical Review B](#) **78**, 220501 (2008).
- [85] J. F. Nye, *Physical properties of crystals: their representation by tensors and matrices* (Clarendon Press, Oxford, 1957).
- [86] A. V. Chubukov, B. Jankó, and O. Tchernyshyov, “Dispersion of the neutron resonance in cuprate superconductors”, [Physical Review B](#) **63**, 180507 (2001).
- [87] M. G. Kim, G. S. Tucker, D. K. Pratt, S. Ran, A. Thaler, A. D. Christianson, K. Marty, S. Calder, A. Podlesnyak, S. L. Bud’ko, P. C. Canfield, A. Kreyssig, A. I. Goldman, and R. J. McQueeney, “Magnonlike Dispersion of Spin Resonance in Ni-doped BaFe_2As_2 ”, [Physical Review Letters](#) **110**, 177002 (2013).
- [88] O. Arnold, J. C. Bilheux, J. M. Borreguero, A. Buts, S. I. Campbell, L. Chapon, M. Doucet, N. Draper, R. Ferraz Leal, M. A. Gigg, V. E. Lynch, A. Markvardsen, D. J. Mikkelsen, R. L. Mikkelsen, R. Miller, K. Palmen, P. Parker, G. Passos, T. G. Perring, P. F. Peterson, S. Ren, M. A. Reuter, A. T. Savici, J. W. Taylor, R. J. Taylor, R. Tolchenov, W. Zhou, and J. Zikovsky, “Mantid—Data analysis and visualization package for neutron scattering and SR experiments”, [Nuclear Instruments and Methods in Physics Research Section A: Accelerators, Spectrometers, Detectors and Associated Equipment](#) **764**, 156 (2014).
- [89] M. J. Cooper and R. Nathans, “The resolution function in neutron diffractometry. I. The resolution function of a neutron diffractometer and its application to phonon measurements”, [Acta Crystallographica](#) **23**, 357 (1967).
- [90] M. Popovici, “On the resolution of slow-neutron spectrometers. IV. The triple-axis spectrometer resolution function, spatial effects included”, [Acta Crystallographica Section A: Crystal Physics, Diffraction, Theoretical and General Crystallography](#) **31**, 507 (1975).
- [91] G. S. Tucker, R. M. Fernandes, H.-F. Li, V. Thampy, N. Ni, D. L. Abernathy, S. L. Bud’ko, P. C. Canfield, D. Vaknin, J. Schmalian, and R. J. McQueeney, “Magnetic excitations in underdoped $\text{Be}(\text{Fe}_{1-x}\text{Co}_x)_2\text{As}_2$ with $x=0.047$ ”, [Physical Review B](#) **86**, 024505 (2012).
- [92] G. S. Tucker, R. M. Fernandes, D. K. Pratt, A. Thaler, N. Ni, K. Marty, A. D. Christianson, M. D. Lumsden, B. C. Sales, A. S. Sefat, S. L. Bud’ko, P. C. Canfield, A. Kreyssig, A. I. Goldman, and R. J. McQueeney, “Crossover from spin waves to diffusive spin excitations in underdoped $\text{Be}(\text{Fe}_{1-x}\text{Co}_x)_2\text{As}_2$ ”, [Physical Review B](#) **89**, 180503 (2014).
- [93] B. Fultz, *Distributed Data Analysis for Neutron Scattering Experiments*, Mar. 2009.
- [94] R. Coldea, *MSLICE*, version 248, Rutherford Appleton Laboratory, UK, June 11, 2013.

- [95] S. O. Diallo, V. P. Antropov, T. G. Perring, C. Broholm, J. J. Pulikkotil, N. Ni, S. L. Bud'ko, P. C. Canfield, A. Kreyssig, A. I. Goldman, and R. J. McQueeney, "Itinerant Magnetic Excitations in Antiferromagnetic CaFe_2As_2 ", [Physical Review Letters](#) **102**, 187206 (2009).
- [96] L. W. Harriger, H. Q. Luo, M. S. Liu, C. Frost, J. P. Hu, M. R. Norman, and P. Dai, "Nematic spin fluid in the tetragonal phase of BaFe_2As_2 ", [Physical Review B](#) **84**, 054544 (2011).
- [97] H.-F. Li, C. Broholm, D. Vaknin, R. M. Fernandes, D. L. Abernathy, M. B. Stone, D. K. Pratt, W. Tian, Y. Qiu, N. Ni, S. O. Diallo, J. L. Zarestky, S. L. Bud'ko, P. C. Canfield, and R. J. McQueeney, "Anisotropic and quasipropagating spin excitations in superconducting $\text{Be}(\text{Fe}_{0.926}\text{Co}_{0.074})_2\text{As}_2$ ", [Physical Review B](#) **82**, 140503 (2010).
- [98] A. Zheludev, *ResLib*, version 3.4c, Oct. 2009.
- [99] G. Xu, Z. Xu, and J. M. Tranquada, "Absolute cross-section normalization of magnetic neutron scattering data", [Review of Scientific Instruments](#) **84**, 083906 (2013).
- [100] C. Lester, J.-H. Chu, J. G. Analytis, T. G. Perring, I. R. Fisher, and S. M. Hayden, "Dispersive spin fluctuations in the nearly optimally doped superconductor $\text{Be}(\text{Fe}_{1-x}\text{Co}_x)_2\text{As}_2$ ($x=0.065$)", [Physical Review B](#) **81**, 064505 (2010).
- [101] J. Zhao, D. T. Adroja, D.-X. Yao, R. Bewley, S. Li, X. F. Wang, G. Wu, X. H. Chen, J. Hu, and P. Dai, "Spin waves and magnetic exchange interactions in CaFe_2As_2 ", [Nature Physics](#) **5**, 555 (2009).
- [102] S. O. Diallo, D. K. Pratt, R. M. Fernandes, W. Tian, J. L. Zarestky, M. Lumsden, T. G. Perring, C. L. Broholm, N. Ni, S. L. Bud'ko, P. C. Canfield, H.-F. Li, D. Vaknin, A. Kreyssig, A. I. Goldman, and R. J. McQueeney, "Paramagnetic spin correlations in CaFe_2As_2 single crystals", [Physical Review B](#) **81**, 214407 (2010).
- [103] J. T. Park, D. S. Inosov, A. Yaresko, S. Graser, D. L. Sun, P. Bourges, Y. Sidis, Y. Li, J.-H. Kim, D. Haug, A. Ivanov, K. Hradil, A. Schneidewind, P. Link, E. Faulhaber, I. Glavatskyy, C. T. Lin, B. Keimer, and V. Hinkov, "Symmetry of spin excitation spectra in the tetragonal paramagnetic and superconducting phases of 122-ferropnictides", [Physical Review B](#) **82**, 134503 (2010).
- [104] P. Goswami, R. Yu, Q. Si, and E. Abrahams, "Spin dynamics of a J_1 - J_2 antiferromagnet and its implications for iron pnictides", [Physical Review B](#) **84**, 155108 (2011).
- [105] R. A. Ewings, T. G. Perring, J. Gillett, S. D. Das, S. E. Sebastian, A. E. Taylor, T. Guidi, and A. T. Boothroyd, "Itinerant spin excitations in SrFe_2As_2 measured by inelastic neutron scattering", [Physical Review B](#) **83**, 214519 (2011).
- [106] H. Park, K. Haule, and G. Kotliar, "Magnetic Excitation Spectra in BaFe_2As_2 : A Two-Particle Approach within a Combination of the Density Functional Theory and the Dynamical Mean-Field Theory Method", [Physical Review Letters](#) **107**, 137007 (2011).

- [107] J. T. Park, G. Friemel, T. Loew, V. Hinkov, Y. Li, B. H. Min, D. L. Sun, A. Ivanov, A. Piovano, C. T. Lin, B. Keimer, Y. S. Kwon, and D. S. Inosov, “Similar zone-center gaps in the low-energy spin-wave spectra of $\text{Na}_{1-\delta}\text{FeAs}$ and BaFe_2As_2 ”, [Physical Review B **86**, 024437 \(2012\)](#).
- [108] M. Ramazanoglu, J. Lamsal, G. S. Tucker, J.-Q. Yan, S. Calder, T. Guidi, T. Perring, R. W. McCallum, T. A. Lograsso, A. Kreyssig, A. I. Goldman, and R. J. McQueeney, “Two-dimensional magnetic interactions in LaFeAsO ”, [Physical Review B **87**, 140509 \(2013\)](#).
- [109] R. S. Fishman and S. H. Liu, “Spin-wave gap and spin dynamics of γ -Mn alloys”, [Physical Review B **58**, R5912 \(1998\)](#).
- [110] I. Eremin and A. V. Chubukov, “Magnetic degeneracy and hidden metallicity of the spin-density-wave state in ferropnictides”, [Physical Review B **81**, 024511 \(2010\)](#).
- [111] K. Matan, S. Ibuka, R. Morinaga, S. Chi, J. W. Lynn, A. D. Christianson, M. D. Lumsden, and T. J. Sato, “Doping dependence of spin dynamics in electron-doped $\text{Be}(\text{Fe}_{1-x}\text{Co}_x)_2\text{As}_2$ ”, [Physical Review B **82**, 054515 \(2010\)](#).
- [112] J. W. Lynn, “Temperature dependence of the magnetic excitations in iron”, [Physical Review B **11**, 2624 \(1975\)](#).
- [113] J. P. Wicksted, P. Böni, and G. Shirane, “Polarized-beam study of the paramagnetic scattering from bcc iron”, [Physical Review B **30**, 3655 \(1984\)](#).
- [114] R. M. Fernandes, A. V. Chubukov, J. Knolle, I. Eremin, and J. Schmalian, “Preemptive nematic order, pseudogap, and orbital order in the iron pnictides”, [Physical Review B **85**, 024534 \(2012\)](#).
- [115] Q. Si and E. Abrahams, “Strong Correlations and Magnetic Frustration in the High T_c Iron Pnictides”, [Physical Review Letters **101**, 076401 \(2008\)](#).
- [116] R. Yu, Z. Wang, P. Goswami, A. H. Nevidomskyy, Q. Si, and E. Abrahams, “Spin dynamics of a J_1 - J_2 - K model for the paramagnetic phase of iron pnictides”, [Physical Review B **86**, 085148 \(2012\)](#).
- [117] T. M. Rice, “Band-Structure Effects in Itinerant Antiferromagnetism”, [Physical Review B **2**, 3619 \(1970\)](#).
- [118] W. Z. Hu, J. Dong, G. Li, Z. Li, P. Zheng, G. F. Chen, J. L. Luo, and N. L. Wang, “Origin of the Spin Density Wave Instability in $A\text{Fe}_2\text{As}_2$ ($A=\text{Ba},\text{Sr}$) as Revealed by Optical Spectroscopy”, [Physical Review Letters **101**, 257005 \(2008\)](#).
- [119] A. B. Vorontsov, M. G. Vavilov, and A. V. Chubukov, “Superconductivity and spin-density waves in multiband metals”, [Physical Review B **81**, 174538 \(2010\)](#).
- [120] S. Sachdev, *Quantum phase transitions* (Cambridge University Press, Cambridge; New York, 2011).

- [121] D. K. Pratt, W. Tian, A. Kreyssig, J. L. Zarestky, S. Nandi, N. Ni, S. L. Bud'ko, P. C. Canfield, A. I. Goldman, and R. J. McQueeney, "Coexistence of Competing Antiferromagnetic and Superconducting Phases in the Underdoped $\text{Be}(\text{Fe}_{0.953}\text{Co}_{0.047})_2\text{As}_2$ Compound Using X-ray and Neutron Scattering Techniques", [Physical Review Letters](#) **103**, 087001 (2009).
- [122] A. D. Christianson, M. D. Lumsden, S. E. Nagler, G. J. MacDougall, M. A. McGuire, A. S. Sefat, R. Jin, B. C. Sales, and D. Mandrus, "Static and Dynamic Magnetism in Underdoped Superconductor $\text{BaFe}_{1.92}\text{Co}_{0.08}\text{As}_2$ ", [Physical Review Letters](#) **103**, 087002 (2009).
- [123] T. J. Sato, K. Matan, S. Ibuka, R. Morinaga, S. Chi, J. W. Lynn, A. D. Christianson, and M. D. Lumsden, "Erratum: Doping dependence of spin dynamics in electron-doped $\text{Be}(\text{Fe}_{1-x}\text{Co}_x)_2\text{As}_2$ [Phys. Rev. B 82, 054515 (2010)]", [Physical Review B](#) **83**, 059901 (2011).
- [124] M. Wang, C. Zhang, X. Lu, G. Tan, H. Luo, Y. Song, M. Wang, X. Zhang, E. A. Goremychkin, T. G. Perring, T. A. Maier, Z. Yin, K. Haule, G. Kotliar, and P. Dai, "Doping dependence of spin excitations and its correlations with high-temperature superconductivity in iron pnictides", [Nature Communications](#) **4**, 2874 (2013).
- [125] G. S. Tucker, D. K. Pratt, M. G. Kim, S. Ran, A. Thaler, G. E. Granroth, K. Marty, W. Tian, J. L. Zarestky, M. D. Lumsden, S. L. Bud'ko, P. C. Canfield, A. Kreyssig, A. I. Goldman, and R. J. McQueeney, "Competition between stripe and checkerboard magnetic instabilities in Mn-doped BaFe_2As_2 ", [Physical Review B](#) **86**, 020503 (2012).
- [126] D. K. Pratt, A. Kreyssig, S. Nandi, N. Ni, A. Thaler, M. D. Lumsden, W. Tian, J. L. Zarestky, S. L. Bud'ko, P. C. Canfield, A. I. Goldman, and R. J. McQueeney, "Dispersion of the superconducting spin resonance in underdoped and antiferromagnetic BaFe_2As_2 ", [Physical Review B](#) **81**, 140510 (2010).
- [127] M. G. Kim, J. Lamsal, T. W. Heitmann, G. S. Tucker, D. K. Pratt, S. N. Khan, Y. B. Lee, A. Alam, A. Thaler, N. Ni, S. Ran, S. L. Bud'ko, K. J. Marty, M. D. Lumsden, P. C. Canfield, B. N. Harmon, D. D. Johnson, A. Kreyssig, R. J. McQueeney, and A. I. Goldman, "Effects of Transition Metal Substitutions on the Incommensurability and Spin Fluctuations in BaFe_2As_2 by Elastic and Inelastic Neutron Scattering", [Physical Review Letters](#) **109**, 167003 (2012).
- [128] M. D. Lumsden, L. Robertson, and M. Yethiraj, *Spectrometer Instrument Control Environment*, Oak Ridge National Laboratory.